Low Temperature Capacitive Dilatometry on Quadrupolar Kondo Metals

Dissertation

zur Erlangung des akademischen Grades

Dr. rer. nat.

eingereicht an der Mathematisch-Naturwissenschaftlich-Technischen

Fakultät

der Universität Augsburg

von

Andreas Stephan Wörl

Augsburg, Oktober 2021

Erstgutachter: Prof. Dr. Philipp Gegenwart
Zweitgutachter: Priv.-Doz. Dr. Hans-Albrecht Krug von Nidda
Drittgutachter: Prof. Dr. Michael Lang
Tag der mündlichen Prüfung: 11. Februar 2022

List of Abbreviations

AFQ Antiferroquadrupolar

AF Antiferro

AFM Antiferromagnetic

CEF Crystal electric field

CMN Cerium magnesium nitrate

EPMA Electron probe microanalysis

F Ferro

FH Ferrohastatic

FL Fermi liquid

FQ Ferroquadrupolar

HF Heavy-fermion

NFL Non-Fermi liquid

QC Quantum criticality

QCP Quantum critical point

QPT Quantum phase transition

RKKY Ruderman-Kittel-Kasuya-Yosida

RRR Residual resistivity ratio

RTL Random two level

SM Supplemental material

TRP Temperature regulation plate

Contents

Chapter 1

Introduction

With its numerous discoveries that paved the way for groundbreaking technological advancement and innovation, fundamental solid state research plays a decisive role in shaping the society of today. One of its many subdisciplines is the field of strongly correlated electron physics. As the name implies, the research area covers physical phenomena that arise from the interaction between electrons. A prime example of such an effect is the Mott insulating state. Here, the Coulomb repulsion between electrons causes insulating behavior in a material that would theoretically classify as electrically conductive [1]. Another well studied electronic correlation phenomenon is the heavy-fermion (HF) state in 4f- and 5f-based intermetallic systems, where the strong correlation between the localized magnetic moments and conduction electrons results in a full screening of the former and in a significant enhancement of the effective electron mass as compared to ordinary metals [2–4].

For this work, the latter phenomenon that links to a variety of intriguing novel physical behaviors is of major interest. It all began in the early 1930's with the peculiar experimental finding that the electrical resistivity of a metal that includes a small fraction of magnetic impurities does not decrease monotonically towards a constant as temperature declines but exhibits a low temperature minimum [5, 6]. Describing this phenomenon theoretically turned out as a rather complex problem, which was partially solved by Jun Kondo in 1964 [7]. The key aspect of Kondo's theory was to demonstrate that it is the spin flip scattering of conduction electrons off a localized magnetic impurity that triggers the unconventional low temperature behavior in the electrical resistivity [8, pp. 170-172]. Years later it was shown numerically by Wilson that this scattering process ultimately leads to the formation of a non-magnetic singlet ground state [9]. Even though the main focus was on impurity systems at the beginning, the research field quickly moved in the direction of 4f- and 5f-based Kondo lattice systems, commonly known as HF metals. In this material class, where the localized magnetic moments are periodically arranged on the lattice, the Kondo screening shows a coherent nature and heavy quasiparticles form that feature effective electron masses increased by several orders of magnitude as compared to conventional metals [2–4]. As originally suggested by Doniach, an interesting aspect of a Kondo lattice is the fact that its ground state can be changed to antiferromagnetically ordered by adjusting a non-thermal control parameter [10,11]. Fascinatingly, the two possible ground states of a HF metal are usually separated by a quantum phase transition (QPT), a zero temperature critical point at which conventional metallic behavior collapses and exotic states, such as unconventional superconductivity, emerge [11].

The significant progress in the field of magnetic Kondo lattice systems opened up the question as to whether comparable behavior is present in 4f-based intermetallics that

feature a non-magnetic ground state. Based on Kramers theorem, such a non-magnetic ground state is only possible for ions with integer spin, i.e. an even number of 4f electrons [12, p. 63]. Both the Pr^{3+} and the U^{4+} ion classify as such and offer when embedded in a metallic host the possibility to explore correlation effects of non-magnetic nature. Inspired by the emergence of the unconventional HF behavior in UBe_{13}, Cox proposed that the hybridization between the material's localized quadrupole moments and conduction electrons evokes exotic Kondo physics that is of entirely different nature than the one observed in magnetic Kondo systems [13, 14]. The so called quadrupole Kondo effect is a direct manifestation of the two-channel Kondo scenario[1] and describes the over screening of a quadrupole moment by two conduction electron channels [16]. For the single-impurity case, theory predicts a highly fragile ground state featuring characteristic non-Fermi liquid (NFL) behavior and an unconventional residual entropy [16–18], which is fundamentally different to the behavior linked to the stable single-channel Kondo ground state present in magnetic impurity systems. Extensive research followed Cox's initial suggestion, with the objective of finding hard evidence for this highly unconventional state of matter. Initially, the main focus was on diluted U-based materials and indication of the quadrupole Kondo related NFL behavior was indeed found in selected systems, which include, among others, $U_xTh_{1-x}Be_{13}$ [19,20], $Y_{1-x}U_xPd_3$ [21,22] and $U_xTh_{1-x}Ru_2Si_2$ [23,24]. A general problem with U-based materials, however, is the presence of significant hybridization effects, which complicate the measurement of crystal electric field (CEF) excitations. It therefore often remained ambiguous as to whether the findings are indeed a signature of over screened quadrupole moments or triggered by another mechanism.

Recently, the focus shifted towards Pr-based systems, in which the 4f electrons are more localized, hybridization effects more moderate and CEF excitations therefore better determinable. Especially the class of the Pr-based 1-2-20 materials has been subject to extensive research and initial evidence of the quadrupole Kondo effect and other novel correlation phenomena was revealed [25, 26]. The Zn-based systems $PrIr_2Zn_{20}$ [27, 28] and $PrRh_2Zn_{20}$ [29, 30] as well as the Al-based materials PrV_2Al_{20} [26, 31, 32] and $PrTi_2Al_{20}$ [26, 33, 34] attracted thereby particular attention. In these materials, the Pr^{3+} ions are exposed to a cubic CEF and the resulting ground state was identified as either the quadrupolar non-Kramers Γ_3 or Γ_{23} doublet [25]. As the number of metallic ions located around a Pr site is high, a pronounced hybridization effect between the localized quadrupole ground state moments and conduction electrons is expected [25]. Indeed, signatures of the quadrupole Kondo lattice effect were reported for both Zn-based systems [28, 30] and PrV_2Al_{20} [35]. At very low temperature, all four compounds exhibit an ordering of their multipolar ground state moments that is followed by a superconducting transition at even lower temperature [26, 27, 29, 31, 36]. For the Zn-based materials, the order proved to be of antiferroquadrupolar (AFQ) nature [27, 29, 37, 38]. In the case of the Al-based systems, ferroquadrupolar (FQ) order was found in $PrTi_2Al_{20}$ [26, 34], while for PrV_2Al_{20} its nature has not been fully clarified so far. In case of the latter material, a double transition was reported and a combination of AFQ and octupolar order is under discussion [39]. Microscopic evidence for this scenario is, however, still missing. While the discovery of the quadrupole Kondo lattice effect in aforementioned materials can be considered as a great success [28, 30, 35], the inter-site interaction between the Pr^{3+} ions complicates the theoretical modeling of this effect [40] and also results in a quadrupolar ordered instead of a quadrupolar Kondo ground state. It is thus desirable to scrutinize the emergent NFL behavior by tuning a quadrupole Kondo lattice towards

[1] The two-channel Kondo effect is a special case of the multichannel Kondo scenario, with an impurity spin $S = 1/2$ and $n = 2$ screening channels, originally introduced by Nozières and Blandin [15].

a single-impurity quadrupole Kondo ground state for which unambiguous theoretical predictions exist [16, 18, 41]. The absence of quadrupolar order in an impurity system also allows to search for the theoretically predicted residual quadrupole Kondo entropy [17]. Lately, the theoretically predicted single-impurity quadrupole Kondo NFL behaviors were indeed revealed in highly diluted $Y_{1-x}Pr_xIr_2Zn_{20}$ with $x \leq 0.044$ [42–44].

This thesis aims to further examine the novel quadrupolar driven phenomena emerging in the Zn-based materials $PrIr_2Zn_{20}$ and $Y_{1-x}Pr_xIr_2Zn_{20}$ by using low temperature thermal expansion and magnetostriction measurements and is structured as follows: **Chapter 2** outlines the theoretical concepts essential for the understanding of the experimental results. At first, the relevant thermodynamic quantities are introduced and the role of CEF interactions in f electron systems is discussed. Furthermore, the basics of elasticity are addressed and the relevance of symmetrized strain and elastic constant measurements for the characterization of non-Kramers CEF states is stressed. Finally, the single- and two-channel Kondo effect are reviewed. **Chapter 3** deals with the experimental methods employed in this work. To start with, the generation of ultra-low temperatures by means of dilution refrigeration is briefly outlined and the utilized experimental setup is detailed. Afterwards, the focus is on the measurement technique capacitive dilatometry. The capacitive dilatometers used for the research on this thesis are introduced and their background contributions discussed. **Chapter 4** deals with $PrIr_2Zn_{20}$, a cubic quadrupolar Kondo lattice that features AFQ order at $T_Q = 0.11\,K$ and a peculiar FL phase in close vicinity of its critical magnetic field of quadrupolar order [27, 28, 37]. The first part of the chapter reviews previous results from literature that served as a motivation for the thermal expansion and magnetostriction experiments carried out in this work. The experimental findings are discussed in the second part. Based on the anomalous behavior found in the electrical resistivity and the Seebeck coefficient that emerge just above the critical field of AFQ order [28, 45, 46], the primary focus of the measurements was to quantify possible volume changes in close vicinity of this novel phase. Another key motivation of the experiments was to set the anisotropic and volume effects present in $PrIr_2Zn_{20}$ in relation to the well studied behaviors in magnetic Kondo metals. **Chapter 5** covers the system $Y_{1-x}Pr_xIr_2Zn_{20}$. Diluting $PrIr_2Zn_{20}$ by gradually substituting the Pr^{3+} ions with Y^{3+} ions is an effective way to reduce the inter-site interaction between the Pr^{3+} ions and to tune the material towards a possible single-impurity quadrupolar Kondo ground state. The first part of the chapter reviews previous literature results on the system that pointed towards the formation of the single-impurity quadrupole Kondo effect in weakly doped single crystals [42–44]. Subsequently, the thermal expansion and magnetostriction results obtained on differently doped $Y_{1-x}Pr_xIr_2Zn_{20}$ single crystals are presented and discussed. Motivated by previous studies, the experiments focused on a highly diluted single crystal on which uniaxial and volume thermal expansion as well as magnetostriction measurements were carried out. The obtained findings are discussed within the framework of the single-impurity quadrupole Kondo model and also compared with the behaviors found in two moderately doped single crystals. **Chapter 6** gives a brief summary of the key experimental results presented in this thesis and provides an outlook on how they might impact future research.

Chapter 2

Theoretical Foundations

This chapter introduces selected theoretical topics that are helpful for a better understanding of the experimental results obtained in the scope of this thesis. Firstly, the relevant thermodynamic quantities are introduced. Major focus is thereby on the thermal expansion and the magnetostriction, as these two measurements are central to this work. Subsequently, the effect of CEF interactions in 4f-based intermetallic materials is addressed and its implications for a Pr^{3+} ion in a cubic CEF environment are discussed. The basics of elasticity are the topic of the following section. Here, a special emphasis is put on the case of cubic symmetry and the importance of strain and elastic constant measurements when dealing with non-Kramers CEF states is stressed. Finally, the focus is on the Kondo effect, an electronic correlation phenomenon that leads to the full screening of a localized magnetic moment via the conduction electrons. In this context, also exotic variations of the effect are detailed, whereby a particular focus is on the two-channel Kondo effect, which manifests itself in selected Pr-based 1-2-20 materials and is thus highly relevant for this work.

2.1 Thermodynamics

This section introduces the relevant thermodynamic quantities. To start with, the specific heat is briefly discussed. Even though its measurement is not a topic of this thesis, it is an indispensable quantity for the characterization of strongly correlated electron materials and inherently connected to the thermal expansion coefficient, which is detailed afterwards. Besides the thermal expansion, the magnetostriction is the second central thermodynamic probe used in this work to examine the quadrupolar ground state of selected Pr-based intermetallic materials and therefore briefly introduced as well. Finally, the Grüneisen parameter is discussed. It quantifies the pressure dependence of an energy scale and is considered as the most relevant probe to track down a pressure sensitive quantum critical point (QCP).

2.1.1 Specific Heat

The specific heat is likely one of the most prevalent measurement parameters to characterize the ground state of HF metals, as it is not only a powerful probe to detect phase transitions but also to obtain information on the electronic nature of the ground state. Thermodynamically, the specific heat coefficient C can either be defined at constant pres-

sure P as

$$C_P = T\left(\frac{\partial S}{\partial T}\right)_P, \tag{2.1}$$

or at constant volume V as

$$C_V = T\left(\frac{\partial S}{\partial T}\right)_V, \tag{2.2}$$

where T denotes the temperature and S the entropy. At low temperatures, C_P and C_V are basically identical and distinction between the two measurements is not required. In the field of low temperature physics it is therefore common to simply denote the specific heat by the universal symbol C. Based on its relation to the temperature derivative of entropy, integration of C/T with respect to temperature is a straightforward and widely employed approach to deduce a material's temperature dependent entropy.

In metallic systems, the low temperature[1] specific heat is described by the relation [2]

$$C = \gamma T + \beta T^3, \tag{2.3}$$

where the first term specifies the electronic and the second term the lattice contribution. The prefactor γ of the first term is commonly known as Sommerfeld coefficient and shows proportionality to the effective electron mass m^* [47, p. 136]. The mass renormalization is a direct consequence of the interaction between electrons and has been theoretically proposed by Lev Landau in the scope of his FL theory [47, p. 129]. A central aspect of Landau's theory[2] are the so called quasiparticles that provide an explanation for certain metallic behaviors that could not be captured by the preceding theories of Drude and Sommerfeld. In a nutshell, quasiparticles are excitations that form close to the Fermi energy ϵ_F and exhibit a remarkably long life-time [47, p. 127]. For further reading on the concept of Landau's FL theory see, for instance, Refs. [47, 48]. Now, back to the specific heat. The proportionality of its electronic component to the effective electron mass becomes particularly evident in the material class of HF metals, where the formation of heavy quasiparticles leads to a substantial enhancement of the γ coefficient [4]. A prime example to illustrate this effect is the HF metal $CeAl_3$ that shows a gigantically increased Sommerfeld coefficient of $\gamma = 1620\,\mathrm{mJ\ mol^{-1}\ K^{-2}}$ [49]. For comparison, the Sommerfeld coefficient of conventional metals is approximately $\gamma \approx 1\,\mathrm{mJ\ mol^{-1}\ K^{-2}}$ [50, p. 171] and thus around one thousand times smaller than the value derived for $CeAl_3$.

Even though the low temperature behavior of a large number of metals is captured very well by FL theory, there are also metallic states that cannot be accounted for by the former theory and their experimental and theoretical exploration is one of the hot topics in the field of solid state research. Such unconventional states of matter are generally termed NFL phases and emerge, for instance, when a HF metal is tuned away from its HF liquid ground state towards a magnetic QCP [11]. Another intriguing hybridization phenomenon that triggers exotic metallic behavior is the two-channel Kondo effect [15, 17, 18], which is central to the research carried out in the scope of this thesis. Both effects are discussed in detail at a later stage of this chapter.

2.1.2 Thermal Expansion

Besides the specific heat, the thermal expansion coefficient is another frequently employed thermodynamic probe to physically characterize solid state materials. It is a particularly

[1] Meant are temperatures well below the Debye and Fermi temperatures.

[2] Landau's theory provides a theoretical framework for the description of an interacting fluid of fermions. Consequently, it is not limited to electrons in metals but has also been successfully applied to other fermionic fluids, such as ^{3}He.

insightful measurement to quantify anisotropy effects and plays a paramount role for the characterization of the electronic state of HF metals.

The volume thermal expansion coefficient β quantifies a material's volume change upon the variation of temperature and is defined as

$$\beta = \frac{1}{V}\left(\frac{\partial V}{\partial T}\right)_P = -\frac{1}{V}\left(\frac{\partial S}{\partial P}\right)_T, \tag{2.4}$$

whereby the relation between β and the pressure derivative of entropy follows from a Maxwell relation. In analogy to the volume thermal expansion coefficient β, one can define the linear thermal expansion coefficient α as

$$\alpha = \frac{1}{L}\left(\frac{\partial L}{\partial T}\right)_P, \tag{2.5}$$

where L denotes the length of the considered sample. The thermal expansion coefficient classifies as a tensor of rank two and is therefore isotropic for materials with cubic crystal symmetry [51, p. 45]. This implies that the volume thermal expansion coefficient of a cubic material derives as $\beta = 3\alpha$. Given that the crystal symmetry of a system is lower than cubic, α varies along certain crystallographic directions and depending on the symmetry of the crystal, the measurement of α along various crystallographic directions is required in order to deduce β. In the case of a tetragonal, rhombohedral or hexagonal crystal symmetry, for instance, the thermal expansion tensor has two different components and in the case of triclinic, monoclinic or rhombic crystal symmetry, even three independent components exist [51, p. 45].

As this thesis deals with thermal expansion measurements on Pr-based intermetallic systems, the driving forces of the thermal expansion in a metallic solid shall be briefly addressed. For further reading on the topic, see Ref. [48] on which the following lines are based and Ref. [52], which is a very detailed treatise of the thermal expansion of solids. In general, the thermal expansion coefficient can be directly related to a temperature dependent pressure [48, p. 492]

$$\alpha = \frac{1}{3V}\left(\frac{\partial V}{\partial T}\right)_P = \frac{1}{3c_\mathrm{B}}\left(\frac{\partial P}{\partial T}\right)_V, \tag{2.6}$$

where $c_\mathrm{B} = -V(\mathrm{d}P/\mathrm{d}V)$ is the bulk modulus. In analogy to the specific heat, the thermal expansion of a metal at temperatures well below the Debye temperature is governed by a linear in temperature electronic and a cubic lattice contribution [48, p. 495]. With respect to Eq. (2.6), these temperature dependencies must stem from the temperature derivatives of the respective pressures generated by the electrons and the phonons. This is elucidated in the following by considering both pressure contributions in detail.

At first, the focus is on the pressure evoked by the phonons [48, p. 490]

$$P_\mathrm{phon} = -\frac{\partial}{\partial V}[U_\mathrm{zp} + \sum \frac{1}{2}\hbar\omega_s(\boldsymbol{k})] + \sum_{\boldsymbol{k}s}\left(-\frac{\partial}{\partial V}(\hbar\omega_s(\boldsymbol{k}))\right)\frac{1}{e^{\frac{\hbar\omega_s(\boldsymbol{k})}{k_\mathrm{B}T}} - 1}, \tag{2.7}$$

where U_zp denotes the zero-point energy, $\omega_s(\boldsymbol{k})$ the phonon frequencies with wave vector $\boldsymbol{k}$, $\hbar$ the Planck constant and k_B the Boltzmann constant. As the first term of Eq. (2.7) in square brackets does not depend on temperature, it is not of relevance for the following consideration and can be disregarded. The second term is more interesting, as it shows a temperature dependence provided that $\omega_s(\boldsymbol{k})$ depends on the volume, which

is, however, only given when the anharmonicity of the lattice potential is taken into account [48, pp. 490-491]. The temperature derivative of the second term of Eq. (2.7) yields the phononic thermal expansion coefficient $\alpha_{\mathrm{phon}} = \gamma_{\mathrm{phon}} C_V^{\mathrm{phon}} / 3c_{\mathrm{B}}$, where C_V^{phon} and γ_{phon} are the lattice contributions to the specific heat and the Grüneisen parameter, respectively [48, p. 493]. The second contribution to the thermal expansion of a metal stems from the temperature dependent pressure generated by the free electron gas $P_{\mathrm{elec}} = 2/3(U_{\mathrm{elec}}/V)$ [48, p. 495]. Plugging this expression into Eq. (2.6) gives back the electronic thermal expansion coefficient $\alpha_{\mathrm{elec}} = 2/3(C_V^{\mathrm{elec}}/3c_{\mathrm{B}})$, with the electronic specific heat C_V^{elec} [48, p. 495]. Note that the prefactor 2/3 corresponds to the Grüneisen parameter of the free electron gas γ_{elec}, which measures the volume dependence of the density of states at the Fermi level $\gamma_{\mathrm{elec}} = (\partial \ln N(\epsilon_{\mathrm{F}})/\partial \ln V)_T = 2/3$ [52, p. 641]. By combining electronic and lattice contribution, the low temperature thermal expansion coefficient of a metal consequently reads as [48, p. 495]

$$\alpha = \alpha_{\mathrm{elec}} + \alpha_{\mathrm{phon}} = \frac{1}{3c_{\mathrm{B}}} \left(\frac{2}{3} C_V^{\mathrm{elec}} + \gamma_{\mathrm{phon}} C_V^{\mathrm{phon}} \right), \tag{2.8}$$

whereby the proportionality of α_{elec} and α_{phon} to the respective heat capacities demonstrates the initially noted linear and cubic temperature dependencies of the electronic and lattice thermal expansion coefficient, respectively. At temperatures well above the Debye temperature, the thermal expansion coefficient converges against a constant value [48, p. 493], which is in analogy to the constant high temperature Dulong-Petit specific heat. The proportionality between the thermal expansion and the specific heat contribution that assign to the same energy scale is known as Grüneisen law [53]. An exceptional breakdown of this generally valid scaling relation is present at a pressure sensitive QCP, where the Grüneisen parameter diverges upon approaching absolute zero [54]. An detailed discussion of this intriguing effect is provided in Section 2.1.4.

In the cubic Pr-based intermetallic materials examined in the scope of this thesis, another considerable contribution to the low temperature thermal expansion arises from the linear coupling between the quadrupolar moments of the Pr^{3+} ion's non-Kramers Γ_3 ground state doublet and strain of the same symmetry. This corresponds to a CEF effect that measures the splitting of the Γ_3 ground state doublet and is therefore only of relevance when the material's cubic crystal symmetry is broken and the degeneracy of the quadrupolar ground state doublet lifted. More details on this effect are provided in Section 2.3.2.

2.1.3 Magnetostriction

The volume of a material does not only change upon the variation of temperature but also with magnetic field. This effect is known as volume magnetostriction and the respective coefficient is defined as

$$\lambda_V = \frac{1}{V} \left(\frac{\partial V}{\partial B} \right)_{P,T} = -\frac{1}{V} \left(\frac{\partial M}{\partial P} \right)_{B,T}, \tag{2.9}$$

where $B = \mu_0 H$ denotes an external magnetic field. A Maxwell relation links the volume magnetostriction coefficient to the hydrostatic pressure dependence of magnetization. The linear magnetostriction coefficient λ quantifies the change in length with magnetic field and is defined as

$$\lambda = \frac{1}{L} \left(\frac{\partial L}{\partial B} \right)_{P,T}. \tag{2.10}$$

The direct connection between the volume magnetostriction and the pressure dependence of magnetization has been demonstrated for a number of 4f-based intermetallic compounds, whereby the Ce- and Yb-based intermediate valence systems are likely the best examples to illustrate this effect [55]. When Yb ions are placed in a metallic host, they typically display a mixed valence state lying in between Yb^{3+} and Yb^{2+}, which corresponds to electronic configurations of $4f^{13}$ and $4f^{14}$, respectively [55]. As the application of hydrostatic pressure results in a reduction of volume, a pressurized mixed valent Yb ion is pushed towards the smaller and magnetic $4f^{13}$ configuration. This implies an increase of magnetization and according to Eq. (2.9) a negative volume magnetostriction. For a Ce-based intermediate valence system, the pressure effect is reversed. Its valence state usually lies in between Ce^{4+} and Ce^{3+}, which is equivalent to electronic configurations of $4f^0$ and $4f^1$, respectively [55]. As the non-magnetic $4f^0$ configuration occupies a smaller volume, the application of hydrostatic pressure results in a decrease of magnetization and the respective volume magnetostriction is positive. By contrast, in 4f-based intermetallic systems, where the valence state of the rare earth ions is close to integer, anisotropic magnetostriction effects are dominant [55]. Such uniaxial response to magnetic field stems from the anisotropic shape of the 4f electron charge distribution, which in turn is a direct consequence of the CEF effect [56, p. 11]. Note that the degree of anisotropy of the electron distribution varies among the different rare earth ions and is quantified by the Stevens factor α_j, whose sign dictates whether the 4f electron cloud is squeezed ($\alpha_j < 0$) or stretched ($\alpha_j > 0$) with respect to the orbital angular momentum axis [57]. Consider, for instance, the Gd^{3+} ion, which exhibits a spherical distribution of the 4f electrons and a Stevens factor of $\alpha_j = 0$ [57]. In consequence, an anisotropic CEF magnetostriction is not expected for this ion. Counterexamples are the Ce^{3+} and the Pr^{3+} ion, which show the most negative and the Tm^{3+} and the Yb^{3+} ion, which exhibit the most positive Stevens factors among the 4f ions [57]. Consequently, it can be assumed that the associated CEF magnetostriction shows a distinct anisotropy. As outlined a few lines before, Yb- and Ce-based intermetallic materials often exhibit intermediate valence states, which come along with pronounced volume magnetostriction effects and therefore counteract the anisotropic CEF magnetostriction [55]. In the view of the just reviewed behavior in Ce- and Yb-based intermetallics, the quantification of uniaxial and volume magnetostriction effects in selected Pr-based 1-2-20 materials is a central aspect of this thesis. As reduction of CEF anisotropy and the emergence of volume changes is a distinct signature of hybridization effects, the magnetostriction measurements carried out in the scope of this work aimed to shed light on the strength of correlation effects in the just specified material class.

2.1.4 Grüneisen Parameter

The Grüneisen law goes back to Eduard Grüneisen [53] who proposed that the ratio of the volume thermal expansion to the specific heat, generally referred to as Grüneisen parameter Γ, does not depend on temperature provided that the system under consideration is governed by a single energy scale $E^\star$ [54]. Commonly, the Grüneisen parameter is expressed as a dimensionless quantity [58]

$$\Gamma = \frac{V_\mathrm{m}}{\kappa_T}\frac{\beta}{C}, \tag{2.11}$$

where V_m denotes the molar volume and κ_T the isothermal compressibility. Note that depending on the consulted literature, the definition of Γ and therefore its dimension varies. Zhu et al. [54], for instance, disregard the prefactor in Eq. (2.11) in their work and simply define Γ as the ratio of the volume thermal expansion to the specific heat.

In the experimental section of this thesis, the Grüneisen parameter of a single-impurity quadrupolar Kondo metal is expressed in units of Pa^{-1} in order to emphasize the direct relation of Γ to the pressure dependence of the relevant energy scale. This relation is briefly discussed below.

When only a single energy scale is concerned, the molar entropy can be expressed as $S/N = f(T/E^\star)$ [54] and it follows for the dimensionless Grüneisen parameter [58]

$$\Gamma = \frac{1}{\kappa_T E^\star} \frac{\partial E^\star}{\partial p}. \tag{2.12}$$

Apparently, Γ does not depend on temperature and measures the pressure dependence of $E^\star$ [54]. While the electronic Grüneisen parameter of an ordinary metal is typically order of unity, HF metals are distinguished by Γ values that are up to two orders of magnitude increased [59]. With respect to Eq. (2.12), this enhancement implies a considerable pressure dependence of the relevant energy scale and also emphasizes the significance of thermal expansion measurements to characterize the emerging effects in this materials class [59].

As outlined before, the temperature independence of the Grüneisen parameter is only given when a single energy scale is concerned. In real materials, however, this condition is often not fulfilled, as a range of different energy scales with different pressure dependencies contribute, which results in a temperature dependence of the Grüneisen parameter [58,59]. It is therefore common to define an effective Grüneisen parameter Γ_{eff} as [59]

$$\Gamma_{\mathrm{eff}} = \sum_i \Gamma_i \frac{C_i}{C}, \tag{2.13}$$

where Γ_i and C_i are the different Grüneisen and specific heat contributions and C the total specific heat. This effect becomes particularly evident in the case of HF materials, where Γ_{eff} typically shows a pronounced temperature dependence at elevated temperatures [59]. Below liquid helium temperature it is usually justified to assume that a single energy scale, namely the one related to the 4f electrons, dominates [58].

Zhu et al. [54] demonstrated theoretically that the generally valid Grüneisen scaling between thermal expansion and specific heat breaks down at a QCP. In a nutshell, a QCP denotes a second order phase transition that manifests itself at absolute zero and comes along with NFL and other unconventional behaviors [11]. Key difference to a classical phase transition is that quantum and not thermal fluctuations are the driving force behind a QPT [60]. Quantum fluctuations are described by the energy scale $\hbar\omega_\mathrm{c}$ and become relevant at very low temperature, where $\hbar\omega_\mathrm{c} > k_\mathrm{B}T$ holds true [60]. Despite the fact that a QCP forms at absolute zero, the related behavior manifests itself in a finite temperature region specified by $k_\mathrm{B}T > \hbar\omega_\mathrm{c} \sim |r - r_\mathrm{c}|^{\nu z}$, where r is the control parameter and ν and z are critical exponents [60]. The critical exponents relate to the correlation length $\xi \sim |r|^{-\nu}$ and to the imaginary correlation time $\xi_\tau \sim \xi^z$, which both diverge at a QCP [54, 60]. This is analogously to a classical second order phase transition, with the key difference that r is a non-thermal control parameter [11, 60]. By considering the critical free energy contribution, Zhu et al. [54] revealed the divergence of $\Gamma \sim 1/T^{1/\nu z}$ at a QCP. The power law dependence of Γ depends on the critical exponents ν and z, which show characteristic values for different scenarios of QC, as explicitly discussed in Ref. [54]. Extensive experimental evidence for QC and the related divergence of Γ was found in the material class of magnetic HF metals [11, 58]. While the divergence of Γ at a magnetic QCP is with certainty the most prominent and most thoroughly studied example, also other scenarios that lead to a breakdown of the Grüneisen law are conceivable. Zacharias

et al. [61], for instance, studied the divergence of Γ at an elastic QCP. Such elastic criticality arises when a linear coupling between strain and criticality is present [61] and is of relevance for this work, as it can be applied to the quadrupolar Kondo effect. More details on the latter phenomenon are provided in Section 2.4.2, which also clarifies that uniaixal strain of suitable symmetry is a direct control parameter for the critical quadrupole Kondo state.

2.2 Crystal Electric Field Theory

In the following, a single ion is considered, which is located inside a crystal structure and the impact of the electric field gradient generated by the charge density of the adjacent ions on the just specified single ion is elucidated. This effect is termed CEF effect and its consideration is crucial in order to understand and explain a large variety of physical phenomena that arise in d and f electron systems. As this thesis deals with Pr-based intermetallics, the following review focuses on the case of f electron systems. In materials of this class, the CEF energy is distinctly small as compared to the spin-orbit coupling energy [62, p. 116]. This implies that the total angular momentum quantum number J is a suitable means to characterize the localized f electrons [62, p. 116]. In presence of a CEF, the degeneracy associated to the ground state of a free f ion is lifted and, depending on the symmetry of the CEF, a characteristic set of energetically different CEF states forms. These states are commonly referred to as irreducible representations of the respective CEF point group symmetry.

While classically the CEF potential can be expressed in terms of spherical harmonics, Stevens introduced an elegant alternative to evaluate CEF effects in f electron systems by using the total angular momentum operators [63]. The corresponding CEF Hamiltonian reads as [62, p. 124]

$$\mathcal{H}_{\mathrm{CEF}} = \sum_m \sum_n B_n^m O_n^m, \tag{2.14}$$

where B_n^m are the CEF parameters that have to be specified by suitable experiments and O_n^m denote the Stevens operators. Generally, the number of the different coefficients and thus the form of $\mathcal{H}_{\mathrm{CEF}}$ depends on the symmetry of the CEF. In the following, the focus shall be on a cubic CEF, as it is present in the Pr-based 1-2-20 materials examined in the scope of this work. According to Lea et al. [64], the CEF Hamiltonian given by Eq. (2.14) distinctly simplifies in this case to the form [64]

$$\mathcal{H}_{\mathrm{CEF}}^{\mathrm{Cubic}} = B_4(O_4^0 + 5O_4^4) + B_6(O_6^0 - 21O_6^4). \tag{2.15}$$

Lea et al. [64] then defined two coefficients $B_4 = Wx/F(4)$ and $B_6 = W(1-|x|)/F(6)$, so that Eq. (2.15) takes the form [64]

$$\mathcal{H}_{\mathrm{CEF}}^{\mathrm{Cubic}} = W\left[x\left(\frac{O_4^0 + 5O_4^4}{F(4)}\right) + (1-|x|)\left(\frac{O_6^0 - 21O_6^4}{F(6)}\right)\right]. \tag{2.16}$$

Here, $F(4)$ and $F(6)$ are parameters, which depend on the total angular momentum quantum number J of the ion under consideration [64]. In the case of a Pr^{3+} ion with $J = 4$, the parameters are specified by $F(4) = 60$ and $F(6) = 1260$ [64]. The parameter x determines the energetic arrangement of the different eigenstates and W is simply a scaling factor [64]. Note that both W and x have to be specified via the experiment. When subjected to a cubic CEF, as denoted by the Hamiltonian in Eq. (2.16), the nine-fold degenerate ground state of a free Pr^{3+} ion splits into four states, namely a Γ_1 singlet, a Γ_3 doublet, a Γ_4 triplet and a Γ_5 triplet [64]. The corresponding eigenstates for each of the

Irreducible Representation	Degeneracy	Eigenstates
Γ_1	1	$\lvert\Gamma_1\rangle = \sqrt{\frac{5}{24}}\lvert 4\rangle + \sqrt{\frac{7}{12}}\lvert 0\rangle + \sqrt{\frac{5}{24}}\lvert -4\rangle$
Γ_3	2	$\left\lvert\Gamma_3^{(1)}\right\rangle = \sqrt{\frac{7}{24}}\lvert 4\rangle - \sqrt{\frac{5}{12}}\lvert 0\rangle + \sqrt{\frac{7}{24}}\lvert -4\rangle$ $\left\lvert\Gamma_3^{(2)}\right\rangle = \sqrt{\frac{1}{2}}\lvert 2\rangle + \sqrt{\frac{1}{2}}\lvert -2\rangle$
Γ_4	3	$\left\lvert\Gamma_4^{(1)}\right\rangle = \sqrt{\frac{1}{8}}\lvert 3\rangle + \sqrt{\frac{7}{8}}\lvert -1\rangle$ $\left\lvert\Gamma_4^{(2)}\right\rangle = \sqrt{\frac{1}{2}}\lvert 4\rangle - \sqrt{\frac{1}{2}}\lvert -4\rangle$ $\left\lvert\Gamma_4^{(3)}\right\rangle = \sqrt{\frac{1}{8}}\lvert -3\rangle + \sqrt{\frac{7}{8}}\lvert +1\rangle$
Γ_5	3	$\left\lvert\Gamma_5^{(1)}\right\rangle = \sqrt{\frac{7}{8}}\lvert 3\rangle - \sqrt{\frac{1}{8}}\lvert -1\rangle$ $\left\lvert\Gamma_5^{(2)}\right\rangle = \sqrt{\frac{7}{8}}\lvert -3\rangle - \sqrt{\frac{1}{8}}\lvert 1\rangle$ $\left\lvert\Gamma_5^{(3)}\right\rangle = \sqrt{\frac{1}{2}}\lvert 2\rangle - \sqrt{\frac{1}{2}}\lvert -2\rangle$

Table 2.1: Irreducible representations, corresponding degeneracy and eigenstates of a Pr^{3+} ion, described by a total angular momentum quantum number $J = 4$, which is located in a cubic CEF with O_h or T_d point group symmetry. The eigenstates were originally reported in Ref. [64].

four irreducible representations are listed in Table 2.1. In the case of $PrIr_2Zn_{20}$, Iwasa et al. [65] determined the CEF parameters at $W = -1.22\,\mathrm{K}$ and $x = 0.537$ by using inelastic neutron scattering. This parameter constellation suggests a Γ_3 ground state, a Γ_4 first excited state that is followed by a Γ_1 singlet and a Γ_5 triplet state [65]. For further details it is referred to Section 4.1.2, which provides specific information on the exact energetic arrangement of the different CEF eigenstates of $PrIr_2Zn_{20}$. The just referenced work by Lea et al. [64] is very helpful when dealing with CEF effects in cubic rare earth ions, as it specifies the CEF eigenstates for a wide range of J values. In addition, graphs are provided based on which the energy values and therefore the energetic arrangement of the different eigenstates as a function of the CEF parameter x can be deduced [64].

Each of the four CEF states of a Pr^{3+} ion in a cubic crystal environment carries a set of different multipolar degrees of freedom. Multipole moments can be either of magnetic or quadrupolar nature and are generally described by a tensor of rank k [66]. When k takes an even number, the multipole moment is electric and when k takes an uneven number, it is magnetic [66, 67]. More specifically, a tensor of rank zero denotes a magnetic monopole, a tensor of rank one a magnetic dipole, a tensor of rank two an electric quadrupole and a tensor of rank three a magnetic octupole [67]. The corresponding multipole operators ranging from rank one to rank three and their commonly employed denotations are specified below [66].

- Magnetic dipole operators ($k = 1$): J_x, J_y J_z
- Electric quadrupole operators ($k = 2$): O_2^0, O_2^2, O_{xy}, O_{xz}, O_{yz}
- Magnetic octupole operators ($k = 3$): T_{xyz}, T_x^α, T_x^β, T_x^γ, T_y^α, T_y^β, T_y^γ

For details on how the electric quadrupole and magnetic octupole operators depend on the angular momentum operators, see, for instance, Ref. [68]. This thesis examines electronic correlation effects at very low temperature, where the physics of a system is governed by the CEF ground state and its multipolar degrees of freedom. In the case of $PrIr_2Zn_{20}$, the energetically lowest lying state is a non-Kramers Γ_3 doublet [27, 65], for which only the quadrupole operators O_2^0 and O_2^2 as well as the magnetic octupole operator T_{xyz} show finite expectation values. The absence of magnetic dipole degrees of freedom therefore allows for the exploration of novel quadrupole related correlation effects.

2.3 Elasticity

In order to characterize the ground state of a quadrupolar Kondo metal, it is crucial to study its elastic properties. In this regard, the three physical quantities stress, strain and elastic constant shall be introduced in this section. In addition, the elastic free energy is discussed, whereby a special focus is put on the case of cubic symmetry. Finally, the paramount role of symmetrized elastic constant and strain measurements to characterize non-Kramers CEF states is addressed.

2.3.1 Strain, Stress and Elastic Constant

As subsequently only a very basic introduction to the physical quantities strain, stress and elastic constant is provided, it is referred to Refs. [51, 69] for further details on which the following lines are based. Note that Ref. [51] provides an elementary yet explicit introduction to the topic of elasticity, while Ref. [69] shows how these concepts find application in order to physically characterize solid state materials by means of ultrasonic measurements.

Displacement Vector and Strain Tensor

Generally speaking, the physical quantity of strain describes the deformation of a body and manifests itself either in the form of a normal or a shear strain. In order to give a precise definition of strain, at first, a three dimensional coordinate system with a coordinate vector $\boldsymbol{r} = (x, y, z)$ is introduced. When a point located at the coordinate position $\boldsymbol{r}$ is now moved to a different coordinate at position $\boldsymbol{r'}$, then the vector $\boldsymbol{u} = \boldsymbol{r} - \boldsymbol{r'} = (u_x, u_y, u_z)$ specifies the point's displacement [51, p. 1].

In the following the focus is on a body that undergoes a deformation process. In this case, not only the coordinate position of a particular point of the body but also the distance l between the just specified point and another point of the body may change to a different value l' [51, p. 1]. It then holds for the altered distance after the deformation process [51, p. 2]

$$\mathrm{d}l'^2 = \mathrm{d}l^2 + 2\varepsilon_{ij}\mathrm{d}x_i\mathrm{d}x_j, \tag{2.17}$$

where ε_{ij} denotes the strain tensor with $i, j = x, y, z$. This tensor of rank two is directly connected to the components of the displacement vector via the equation [51, p. 2]

$$\varepsilon_{ij} = \frac{1}{2}\left(\frac{\partial u_i}{\partial x_j} + \frac{\partial u_j}{\partial x_i} + \frac{\partial u_k}{\partial x_i}\frac{\partial u_k}{\partial x_j}\right), \tag{2.18}$$

which demonstrates a key characteristic of the strain tensor, namely its symmetry $\varepsilon_{ij} = \varepsilon_{ji}$. When a body undergoes only a small deformation, it is justified to disregard the third term of Eq. (2.18) and the strain tensor simplifies to the well known expression [51, p. 3]

$$\varepsilon_{ij} = \frac{1}{2}\left(\frac{\partial u_i}{\partial x_j} + \frac{\partial u_j}{\partial x_i}\right), \tag{2.19}$$

whereby the case $i = j$ denotes a normal strain and the case $i \neq j$ a shear strain. By calculating the trace of the strain tensor, one can derive the relative volume change $(\mathrm{d}V' - \mathrm{d}V)/\mathrm{d}V = \varepsilon_{xx} + \varepsilon_{yy} + \varepsilon_{zz}$, which is generally termed bulk strain ε_B [51, p. 4].

Stress Tensor

Strains are generated when a body is put under stress. Consequently, the stress tensor σ_{ij} is an equally crucial quantity when addressing the elastic properties of a solid. Stress generally relates to a force, as indicated by the relation [51, p. 6]

$$\int F_i \mathrm{d}V = \int \frac{\partial \sigma_{ij}}{\partial x_j} \mathrm{d}V = \int_S \sigma_{ij} \mathrm{d}f_j, \tag{2.20}$$

where F_i and $\mathrm{d}f_j$ denote a force and a surface element component, respectively. Specifically, Eq. (2.20) reveals that the stress tensor σ_{ij} connects the i-th force component F_i with the j-th component of the surface element $\mathrm{d}f_j$. Provided that $i = j$, the force acts parallel to the surface normal and the respective stress is said to be normal. In the case of $i \neq j$, the force acts perpendicular to the surface normal and the respective stress denoted as a shear stress.

Just like the strain tensor, also the stress tensor is symmetric [51, p. 7]

$$\sigma_{ij} = \sigma_{ji}, \tag{2.21}$$

which can be derived by calculations of the angular momentum [51, p. 6-7]. Besides the application of the just mentioned normal and shear stresses to a body, one can also compress the latter uniformly, which corresponds to a hydrostatic pressure P. In this case, the stress tensor fulfills the condition $\sigma_{ij} = -P\delta_{ij}$, which indicates that only its diagonal elements differ from zero [51, p. 7].

Thermodynamic Relations

Next, the relations of the strain and stress tensor to the derivatives of different thermodynamic potentials are detailed. The energies of relevance are the internal energy U, the free energy F and the Gibbs free energy G, which are defined by using Einstein notation as [69, pp. 47-48]

$$\mathrm{d}U = T\mathrm{d}S + V\sigma_{ij}\mathrm{d}\varepsilon_{ij} + \mu \mathrm{d}N, \tag{2.22}$$

$$\mathrm{d}F = -S\mathrm{d}T + V\sigma_{ij}\mathrm{d}\varepsilon_{ij} + \mu \mathrm{d}N, \tag{2.23}$$

$$\mathrm{d}G = -S\mathrm{d}T - V\varepsilon_{ij}\mathrm{d}\sigma_{ij} + \mu \mathrm{d}N, \tag{2.24}$$

where μ denotes the chemical potential and N the number of particles.

Evidently, the stress tensor σ_{ij} can be directly deduced via the partial derivative of either the internal energy U or the free energy F with respect to the strain tensor ε_{ij}

$$\sigma_{ij} = \frac{1}{V}\left(\frac{\partial U}{\partial \varepsilon_{ij}}\right)_{S,N} = \frac{1}{V}\left(\frac{\partial F}{\partial \varepsilon_{ij}}\right)_{T,N}. \tag{2.25}$$

The strain tensor ε_{ij}, on the other hand, follows from the partial derivative of the Gibbs free energy G with respect to the stress tensor σ_{ij}.

$$\varepsilon_{ij} = -\frac{1}{V}\left(\frac{\partial G}{\partial \sigma_{ij}}\right)_{T,N}. \tag{2.26}$$

In particular, the relation of the stress tensor to the partial derivative of the free energy with respect to strain, as described by Eq. (2.25), should be kept in mind. It is an important relation and repeatedly used in the following to deduce some basic relations.

Elastic Constant Tensor

In case the deformation is small, the stress and the strain tensor are directly proportional quantities, whereby the elastic constant tensor c_{ijkl} denotes the constant of their proportionality. This famous relation is known as Hook's law and one of the most fundamental equations in the field of elasticity.

For its derivation, at first, the elastic free energy, which is expressed as an energy density in the following, is considered [51, p. 40]

$$F_{\mathrm{el}} = \frac{1}{2} c_{ijkl} \varepsilon_{ij} \varepsilon_{kl}. \tag{2.27}$$

Note that again Einstein notation is used. The direct proportionality between stress and strain can then simply be demonstrated by differentiating F_{el} with respect to ε_{ij}, which yields, according to Eq. (2.25), the stress tensor [51, p. 40]

$$\sigma_{ij} = \left(\frac{\partial F_{\mathrm{el}}}{\partial \varepsilon_{ij}} \right)_T = c_{ijkl} \varepsilon_{kl}. \tag{2.28}$$

Note that the elastic free energy specified by Eq. (2.27) is already expressed in the form of an energy density and an additional normalization to volume, as suggested by Eq. (2.25), therefore not necessary. Since strain ε is a dimensionless quantity, the elastic constant must denote an energy density having the unit of Pa. Equation (2.28) is a relation of fundamental importance, as it reveals a direct proportionality between the stress and the strain tensor and specifies the elastic constant tensor as their proportionality constant. It is crucial to keep in mind that this linear dependence between stress and strain only holds true in case the deformation is small. When the applied stress exceeds a certain threshold value, non-linear behavior sets in and ultimately plastic deformation of the material under stress appears.

Thanks to the symmetry of the elastic constant tensor [51, p. 40]

$$c_{ijkl} = c_{jikl} = c_{ijlk} = c_{klij}, \tag{2.29}$$

its different components decrease from a relatively large number of eighty one to a moderate number of twenty one. Note that the equivalency of the first three terms in Eq. (2.29) is a direct consequence of the symmetry of the stress and the strain tensor, which was discussed a few lines before. The equivalency of the first and the fourth term, on the other hand, follows from the fact that it is irrelevant as to whether one calculates the elastic constant tensor by partially differentiating F_{el} at first with respect to ε_{ij} and then with respect to ε_{kl} or the other way around. The just mentioned twenty one different components of the elastic constant tensor further reduce when a material with a certain crystal symmetry is considered. While for triclinic crystal symmetry still a quite large number of eighteen elastic constants are present, the number reduces to six in case of tetragonal crystal symmetry and to three when the crystal shows cubic symmetry [51, p. 44]. As the latter case applies to the materials examined in this thesis, it is discussed more in detail in the following subsection. In addition, the paramount role of elastic constant and strain measurements for the characterization of materials that feature non-Kramers CEF states is addressed.

2.3.2 Implications for Cubic Non-Kramers States

In the following, the just detailed basic concepts of elasticity are applied to materials that feature cubic crystal symmetry. This special case is of particular relevance for this thesis, as the here examined Pr-based 1-2-20 systems classify as such. To begin with, the cubic elastic free energy is specified and the related symmetrized elastic constants and strains are introduced. Subsequently, it is shown that the measurement of symmetrized strains and elastic constants is a powerful means to characterize materials that feature quadrupolar non-Kramers CEF states.

In the case of cubic symmetry, the large number of independent elastic constants reduces to three and the elastic free energy density introduced in Eq. (2.27) simplifies distinctly to the form [51, p. 44]

$$F_{\mathrm{el}}^{\mathrm{cubic}} = \frac{c_{xxxx}}{2}(\varepsilon_{xx}^2 + \varepsilon_{yy}^2 + \varepsilon_{zz}^2) + c_{xxyy}(\varepsilon_{xx}\varepsilon_{yy} + \varepsilon_{xx}\varepsilon_{zz} + \varepsilon_{yy}\varepsilon_{zz}) + 2c_{xyxy}(\varepsilon_{xy}^2 + \varepsilon_{xz}^2 + \varepsilon_{yz}^2). \quad (2.30)$$

To be in line with the relevant literature on the materials examined in the scope of this work [37, 44], in the following, the indices of the elastic constant tensor are expressed by digits instead of letters, whereby $x \to 1, y \to 2$ and $z \to 3$. In case of the strains, by contrast, the letters are kept as indices. For reasons of clarity, elastic constants are often expressed by the shortened Voigt notation[3], where two indices are summarized to a single one. This notation is used here as well and the so abbreviated form of Eq. (2.30) consequently reads as

$$F_{\mathrm{el}}^{\mathrm{cubic}} = \frac{c_{11}}{2}(\varepsilon_{xx}^2 + \varepsilon_{yy}^2 + \varepsilon_{zz}^2) + c_{12}(\varepsilon_{xx}\varepsilon_{yy} + \varepsilon_{xx}\varepsilon_{zz} + \varepsilon_{yy}\varepsilon_{zz}) + 2c_{44}(\varepsilon_{xy}^2 + \varepsilon_{xz}^2 + \varepsilon_{yz}^2). \quad (2.31)$$

This relation can then be rewritten in terms of the symmetrized cubic strains and elastic constants[4], as summarized in Table 2.2, and takes the form

$$F_{\mathrm{el}}^{\mathrm{cubic}} = \frac{(c_{11} + 2c_{12})/3}{2}\varepsilon_{\mathrm{B}}^2 + \frac{(c_{11} - c_{12})/2}{2}(\varepsilon_{\mathrm{u}}^2 + \varepsilon_{\mathrm{v}}^2) + \frac{4}{2}c_{44}(\varepsilon_{xy}^2 + \varepsilon_{xz}^2 + \varepsilon_{yz}^2). \quad (2.32)$$

The first term of the equation denotes the isotropic bulk contribution, which has Γ_1 symmetry and contains the bulk modulus $c_{\mathrm{B}} = (c_{11} + 2c_{12})/3$ and the bulk strain $\varepsilon_{\mathrm{B}} = \varepsilon_{xx} + \varepsilon_{yy} + \varepsilon_{zz}$. The second term has Γ_3 symmetry and covers the two strains $\varepsilon_{\mathrm{u}} = (2\varepsilon_{zz} - \varepsilon_{xx} - \varepsilon_{yy})/\sqrt{3}$ and $\varepsilon_{\mathrm{v}} = \varepsilon_{xx} - \varepsilon_{yy}$ as well as the elastic constant $(c_{11} - c_{12})/2$. The third term is of Γ_5 symmetry with the three shear strains ε_{xy}, ε_{xz}, ε_{yz} and the related elastic constant $4c_{44}$.

Each of the symmetrized strains listed in Table 2.2 can also couple to a multipole moment of the same symmetry, whereby the coupling strength between symmetrized strain and multipole moment is quantified by the multipole-strain coupling constant g_Γ [70–72]. By taking account of this additional contribution, the cubic elastic free energy density

[3] In the Voigt notation double indices ij and kl are summarized to a single index as follow: $xx = 11 \to 1, yy = 22 \to 2, zz = 33 \to 3, yz = 23 \to 4, xz = 13 \to 5, xy = 12 \to 6$.

[4] Here, the same irreducible cubic strain representations as in the literature dealing with elastic constant measurements relevant for this thesis (cf. Ref. [44]) are used. It is noted that another representation which uses normalized eigenstrains is also often employed (cf. Ref. [70]). For reasons of consistency with the relevant literature, the former representation is chosen in this work.

Irreducible Representation	Symmetrized Strain	Symmetrized Elastic Constant
Γ_1	$\varepsilon_{\mathrm{B}} = \varepsilon_{xx} + \varepsilon_{yy} + \varepsilon_{zz}$	$(c_{11} + 2c_{12})/3$
Γ_3	$\varepsilon_{\mathrm{u}} = (2\varepsilon_{zz} - \varepsilon_{xx} - \varepsilon_{yy})/\sqrt{3}$	$(c_{11} - c_{12})/2$
	$\varepsilon_{\mathrm{v}} = \varepsilon_{xx} - \varepsilon_{yy}$	
Γ_5	ε_{xy}	$4c_{44}$
	ε_{xz}	
	ε_{yz}	

Table 2.2: Irreducible representations, symmetrized strains and symmetrized elastic constants for cubic symmetry.

given by Eq. (2.32) modifies to the form

$$F_{\mathrm{el}}^{\mathrm{cubic}} = \frac{(c_{11}+2c_{12})/3}{2}\varepsilon_{\mathrm{B}}^2 + \frac{(c_{11}-c_{12})/2}{2}(\varepsilon_{\mathrm{u}}^2+\varepsilon_{\mathrm{v}}^2) + \frac{4}{2}c_{44}(\varepsilon_{xy}^2+\varepsilon_{xz}^2+\varepsilon_{yz}^2) - \frac{N_{\mathrm{RE}}}{V}[g_{\Gamma_1}\langle O_0^0\rangle\varepsilon_{\mathrm{B}} + g_{\Gamma_3}(\langle O_2^0\rangle\varepsilon_{\mathrm{u}} + \langle O_2^2\rangle\varepsilon_{\mathrm{v}}) + g_{\Gamma_5}(\langle O_{xy}\rangle\varepsilon_{xy} + \langle O_{yz}\rangle\varepsilon_{yz} + \langle O_{xz}\rangle\varepsilon_{xz})], \quad (2.33)$$

whereby the multipole moments are denoted by the expectation values of the respective Stevens operators $\langle O_\Gamma \rangle$. In rare earth based intermetallics, it are the localized 4f electrons exposed to a cubic CEF that principally generate the just specified multipole moments. Consequently, the term of Eq. (2.33) in square brackets scales with the number of rare earth ions N_{RE} that are located in the considered volume. Note that Eq. (2.33) is based on the assumption that only one particular type of rare earth ion is embedded in the metallic host system. In the materials examined in the scope of this work, the rare earth ion is the Pr^{3+} ion whose CEF ground state has been specified by various experiments as the non-Kramers Γ_3 doublet [27, 42, 43, 65]. Consequently, the second and the fifth term of Eq. (2.33) with Γ_3 symmetry are of particular relevance.

In consequence of the multipole-strain coupling, both symmetrized elastic constant and strain measurements are effective probes to characterize CEF states with regard to their multipolar nature. This is elucidated in the following two subsubsections, whereby the focus is at first on the cubic symmetrized strains. In this regard, an important implication of Eq. (2.33), namely the linear dependence between a symmetrized strain and the expectation value of the respective Stevens operator, is discussed. In addition, the cubic symmetrized strains are set in relation to the strains along certain cubic crystallographic directions. This is important, as the symmetrized strains with Γ_3 and Γ_5 symmetry cannot be measured directly, but have to be deduced from measurements along selected crystallographic directions. Finally, the direct relation between symmetrized elastic constant and strain susceptibility of a non-Kramers 4f state is reviewed.

Symmetrized Strains

As thermal expansion and magnetostriction measurements were employed in this work to examine the quadrupolar non-Kramers Γ_3 ground state of different cubic Pr-based 1-2-20 materials, the following lines, which detail the linear dependence between the cubic symmetrized strains and the expectation value of the respective Stevens operators, are paramount for the interpretation of the experimental results presented later on. This

important relation was originally revealed by Callen and Callen [71]. Pioneering work on symmetrized strain measurements was also done by Morin et al. [70, 72, 73], who took advantage of the quadratic coupling between quadrupole moment and strain to derive quadrupole-strain coupling constants at elevated temperatures.

The just mentioned linear dependence between a symmetrized strain ε_Γ and the respective multipole moment $\langle O_\Gamma \rangle$ becomes directly evident when Eq. (2.33) is minimized with respect to ε_Γ. This gives back the generalized expression

$$\varepsilon_\Gamma = \frac{n_{\mathrm{RE}} g_\Gamma}{c_\Gamma} \langle O_\Gamma \rangle \,, \tag{2.34}$$

where $n_{\mathrm{RE}} = N_{\mathrm{RE}}/V$ is the rare earth ion density. Note that the lattice contribution to the symmetrized elastic constant is denoted from now on by c_Γ^0, as the following subsubsection introduces another contribution to c_Γ that assigns to the 4f electrons. Equation (2.34) is of fundamental importance for this work and frequently employed at a later stage when the experimental results are detailed. Specifically, Eq. (2.34) allows to calculate the CEF thermal expansion and magnetostriction coefficients via the temperature or magnetic field dependence of the quadrupolar expectation values.

As the cubic materials $PrIr_2Zn_{20}$ and $Y_{1-x}Pr_xIr_2Zn_{20}$ examined in the scope of this thesis exhibit a Γ_3 ground state doublet, the two Γ_3-type strains ε_u and ε_v are most relevant and therefore introduced at first. According to Eq. (2.34) and by taking into account that the strain ε_u has the same symmetry as the O_2^0 Stevens operator it follows

$$\varepsilon_\mathrm{u} = \frac{n_{\mathrm{RE}} g_{\Gamma_3}}{(c_{11}^0 - c_{12}^0)/2} \left\langle O_2^0 \right\rangle . \tag{2.35}$$

For the second Γ_3-type symmetrized strain ε_v, which is of identical symmetry as the O_2^2 Stevens operator, it holds

$$\varepsilon_\mathrm{v} = \frac{n_{\mathrm{RE}} g_{\Gamma_3}}{(c_{11}^0 - c_{12}^0)/2} \left\langle O_2^2 \right\rangle . \tag{2.36}$$

The Γ_5-type shear strain ε_{xy}, on the other hand, corresponds to the O_{xy} Stevens operator and thus calculates as

$$\varepsilon_{xy} = \frac{n_{\mathrm{RE}} g_{\Gamma_5}}{4c_{44}^0} \langle O_{xy} \rangle . \tag{2.37}$$

The relations for the other symmetrized strains ε_{xz} and ε_{yz} with Γ_5 symmetry are not explicitly detailed here. Their calculation is analogously to the one of ε_{xy}, whereby the respective Stevens operators O_{xz} and O_{yz} have to be used. For the sake of completeness also the volume strain that derives as

$$\varepsilon_\mathrm{B} = \frac{n_{\mathrm{RE}} g_{\Gamma_1}}{(c_{11}^0 + 2_{12}^0)/3} \left\langle O_0^0 \right\rangle , \tag{2.38}$$

is given. As $\langle O_0^0 \rangle$ is a constant, ε_B does not depend on temperature or magnetic field and is therefore not of relevance in the following.

Among the just detailed relations, Eq. (2.35), which sets the strain ε_u in relation to the quadrupolar expectation value $\langle O_2^0 \rangle$, is the most crucial one for this work. While in presence of cubic crystal symmetry the expectation values of the Stevens operators with Γ_3 and Γ_5 symmetry vanish to zero, they are finite when the system is subjected to a symmetry breaking perturbation that matches the symmetry of the respective multipole moment. $\langle O_2^0 \rangle$, for instance, exhibits a finite expectation value when an uniaxial stress or a magnetic field is applied along the cubic [001] direction, which distorts the crystal symmetry from cubic to tetragonal. $\langle O_{xy} \rangle$, by contrast, is induced by a magnetic field or an uniaxial stress along the [110] direction, which evokes a shear strain ε_{xy}.

With the exception of the bulk strain ε_{B}, it is not possible to directly measure the cubic symmetrized strains. Therefore, it is important to quantify their contributions to the strains along certain cubic crystallographic directions that can be accessed in the experiment. By employing the cubic symmetrized strains presented in Table 2.2, the relative length changes along the cubic main directions are directly deducible. Note that only the strains relevant for this work are specified in the following. Under the assumption that a symmetry breaking magnetic field or uniaxial stress is applied along the crystallographic [001] direction, the strains along the three cubic directions [100], [010] and [001] derive as

$$\varepsilon_{[001]} = \left.\frac{\Delta L}{L}\right|_{[001]} = \frac{1}{3}\varepsilon_{\mathrm{B}} + \frac{1}{\sqrt{3}}\varepsilon_{\mathrm{u}}, \tag{2.39}$$

$$\varepsilon_{[100]} = \left.\frac{\Delta L}{L}\right|_{[100]} = \frac{1}{3}\varepsilon_{\mathrm{B}} - \frac{1}{2\sqrt{3}}\varepsilon_{\mathrm{u}} + \frac{1}{2}\varepsilon_{\mathrm{v}}, \tag{2.40}$$

$$\varepsilon_{[010]} = \left.\frac{\Delta L}{L}\right|_{[010]} = \frac{1}{3}\varepsilon_{\mathrm{B}} - \frac{1}{2\sqrt{3}}\varepsilon_{\mathrm{u}} - \frac{1}{2}\varepsilon_{\mathrm{v}}. \tag{2.41}$$

The strain along the [110] direction, on the other hand, derives as

$$\varepsilon_{[110]} = \left.\frac{\Delta L}{L}\right|_{[110]} = \frac{1}{3}\varepsilon_{\mathrm{B}} - \frac{1}{2\sqrt{3}}\varepsilon_{\mathrm{u}} + \varepsilon_{xy}. \tag{2.42}$$

Finally, the strain along the [111] direction is provided, which reads as

$$\varepsilon_{[111]} = \left.\frac{\Delta L}{L}\right|_{[111]} = \frac{1}{3}\varepsilon_{\mathrm{B}} + \frac{2}{3}(\varepsilon_{xy} + \varepsilon_{xz} + \varepsilon_{yz}). \tag{2.43}$$

It is recalled that the Γ_3- and Γ_5-type strain contributions ε_{u}, ε_{v}, ε_{xy}, ε_{yz} and ε_{xz} are only activated when a perturbation of suitable symmetry is applied to the system. Given that magnetic field and uniaxial stress are zero and the considered material in the paraquadrupolar phase, the strain along any cubic direction is simply given by $\varepsilon_{\mathrm{B}}/3$. The just mentioned equations indicate that the quadrupolar Γ_3-type symmetrized strains are only induced when the cubic symmetry is broken by an uniaxial stress or a magnetic field applied, for instance, along the [001] or the [110] direction. In the latter scenario also the contribution ε_{xy} with Γ_5 symmetry becomes active, as indicated by Eq. (2.42). By contrast, an uniaxial stress along the [111] direction, which induces a strain $\varepsilon_{[111]}$, couples only to the strains with Γ_5 symmetry, as Eq. (2.43) implies. Consequently, an important implication of the just detailed equations is that only a distortion along a cubic $\langle 100\rangle$ or a $\langle 110\rangle$ direction results in a linear splitting of the cubic non-Kramers Γ_3 doublet.

As mentioned in the outline, symmetrized strain measurements have so far mainly been used to determine quadrupole-strain coupling constants at elevated temperatures [73]. In this work it is demonstrated that such symmetrized strain measurements are a powerful and direct means to track down possible variations in the CEF quadrupole-field susceptibility of quadrupolar Kondo metals. The most common approach to physically characterize this material class is the measurement of symmetrized elastic constants by using the ultrasonic technique. This is the central topic of the following subsubsection.

Symmetrized Elastic Constants

The strain susceptibility χ_Γ describes the response of a multipole moment $\langle O_\Gamma\rangle$ to a symmetrized strain ε_Γ and is defined as

$$\chi_\Gamma = \left.\frac{\partial\langle O_\Gamma\rangle}{\partial\varepsilon_\Gamma}\right|_{\varepsilon_\Gamma\to 0}. \tag{2.44}$$

In case of a degenerate non-Kramers state Γ with quadrupolar degrees of freedom, χ_Γ shows a divergent $1/T$ Curie-type temperature dependence and is therefore a direct means to examine the quadrupolar nature of a CEF state. An elegant way to determine χ_Γ is via the measurement of symmetrized elastic constants. The direct relation between these two quantities is reviewed subsequently by following the notation of Ref. [74, pp. 243-244]. Also Ref. [69] has to be mentioned in the context of this subsubsection, as it is another elementary book on the elastic constant topic.

As indicated by Eq. (2.27), the symmetrized elastic constant c_Γ can be derived via the second derivative of free energy F with respect to the symmetrized strain ε_Γ. As this thesis deals with correlation phenomena related to 4f electrons, the main focus of this review is on the 4f contribution to c_Γ, which calculates by means of the 4f electron free energy $F_{4\mathrm{f}}$ as [74, p. 243]

$$c_\Gamma^{4\mathrm{f}} = \frac{1}{V}\left(\frac{\partial^2 F_{4\mathrm{f}}}{\partial \varepsilon_\Gamma^2}\right)_T = -\frac{1}{V}\left(\frac{\partial^2}{\partial \varepsilon_\Gamma^2} N_{\mathrm{RE}} k_{\mathrm{B}} T \ln \sum_i \exp\left(-E_i(\varepsilon_\Gamma)/k_{\mathrm{B}}T\right)\right)_T, \tag{2.45}$$

where $E_i(\varepsilon_\Gamma)$ denotes the energy of a CEF level, which shows a dependence on strain. $E_i(\varepsilon_\Gamma)$ calculated to second order in perturbation theory is given by [74, p. 243]

$$E_i(\varepsilon_\Gamma) = E_i - g_\Gamma \varepsilon_\Gamma \langle i| O_\Gamma |i\rangle + g_\Gamma^2 \varepsilon_\Gamma^2 \sum_{i \neq j} \frac{|\langle i| O_\Gamma |j\rangle|^2}{E_i - E_j}. \tag{2.46}$$

Besides the 4f contribution $c_\Gamma^{4\mathrm{f}}$, one also has to take account of the lattice contribution c_Γ^0, which the literature commonly refers to as background elastic constant. c_Γ^0 contains both temperature independent harmonic and temperature dependent anharmonic lattice contributions [74, p. 243]. This is in analogy to the lattice thermal expansion coefficient detailed in Section 2.1.2, for which a temperature dependence only arises when the higher order anharmonic terms in the lattice potential are taken into account. As the research on this thesis was carried out at very low temperature $T < 4\,\mathrm{K}$, it is safe to assume that c_Γ^0 is constant in the here accessed temperature range.

By summing up the 4f contribution, evaluated by Eq. (2.45), and the lattice part, the symmetrized elastic constant deduces as [74, p. 244]

$$c_\Gamma = c_\Gamma^0 + n_{\mathrm{RE}}\left[\left\langle \frac{\partial^2 E}{\partial \varepsilon_\Gamma^2}\right\rangle - \frac{1}{k_{\mathrm{B}}T}\left\langle \left(\frac{\partial E}{\partial \varepsilon_\Gamma}\right)^2\right\rangle + \frac{1}{k_{\mathrm{B}}T}\left\langle \frac{\partial E}{\partial \varepsilon_\Gamma}\right\rangle^2\right]. \tag{2.47}$$

The term in square brackets reminds on the definition of the magnetic susceptibility, for which E depends on magnetic field and the respective partial derivatives are calculated with respect to magnetic field instead of strain. This analogy implies a direct relation between the symmetrized elastic constant c_Γ and the strain susceptibility χ_Γ. Consequently, when expressing the term in square brackets of Eq. (2.47) as a strain susceptibility, a simplified relation for the symmetrized elastic constant follows [74, p. 244]

$$c_\Gamma = c_\Gamma^0 - n_{\mathrm{RE}} g_\Gamma^2 \chi_\Gamma, \tag{2.48}$$

whereby the single-ion strain susceptibility χ_Γ reads as [74, p. 244]

$$\chi_\Gamma = \sum_{i \neq j} \frac{p_i - p_j}{E_i - E_j} |\langle i|O_\Gamma|j\rangle|^2 + \frac{1}{k_{\mathrm{B}}T}\sum_i p_i |\langle i|O_\Gamma - \langle O_\Gamma\rangle|i\rangle|^2 = \chi_{\mathrm{VV}} + \frac{C}{k_{\mathrm{B}}T}, \tag{2.49}$$

with $p_i = \exp(-E_i/k_{\mathrm{B}}T)Z^{-1}$ and $Z = \sum_i \exp\left(-E_i/k_{\mathrm{B}}T\right)$. Eq. (2.49) indicates that χ_Γ has two major contributions arising, on the one hand, from diagonal and, on the

other hand, from off-diagonal matrix elements of the respective Stevens operator. The off-diagonal elements thereby correspond to a temperature independent Van Vleck contribution χ_{VV} and the diagonal ones to a temperature dependent Curie contribution $\chi_{\mathrm{C}} = C/(k_{\mathrm{B}}T)$ [74, p. 244]. Note that in case of a magnetic Kramers state, only a Van Vleck but no Curie contribution to the strain susceptibility is present [74, p. 244]. Consequently, elastic constant measurements can directly identify quadrupolar non-Kramers states via a characteristic Curie-type softening and therefore play an equally crucial role for the characterization of non-Kramers states as magnetic susceptibility measurements do for magnetic Kramers state.

For a wide range of materials, the assumption of independent rare earth ions, on which the preceding review is based, is, however, not applicable. In rare earth based intermetallic compounds, for instance, the rare earth ions are periodically arranged on the lattice and interact with each other by means of the conduction electron mediated Ruderman-Kittel-Kasuya-Yosida (RKKY) exchange. By taking account of this additional interaction, whose strength is quantified by the interaction constant K, Eq. (2.48) modifies to [69, p. 82]

$$c_{\Gamma} = c_{\Gamma}^{0} - n_{\mathrm{RE}} g_{\Gamma}^{2} \frac{\chi_{\Gamma}}{1 - K\chi_{\Gamma}}. \tag{2.50}$$

Note that the second term, which assigns to the localized 4f electrons has the same form as the Curie Weiss-type magnetic susceptibility that describes interacting magnetic Kramers states.

The direct relation between the symmetrized elastic constant and the respective strain susceptibility emphasizes the crucial role of elastic constant measurements when studying materials that feature quadrupolar degrees of freedom. Strikingly, the measurement of symmetrized elastic constants is not only a powerful means to obtain information on the quadrupolar nature of a CEF state but also to specify the symmetry of the possible quadrupolar response. Just to recall, the Pr^{3+} ions of the cubic Pr-based 1-2-20 materials examined in this work are subject to a cubic CEF with T_d point group and the ground state was specified as the non-Kramers Γ_3 doublet [27, 42, 43, 65]. According to Table 2.2, $(c_{11} - c_{12})/2$ is the respective symmetrized elastic constant with Γ_3 symmetry and its measurement thus paramount for the characterization of the materials' non-Kramers Γ_3 ground state doublet. On the basis of the above, a Curie-type softening of $(c_{11} - c_{12})/2$ is expected in case of the highly diluted material $Y_{1-x}Pr_xIr_2Zn_{20}$ and a Curie-Weiss-type softening in case of the dense material $PrIr_2Zn_{20}$ at low temperature, where the ground state dominates. In reality, different mechanisms, such as quadrupolar order or the quadrupolar Kondo effect, can lead to deviations from the theoretically expected behavior. The latter effect is an intriguing phenomenon that comes along with a characteristic renormalization of χ_{Γ} to a logarithmic temperature dependence [16]. The measurement of the $(c_{11} - c_{12})/2$ elastic constant is therefore a direct and powerful means to track down possible quadrupolar Kondo correlations in cubic non-Kramers systems. More details on the quadrupole Kondo effect are provided in the subsequent section. In solid state physics, elastic constants are usually measured by the ultrasonic technique, whereby detailed information on the topic is provided in Ref. [69]. Note that the strain susceptibility with Γ_3 symmetry χ_{Γ_3} is hereinafter simply referred to as the quadrupole susceptibility χ_{Q}.

2.4 Kondo Physics

The Kondo effect is likely one of the most thoroughly researched hybridization phenomena in condensed matter physics. In a nutshell, it describes the screening of a localized impurity

magnetic moment by conduction electrons that ultimately results in the vanishment of the impurities' magnetic character. When the local magnetic moments are periodically placed on a crystal lattice, as it is the case in 4f- and 5f-based HF metals, a so called Kondo lattice forms. Of direct relevance for this work is an exotic variation of this hybridization phenomenon, known as two-channel Kondo effect. In this case, a localized moment is over screened by two conduction electron channels, which evokes NFL behavior and a remarkable residual entropy. While the Kondo effect is a well understood phenomenon that has been extensively studied over the last decades, clear experimental evidence for its two-channel version remains still elusive. Finding and exploring new materials that feature this intriguing state of matter is therefore a hotly disputed topic in the field of solid state research.

2.4.1 Single-Channel Kondo Effect

This subsection provides a basic introduction to the Kondo effect, also referred to as single-channel Kondo effect. At first, the single-impurity case is addressed and a brief overview over the historical development is given. Subsequently, the Kondo lattice effect is discussed and its implications for the class of HF metals are elaborated.

Single-Impurity Kondo Effect

Nowadays, it is a well established fact that the contamination of a pure metal with a small fraction of magnetic impurities has a tremendous impact on its low temperature physical properties. This phenomenon becomes particularly evident when considering the electrical resistivity. In contrast to a conventional metal, for which the resistivity decreases monotonically down to a constant value as temperature declines, the resistivity of a metal with a small fraction of magnetic impurities passes through a minimum at low temperatures and shows a divergent like increase as temperature is further reduced. This phenomenon, which was initially reported in the early 1930's [5,6], is termed Kondo effect. It is named after the Japanese theoretical physicist Jun Kondo who made with his theory from 1964 a major contribution to resolve this experimentally found peculiarity [7].

The key aspects of Kondo's theoretical considerations are briefly reviewed in the following. At the theory's core is the Kondo Hamiltonian, which reads as [75]

$$H_{\mathrm{K}} = \sum_{k\mu} \epsilon_k c^{\dagger}_{k\mu} c_{k\mu} + J \sum_{kk'\mu\mu'} \boldsymbol{S} \cdot c^{\dagger}_{k\mu} \boldsymbol{\sigma}_{\mu\mu'} c_{k'\mu'}, \tag{2.51}$$

where the first term describes the free electron gas, with the kinetic energy ϵ_k and the annihilation and creation operators $c_{k\mu}$ and $c^{\dagger}_{k\mu}$, respectively. k is the wavenumber and μ the electron spin, which can either point up or down. The second term, generally labeled as s−d term, denotes the interaction between the conduction electrons, whose spin vector $\boldsymbol{\sigma} = (\sigma_1, \sigma_2, \sigma_3)$ is described by the Pauli matrices, and a localized impurity spin $\boldsymbol{S} = (S_1, S_2, S_3)$ [75]. The interaction strength between impurity and conduction electron spin is quantified by a constant denoted as $J > 0$ [75]. A key assumption of the model is that the conduction electron channel has no orbital degrees of freedom, meaning that $l = 0$ [75]. As Kondo pointed out in his original publication from 1964 [7], the employed s−d exchange model is based on previous theoretical work by Kasuya [76], Zehner [77] and Yosida [78,79]. The central point of Kondo's theory was to demonstrate by means of a second order Born approximation that the interaction between the localized magnetic impurity and the conduction electrons, which is described by the s−d term in the Kondo Hamiltonian, leads to a low temperature divergence in the electron scattering

rate [7]. Specifically, this implies a correction to the low temperature electrical resistivity that depends logarithmically[5] on temperature [7]

$$\rho = c\rho_{\mathrm{M}}[1 - (3zJ/\epsilon_{\mathrm{F}}) \log T], \tag{2.52}$$

where c is the impurity concentration, $\rho_{\mathrm{M}} = 3\pi m J^2 S(S+1)(V/N)/2e^2\hbar\epsilon_{\mathrm{F}}$, z quantifies how many conduction electrons assign to an atom and ϵ_{F} is the Fermi energy. According to Eq. (2.52), a divergence in the electrical resistivity is, however, only present, when the Kondo interaction J is AFM [7]. As Kondo pointed out, a first order Born approximation would only yield a temperature independent term in the scattering rate and is therefore not sufficient to explain the experimentally observed divergence in the low temperature electrical resistivity [7].

The combination of the logarithmically divergent electrical resistivity contribution specified by Eq. (2.52) with the lattice contribution $\rho_{\mathrm{phon}} = aT^5$, provides indeed a very good description of the experimentally observed low temperature minimum and divergence in the electrical resistivity [7]. Kondo could therefore successfully derive a relatively simple mathematical relation that provides an excellent description of the electrical resistivity of a metal with a small fraction of magnetic impurities [7]

$$\rho = aT^5 + c\rho_0 - c\rho_1 \log T, \tag{2.53}$$

where a is a constant and ρ_0 the residual resistivity.

Nevertheless, Kondo's theory also had a significant inconsistency, namely the divergence in the electrical resistivity on approaching absolute zero. Shortly after Kondo's original publication, Abrikosov [80] identified a characteristic temperature to which the divergence in the electrical resitivity can be assigned to. This is the well known Kondo temperature, defined as [80]

$$T_{\mathrm{K}} \sim \exp\left(-1/|J|\right). \tag{2.54}$$

In 1961, a few years before Kondo's groundbreaking work, Philip Anderson published his theory on local moment formation in metals [81]. While Kondo took the existence of local moments for granted, Anderson addressed the problem of how a local moment actually develops from scratch. The two key constituents of Anderson's theory are the Coulomb repulsion U between the d electrons of the impurity and the tunneling between localized d and conduction states, resulting in a resonance with a finite width Δ that is generally referred to as hybridization energy [81, 82]. In case of $U = 0$, this resonance is directly located at the energy of the d state ϵ_{d} [81, 82]. The essential point of Anderson's theory is that the formation of local moments depends sensitively on the interplay of the two parameters U and Δ. By employing a Harte Fock approximation, Anderson showed that, in case the conditions $\epsilon_{\mathrm{F}} > \epsilon_{\mathrm{d}}$ and $\Delta/U < \pi$ are fulfilled, a separation of the single resonance into two takes place and a local moment forms [81, 82]. For more details it is referred to Anderson's original work [81] and to a subsequent review article [82]. As Anderson's considerations are based on a hybridization between local moment and conduction electrons, they differ from the approach taken by Kondo who described the interaction between localized magnetic moment and conduction electrons by means of an exchange interaction J. Notably, in 1966 it was shown by Schrieffer and Wolff that the approaches of Anderson and Kondo are equivalent given that s−d mixing is small [83].

[5] Note, as Kondo assumed in his original publication that an AFM interaction corresponds to $J < 0$, which is in contrast to the presented Hamiltonian from Ref. [75], where an AFM interaction is denoted by $J > 0$, the sign of the logarithmic term in Eq. (2.52) was flipped from positive to negative as compared to Kondo's cited original publication [7], to be in line.

Tackling the problem with the low temperature divergence in the electrical resistivity was the topic of subsequent research. In the end it was Wilson [9] who gave an exact solution of this long standing problem by means of renormalization group theory. Wilson's calculations suggested a temperature independent impurity magnetic susceptibility at very low temperature [84, p. 89]

$$\chi_{\mathrm{imp}} = \frac{(g\mu_{\mathrm{B}})^2 w}{4k_{\mathrm{B}}T_{\mathrm{K}}}, \tag{2.55}$$

which demonstrated the vanishment of the impurities' magnetic character due its full screening by the conduction electrons. Here, $w = 0.4128$ denotes the Wilson number, which links the Kondo temperature to the impurity magnetic susceptibility [84, p. 90]. The specific heat assigned to the impurity, on the other hand, shows a linear dependence on temperature $C_{\mathrm{imp}} = \gamma_{\mathrm{imp}} T$ [84, p. 90]. With the help of these two quantities, the Wilson ratio R can be calculated as [84, p. 90]

$$R = \frac{\chi_{\mathrm{imp}}/\chi_{\mathrm{c}}}{\gamma_{\mathrm{imp}}/\gamma_{\mathrm{c}}} = \frac{4\pi^2 k_{\mathrm{B}}^2}{3(g\mu_{\mathrm{B}})^2} \frac{\chi_{\mathrm{imp}}}{\gamma_{\mathrm{imp}}} = 2, \tag{2.56}$$

where χ_{c} and γ_{c} denote the susceptibility and the Sommerfeld coefficient assigned to the conduction electrons. This is a surprising finding, as the value of $R = 2$ differs from the one of electrons that do not interact with each other, which are generally described by $R = 1$ [84, p. 90]. Later it became apparent that this enhancement is due to the formation of quasiparticles and therefore a direct consequence of the interaction between electrons [84, p. 90]. Pioneering work on this topic was done by Nozières [85], who proposed that the Kondo effect corresponds to a local FL at very low temperature.

Kondo Lattice Effect

A central assumption of the just detailed single-impurity Kondo model is the independence of the local moments, meaning that Kondo's theory only applies to materials containing a tiny fraction of magnetic ions. For a large variety of 4f- and 5f-based intermetallic compounds, this prerequisite is, however, not fulfilled, as the magnetic ions are periodically arranged on the lattice and their inter-site interaction is not negligible. Such materials are classified as Kondo lattice systems. The terminology goes back to Doniach, who suggested back in 1977 that the ground state of a dense local moment system is either a sort of non-magnetic Kondo screened or an antiferromagnetically ordered state [10]. Since this initial proposal, the physical characteristics of dense local moment systems have been studied extensively, mainly on the example of magnetic HF metals [2,4]. Before discussing the key signatures of Kondo lattice systems more in detail, some important theoretical aspects are outlined.

The Kondo lattice Hamiltonian reads as [86]

$$H_{\mathrm{KL}} = \sum_{k\mu} \epsilon_k c_{k\mu}^{\dagger} c_{k\mu} + J \sum_{i\mu\mu'} \boldsymbol{S}_i \cdot c_{i\mu}^{\dagger} \boldsymbol{\sigma}_{\mu\mu'} c_{i\mu'}, \tag{2.57}$$

where the first term describes the conduction electrons and the second term their interaction with the local moments that are sitting at different lattice sites i. In addition to the Kondo temperature T_{K}, a Kondo lattice is distinguished by a second energy scale, namely the Kondo coherence temperature T_{coh} that is generally smaller than T_{K} [87]. The effect of coherence can be nicely illustrated by taking the example of HF metals. At elevated temperatures, a HF metal exhibits basically the same characteristics as a single-impurity system, i.e. its electrical resistivity increases logarithmically as temperature declines [88].

At low temperature, however, the periodicity of the local moment sublattice leads to the formation of Bloch waves [47, p. 658]. In consequence, the independent and therefore incoherent scattering processes happening at each local moment site show a coherent character, which manifests itself in a sudden decrease of the HF metal's electrical resistivity [47, p. 659]. This coherent low temperature behavior is typically captured by FL theory and therefore distinguished by a quadratic temperature variation of the electrical resistivity, a linear in temperature dependence of the specific heat coefficient and a temperature independent magnetic susceptibility [2, 87]. As pointed out by Doniach, the coherent low temperature Kondo ground state is in competition with AFM order, which provides the basis for the phenomenon of magnetic HF QC [10, 11]. Note that AFM order in local moment systems is induced by the RKKY interaction via the conduction electrons [89]. Since the Kondo and the RKKY energy scales depend differently on the interaction constant J, whereby $T_{\mathrm{K}} \sim \exp(-1/|J|)$ and $T_{\mathrm{RKKY}} \sim J^2$, it is the magnitude of J, which specifies the ground state of a Kondo lattice [10]. The just detailed dependencies of the characteristic temperatures on J demonstrate that for small J the RKKY energy scale dominates, while the Kondo energy scale prevails for large J. Of particular interest is the point of the phase diagram, at which both energy scales cross. Here, typically a QCP forms that is linked to NFL and other peculiar behavior, such as unconventional superconductivity [11]. More specific details on the phenomenon of QC were already provided in Section 2.1.4 to which it is referred at this point for further details.

2.4.2 Two-Channel Kondo Effect

An exotic variation of the just detailed Kondo effect that triggers NFL behavior in various thermodynamic quantities as well as an unconventional residual entropy is the two-channel Kondo effect. This unconventional hybridization effect is of particular relevance for this thesis, as there has been initial evidence for its emergence in the here investigated class of Pr-based 1-2-20 systems [28, 30, 35, 42–44]. By contrast to the well studied single-channel Kondo effect, conclusive experimental evidence for the two-channel Kondo effect remains still elusive. This subsection provides a brief introduction to the latter effect and reviews its thermodynamic signatures with respect to both the single-impurity and the lattice version.

Single-Impurity Two-Channel Kondo Effect

The two-channel Kondo effect is a special case of the multichannel Kondo scenario, which was originally proposed by Nozières and Blandin back in 1980 [15]. Their theory addresses shortcomings of both the Kondo and the Anderson model, as neither of the two takes account of the orbital contribution of the localized magnetic impurity [15]. The multichannel Kondo Hamiltonian has a similar form as the conventional single-impurity Kondo Hamiltonian, specified by Eq. (2.51), with the key difference that the number of electron screening channels is not limited to a single one [15, 90]

$$H_{\mathrm{MCK}} = \sum_{km\mu} \epsilon_k c^{\dagger}_{km\mu} c_{km\mu} + J \sum_{kk'm\mu\mu'} \boldsymbol{S} \cdot c^{\dagger}_{km\mu} \boldsymbol{\sigma}_{\mu\mu'} c_{k'm\mu'}, \tag{2.58}$$

where the summation over m takes account of the various orbital screening channels. The multichannel Kondo model differs among three distinct screening scenarios, which set the impurity spin S in relation to the total number of orbital screening channels n and lead to different ground states [15]. These are listed and briefly discussed in the following.

- In the first scenario it holds $\boldsymbol{n = 2S}$. Here, the localized impurity spin is fully screened by the conduction electron channels and the resulting ground state is a singlet featuring FL behavior. An example is the conventional Kondo effect, which arises in magnetic impurity systems, as discussed in the preceding subsection. [15,91]
- The second scenario describes the case where $\boldsymbol{n < 2S}$. Here, the number of conduction electron channels is not sufficient to fully screen the impurity spin. The impurity is therefore under screened and the resulting ground state remains partially degenerate. In this case, the Kondo interaction between impurity and conduction electrons is ferromagnetic (FM). [15,91]
- The third scenario denotes a situation where $\boldsymbol{n > 2S}$. Here, the impurity spin is over screened by the conduction electron channels and the Kondo interaction of AFM nature. In consequence, criticality arises in various thermodynamic quantities, which implies intriguing physics to explore. This case is of particular relevance for this thesis, as it covers the two-channel Kondo scenario where $S = 1/2$ and $n = 2$. [15,91]

In the following, the focus is on the third scenario, which describes the over screening of the impurity spin by the conduction electron channels. After the original proposal of the model by Nozières and Blandin [15], different approaches were taken to solve the multichannel Kondo problem that included, for instance, the Bethe Ansatz method [17,92] or conformal field theory [41,93].

For the over screened case with $S = 1/2$, calculations by Tsvelick [17] suggested that NFL behaviors arise in the impurity specific heat and the impurity susceptibility. The NFL behaviors depend sensitively on the number of conduction electron screening channels, as described by the following relations [17,18]

$$\frac{C}{T} \sim \left(\frac{T}{T_\mathrm{K}}\right)^{\frac{4}{(n+2)}-1}, \tag{2.59}$$

$$\chi \sim \left(\frac{T}{T_\mathrm{K}}\right)^{\frac{4}{(n+2)}-1}, \tag{2.60}$$

where T_K is the characteristic multichannel Kondo temperature. In addition, Tsvelick [17] proposed that the over screening comes along with an unconventional zero field residual entropy in the limit $T \to 0$ that is given by [17]

$$S = \ln \frac{[\sin\left(\pi(2S+1)\right)/(n+2)]}{\sin\left[\pi/(n+2)\right]}. \tag{2.61}$$

As the two-channel Kondo effect, where an impurity spin with $S = 1/2$ is over screened by two channels of conduction electrons $n = 2$, manifests itself in selected Pr-based 1-2-20 materials [42–44,94], its implications for the just detailed NFL behaviors shall be discussed in the following. Generally, a two-channel Kondo effect can appear both in magnetic and quadrupolar systems [95]. Given that the localized moment carries quadrupolar degrees of freedoms, the relevant susceptibility is the quadrupole-strain susceptibility [16]. In the single-impurity two-channel Kondo scenario, the just detailed relations simplify and both the specific heat over temperature and the susceptibility of the impurity depend logarithmically on temperature [16,18]

$$\frac{C}{T} = -a \ln\left(\frac{T}{T_\mathrm{K}}\right), \tag{2.62}$$

$$\chi = -b \ln\left(\frac{T}{T_{\mathrm{K}}}\right), \tag{2.63}$$

where a and b are constants. In addition, Affleck and Ludwig [41] suggested a square root temperature dependence of the electrical resistivity [41]

$$\rho \sim 1 + c\sqrt{T}, \tag{2.64}$$

where c is a constant. Also the complex expression for the residual entropy given by Eq. (2.61) simplifies and yields a characteristic value of [17]

$$S = \frac{1}{2} \ln 2. \tag{2.65}$$

These clear theoretical predictions of the NFL associated to the single-impurity two-channel Kondo effect quested for real materials that feature this unconventional physics. In this regard, Cox [95] made a crucial contribution with his proposal of selection rules that allow for the identification of suitable 4f and 5f ions that can principally host two-channel Kondo physics. A potential candidate is, for instance, the Ce^{3+} ion located in a cubic crystal environment [95]. Given that the CEF ground state is the Γ_7 doublet, its hybridization with conduction electrons of Γ_8 symmetry can evoke the magnetic two-channel Kondo effect [95]. By contrast, Cox deems the formation of a two-channel Kondo effect in a Yb^{3+} ion for unlikely [95]. Another possible candidate is the U^{4+} ion [95]. Provided that a cubic CEF is present, the Γ_3 doublet is a possible CEF ground state of this ion that can hybridize with conduction electrons of Γ_8 symmetry and lead to a two-channel Kondo effect [95]. As the Γ_3 doublet of the non-Kramers U^{4+} ion is of quadrupolar nature, the term quadrupolar Kondo effect is generally employed. This terminology also goes back to Cox, who introduced the quadrupole Kondo model in order to explain exotic NFL behavior emerging in UBe_{13} [13,14]. Note that the just mentioned examples are just a fraction of all possible ones and it is referred to the original publication by Cox [95] for more details. Initially, there has been comprehensive research on diluted U-based materials, which included, for instance, the compounds $U_xTh_{1-x}Be_{13}$ [19, 20], $U_xTh_{1-x}Ru_2Si_2$ [23, 24] and $Y_{1-x}U_xPd_3$ [21, 22], in order to find experimental evidence for the quadrupolar Kondo effect. While unconventional behaviors were indeed revealed that were in partial agreement with the theoretical predictions, it has so far not been possible to find hard and unambiguous evidence for the formation of the quadrupolar Kondo effect in bulk materials. In the U-based materials, the hybridization strength is usually significant, which in turn complicates the measurement of CEF excitations. Specifying the CEF ground state of the material under consideration is, however, essential in order to evaluate as to whether quadrupole moments are involved in the formation of the NFL state.

In addition to the just detailed 4f ions, the non-Kramers Pr^{3+} ion is another noteworthy candidate [96]. If exposed to a cubic CEF, the Pr^{3+} ion with $J = 4$ can principally show a non-Kramers Γ_3 ground state doublet [64]. The quadrupolar ground state moments with Γ_3 symmetry can then, analogously to the U^{4+} ion, hybridize with conduction electrons of Γ_8 symmetry, which provides the basis for a quadrupolar two-channel Kondo effect [96]. With the recent discovery of the class of cubic Pr-based 1-2-20 systems [25, 26, 97], new prototype materials were found that feature such a non-Kramers Γ_3 ground state doublet. These materials are therefore well suited to explore the quadrupolar Kondo effect, whereby $PrIr_2Zn_{20}$ has to be mentioned as a prime example [27, 28, 65]. Consequently, its highly diluted sister compound $Y_{1-x}Pr_xIr_2Zn_{20}$ is a promising candidate to feature the single-impurity quadrupole Kondo effect and the just detailed measurements of the specific heat,

quadrupole susceptibility and electrical resistivity are essential probes to verify its possible formation in the material [42–44, 94].

Two-Channel Kondo Lattice Effect

As aforementioned equations only hold true for the single-impurity case, they cannot be applied to dense two-channel Kondo lattice systems, for which the localized magnetic or quadrupolar moments are arranged in a periodic manner within the crystal structure and interact with each other. Even though various approaches were taken from the theory side to tackle this problem and to provide a general framework for the theoretical description of the two-channel Kondo lattice effect, universally applicable mathematical relations that unambiguously predict the related behavior have, as of yet, not been found.

An early work by Jarell et al. [98] used a quantum Monte Carlo simulation and demonstrated that a two-channel Kondo lattice displays NFL behavior and transitions into an AFM ordered state at low temperature. The formation of the latter phase depends thereby sensitively on the filling of the conduction electron band and is only realized for the case of half filling [98]. Recently, Tsuruta et al. [40] took another theoretical approach that was successfully applied to describe the NFL behaviors present in selected Pr-based 1-2-20 materials [28, 30, 35]. Their theory is based on a two-channel Anderson lattice model, which is evaluated by means of the $1/N$ expansion technique [40]. This yields characteristic NFL temperature dependencies in the specific heat, electrical resistivity and magnetic susceptibility [40]

$$C \sim 1 - a\sqrt{T}, \tag{2.66}$$

$$\rho \sim \frac{1}{1 + \frac{b}{T}}, \tag{2.67}$$

$$\chi \sim 1 - c\sqrt{T}, \tag{2.68}$$

where are a, b and c are constants. Strikingly, the model provides a very good description of the unconventional temperature dependencies found in the electrical resistivity and the specific heat of the material $PrIr_2Zn_{20}$ [28]. Also the temperature dependence of the electrical resistivity of $PrRh_2Zn_{20}$ could be well accounted for [30]. In addition, Fu et al. [35] used the model to successfully describe the NFL behavior emerging in the electrical resistivity and magnetic susceptibility of PrV_2Al_{20}.

As temperature approaches absolute zero, a two-channel Kondo lattice typically undergoes some kind of ordering that ultimately quenches the exotic NFL behavior [99]. The most straightforward scenario is the RKKY-type ordering of the ground state's multipole moments, which was observed in various Pr-based 1-2-20 materials [28, 30]. In $PrIr_2Zn_{20}$, for instance, the NFL behavior is suppressed by AFQ order at 0.11 K [27, 28], while $PrRh_2Zn_{20}$ undergoes AFQ ordering at 0.06 K [29] and PrV_2Al_{20} shows a yet unidentified double transition at around 0.6 K [39]. An alternative and more exotic ordering mechanism, termed composite order, was proposed by Hoshino et al. [99, 100]. In the case of F-channel diagonal composite order, the degeneracy of both electron screening channels related to the quadrupole Kondo effect is lifted, as one of the two conduction electron channels hybridizes with the local moments into Kondo singlets [99, 100]. Interestingly, this effect is accompanied by characteristic FL behavior [99]. A very similar scenario to the just mentioned model by Hoshino et al. [99, 100] was recently introduced by Zhang et al. [101] and Van Dyke et al. [102] termed hastatic order. Specifically, Van Dyke et al. [102] deduced a magnetic field phase diagram for the case of half filling, which implies

the formation of AFQ order at low magnetic field followed by ferrohastatic (FH) order at intermediate magnetic field and an uncorrelated singlet state at high magnetic field. This theoretical prediction matches well with the low temperature phase diagram of $PrIr_2Zn_{20}$ derived by Onimaru et al. [28], which provides indication for the possible formation of composite or hastatic order in the material.

Chapter 3

Experimental Methods

Carrying out thermal expansion and magnetostriction measurements at very low temperature is a challenging task. While it is rather straightforward to cool down to a temperature as low as 4.2 K, which is the boiling temperature of liquid helium, reaching temperatures in the mK range takes much greater effort. In this environment, also the measurement of physical quantities becomes more tricky, as measurement signals are typically tiny and easily affected by external noise. Consequently, a well optimized experimental setup is essential in order to obtain reliable data in the mK range.

This chapter deals with the experimental methods and the setup utilized for the research on this thesis and is structured as follows. The first section is dedicated to the physics behind dilution refrigeration, a cooling technique that allows for the generation of temperatures in the low mK range. In the following section, the measurement technique capacitive dilatometry is introduced and the two capacitive dilatometers utilized in this work are detailed. The final section gives insights into the experimental setup, whereby a special focus lies on its optimization with respect to noise generating ground loops.

3.1 Low Temperature Physics

As the term low temperature is a rather broad one, its interpretation lies in the eye of the beholder. In daily life, for instance, where typically a quite narrow temperature range is accessed, already the freezing temperature of water is considered as low. In a scientific environment, however, the definition of low temperature is a much different one. Here, it is common to quantify temperature by use of the Kelvin scale that defines 0 K as absolute zero temperature. A view on this temperature scale suggests that the freezing temperature of water, which is located at around 273 K, is still a comparably high one. Thanks to the technical progress made in the last century, temperatures at the lower end of the Kelvin temperature scale became readily accessible. In particular, the liquefaction of ^{4}He by Heike Kamerlingh Onnes back in 1908 was a major breakthrough due to its very low boiling point of 4.2 K. Nowadays, highly advanced refrigeration lab equipment even allows for the generation of temperatures close to absolute zero. A dilution refrigerator is such a machine, which typically allows for cooling down to temperatures as low as $0.01\,\mathrm{K} - 0.02\,\mathrm{K}$. As a dilution refrigerator was employed in this work, the underlying basic physical principles are outlined in this section. Furthermore, the topic temperature and its measurement close to absolute zero is briefly addressed.

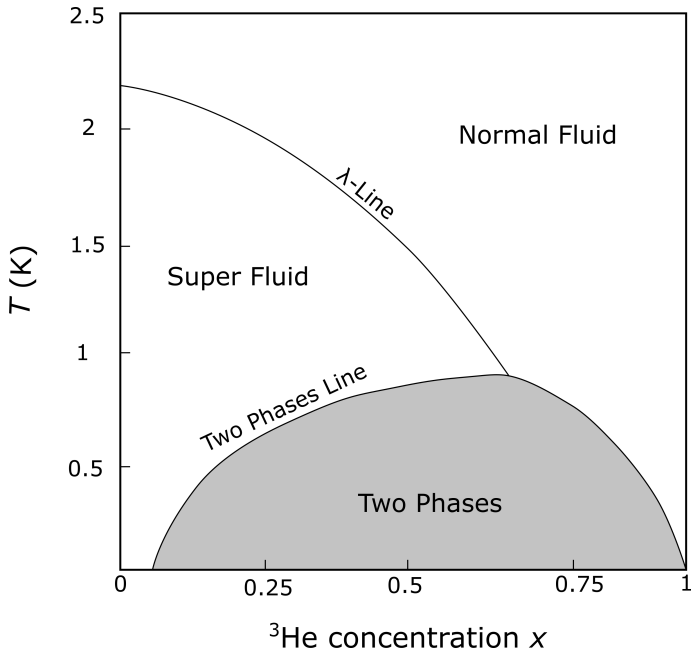

Figure 3.1: Rough phase diagram sketch of a ^{3}He/^{4}He mixture, whereby temperature against the ^{3}He concentration x is shown. The λ-line and the two phases line are indicated. Sketched based on Ref. [104, p. 106], which in turn used data from Refs. [105–110].

3.1.1 Generating Ultra-Low Temperatures

In this thesis, dilution refrigeration, which makes use of the physical properties of a mixture of ^{3}He and ^{4}He isotopes, was used to generate temperatures in the low mK range. The basic physical principles behind are briefly outlined in this subsection. For more in-depth explanations, it is referred to Ref. [103] on which the following lines on dilution refrigeration are mainly based. In addition, Refs. [8, 104] provide further information on liquid helium.

The isotopes ^{3}He and ^{4}He have boiling points of 3.19 K and 4.21 K and transition into the superfluid state at 0.0025 K and 2.177 K, respectively [103, p. 15]. Superfluidity is an intriguing state of matter with fascinating physical properties. Key characteristics of superfluid ^{4}He, which is commonly termed as Helium II, are zero viscosity, zero entropy and a by five orders of magnitude enhanced thermal conductivity as compared to normal fluid ^{4}He [8, chap. 2]. Based on the extremely low superfluid transition temperature of ^{3}He, experiments on its superfluid phase are much more challenging than on the one of ^{4}He. In addition, ^{3}He shows a more complex phase diagram, as three different superfluid phases emerge as a function of pressure and of magnetic field [8, p. 85].

A mixture of both isotopes shows no less fascinating characteristics that set the basis for refrigeration down to mK temperatures. In order to understand the physical principles behind dilution refrigeration, the phase diagram of a ^{3}He/^{4}He mixture has to be considered. The latter is sketched in Fig. 3.1, which illustrates temperature against the ^{3}He concentration x [104, p. 106]. Highlighted are the λ-line, which separates the normal fluid from the superfluid phase, and the phase-separation line, below which a phase rich in ^{4}He and a phase rich in ^{3}He forms [104, p. 105]. The phenomenon of phase separation at low temperatures and in particular the properties of the ^{4}He rich phase are key for dilution

refrigeration. While the ^{4}He content of the ^{3}He rich phase vanishes to zero as temperature declines to zero, a finite fraction of 6.6 % ^{3}He remains in the ^{4}He rich phase even close to zero temperature [103, p. 122]. To facilitate dilution refrigeration, ^{3}He atoms are forced from the phase rich in ^{3}He into the phase rich in ^{4}He and the enthalpy change ΔH related to this process results in cooling [103, p. 123]. ΔH can be deduced by integrating the specific heat change ΔC between the ^{3}He rich and the ^{4}He rich phase [103, p. 123]

$$\Delta H \sim \int \Delta C \mathrm{d}T. \tag{3.1}$$

Consequently, the cooling power $\dot{Q}$ reads as [103, p. 124]

$$\dot{Q} \sim x\Delta H \sim T^2. \tag{3.2}$$

With this key characteristic of a ^{3}He/^{4}He mixture in mind, the focus is now on the working principle of a dilution refrigerator, in which the before detailed properties of a ^{3}He/^{4}He mixture find application. The hearth of the dilution refrigerator is the dilution refrigerator insert that contains the dilution circuit. The insert sits in a bath of liquid ^{4}He, which cools the system down to a temperature of approximately 4.2 K. To generate mK temperatures, initially a ^{3}He/^{4}He mixture has to be condensed into the dilution circuit of the dilution refrigerator insert. After finishing the condensation process, the mixture is circulated through the dilution unit by means of an automated gas handling system. As it will become evident at the end of this subsection, it is nearly pure ^{3}He, which is pumped through the dilution circuit during operation. When the ^{3}He gas enters the dilution circuit at room temperature, it is cooled to liquid helium temperature of 4.2 K with the help of a ^{4}He bath. Inside the dilution refrigerator insert, different cooling stages, as illustrated in Fig. 3.2, gradually reduce the temperature of the ^{3}He [103, p. 136]. Note that the lowest accessible temperature of a dilution refrigerator depends on the employed system. The dilution refrigerator used for the research on this thesis, for instance, generates temperatures as low as approximately 0.02 K. To better understand the refrigeration process, the purpose of each of the different cooling stages is briefly outlined in the following. The first cooling stage is the 1 K pot, which operates at a temperature of approximately 1.5 K and aims to further reduce the temperature of the ^{3}He gas [103, p. 136]. The cooling process in the 1 K pot is realized by means of ^{4}He evaporation cooling. After leaving the 1 K pot, the ^{3}He passes through the main flow impedance, which guarantees its condensation [103, p. 136]. It is further cooled by an array of heat exchangers and finally reaches the mixing chamber, the stage with the lowest temperature [103, p. 136]. Before the mixing chamber, a secondary flow impedance makes sure that the liquid ^{3}He does not vaporize again [103, p. 136]. The mixing chamber is the coldest stage of the dilution refrigerator and consists of both ^{4}He rich and ^{3}He rich phase [103, p. 136]. As outlined before, at very low temperatures the ^{4}He rich phase still contains a finite percentage of 6.6% ^{3}He, while the ^{3}He rich phase releases its ^{4}He component and tends towards a pristine ^{3}He liquid [103, p. 122]. The ^{3}He rich phase is thereby located at the top part of the mixing chamber due to its lower density and the ^{4}He rich phase at its bottom [103, p. 122]. To reach mK temperatures, ^{3}He is continuously removed from the ^{4}He rich phase, which forces ^{3}He atoms from the ^{3}He rich phase into the ^{4}He rich phase in order to maintain the finite fraction of 6.6% ^{3}He in the ^{4}He rich phase [103, p. 123]. As indicated by Eq. (3.2), it is the mixing enthalpy related to the movement of the ^{3}He atoms from the ^{3}He rich into the ^{4}He rich phase, which ultimately facilitates the refrigeration down to mK temperatures [103, p. 123]. To remove ^{3}He atoms from the ^{4}He rich phase in the mixing chamber, the bottom of the mixing chamber is directly connected to the still, whose temperature

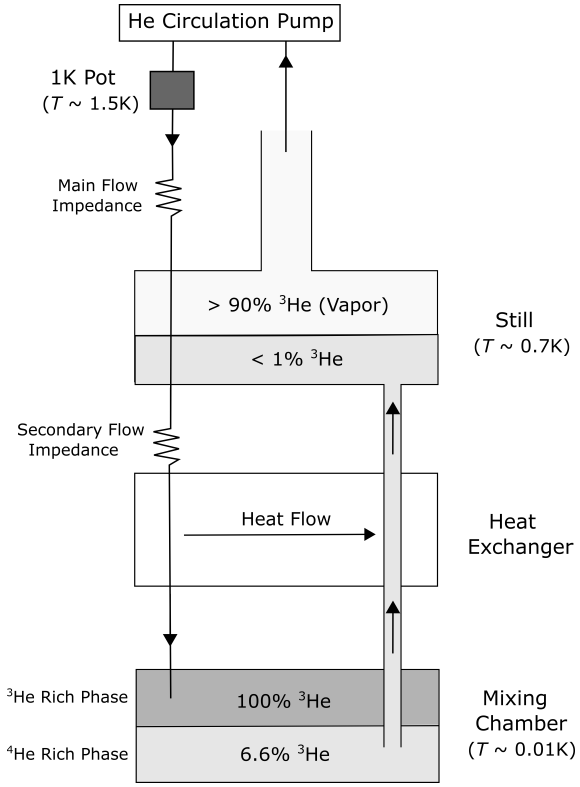

Figure 3.2: Illustration of the dilution circuit of a conventional ^{3}He/^{4}He dilution refrigerator. Sketched based on Ref. [103, p. 136].

ranges in between $0.6\,\mathrm{K} - 0.7\,\mathrm{K}$ [103, p. 139]. As the vapor pressure of ^{3}He is higher than the one of ^{4}He, the liquid phase in the still consists of nearly pure ^{4}He with a very little ^{3}He fraction of less than 1% [103, p. 137]. On the other hand, the vapor inside the still contains nearly pure ^{3}He [103, p. 137]. In consequence of the significant difference in the ^{3}He concentration between the two phases in the mixing chamber and the still, osmotic pressure causes the ^{3}He atoms to move from the mixing chamber through aforementioned connection into the still [103, p. 135]. To establish a cooling cycle, the ^{3}He vapor in the still is continuously removed by means of the He circulation pump, cleaned from impurities by two cold traps and finally pumped back into the dilution circuit. It is therefore basically ^{3}He that circulates through a dilution refrigerator during operation.

3.1.2 Measurement of Temperature in the mK Range

In order to quantify temperature in the mK range, resistive thermometry is the most prevalent method. As a thermometer material, thick film RuO_2 chips are commonly employed based on their semiconducting property and their inexpensiveness [103, p. 265]. A key characteristic of a semiconducting material is the exponential increase of its resistance as temperature approaches absolute zero. Consequently, a tiny change in temperature relates to a substantial change in resistance, which allows for ultra-high resolution temperature measurements in the low mK range. A downside of such a semiconducting temperature sensor is the loss of sensitivity as temperature increases. However, as it is typically the boiling temperature of liquid helium that limits the highest accessible temperature in a dilution refrigerator, the sensitivity of a RuO_2 sensor is generally sufficient to fully

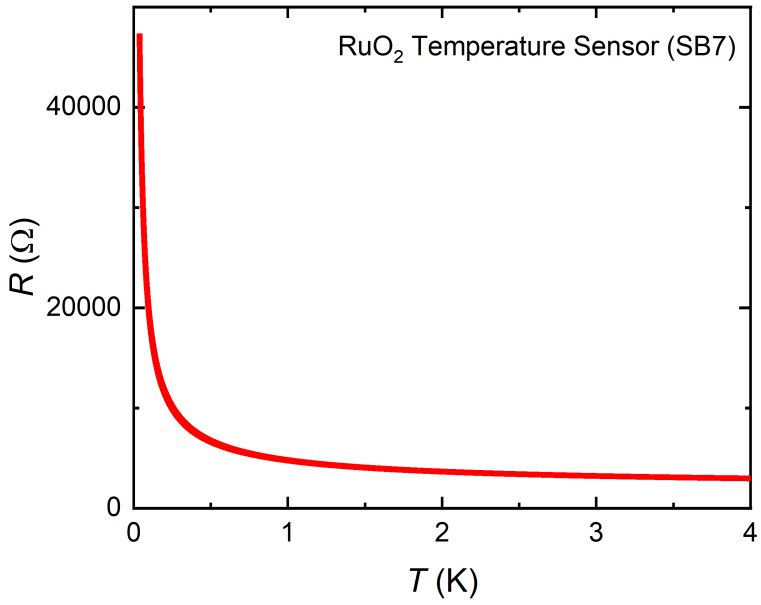

Figure 3.3: Resistance versus temperature curve of the RuO_2 thick film resistor (SB7) utilized in this thesis for the measurement of temperature.

cover the accessible temperature range. RuO_2 resistive thermometers classify as secondary thermometers. Before usage they have to be calibrated, typically against a primary thermometer. Here, commonly a combination of a superconducting fixed point device and a cerium magnesium nitrate (CMN) thermometer is used. The fixed point device contains an array of different superconducting samples with well known transition temperatures. The CMN thermometer consists of the paramagnetic salt CMN, whose magnetic susceptibility exhibits a $1/T$ Curie-type temperature dependence at low temperature. Combining both devices is therefore a powerful means to calibrate a low temperature RuO_2 sensor. In general, the calibration against an already calibrated resistance thermometer is also conceivable, whereby the calibration against a primary thermometer is more desirable.

In this thesis, temperature was measured with such a RuO_2 thick film resistor. The thermometer itself was setup in the framework of my master thesis [111]. To contact the sensor, superconducting wires by the company SUPERCON (Type SW-M) were used [111]. At temperatures well below the superconducting transition temperature, superconductors display a very low thermal conductivity. This characteristic ensures that no external heat is transported to the thermometer through the connecting wires and the measured temperature corresponds to the one of the sensor's close environment. The superconducting wire is made from the material NbTi whose critical field is much higher than the relatively small stray fields to which the sensor is exposed [111]. The here utilized RuO_2 thick film resistor was thermally cycled for approximately fifty times between liquid helium and room temperature before calibration [111], following the suggestion by Pobell [103, p. 265]. This process is necessary as the resistance of a RuO_2 sensor slightly changes during the first thermal cycles, which is commonly known as aging effect [103, p. 265]. Calibration of the sensor was done by S. Bachus[1] back in 2017 together with a bunch of other sensors. S. Bachus calibrated the thermometer against a superconducting fixed point device and a CMN thermometer at very low temperatures $0.023\,\mathrm{K} \leq T \leq 0.18\,\mathrm{K}$ and against

[1]Chair of Experimental Physics VI, University of Augsburg, 86159 Augsburg, Germany.

an ex factory calibrated Cernox® sensor from Lake Shore Cryotronics at temperatures $0.18\,\mathrm{K} < T \leq 8.3\,\mathrm{K}$. The RuO_2 thermometer, referred to as SB7, consequently allows for temperature measurements in the range $0.023\,\mathrm{K} - 8.3\,\mathrm{K}$. Its resistance versus temperature curve for $T \leq 4\,\mathrm{K}$ is presented in Fig. 3.3.

3.2 Capacitive Dilatometry

This section covers the experimental technique capacitive dilatometry, a standard method to measure the low temperature thermal expansion and magnetostriction of solids. At first, the setup and the working principle of the two ultra-high resolution capacitive dilatometers, utilized for the research on this thesis, is described. Subsequently, the calculation of the relative length change, the determination of the background contributions of the dilatometers and the procedure of data analysis are discussed.

3.2.1 Capacitive Dilatometers

Capacitive dilatometry takes advantage of the direct relation between the capacitance of a parallel plate capacitor and the distance between its two capacitor plates. A capacitive dilatometer is designed in a way that a change in the mounted sample's length induces an identical change in the distance between the two capacitor plates. This allows to directly deduce the relative length change of a sample as a function of temperature or magnetic field by measuring the respective change in capacitance. The experimental results of the thermal expansion and magnetostriction measurements presented in this thesis were obtained by use of a ultra-high resolution miniaturized capacitive dilatometer [112]. Two selected single crystals were additionally examined with an uniaxial stress capacitive dilatometer [113] in order to evaluate the effect of uniaxial stress on their thermal expansion. Both dilatometers were developed by R. Küchler[2] and are capable of resolving tiny relative length changes in the range $0.01\,\text{Å} - 0.02\,\text{Å}$ [112, 113].

Miniaturized Capacitive Dilatometer

The major part of the relative length change measurements presented in this thesis was carried out by use of a miniaturized capacitive dilatometer, developed by R. Küchler. A detailed description of the miniaturized capacitive dilatometer can be found in Ref. [112] of which I am a coauthor. My contribution was to test the performance of the miniaturized capacitive dilatometer at mK temperatures. The miniaturized dilatometer measures only $1.50\,\mathrm{cm} \times 1.40\,\mathrm{cm} \times 1.47\,\mathrm{cm}$, which corresponds to a volume of roughly $3\,\mathrm{cm}^2$, and weighs just $12\,\mathrm{g}$ [112]. Compared with a preceding model [114] both size and weight of this newly developed dilatometer are significantly reduced. This results in a more rapid thermalization process of the dilatometer and the sample, which is particularly crucial at low temperatures and high magnetic fields [112]. Besides, the miniaturized design enables for the rotation of the capacitive dilatometer inside the tiny sample space of a dilution refrigerator insert, which facilitates, for instance, relative length change measurements perpendicular to the magnetic field direction. The dilatometer is manufactured from a CuBe alloy with a tiny beryllium fraction of 1.84 % [112]. This small amount of beryllium is sufficient to significantly reduce the electrical conductivity of the alloy by a factor of thirty as compared to copper [112], which is of high relevance for low temperature magnetostriction measurements. This is due to eddy currents, which arise when a conducting

[2] Max Planck Institute for Chemical Physics of Solids, 01187 Dresden, Germany.

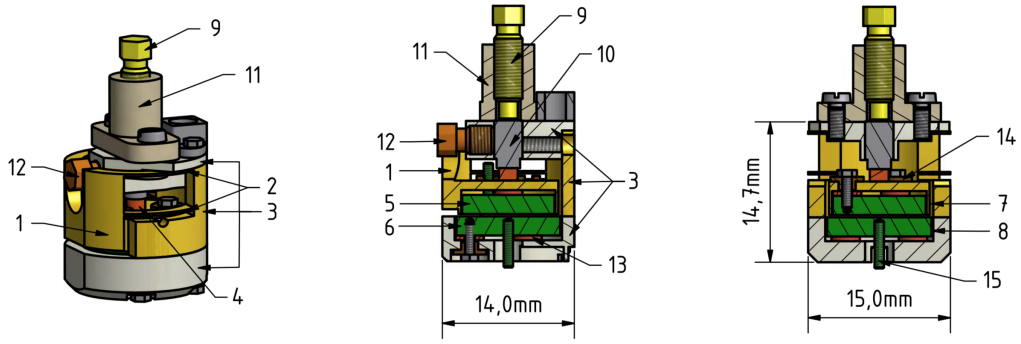

Figure 3.4: Technical drawings of the miniaturized capacitive dilatometer. Depicted are three-dimensional view (left), full section side view (middle) and full section front view (right). The different components of the capacitive dilatometer are indicated by numbers ranging from (1) to (15), which are explicitly explained in the main text. [112]
Reprinted figure from Ref. [112], whereby the three figure elements were rearranged for horizontal display. ©2017 Author(s). With permission from R. Küchler who created this figure.

material is subject to a changing magnetic field. At low temperatures, these current loops cause small heating effects, which are, however, already sufficient to disturb a low temperature magnetostriction measurement for which a stable temperature is essential.

Figure 3.4 shows schematic views of the miniaturized capacitive dilatometer [112]. With reference to Ref. [112], the following lines provide a brief overview of the dilatometer's main components. The dilatometer body is composed of three major parts (3). Firstly, the lower body part, which houses the lower capacitor plate (6). Secondly, the middle body part, which consist of a fixed and a movable part (1), whereby the two components are connected by two flat springs (2). The latter allow for the displacement of the movable part and the upper capacitor plate (5). Both capacitor plates are electrically insulated against the dilatometer body parts by thin washers, as indicated by (13) and (14). The capacitor plates can be connected to the inner conductor of a coaxial cable via a small metallic pin (15). The outer conductor of the coaxial cable, which is connected to ground, can be soldered on an additional pin on the dilatometer body, which is, however, not shown in the technical drawings of Fig. 3.4. A guard ring, indicated by (7) and (8), is placed around each capacitor plate in order to reduce interference through stray fields. The lower and middle dilatometer body parts are connected with each other by four screws and can be detached if necessary, for instance, to clean the capacitor plates from dust. The third key component is the upper dilatometer body part, which is attached by two screws to the middle dilatometer body part and serves as a mechanism to clamp the sample (4) into the dilatometer, which is realized by a piston (10). On top of the upper dilatometer body part, a detachable clamping device, specified by (9) and (11), can be mounted. With the adjustment screw (9) one can press the piston on top of the sample and thus change the distance between the two capacitor plates and the capacitance value. After the desired capacitance value has been set, the piston can be fixed by a screw (12) from the side.

Fig. 3.5 illustrates a typical sample mounting process by a series of photos. In order to place a sample, in this case a $Y_{1-x}Pr_xIr_2Zn_{20}$ single crystal with $x = 0.09$, into the dilatometer, the upper body part of the dilatometer has to be removed. This process is illustrated in Fig. 3.5(a). Afterwards, the upper part, which also includes the clamping

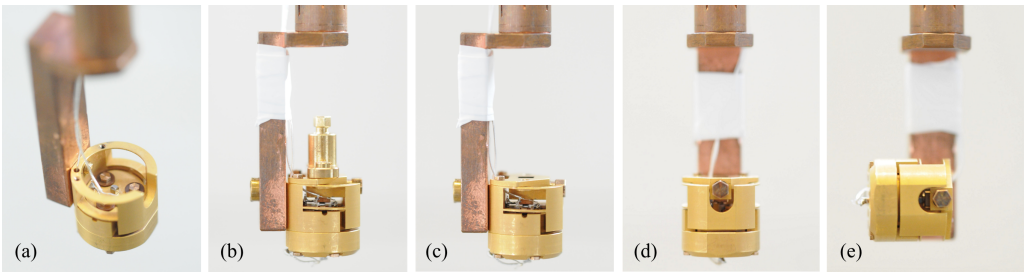

Figure 3.5: Photo series showing the miniaturized capacitive dilatometer attached to a low temperature probe. (a) Illustrates a sample mounting process, where the upper part of the dilatometer is detached from the dilatometer body in order to place a $Y_{1-x}Pr_xIr_2Zn_{20}$ single crystal with $x = 0.09$ into the dilatometer. (b) The upper dilatometer part including the clamping device is attached again to the dilatometer body in order to fix the sample and to adjust the desired capacitance value by turning the pushing screw on the top. (c) After tightening the side screw, the clamping device is removed in order to carry out a measurement. (d) Front photo of the miniaturized capacitive dilatometer aligned parallel to the magnetic field direction. (e) Front photo of the miniaturized capacitive dilatometer rotated by 90° in order to carry out relative length change measurements perpendicular to the magnetic field direction.

device, is attached to the middle body part by two screws. As depicted in Fig. 3.5(b), the capacitance value can be carefully adjusted by slowly turning the pushing screw, which presses the piston on the sample. After reaching the desired capacitance value, which is typically in the range $18\,\mathrm{pF} - 20\,\mathrm{pF}$ at room temperature, the piston is fixed by the side screw and the clamping mechanism can be removed, as illustrated in Fig. 3.5(c). In this configuration, a measurement is performed. Figure 3.5(d) shows a front view of the capacitive dilatometer being aligned parallel to the magnetic field direction. The cell can also be rotated to measure the relative length change for different angles with respect to the applied magnetic field direction. One possible configuration is shown in Fig. 3.5(e), where the capacitive dilatometer is rotated through 90° in order to perform relative length change measurements perpendicular to the magnetic field direction. Since the sample is clamped into the dilatometer by the flat springs, it is subjected to a small force. At a typical working capacitance of $C = 20\,\mathrm{pF}$, this force is approximately $4\,\mathrm{N}$ [112]. In case of a sample cross sectional area of $1\,\mathrm{mm} \times 1\,\mathrm{mm}$, this corresponds to a small uniaxial stress of $\sigma = -4\,\mathrm{MPa}$ on the installed sample, whereby the negative sign indicates that the stress is compressive. It is generally assumed that such a small uniaxial stress does not have any influence on the thermal expansion of the investigated sample [112]. However, this assumption is not always justified, as this thesis demonstrates on the example of selected Pr-based 1-2-20 systems that feature a quadrupolar ground state. Because of the linear coupling between the quadrupolar moments and strain, the small uniaxial stress exerted by the miniaturized capacitive dilatometer on the sample has to be considered carefully when interpreting the experimental results.

Uniaxial Stress Capacitive Dilatometer

Uniaxial stress is a highly sensitive tuning parameter for a variety of strongly correlated electron systems and the development of new experimental devices that allow for the measurement of thermodynamic quantities under high uniaxial stress is therefore desirable.

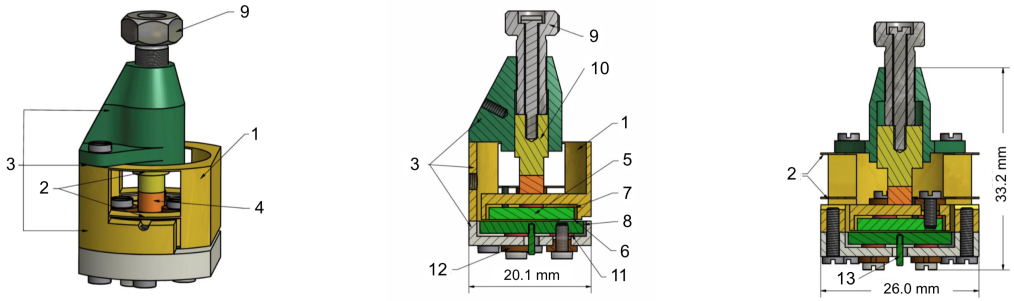

Figure 3.6: Technical drawings of the uniaxial stress capacitive dilatometer. Shown are three dimensional view (left), full section side view (middle) and full section front view (right). The different constituents of the uniaxial stress dilatometer are indicated by numbers ranging from (1) to (13). A detailed explanation of the components is provided in the main text. [113]
Adapted figure from Ref. [113], whereby the three figure elements were rearranged for horizontal display. ©2016 Author(s). With permission from R. Küchler who created this figure.

Even though the miniaturized capacitive dilatometer, which was detailed in the previous subsubsection, can already be considered as an uniaxial stress device, the small force of 4 N [112] applied to the sample in measurement direction is not sufficient to alter the physical properties of most strongly correlated materials and can thus be considered as negligible small. A relatively straight forward approach to enhance the force on the sample is to simply increase the thickness of the dilatometer's flat springs. Based on this idea, R. Küchler designed a new type of uniaxial stress dilatometer [113], which features a more rigid body and flat springs. The latter have an increased thickness of 0.7 mm, which results in a higher force on the examined sample [113]. While the general principle of operation and the design of the uniaxial stress dilatometer is very similar to the just discussed miniaturized capacitive dilatometer, their sizes differ significantly. The dimensions of the uniaxial stress dilatometer are 2.60 cm × 2.01 cm × 3.32 cm [113] and therefore notably larger than the ones of the miniaturized capacitive dilatometer. A direct consequence is a larger mass, which results in a slower thermalization process of the dilatometer at low temperatures. In order to keep eddy current heating effects as low as possible during magnetostriction measurements, the uniaxial stress dilatometer is also made of a CuBe alloy [113].

Figure 3.6 illustrates technical drawings of the uniaxial stress dilatometer, whereby a three-dimensional view of the dilatometer is shown on the left, a full section side view in the middle and a full section front view on the right [113]. With reference to Ref. [113], the following lines provide a brief description of the dilatometer's main components. The body of the dilatometer is composed of three main constituents (3), which categorize as lower dilatometer part, middle dilatometer part and clamping device. Lower and middle dilatometer part contain the lower (6) and the upper (5) capacitor plate, respectively. Both capacitor plates are electrically insulated against the dilatometer body by thin washers denoted as (11) and (12). Via a small metallic pin (13) attached to each capacitor plate, the inner conductor of a coaxial cable can be soldered on either of the dilatometer's capacitor plates. Note that the outer conductor of the coaxial cable, which establishes the connection to ground, is soldered onto the dilatometer body. To reduce interference arising from stray fields, guard rings, indicated by (7) and (8), encompass either of the

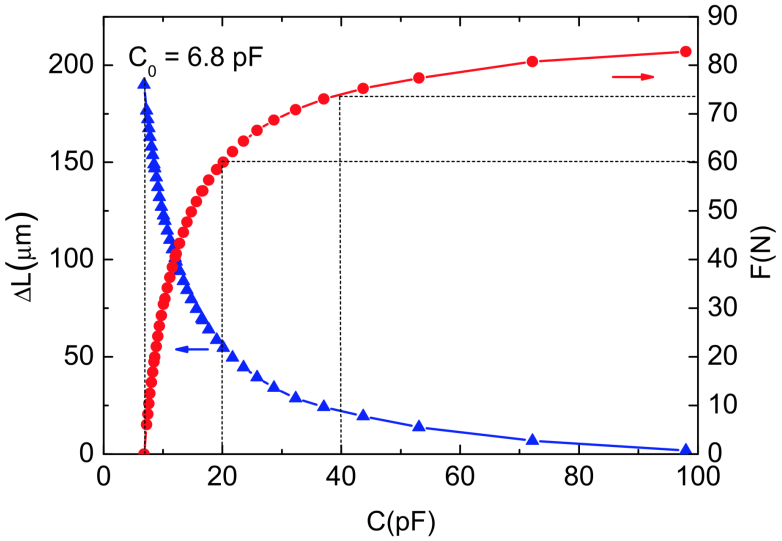

Figure 3.7: Displacement of the upper capacitor plate ΔL (left axis) as well as the force exerted by the flat springs F (right axis) versus the dilatometer's capacitance value. Dashed lines indicate the capacitance regime in which measurements are usually carried out and the respective force exerted via the dilatometer's flat springs on the sample. [113]
Reprinted figure from Ref. [113]. ©2016 Author(s). With permission from R. Küchler who created this figure.

two capacitor plates. As already discussed in the preceding subsubsection dealing with the miniaturized capacitive dilatometer, the housing (1) of the upper capacitor plate is movably attached to the middle dilatometer part by two flat springs (2). In the case of the uniaxial stress dilatometer, the flat springs are more rigid as compared to the miniaturized dilatometer, which results in a higher force on the sample (4). The design of the clamping device differs from the one of the miniaturized capacitive dilatometer. Because of the thicker flat springs, this part has to be more rigid as compared to the miniaturized dilatometer and also remains attached during the measurement process. To clamp a sample inside the dilatometer, a piston (10) is used. This piston can be adjusted by a pushing screw (9).

Owing to the thicker flat springs, the uniaxial stress dilatometer exerts a significantly higher force on the sample than the miniaturized capacitive dilatometer. For typical working capacitance values of $15\,\mathrm{pF} - 40\,\mathrm{pF}$, the respective force on the sample ranges in between $40\,\mathrm{N} - 75\,\mathrm{N}$ [113]. This is at least by a factor ten higher than the force applied by the miniaturized capacitive dilatometer. Figure 3.7 illustrates how the capacitor plate displacement, shown in blue, and the spring force, plotted in red, relate to the capacitance value of the dilatometer [113]. With the help of this graph, the force on the sample can be directly estimated from the measured capacitance value. By taking account of the sample's cross sectional area, it is then possible to directly calculate the exerted uniaxial stress. Assuming a typical sample cross sectional area of $1\,\mathrm{mm} \times 1\,\mathrm{mm}$, the just detailed force values correspond to uniaxial stress values ranging from $-40\,\mathrm{MPa}$ to $-75\,\mathrm{MPa}$. Higher uniaxial stresses can be generated by reducing the sample's cross sectional area. By using this technique, Küchler et al. [115] were able to exert significant uniaxial stresses up to $-200\,\mathrm{MPa}$ on a CeRhSn single crystalline sample and tune the material's ground state

from quantum critical towards an AFM ordered state. It is important to keep in mind that the capacitance value of the dilatometer changes by the variation of temperature, which in turn results in a change of the exerted uniaxial stress [113]. Note that the capacitance change of the dilatometer, which is either generated by a length change of the examined sample or by the dilatometer itself, is most significant at temperatures ranging from liquid helium to room temperature. As the experiments performed in the scope of this thesis were carried out below 4 K, this effect can be safely neglected.

3.2.2 Relative Length Change

When a sample is clamped into one of the just described capacitive dilatometers and undergoes a change in length, the distance between the two capacitor plates changes respectively, which in turn alters the capacitance. A mathematical relation between the relative change in length of the sample and the capacitance change of the capacitive dilatometer can be deduced by considering a parallel plate capacitor whose capacitance value C derives as

$$C = \epsilon_0 \epsilon_\mathrm{r} \frac{A}{d}, \tag{3.3}$$

where ϵ_0 is the permittivity of free space, ϵ_r the relative permittivity, A the surface area of a capacitor plate and d the distance between the two capacitor plates.

The relative change in distance $\Delta d = d - d_0$ between the two capacitor plates depends on the respective capacitance values C and C_0 and calculates by use of Eq. (3.3) as

$$\Delta d = d - d_0 = \epsilon_0 \epsilon_\mathrm{r} A \left(\frac{C_0 - C}{C \cdot C_0} \right). \tag{3.4}$$

As an expansion/contraction of the sample reduces/increases the distance between the two capacitor plates, the respective relative length change ΔL of the sample is obtained by flipping the sign of Δd. By taking account of the circular capacitor plates of the miniaturized capacitive dilatometer with a surface area of $A = r^2\pi$ and the fact that experiments are carried out in vacuum, where $\epsilon_R = 1$, the relative length change calculates as

$$\Delta L = -\Delta d = \epsilon_0 \pi r^2 \left(\frac{C - C_0}{C \cdot C_0} \right). \tag{3.5}$$

Since the here assumed idealized case, where the capacitor has two perfectly parallel capacitor plates, cannot be realized experimentally, strictly speaking, Eq. (3.5) is only an approximate calculate of the relative length change. Pott and Schefzyk [116] addressed this problem by considering the dilatometer's maximal adjustable capacitance value C_max and proposed a modified version of Eq. (3.5), which corrects a possible error due to a small capacitor plate tilting. The corrected formula, which was used in this work to deduce the relative length change from the measured capacitance values, reads as [116]

$$\Delta L_\mathrm{corr} = \epsilon_0 \pi r^2 \frac{C - C_0}{C \cdot C_0} \left(1 - \frac{C \cdot C_0}{C_\mathrm{max}^2} \right). \tag{3.6}$$

Miniaturized Capacitive Dilatometer

By using the plate radius of the utilized miniaturized capacitive dilatometer $r = 5\,\mathrm{mm}$ [112], the dielectric constant in vacuum $\epsilon_0 = 8.85419 \cdot 10^{-12}\,\mathrm{F/m}$ and $\pi = 3.14159$ one obtains the relation

$$\Delta L_\mathrm{corr}\,(10^{-6}\,\mathrm{cm}) = 6.95406 \cdot 10^4\,\mathrm{pF} \cdot \frac{C - C_0}{C \cdot C_0} \left(1 - \frac{C \cdot C_0}{C_\mathrm{max}^2} \right). \tag{3.7}$$

The maximal adjustable capacitance value of the miniaturized capacitive dilatometer was determined at $C_{\max} = 50\,\mathrm{pF}$. Note that this is an average value and cannot be reached exactly at every measurement run. The maximal adjustable capacitance usually takes a value in the range $45\,\mathrm{pF} \leq C_{\max} \leq 55$ pF. For reasons of consistency, the average value of 50 pF was used for the calculation of the relative length change. The $C_{\max}$ value was confirmed before every measurement run and in case the maximal capacitance could not be reached, the capacitance cell was cleaned before starting the experiment. In the latter case, the lower body part was detached from the middle body part and the capacitor plates were cleansed by use of isopropanol and a lens cleaning paper. Sometimes this process turned out as not being sufficient and the detached lower and middle dilatometer parts were put inside a beaker filled with isopropanol and purged for several minutes inside an ultrasonic bath. After cleansing the dilatometer parts with either of the two described procedures, the desired $C_{\max}$ value could always be set.

Uniaxial Stress Capacitive Dilatometer

In case of the uniaxial stress capacitive dilatometer, the capacitor plate radius has a larger value of $r = 7\,\mathrm{mm}$ [113]. Consequently, one obtains for the relative length change

$$\Delta L_{\mathrm{corr}}\,(10^{-6}\,\mathrm{cm}) = 1.36300 \cdot 10^{5}\,\mathrm{pF} \cdot \frac{C - C_0}{C \cdot C_0}\left(1 - \frac{C \cdot C_0}{C_{\max}^2}\right). \tag{3.8}$$

The maximal adjustable capacitance of the uniaixal stress dilatometer was determined at $C_{\max} = 90\,\mathrm{pF}$. Like for the miniaturized capacitive dilatometer, this number is an average value that slightly varies from one measurement run to the other.

3.2.3 Dilatometer Background

To correctly determine the relative length change of a material, it is necessary to take account of a possible background contribution of the measurement setup. The background contributions of both capacitive dilatometers were determined by measuring the capacitance change as a function of temperature or magnetic field with a high purity oxygen free (99.95 %) copper dummy sample with a length of $L = 2.34\,\mathrm{mm}$ clamped in. A copper specimen was chosen for the background determination, as its low temperature thermal expansion is negligibly small and has therefore no notable impact on the background measurement. This assumption is based on a copper reference measurement performed by Ackerman et al. [117]. By utilizing a SQUID detector, the authors were capable of resolving relative length changes down to 2×10^{-4} Å [117], which is a two orders of magnitude higher resolution than the one achieved by the capacitive dilatometers used in this thesis. Their findings suggest that FL behavior sets in below 1 K, with a tiny thermal expansion coefficient of $\alpha_{1\,\mathrm{K}} \approx 0.3 \times 10^{-9}\,\mathrm{K}^{-1}$ [117], which decreases linearly as temperature declines. Only above 1 K, phonons, which display a T^3 temperature dependence, become noticeable and cause a much stronger dependence of the thermal expansion on temperature [117]. However, even at 4.2 K, the thermal expansion coefficient of copper is only slightly larger than the resolution of the here utilized measurement setup [117]. For this reason, the thermal expansion background of the copper specimen is disregarded and the measured signal of the capacitive dilatometer and the copper sample were taken as the dilatometer background. The results of the background measurements are discussed in the following.

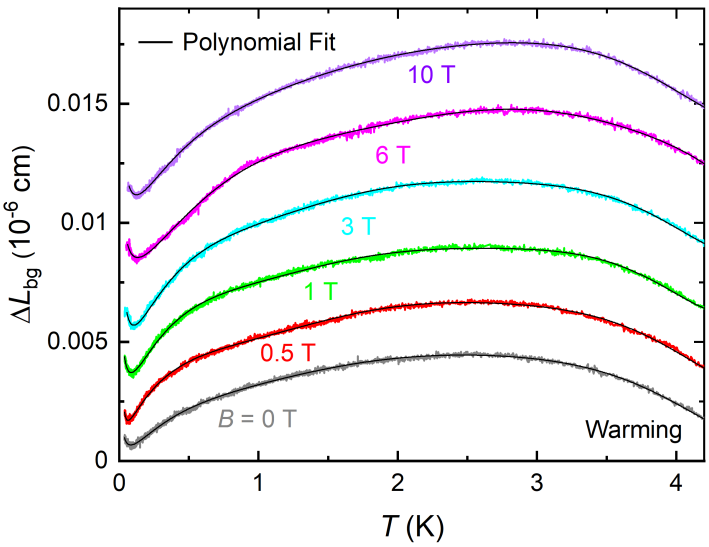

Figure 3.8: Background relative length change ΔL_{bg} as a function of temperature at different magnetic fields. Black solid lines are polynomial fits to the experimentally obtained data. The fit parameters are summarized in Table 3.1. Note that the ΔL_{bg} measurement curves and the respective fits are shifted arbitrarily along the y-axis for reasons of clarity.

Miniaturized Capacitive Dilatometer

In the case of the miniaturized capacitive dilatometer, both temperature and magnetic field dependent background contributions were measured. As the tiny background signal is close to the resolution limit of the capacitance bridge, several background data sets were collected at each magnetic field and temperature. Subsequently, the experimental findings were compared against each other with respect to reproducibility and the best reproducible data sets were selected. When measuring tiny signals close to the resolution limit of the capacitance bridge, a major cause for error is a small time dependent drift of the measured capacitance value. As the measurements are typically performed by changing temperature or magnetic field very slowly, in order to guarantee the thermal equilibrium of the sample, this small superimposed time dependent drift can have a substantial impact on the data. Performing a series of measurements is therefore a good strategy to sort out data sets, which are influenced by such a drift.

At first, the temperature dependent background relative length change ΔL_{bg} of the miniaturized capacitive dilatometer at various external[3] magnetic fields $B = \mu_0 H$, which is shown in Fig. 3.8, is discussed. The black solid lines are polynomial fits to the data by use of the formula

$$\Delta L_{\mathrm{bg}}(10^{-6}\,\mathrm{cm}) = a_0 + a_1 T^1 + a_2 T^2 + a_3 T^3 + a_4 T^4 + a_5 T^5 + a_6 T^6 + a_7 T^7 + a_8 T^{-1/2} + a_9 T^{-2}, \quad (3.9)$$

where T denotes the temperature and a_i, with $0 \leq i \leq 9$, the fit parameters. The fit parameters obtained at the different magnetic fields and the respective fitting intervals are summarized in Table 3.1.

[3]When using the term magnetic field in the following it is always referred to an external magnetic field for which the relation $B = \mu_0 H$ holds true. It strongly depends on the consulted literature whether the denotation B or $\mu_0 H$ is used. Note that in the following both denotations are used interchangeably.

Fit Range & Parameters	Magnetic Field (Magnetic Field Range used for Data Subtraction)					
	0 ($0 \leq B < 0.25\,\mathrm{T}$)	0.5 T ($0.25\,\mathrm{T} \leq B < 0.75\,\mathrm{T}$)	1 T ($0.75\,\mathrm{T} \leq B < 2\,\mathrm{T}$)	3 T ($2\,\mathrm{T} \leq B < 4.5\,\mathrm{T}$)	6 T ($4.5\,\mathrm{T} \leq B < 8\,\mathrm{T}$)	10 T ($8\,\mathrm{T} \leq B \leq 13\,\mathrm{T}$)
Fit Range	$0.038\,\mathrm{K} - 4.2\,\mathrm{K}$	$0.038\,\mathrm{K} - 4.2\,\mathrm{K}$	$0.038\,\mathrm{K} - 4.2\,\mathrm{K}$	$0.055\,\mathrm{K} - 4.2\,\mathrm{K}$	$0.06\,\mathrm{K} - 4.2\,\mathrm{K}$	$0.07\,\mathrm{K} - 4.2\,\mathrm{K}$
a_0	-0.0017533362	4.7937358427E-4	-0.0014604424	-0.0012786985	0.0044703108	0.0049993251
a_1	0.0117559719	0.0149189508	0.0249884773	0.0284161091	0.0108785173	0.0210083259
a_2	-0.0153156249	-0.0234910379	-0.0369520907	-0.0390816674	-0.0019355784	-0.0234920971
a_3	0.0129550232	0.0216631596	0.0321785658	0.0324776883	-0.0047299071	0.0174333085
a_4	-0.0064577121	-0.0111662892	-0.0161749002	-0.0157659357	0.0041322839	-0.0080131804
a_5	0.001831704	0.0031997418	0.0046174199	0.004368841	-0.001458019	0.0021878052
a_6	-2.7465912886E-4	-4.7842026975E-4	-6.9488810025E-4	-6.4045398653E-4	2.4061510428E-4	-3.2511718496E-4
a_7	1.6806546427E-5	2.9021591798E-5	4.2642445835E-5	3.8398142045E-5	-1.5383889716E-5	2.0062722847E-5
a_8	4.4674033305E-4	0	9.6171637742E-4	0.0014233878	9.7436203442E-4	0.0013738919
a_9	0	1.4998477692E-6	0	0	0	0

Table 3.1: Fit parameters and fit ranges at different magnetic fields for which Eq. (3.9) describes the temperature dependent background relative length change of the miniaturized capacitive dilatometer.

The zero field background signal is order of magnitude 10^{-9} cm and changes only weakly when magnetic field is applied. Furthermore, the different curves share a very similar temperature dependence. At elevated temperatures, the background has a negative slope, which changes sign to positive below 3 K. In this temperature region, the slope becomes steeper as temperature declines and then suddenly changes sign to negative at a very low temperature of approximately 0.1 K. Note that the sign change temperature depends weakly on the applied magnetic field and shifts to slightly higher temperature as magnetic field is increased. In addition, the positive low temperature slope becomes steeper and the background larger once a small magnetic field is applied, but does not change notably upon the further increase of magnetic field. The high temperature negative slope, by contrast, changes only marginally in presence of a magnetic field.

Next, details on the field dependent background contribution ΔL_{bg}, measured at two different temperatures of 0.05 K and 4 K, is given. The results are summarized in Fig. 3.9, whereby the black solid lines are fits to the data by use of the equation

$$\Delta L_{\mathrm{bg}}(10^{-6}\,\mathrm{cm}) = b_0 + b_1 B + b_2 B^2 + b_3 + (b_4 - b_3)/(1 + (B/b_5)^{b_6}) + b_7 \exp(B - 11), \quad (3.10)$$

where B denotes the magnetic field and b_i, with $0 \leq i \leq 7$, the fit parameters. The fit parameters and the respective fit ranges are summarized in Table 3.2. To obtain a satisfying fit result, a combination of a range of different fitting terms had to be chosen. It shows that there is no notable difference between the data measured at 0.05 K and 4 K, which implies a temperature insensitivity of the field dependent background contribution, at least up to 4 K. For that reason no further background measurements were performed, as it can be assumed that also the data in between 0.05 K and 4 K shows a comparable behavior. While the background barely changes at low magnetic fields, a notable increase appears at around 7 T. The order of magnitude of the background signal is 10^{-8} cm in the investigated magnetic field range, which is slightly larger than the temperature de-

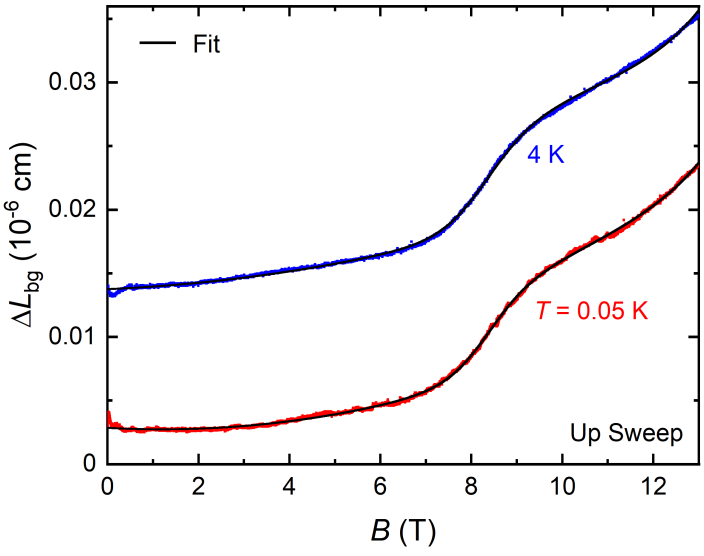

Figure 3.9: Background relative length change ΔL_{bg} as a function of magnetic field at different temperatures. Black solid lines are fits to the measured data, whereby the fit parameters and the fit ranges are summarized in Table 3.2. Note that the ΔL_{bg} background curves and the respective fit curves are shifted arbitrarily along the y-axis for reasons of clarity.

Fit Range & Parameters	Temperature (Temperature Range used for Data Subtraction)	
	0.05 K ($0 < T < 2$ K)	4 K (2 K $\leq T \leq 4$ K)
Fit Range	$0 - 13$ T	$0 - 13$ T
b_0	-0.0063309928	-9.8214952762E-4
b_1	-1.93898943E-4	1.5467308652E-4
b_2	8.1188606468E-5	4.8624246012E-5
b_3	0.0164027207	0.023269873
b_4	0.0091818857	0.014735088
b_5	8.4371992537	8.4265324145
b_6	17.4722602607	15.7647006361
b_7	3.2739277308E-4	4.3015696393E-4

Table 3.2: Fit parameters and and the respective fit range at two different temperatures. By using these parameters, Eq. (3.10) describes the magnetic field dependent background relative length change of the miniaturized dilatometer at the specified temperatures.

pendent background, however, still distinctly small as compared to the relative length changes of most of the single crystalline samples examined in this thesis. Taking account of the dilatometer background is of particular relevance for the thermal expansion and magnetostriction data of the highly diluted $Y_{1-x}Pr_xIr_2Zn_{20}$ single crystal with $x = 0.033$ and $x = 0.036$. The materials show relatively small relative length changes and a careful subtraction of the dilatometer background is crucial. By contrast, both $PrIr_2Zn_{20}$ and the moderately doped $Y_{1-x}Pr_xIr_2Zn_{20}$ single crystals show relatively large relative length changes and the dilatometer background is less critical. Nevertheless, the shown background curves were subtracted from all measured relative length change data sets presented in this thesis, unless, it is stated otherwise.

Uniaxial Stress Capacitive Dilatometer

Thermal expansion measurements by means of the uniaxial stress capacitive dilatometer were only carried out at zero magnetic field. Consequently, it was sufficient to determine the dilatometer background in zero magnetic field. The respective background relative length change ΔL_{bg} as a function of temperature is shown in Fig. 3.10. The red solid line denotes a polynomial fit to the data by using the formula

$$\Delta L_{\mathrm{bg}}(10^{-6}\,\mathrm{cm}) = c_0 + c_1 T + c_2 T^2 + c_3 T^3 + c_4 T^4 + c_5 T^5, \tag{3.11}$$

where T denotes the temperature and c_i, with $0 \leq i \leq 5$, the fit parameters. The fit parameters and the fit range are listed in Table 3.3.

The background relative length change of the uniaxial stress dilatometer shows comparable behavior to the one of the miniaturized capacitive dilatometer. At high temperatures $T \geq 1.5$ K, its slope is negative and the related relative length change up to 4.2 K approximately four times larger than the one of the miniaturized capacitive dilatometer. In the range 0.75 K $\geq T \geq 1.5$ K, the background is nearly temperature independent and its

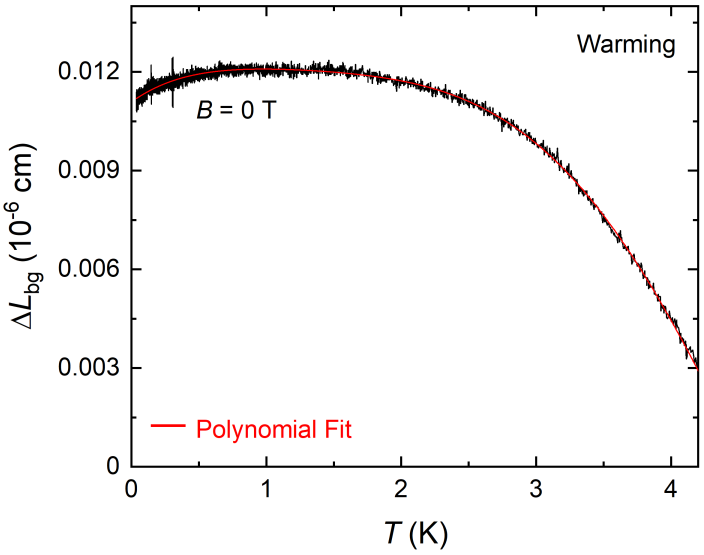

Figure 3.10: Temperature dependent background relative length change ΔL_{bg} of the uniaxial stress capacitive dilatometer at zero magnetic field. The red solid line is a polynomial fit to describe the measured data. The fit parameters and the fit range are summarized in Table 3.3. Note that the ΔL_{bg} curve and the respective fit curve are shifted arbitrarily along the y-axis.

Fit Range & Parameters	Magnetic Field
	0
Fit Range	0.038 K − 4.2 K
c_0	0.0110833485
c_1	0.0029606143
c_2	-0.0032868869
c_3	0.0017387879
c_4	-4.5389526422E-4
c_5	3.8104227771E-5

Table 3.3: Fit parameters and temperature range for which Eq. (3.11) describes the temperature dependent background relative length change of the uniaxial stress capacitive dilatometer.

slope changes sign to positive below 0.75 K. In contrast to the miniaturized dilatometer, the background does not show another sign change at very low temperature. Uniaxial stress measurements were only performed on the two highly diluted $Y_{1-x}Pr_xIr_2Zn_{20}$ single crystals with $x = 0.033$ and $x = 0.036$. Their relative length changes measured in the uniaxial stress dilatometer were corrected for the just detailed background contribution.

3.2.4 Data Analysis

Obtaining high resolved relative length change data at very low temperature is a crucial prerequisite to perform a reliable thermal expansion and magnetostriction analysis. However, this process is typically complicated by various factors, as briefly detailed in the following. Capacitance measurements are highly sensitive to external interference, which can be generated by ground loops or measurement equipment close by. A careful optimization of the experimental setup to minimize such interference is crucial in order to keep external disturbances, which negatively impact the data quality, as low as possible. In addition, at very low temperature, the measured capacitance changes are often close to the resolution limit of the employed measurement equipment, which entails an inevitably low signal to noise ratio. As the relative length change data derived from the measured capacitance has to be differentiated to deduce the thermal expansion and the magnetostriction coefficient, already a small noise level in the raw data appears amplified in the differentiated data. Therefore, like in every other measurement, it is crucial to have raw data with a resolution as high as possible. By optimizing the here employed setup, as it is being discussed in the subsequent section, the noise level of the relative length change measurement could be significantly reduced as compared to the initial measurements, which I carried out in the framework of my master thesis [111]. With the miniaturized capacitive dilatometer, for instance, relative length changes with a very high resolution of up to 0.01 Å could be detected. Here, it has to be noted that the reached resolution slightly varied from one measurement run to the other and was occasionally somewhat lower than the just mentioned optimum. As the measurement setup was not modified during the different experimental runs, the little variation in resolution must be ascribed to uninfluenceable factors, such as interference from measurement equipment located in adjacent laboratories. Another possible cause for error is connected to the extremely low change rates of temperature or magnetic field used for the measurements at very low temperatures. Such low sweep rates are necessary to guarantee that the examined single crystalline sample is in thermal equilibrium during the measurement process and the measured temperature indeed the one of the sample. As a rule of thumb, a thermal expansion measurement at very low temperature, which covers a quite small temperature range from base temperature to 0.3 K, consumes already several hours. At higher temperatures, faster sweep rates can be chosen, as the thermalization process is less critical. In case the measured relative change in length is distinctly small and the change rate of temperature or magnetic field very low, a small time dependent drift in the measured capacitance value that is superimposed to the intrinsic signal of the sample may induce a significant error to the data. While this small drift is not of any concern in the case of single crystals that show large relative length changes, it has to be considered carefully when measuring tiny signals at very low temperature. As an example, the measurements on the highly diluted material $Y_{1-x}Pr_xIr_2Zn_{20}$ with $x = 0.033$ and $x = 0.036$ have to be mentioned. Because of the small Pr doping of only a few percent, the single crystals display distinctly small relative length changes at low temperatures. In this case, it is crucial to repeat each measurement for several times in order to compare the different data sets, identify reproducible behavior and track down data sets that contain a parasitic drift contribution. In general, the thermal expansion measurements were carried out in different temperature ranges, whereby the temperature sweep rate was adjusted accordingly. Commonly, both a warming and a cooling curve was measured, which helped to evaluate possible hysteresis effects and allowed to adjust the temperature sweep rate if necessary. At very low temperature and in presence of an applied magnetic field, a small hysteresis between warming and cooling measurement was often inevitable. The thermal expansion curves presented in the experimental sections are

mostly warming curves. Before starting a warming sweep, the sample was thermalized for a certain amount of time in order to guarantee thermal equilibrium between the sample stage, where the temperature is measured, and the sample. Due to this process, the warming curve is deemed to be the more accurate measurement than the cooling curve. In general, the found hysteresis between warming and cooling were, however, quite small and only manifested themselves at very low temperature. The data sets obtained at different temperature ranges were then combined to a single data set that covers the whole examined temperature range. To deduce the thermal expansion and magnetostriction coefficient from the relative length change data, a numerical differentiation procedure had to be applied. This process is briefly discussed in the following.

The thermal expansion coefficient α and the magnetostriction coefficient λ are first order derivatives of the relative length change $\Delta L/L$ with respect to either temperature or magnetic field. Note that ΔL denotes the measured relative length change as a function of temperature or magnetic field and L the length value of the investigated single crystal at room temperature. Since the experimentally determined $\Delta L/L$ data represents a set of data points, a numerical approach is necessary to approximate its first order derivative. To alter the experimentally obtained data as little as possible, it is refrained from more complex derivative algorithms, which usually require interpolation of the data set and often apply smoothing procedures. Instead, the most basic approach of the interval derivative is employed. To briefly illustrate the differentiation process, in the following, a set of data points is considered, whereby each data point is described by a coordinate (x, y). The x-value thereby corresponds to the measured temperature or magnetic field value and the y-value to the respective relative length change value $\Delta L/L$. Note that the x-values of the data set are sorted in ascending order and are in the range $[x_0; x_i]$. To differentiate the data, a differentiation window Δx is chosen, which is typically distinctly smaller than the measured temperature or magnetic field range. Starting from the first measured data point x_0, a linear regression is calculated on the subset of data points ranging from x_0 to the boundary value $x_n \leq x_0 + \Delta x$. The lower equal sign means that given that there is no data point which equals x_n, the data point with the next smaller value is taken as x_n. The linear regression then gives back the slope associated to this set of data points, which marks the y value of the derivative. The corresponding x value is approximated by the middle value $(x_0 + x_n)/2$. The differentiation window is then shifted point wise to higher temperature and the procedure repeated until x_n reaches the end of the data set. Evidently, the smaller the window size Δx, the better the approximation of the derivative at a given point. At the same time it is important to keep in mind that the data set is composed of measurement points that contain noise. Thus, when choosing a too small differentiation window, the differentiated data may exhibit a significant noise level, which is neither desirable. Therefore, it is important to compromise, i.e. choose a window that is large enough to have a reasonable noise level but small enough to provide a good approximation of the local slope. A small window is in particular necessary when the data shows a sudden and strong change in slope, as it is, for instance, the case in vicinity of a phase transition. A visualization of the just detailed interval differentiation method is detailed in Fig. 3.11, whereby an artificially generated set of data points is shown in the upper panel and the respective derivative value determined by interval differentiation in the lower panel. In this example, a window size of 0.5 was chosen. As just mentioned, the size of the differentiation window has to be adapted depending on the raw data. At very low temperature, usually a very small window of approximately $0.01\,\mathrm{K} - 0.03\,\mathrm{K}$ is used. The same holds in vicinity of a phase transition signature, where the relative length change shows a sudden change within a small temperature interval. With increasing temperature,

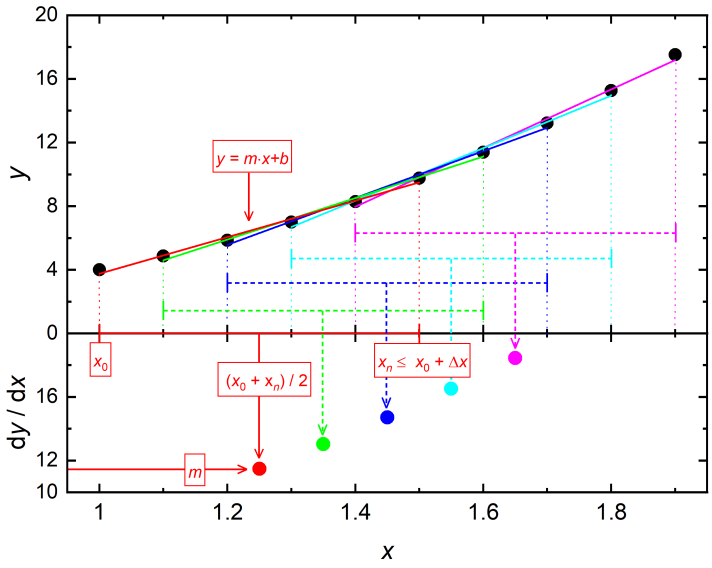

Figure 3.11: Illustration of the derivation process, where an interval Δx is shifted pointwise over a finite set of data points to approximate its derivative by a linear regression.

the size of the window can be increased, whereby for high temperatures in the Kelvin range, the differentiation window was typically adjusted to a value of approximately 0.1 K.

3.3 Experimental Setup

In order to carry out thermal expansion and magnetostriction measurements at very low temperatures, a rather complex measurement setup is necessary. Its different components are detailed in this section. Furthermore, the topic grounding is addressed, as the elimination of ground loops is essential when performing ultra-high resolution capacitance measurements.

Figure 3.12 shows a schematic sketch of the measurement setup, which comprises the three main constituents (a) vacuum pump stand and automated gas handling system, (b) measuring instrument rack and (c) cryogenic dewar with dilution refrigerator insert. In addition, a blowup of the dilatometer probe, which is attached to the mixing chamber of the dilution refrigerator insert, is depicted in (d). The vacuum pump stand is equipped with a 1 K pot, a He circulation and an auxiliary pump. An automated gas handling system, sitting on its top, controls the gas flow through the dilution refrigerator insert. The instrument rack stores all the relevant measurement equipment as well as the magnet power supply and the magnet programmer. The resistance thermometers of the dilution refrigerator insert are operated by a Lakeshore LS370 and a Lakeshore LS372 resistance bridge, which also drive the heaters and therefore control the temperature at the different stages of the system. The LS370 bridge controls the ex factory sensors and heaters sitting at the different cooling stages of the insert and the LS372 bridge controls the RuO_2 sensor and resistance heater at the sample stage. More details on the sample stage are given at the end of this section. An additional filter box is utilized in order to reduce high frequency noise and to increase the resolution of the resistance measurement. The capacitance value

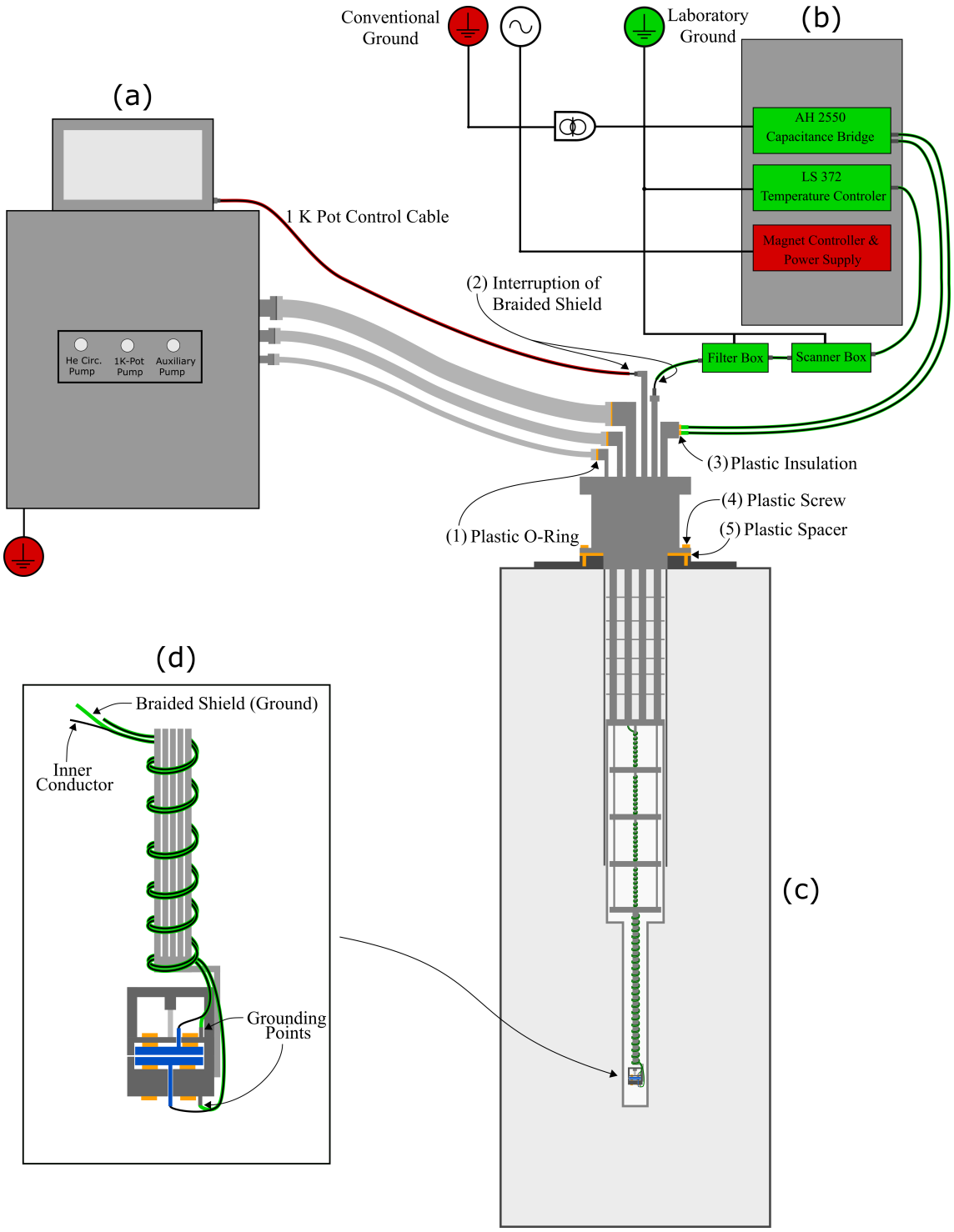

Figure 3.12: Schematic sketch of the experimental setup. Shown are (a) the pump stand with automated gas handling system, (b) the measurement instrument rack, (c) the cryogenic dewar with the dilution refrigerator insert and (d) a blowup of the low temperature dilatometer probe. The conventional ground is highlighted by red color and the clean laboratory ground by green color. Electrical insulation is indicated with dark yellow color and the different electrical insulation points of the setup are specified by numbers ranging from (1) to (5).

of the dilatometer was measured by an Andeen-Hagerling AH2550A ultra-high resolution capacitance bridge. To facilitate high precision measurements, the bridge employs a three-terminal capacitance measurement method, meaning that fully shielded coaxial cables are used with the braid being connected to ground. This is a very efficient way to reduce interfering high frequency noise. When carrying out a capacitance measurement, the average exponent of the Andeen-Hagerling bridge was set to a value of eight. The bridge then averages over a number of measurement points, whereby the averaging time is approximately six seconds.

Optimizing the measurement setup with respect to external interference, which worsens the signal to noise ratio, is paramount in order to obtain reliable data. Likely the most important point to be addressed is the elimination of noise generating ground loops. Also electromagnetic noise caused by adjacent machines and measurement equipment is a problem. Both issues are briefly outlined in the following. The 1 K pot and the He circulation pump are connected to the respective valves of the dilution refrigerator insert with metallic hoses. In consequence of this metallic connection, high frequency noise coming from the pump stand can be easily transmitted into the measurement system. In addition, the hoses connect the insert at various points to ground, which triggers ground loops. In particular with respect to the highly sensitive capacitance measurement, the presence of such ground loops leads to a distinct worsening of the signal to noise ratio. In order to eliminate the latter and the resulting interference, electrically insulating plastic o-rings and clamps (1) have to be installed in between the vacuum hoses and the respective valves of the dilution refrigerator insert. The consequent elimination of ground loops is a necessary measure to conduct ultra-high resolution capacitance measurements. However, ground loops do not only originate from the connection established through the metallic hoses, but also form at various other points. In order to eliminate these, the dilution refrigerator insert has to be electrically insulated from its surrounding. Grounding is then established only at a single point. The dilution refrigerator insert is electrically insulated from the cryogenic dewar by use of a very thin electrically insulating spacer (5) and fixed by plastic (4) instead of metal screws. Additional paths to ground can be realized via the braided shield of the measuring cable. It is therefore crucial to also cut the braided shield (2) of the 1 K pot needle valve control, thermometer and heater cable in order to break ground loops. In addition, the braid of the coaxial cable is insulated by two small custom made vacuum tight plastic spacers (3) from the metallic connector of the dilution refrigerator insert. After eliminating all connections to ground, the grounding of the setup is established only at a single point via the braid of the coaxial cables, which is soldered onto the dilatometer body, as depicted in Fig. 3.12(d). Both, the Andeen-Hagerling capacitance bridge and the Lakeshore LS372 resistance bridge are cut off from the conventionally used ground, which is indicated by red color in Fig. 3.12(b). To do so, an insulating transformer has to be used and both measurement bridges are grounded separately by a clean earth, as indicated by green color in Fig. 3.12(b). This clean earth is reserved for a few measurement systems and contains less noise than the conventional ground. As the grounding of the insert is realized via the braid of the coaxial cable, the ground potential of the insert is the same as the one of the Andeen-Hagerling capacitance bridge.

Finally, the focus is on the key component of the experimental setup, which is the low temperature dilatometer probe, as illustrated in Fig. 3.13. The dilatometer is mounted on a copper bracket, which in turn is attached to a slotted copper rod. Copper was chosen as a material, as it is the best thermal conductor in the here accessed temperature range [103, p. 58]. A high thermal conductivity of the rod is key to achieve a sufficient thermalization of both the dilatometer and the examined single crystal at mK temperatures. The slots

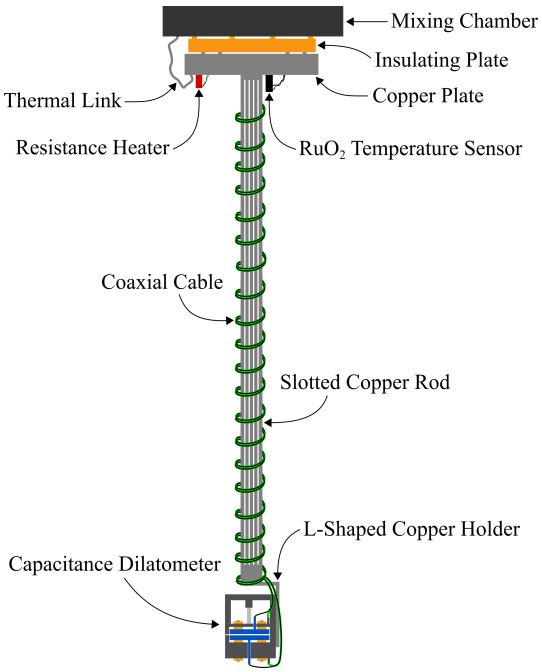

Figure 3.13: Schematic sketch of the low temperature dilatometer probe. The dilatometer is mounted on a L-shaped copper holder, which is attached to a slotted copper rod. A TRP partially thermally insulates the dilatometer probe from the mixing chamber, which facilitates measurements to higher temperature. A resistance heater and a RuO_2 thermometer are sitting on the TRP. The thin green cables denote coaxial cables by which the dilatometer is connected to the capacitance measurement bridge.

in the copper rod aim to reduce eddy current induced heating effects, which arise during magnetostriction measurements. The copper rod is attached to a temperature regulation plate (TRP), which is only weakly thermally coupled to the mixing chamber of the dilution refrigerator insert. This allows for a local heating of the TRP up to temperatures of 4 K, while the mixing chamber remains below its critical value of 1 K. When the mixing chamber is heated to higher temperature, the circulation process becomes abruptly unstable due to a sudden evaporation of a large amount of liquid mixture. In consequence, the pressure in the dilution circuit increases rapidly. In this case, the He circulation pump turns off automatically due to safety reasons and the circulation process stops. Consequently, placing a TRP between the low temperature dilatometer probe and the mixing chamber is an elegant and relatively straightforward method to extent the accessible temperature range of a dilution fridge measurement. The TRP itself consists of a thermally insulating plate on which a copper plate is mounted. The insulating side of the TRP is attached to the mixing chamber of the dilution refrigerator insert and the TRP's copper plate is connected via a thin copper wire to the mixing chamber. Variation of the diameter of the copper wire allows to adjust the cooling power of the TRP and the experimental probe. The temperature at the TRP is measured by a RuO_2 temperature sensor and can be regulated by a resistance heater. It is thereby assumed that the temperature at the TRP is identical to one of the sample.

Chapter 4

$PrIr_2Zn_{20}$

NFL phases show many facets and their exploration has evolved into a comprehensive research field of great popularity. One of the best known and most thoroughly researched examples is the collapse of conventional metallic behavior at a magnetic QCP, a phenomenon that has been extensively studied on the example of HF metals over the last decades [11]. Less conclusive, at least so far, has been the research on exotic behaviors emerging in systems that feature high rank multipolar degrees of freedom, such as electric quadrupoles [25, 26].

A material class that can be considered as highly suitable for the exploration of exotic multipolar phenomena is the one of the Pr-based 1-2-20 systems [25, 26]. Most prominent members of this family are $PrIr_2Zn_{20}$ [27, 28], $PrRh_2Zn_{20}$ [29, 30], PrV_2Al_{20} [26, 31, 32] and $PrTi_2Al_{20}$ [26, 33, 34]. In these materials, the localized nature of the $4f^2$ electrons and their moderate hybridization with conduction electrons are key prerequisites that allow for the accurate classification of the emergent effects. Most eminent cause of NFL behavior is thereby the quadrupolar Kondo effect [28, 30, 35]. This is distinct to magnetic HF materials, where the Kondo screening results in a stable FL ground state and NFL behavior appears close to a magnetic QCP [11]. While the latter phenomenon has been comprehensively studied and is well understood, clear and unambiguous experimental evidence for the quadrupolar Kondo effect and quadrupolar QC remains elusive so far. In this regard, comprehensive research on the Pr-based 1-2-20 systems is a promising approach to reveal experimental signatures of these novel effects. A noteworthy finding is the emergence of NFL behavior in $PrIr_2Zn_{20}$ [28], $PrRh_2Zn_{20}$ [30] and PrV_2Al_{20} [35], which can be well captured by a two-channel Anderson lattice model [40]. Besides, $PrTi_2Al_{20}$ shows a substantial increase of its effective electron mass and superconducting transition temperature under hydrostatic pressure, which is seen as a possible indication of a quadrupolar QCP [33]. PrV_2Al_{20}, on the other hand, displays a further NFL phase when tuned by the application of magnetic field towards the phase boundary of its low temperature ordered state, which points towards a quadrupolar QCP [32]. In $PrIr_2Zn_{20}$ [28] and $PrRh_2Zn_{20}$ [30], by contrast, FL behavior emerges in close vicinity of the critical field of AFQ order. A possible explanation for this unexpected finding is the emergence of FH order, also referred to as F-channel diagonal composite order [28, 30, 99–102].

This chapter deals with the material $PrIr_2Zn_{20}$. The system exhibits a non-Kramers Γ_3 ground state doublet (T_d point group symmetry) that possesses O_2^0 and O_2^2 quadrupole as well as T_{xyz} octupole degrees of freedom and displays AFQ order at $T_Q = 0.11\,\mathrm{K}$ [25, 27]. In the specific heat, a critical magnetic field of $B_c \approx 4.5\,\mathrm{T} - 5\,\mathrm{T}$ applied along the crystallographic [100] direction suppresses the AFQ order, which is replaced by another anomaly [28]. Furthermore, FL behavior arises in the electrical resistivity, which sup-

ports the emergence of a new phase [28]. Here, aforementioned FH or F-channel diagonal composite order are considered as a possible mechanism to explain the experimentally observed behavior [28,99–102]. In addition, the Seebeck coefficient is substantially enhanced at around B_c, which points towards the formation of a strongly hybridized state that is likely linked to the FL behavior in the electrical resistivity [28, 45, 46]. Interestingly, at $T > T_Q$, NFL behaviors are present in the specific heat and the electrical resistivity that can be well accounted for by a two-channel Anderson lattice model [40] and are therefore indicative of the quadrupolar Kondo lattice effect [28].

4.1 Physical Properties Review

This section reviews the physical properties of $PrIr_2Zn_{20}$ with reference to the currently available literature on the system. The material's crystal structure and the CEF effect are introduced at first [65, 97], as these are key for understanding the formation of the material's non-Kramers Γ_3 ground state doublet. Afterwards, the low temperature AFQ order and the quadrupole Kondo lattice effect are discussed [27,28] and possible signatures of the F-channel diagonal composite order (FH order) are briefly reviewed [28,99–102].

4.1.1 Crystal Structure

$PrIr_2Zn_{20}$ forms in the $CeCr_2Al_{20}$ crystal structure with the cubic $Fd\bar{3}m$ space group and a lattice parameter of 14.2729(2) Å [97]. Fig. 4.1 shows a visualization of the crystal structure. Here, the Pr^{3+} ions occupy the 8*a* site and are arranged in a diamond structure [25]. The Ir ions, which are located at the 16*d* site, crystallize in a pyrochlore lattice and the Zn ions sit on the remaining 16*c*, 48*f* and 96*g* sites [25]. The sixteen Zn ions on the 16*c* and 96*g* sites form a cage, which surrounds the Pr^{3+} ion at the 8*a* site, as highlighted by the purple polyhedra in Fig. 4.1. Neutron scattering experiments by Iwasa et al. [65] suggested that the point group symmetry at a Pr site is cubic T_d. In consequence of the

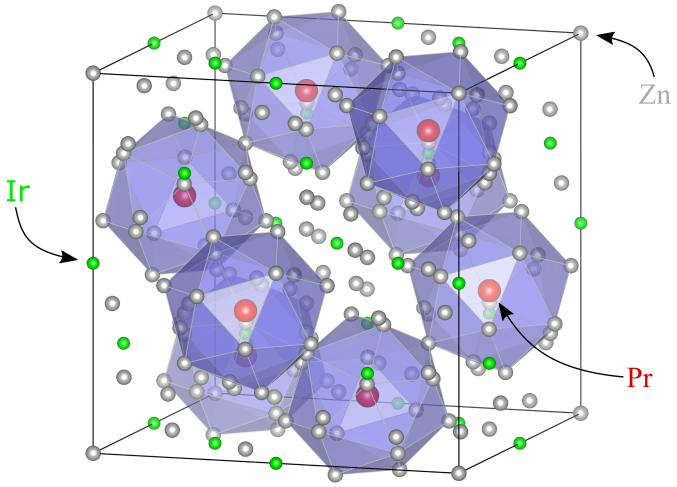

Figure 4.1: Cubic crystal structure of $PrIr_2Zn_{20}$ with $Fd\bar{3}m$ space group. Pr^{3+} ions are shown in red, Ir ions in green and Zn ions in grey color. Each Pr^{3+} ion is surrounded by a cage structure of sixteen Zn ions, as highlighted by purple polyhedra. The crystal structure was visualized with VESTA [118], by using crystallographic data typical for this material class from Ref. [119].

Pr^{3+} ion's high coordination number, a significant overlap of the localized $4f^2$ moment wave functions and the conduction electron wave functions of the surrounding Zn ions is expected [25]. This should result in a pronounced hybridization effect, which in turn sets the basis for novel physical phenomena, such as the quadrupolar Kondo effect [25].

4.1.2 Crystal Electric Field Effect

In $PrIr_2Zn_{20}$, the cage like arrangement of sixteen Zn ions generates a cubic CEF with T_d point group at a Pr site [65]. Before discussing this effect in detail, the ground state characteristics of a free Pr^{3+} ion, which classifies as a 4f ion with an electronic configuration $[Xe]4f^2$, are briefly recalled. By following Hund's rules, its ground state total angular momentum quantum number calculates as $J = |L - S| = 4$, where $L = 5$ is the orbital angular momentum and $S = 1$ the spin angular momentum. In consequence, the degeneracy of the Pr^{3+} ion's ground state is $(2J + 1) = 9$. In presence of a CEF, this degeneracy is lifted and the number and degeneracy of the consequent CEF states is determined by the point group symmetry at a Pr site. As detailed in Section 2.2, in case of a CEF with cubic T_d point group symmetry, the originally nine-fold degenerate J multiplet of a free Pr^{3+} ion breaks down into Γ_1 singlet, Γ_3 doublet, Γ_4 triplet and Γ_5 triplet [64]. The even number of 4f electrons classifies the Pr^{3+} ion as a non-Kramers ion. In consequence, its CEF eigenstates do not necessarily have to be doubly degenerate and can be of non-magnetic nature. By contrast, Kramers ions with an odd number of 4f electrons, such as the Yb^{3+} ion or the Ce^{3+} ion, cannot feature non-magnetic or singlet CEF states, as the Kramers theorem requires at least doubly degenerate states that split in magnetic field [12, p. 63]. While the degeneracy of a Kramers state can be broken by the application of magnetic field, a non-Kramers state's degeneracy is lifted by a symmetry breaking strain. Among the aforementioned CEF eigenstates of the Pr^{3+} ion, the Γ_3 state stands out, as it does not posses a magnetic dipole moment but high rank quadrupole and octupole moments [25]. Discovering new systems that feature such a non-Kramers Γ_3 doublet ground state is of great interest, as it allows to study electronic correlation effects of non-magnetic nature. In order to specify the energetic arrangement of the CEF eigenstates and to identify the CEF ground state of a material, inelastic neutron scattering is generally the method of choice. In the case of $PrIr_2Zn_{20}$, also other thermodynamic probes, such as the specific heat and the magnetization, provided helpful information [27]. In the following subsubsection, the CEF level scheme of $PrIr_2Zn_{20}$ is detailed. Subsequently, the focus lies on the characteristics of the material's non-Kramers Γ_3 ground state doublet.

Crystal Electric Field Level Scheme

In order to examine the possible non-magnetic nature of the ground state of $PrIr_2Zn_{20}$, magnetic susceptibility measurements are a powerful means. Onimaru et al. [97] performed such experiments and reported saturation of the magnetic susceptibility at $T < 10\,\mathrm{K}$ for magnetic field along the [100] direction, which points towards the presence of Van Vleck paramagnetism. This type of magnetism appears when a non-magnetic ground state mixes with an excited magnetic state in magnetic field [12, p. 30]. In this case, second order perturbation theory suggests a finite and temperature independent magnetic susceptibility [12, p. 30] and the finding of Onimaru et al. [97] therefore confirms that the ground state of $PrIr_2Zn_{20}$ is of non-magnetic nature. This explicitly excludes the Γ_4 and Γ_5 triplet as the ground state, since both carry magnetic dipole moments [25]. An anisotropy observed in the magnetic field dependence of the magnetization with respect to the [100] and [110] direction and a Schottky maximum in the specific heat, specified

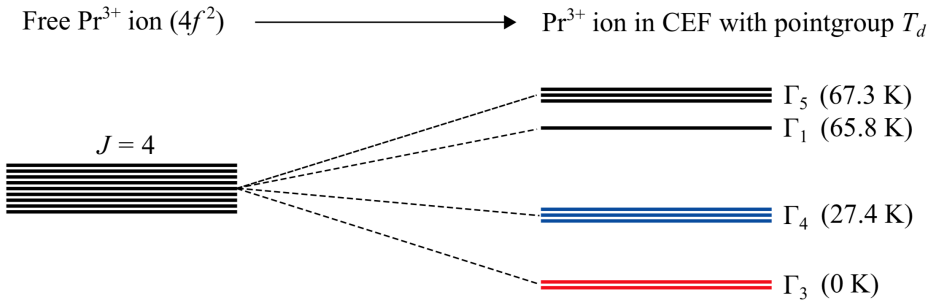

Figure 4.2: Left side shows the nine-fold degenerate $J = 4$ multiplet of a free Pr^{3+} ion. Right side shows the CEF level scheme of $PrIr_2Zn_{20}$, where a CEF with T_d symmetry acts on a Pr^{3+} ion. The CEF level scheme was sketched based on inelastic neutron scattering results from Ref. [65].

the Γ_3 doublet as the ground state and ruled out the Γ_1 singlet [27]. This conclusion by Onimaru et al. [27] is based on the fact that the effects in the magnetization and specific heat can be well described by a theoretical calculation, which assumes a Γ_3 ground state with an energy gap of $\Delta = 30\,\mathrm{K}$ to the first excited Γ_4 triplet state. Later, Iwasa et al. [65] determined the exact CEF level scheme of $PrIr_2Zn_{20}$ by inelastic neutron scattering, which is in very good agreement with the just detailed results by Onimaru et al. [27,97]. The CEF level scheme of $PrIr_2Zn_{20}$, which is based on inelastic neutron scattering results by Iwasa et al. [65], is sketched in Fig. 4.2. The ground state is the Γ_3 doublet, which is followed by the Γ_4 triplet at 27.4 K, the Γ_1 singlet at 65.8 K and the Γ_5 triplet at 67.3 K [65].

Characteristics of the Γ_3 Ground State

A key characteristic of the cubic non-Kramers Γ_3 doublet is its non-magnetic nature. While it carries two electric quadrupole moments O_2^0, O_2^2 and a magnetic octupole moment T_{xyz}, magnetic dipole moments are absent [25]. Consequently, a splitting of an isolated Γ_3 doublet in magnetic field is not expected. In $PrIr_2Zn_{20}$, however, the assumption of the Γ_3 ground state doublet being isolated is not justified, as also higher excited states are present. In particular, the mixing of the Γ_3 ground state with the first excited Γ_4 state is of relevance, as it leads to a quadratic splitting of the Γ_3 doublet in magnetic field.

The fact that an isolated Γ_3 doublet does not split in magnetic field can be demonstrated by considering the expectation value of J_z for both the $\Gamma_3^{(1)}$ and $\Gamma_3^{(2)}$ eigenstate, which were introduced in Table. 2.1. In the following, this is demonstrated for the $\Gamma_3^{(1)}$ state for which the expectation value of J_z vanishes to zero

$$\begin{aligned}\left\langle \Gamma_3^{(1)} \middle| J_z \middle| \Gamma_3^{(1)} \right\rangle &= \frac{7}{24}\langle 4|\, J_z\, |4\rangle + \frac{5}{12}\langle 0|\, J_z\, |0\rangle + \frac{7}{24}\langle -4|\, J_z\, |-4\rangle \\ &= \frac{7}{24}\cdot 4 - \frac{7}{24}\cdot 4 \\ &= 0.\end{aligned} \tag{4.1}$$

Analogously it follows for the $\Gamma_3^{(2)}$ state

$$\left\langle \Gamma_3^{(2)} \middle| J_z \middle| \Gamma_3^{(2)} \right\rangle = \ldots = 0. \tag{4.2}$$

In $PrIr_2Zn_{20}$, the Γ_3 ground state doublet is not isolated but accompanied by the higher excited Γ_4 triplet, Γ_1 singlet and Γ_5 triplet states. Given that the ground state mixes with one of the excited states in magnetic field, i.e. J_z has a finite expectation value in the mixed state, the Γ_3 doublet will split in magnetic field despite its non-magnetic nature. Such a mixing in fact occurs for the $\Gamma_3^{(1)}$ state and the first excited $\Gamma_4^{(2)}$ state, as the expectation value of J_z in the mixed state is finite

$$\begin{aligned}\left\langle \Gamma_3^{(1)} \middle| J_z \middle| \Gamma_4^{(2)} \right\rangle &= \sqrt{\frac{7}{48}} \langle 4| J_z |4\rangle - \sqrt{\frac{7}{48}} \langle -4| J_z |-4\rangle \\ &= \sqrt{\frac{7}{48}} \cdot 4 + \sqrt{\frac{7}{48}} \cdot 4 \\ &= 2\sqrt{\frac{7}{3}}.\end{aligned} \tag{4.3}$$

Note that the higher excited Γ_5 and Γ_1 states are disregarded in this discussion.

The following lines that demonstrate the quadratic splitting of the Γ_3 ground state doublet of $PrIr_2Zn_{20}$ in magnetic field are based on a personal communication with T. Onimaru[1] from 2016. At first, a simple Hamiltonian that contains a CEF term $\mathcal{H}_{\mathrm{CEF}}$ and a Zeeman term $\mathcal{H}_{\mathrm{Z}} = -g_J \mu_{\mathrm{B}} J_z H_z$ is considered

$$\mathcal{H} = \mathcal{H}_{\mathrm{CEF}} + \mathcal{H}_{\mathrm{Z}}. \tag{4.4}$$

In matrix representation this Hamiltonian reads as

$$\mathcal{H} = \begin{pmatrix} 0 & 0 \\ 0 & \Delta \end{pmatrix} + \begin{pmatrix} 0 & Z \\ Z & 0 \end{pmatrix} = \begin{pmatrix} 0 & Z \\ Z & \Delta \end{pmatrix}, \tag{4.5}$$

where $Z = -2\sqrt{7/3} g_J \mu_{\mathrm{B}} H_z$. Note that the $\mathcal{H}_{\mathrm{CEF}}$ matrix has the energy eigenvalues of the Γ_3 and the Γ_4 state on its diagonal and the $\mathcal{H}_{\mathrm{Z}}$ matrix contains only off-diagonal elements Z that correspond to the finite expectation value of J_z in the mixed state. The energy eigenvalues of this Hamiltonian read as

$$\epsilon_{\Gamma_3^{(1)}, \Gamma_4^{(2)}} = \frac{\Delta \pm \sqrt{\Delta^2 + 4Z^2}}{2}. \tag{4.6}$$

Consequently, the magnetic field induced splitting of the ground state's $\Gamma_3^{(1)}$ component approximates for $H_z \approx 0$ to

$$\Delta_{\Gamma_3^{(1)}} = \frac{\Delta - \sqrt{\Delta^2 + 4Z^2}}{2} \approx -\frac{Z^2}{\Delta} \approx -\frac{H_z^2}{\Delta}. \tag{4.7}$$

This suggests a quadratic splitting of the ground state doublet's $\Gamma_3^{(1)}$ component in magnetic field, which scales with the energy gap Δ between the ground and first excited state.

On the other hand, the doublet splits linearly when an uniaxial stress is applied along the crystallographic [001] direction, which in turn induces a strain along the same direction. This can be directly seen when considering Eq. (2.35) and Eq. (2.39), based on which the linear dependence between strain $\varepsilon_{[001]}$ and the Γ_3-type quadrupolar expectation value $\langle O_2^0 \rangle$ becomes evident.

[1] Laboratory for Magnetism in Novel Materials, Graduate School of Advanced Science and Engineering, Department of Quantum Matter, Hiroshima University, Higashi-Hiroshima, 739-8530, Japan.

4.1.3 Antiferroquadrupolar Order

In $PrIr_2Zn_{20}$, the specific heat and the electrical resistivity show a distinct phase transition signature at $T_Q = 0.11\,K$ [27,97]. Since the magnetization does not exhibit any feature at T_Q, a non-magnetic quadrupole order is likely [27]. To scrutinize the nature of the phase transition, the $(c_{11} - c_{12})/2$ elastic constant is a particularly insightful physical quantity, as it provides direct information on its possible quadrupolar character. As outlined in Section 2.3.2, in case of cubic symmetry, the $(c_{11} - c_{12})/2$ elastic constant is directly related to the Γ_3-type quadrupole-strain susceptibility χ_Q and thus measures the response of the Γ_3-type quadrupolar ground state moments $\langle O_2^0 \rangle$ and $\langle O_2^2 \rangle$ to strain of the same symmetry ε_u and ε_v. Just to recall, in the single-impurity case, χ_Q displays a Curie-type temperature dependence $\chi_Q \sim 1/T$, which is modified to $\chi_{QQ} \sim \chi_Q/(1 - K\chi_Q)$ when the quadrupole moments interact with each other, whereby K denotes the interaction constant. In case of a quadrupolar order, the characteristic softening of the $(c_{11} - c_{12})/2$ elastic constant is suddenly suppressed at the phase transition, as the degeneracy of the ground state doublet is lifted. To study the low temperature order of $PrIr_2Zn_{20}$ more in detail, Ishii et al. [37] performed ultrasound measurements and found in fact a softening of the $(c_{11} - c_{12})/2$ elastic constant for temperatures lower than 7 K that is suppressed at T_Q. The softening of $(c_{11} - c_{12})/2$, on the one hand, confirms the Γ_3-type quadrupolar nature of the ground state and its suppression, on the other hand, provides direct evidence that the anomalies in the specific heat and electrical resistivity result in fact from the ordering of the ground state's quadrupole moments [37]. Ishii et al. [37] were able to determine the sign of the quadrupole-quadrupole coupling constant K, based on which they specified the nature of the order as AFQ [37]. With the help of Levy's criterion, the authors ruled out that the transition at T_Q is a cooperative Jahn-Teller distortion [37]. An additional and quite peculiar finding of the just referenced study is that the c_{44} elastic constant, which is not of Γ_3 but of Γ_5 symmetry, also shows a softening at low temperature that is suppressed at T_Q [37]. This result was confirmed on two different single crystalline samples, which makes an experimental error unlikely [37]. As c_{44} is of different symmetry than the system's Γ_3 ground state, the finding is difficult to interpret at a first glance. In their publication, Ishii et al. [37] note that c_{44} displays a frequency dependence and thus attribute the peculiar behavior to a possible rattling of the 16*c* site Zn ions. Inelastic neutron scattering experiments in magnetic field provided additional evidence that the quadrupolar order in $PrIr_2Zn_{20}$ is indeed of AFQ nature and furthermore specified the order parameter as the O_2^2 quadrupole [120]. Note, as neutrons are not sensitive to detect quadrupole moments, Iwasa et al. [120] determined the AFQ order indirectly via the field induced dipole moments. In zero field, the determination of the quadrupolar structure of the material was therefore not possible by means of neutrons [120].

The evolution of the AFQ phase transition for magnetic fields $\boldsymbol{B} \parallel [100]$ was studied by Onimaru et al. [27,28] by means of specific heat and electrical resistivity measurements. Their results on the temperature dependence of the 4f specific heat C_{4f} at various magnetic fields are shown in Fig. 4.3(a) [28]. At low magnetic field, the data indicates a distinct phase transition signature at T_Q, whose magnitude decreases with increasing magnetic field [28]. At a critical field $B_c \approx 4.5\,T - 5\,T$, the AFQ order is suppressed [28]. This can be seen more clearly in the inset of Fig. 4.3(b), which focuses on the temperature evolution of C_{4f} close to B_c [28]. In a first publication, Onimaru et al. [27] reported a separation of T_Q in low magnetic field into two transitions. This could, however, not be reproduced in a following study [28], from which Fig. 4.3 was reprinted. Electrical resistivity measurements do neither give any indication of the initially reported splitting of T_Q for magnetic field $\boldsymbol{B} \parallel [100]$, but confirm the B_c value derived by the specific heat [28]. Interestingly, in a

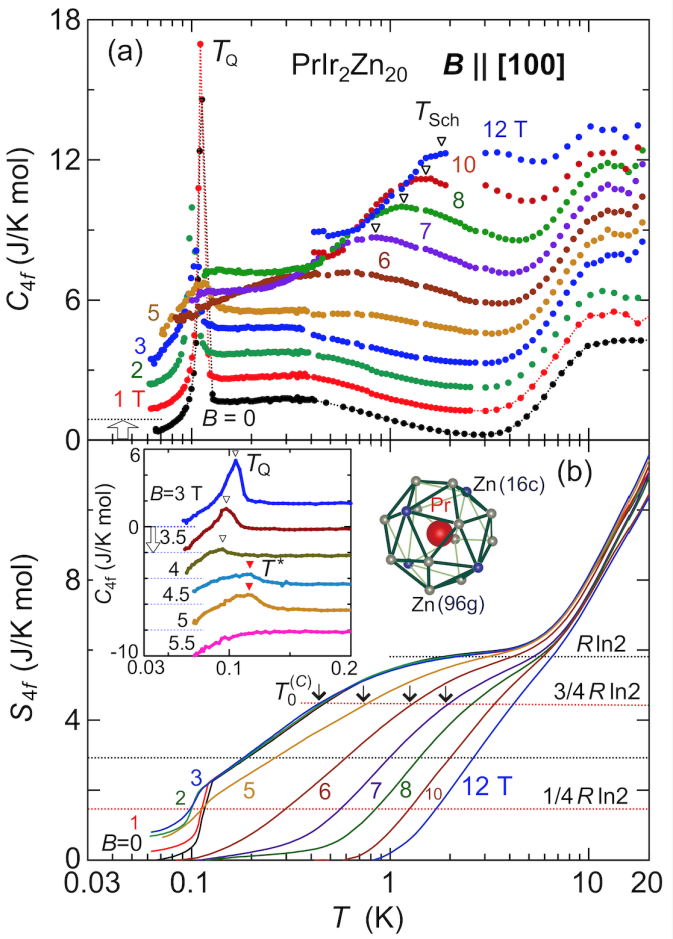

Figure 4.3: (a) Temperature dependence of the 4f specific heat C_{4f} of $PrIr_2Zn_{20}$ at various magnetic fields $\boldsymbol{B} \parallel [100]$. T_Q specifies the onset of AFQ order and T_{Sch} the high field Schottky maximum. (b) Temperature variation of the 4f entropy S_{4f} of $PrIr_2Zn_{20}$ at different magnetic fields. $T_0^{(C)}$ is the characteristic quadrupole Kondo temperature at $S = 3/4R\ln 2$. The inset displays a blowup of the low temperature part of C_{4f} at intermediate magnetic fields. [28]
Reprinted figure with permission from Ref. [28]. ©2016 by the American Physical Society.

small magnetic field regime at around B_c another low temperature anomaly emerges in C_{4f}, which is indicated by T^* in the inset of Fig. 4.3(b) [28]. This finding is corroborated by the electrical resistivity, which exhibits a kink like signature in a comparable field range, marking the onset of FL behavior [28]. More details on this peculiar intermediate phase are provided in the following subsection. Another important quantity to consider when studying hybridization effects is the entropy. Onimaru et al. [28] also deduced the temperature dependence of the 4f entropy S_{4f} at various magnetic fields $\boldsymbol{B} \parallel [100]$, as shown in Fig. 4.3(b). The system acquires an entropy value of $S = R\ln 2$ at around 2 K, which corresponds to the entropy of the two-fold degenerate Γ_3 ground state doublet [28]. Interestingly, the entropy is then readily suppressed as temperature declines and the value just above T_Q is surprisingly small [28]. This implies that quadrupolar fluctuations are present above T_Q, which possibly account for the release of a large fraction of the ground state doublet's entropy well above the phase transition [27, 28]. In this regard, the quadrupole

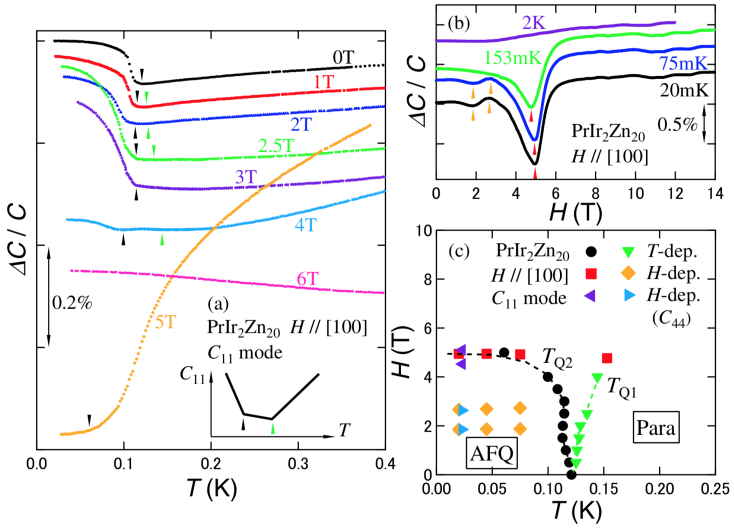

Figure 4.4: (a) Relative change $\Delta c/c$ of the c_{11} elastic constant of $PrIr_2Zn_{20}$ as a function of temperature at different magnetic fields $\boldsymbol{H} \parallel [100]$. Black and green arrows specify the onset of AFQ order. (b) Relative change of c_{11} of $PrIr_2Zn_{20}$ as a function of magnetic field $\boldsymbol{H} \parallel [100]$ at different temperatures. (c) Phase diagram, which summarizes the results from (a) and (b). [37]
Reprinted figure with permission from Ref. [37]. ©2011 The Physical Society of Japan.

Kondo effect is a promising candidate to explain the behavior [28]. Note that the arrows in Fig. 4.3(b) mark the characteristic quadrupole Kondo temperature $T_0^{(C)}$, specified by $S = 3/4R\ln 2$ [28]. $T_0^{(C)}$ was originally defined by Sacramento et al. [18].

Before addressing the quadrupole Kondo behavior in $PrIr_2Zn_{20}$ in detail in the next subsection, elastic constant measurement results by Ishii et al. [37], who studied the evolution of the AFQ order in magnetic field, are briefly reviewed. Figure 4.4(a) shows the temperature dependence of the relative change $\Delta c/c$ of the c_{11} elastic constant at various magnetic fields $\boldsymbol{H} \parallel [100]$ [37]. A reason for the measurement of the c_{11} instead of the Γ_3-type $(c_{11}-c_{12})/2$ elastic constant is not given by Ishii et al. [37]. At low magnetic field and low temperature, c_{11} shows a clear hardening, which indicates the phase transition into the AFQ ordered state [37]. While the data of Ishii et al. [37] shows comparable behavior at low magnetic fields, the data at 5 T stands out due to a substantial softening at elevated temperature, which is suppressed upon approaching absolute zero. At 6 T, c_{11} is nearly temperature independent, which is indicative of a quenching of the Γ_3-type quadrupole moments in consequence of the field induced splitting of the Γ_3 doublet [37]. The field dependence of the relative change of c_{11} at various temperatures for $\boldsymbol{H} \parallel [100]$ is shown in Fig. 4.4(b) [37]. At low temperatures $T \leq 0.15$ K, c_{11} exhibits a pronounced minimum at around 5 T, while at an elevated temperature of 2 K, the anomaly at intermediate magnetic field is suppressed and c_{11} is nearly field independent [37]. A phase diagram, which summarizes the anomalies found in the temperature and field dependent measurements for $\boldsymbol{H} \parallel [100]$ is shown in Fig. 4.4(c) [37]. Ishii et al. [37] also performed elastic constant measurements for magnetic field $\boldsymbol{H} \parallel [110]$. Figure 4.5(a) shows the relative change $\Delta c/c$ of the $(c_{11}-c_{12})/2$ elastic constant as a function of temperature at various magnetic fields $\boldsymbol{H} \parallel [110]$ [37]. The data looks comparable to the just reviewed one for $\boldsymbol{H} \parallel [100]$ with the difference that the phase transition signature in $(c_{11}-c_{12})/2$ persists up to much higher

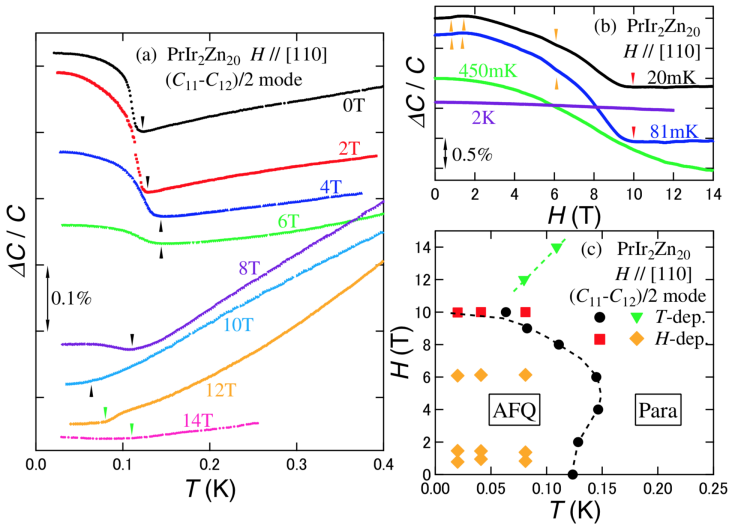

Figure 4.5: (a) Relative change $\Delta c/c$ of the $(c_{11} - c_{12})/2$ elastic constant of $PrIr_2Zn_{20}$ as a function of temperature at various magnetic fields $\boldsymbol{H} \parallel [110]$. The black arrows specify the onset of AFQ order. (b) Relative change of $(c_{11} - c_{12})/2$ of $PrIr_2Zn_{20}$ as a function of magnetic field $\boldsymbol{H} \parallel [110]$ at selected temperatures. (c) Phase diagram, which contains the results from (a) and (b). [37]
Reprinted figure with permission from Ref. [37]. ©2011 The Physical Society of Japan.

magnetic field of approximately 10 T [37]. Figure 4.5(b) shows the field dependence of the relative change of $(c_{11} - c_{12})/2$ for $\boldsymbol{H} \parallel [110]$ at different temperatures [37]. At the lowest temperatures, a continuous softening of $(c_{11} - c_{12})/2$ up to a critical magnetic field of $\mu_0 H_c \approx 10\,\mathrm{T}$ is reported, which is distinct from the behavior derived for $\boldsymbol{H} \parallel [100]$, where c_{11} shows a clear minimum at $\mu_0 H_c \approx 5\,\mathrm{T}$ [37]. The respective phase diagram, which summarizes the anomalies from the temperature and field dependent measurements for $\boldsymbol{H} \parallel [110]$ is shown in Figure 4.5(c) [37].

4.1.4 Quadrupole Kondo Lattice Effect and Diagonal Composite Order

In $PrIr_2Zn_{20}$, the continuous reduction of the ground state's entropy already well above the AFQ phase transition temperature is a surprising finding and indicates the presence of an additional correlation effect at low temperature [27, 28]. Onimaru et al. [28] suggest the quadrupole Kondo effect as a possible mechanism to explain this finding. As outlined in Section 2.4.2, this correlation effect arises when a localized quadrupole moment is over screened by two conduction electron channels. The respective ground state is fragile and distinguished by NFL behavior in the specific heat and the electrical resistivity and a characteristic divergence in the related susceptibility [40]. In order to clarify the presence of the quadrupole Kondo lattice effect in $PrIr_2Zn_{20}$, Onimaru et al. [28] compared their specific heat and electrical resistivity measurement results with the theoretical scaling relations derived by Tsuruta et al. [40] who evaluated a two-channel Anderson lattice model. The key results of Onimaru et al. [28] on the quadrupole Kondo lattice behavior in $PrIr_2Zn_{20}$ are briefly reviewed in the following.

Figure 4.6(a) shows the 4f specific heat normalized to its value at the characteristic temperature $C_{4f}(T)/C_{4f}(T_0^{(C)})$ versus $T/T_0^{(C)}$ at different magnetic fields $\boldsymbol{B} \parallel [100]$ [28].

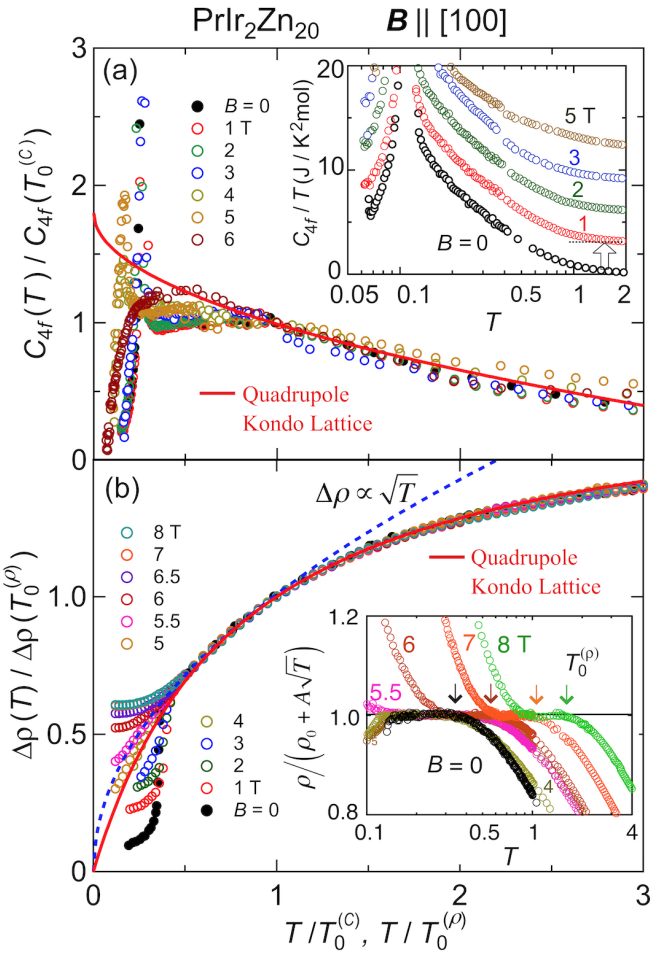

Figure 4.6: (a) 4f specific heat of $PrIr_2Zn_{20}$ normalized to its value at the characteristic temperature $C_{4f}(T)/C_{4f}(T_0^{(C)})$ as a function of $T/T_0^{(C)}$ at various magnetic fields $\boldsymbol{B} \parallel [100]$, together with the theoretically expected quadrupole Kondo lattice behavior [40] as a red solid line. C_{4f}/T as a function of temperature is displayed in the inset. (b) Electrical resistivity of $PrIr_2Zn_{20}$ normalized to its value at the characteristic temperature $\Delta\rho(T)/\Delta\rho(T_0^{(\rho)})$ as a function of $T/T_0^{(\rho)}$ at different magnetic fields $\boldsymbol{B} \parallel [100]$, together with the theoretically expected single-impurity quadrupole Kondo behavior [121] as a blue dashed line and the quadrupole Kondo lattice behavior [40] as a red solid line. The inset illustrates $\rho/(\rho_0 + A\sqrt{T})$ as a function of temperature. [28]
Reprinted figure with permission from Ref. [28]. ©2016 by the American Physical Society.

Just to recall, Onimaru et al. [28], determined $T_0^{(C)}$ as the temperature value at which the entropy takes a value of $S = 3/4R\ln 2$. For temperatures $0.8 < T/T_0^{(C)} < 3$, the scaled specific heat data is indeed in excellent conformity with the theoretical prediction by the two-channel Anderson lattice model [40] plotted as a red solid line, whereby deviations arise at lower temperature [28]. At low magnetic fields, these deviations assign to the emergence of AFQ order, which was already discussed in a preceding subsection. Onimaru et al. [28] performed a similar scaling analysis for their electrical resistivity data.

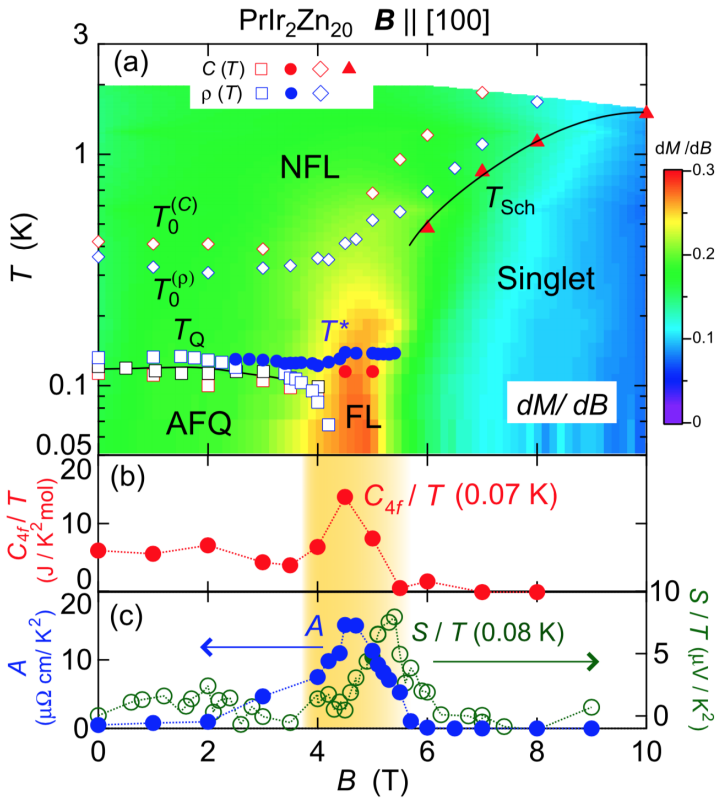

Figure 4.7: (a) Low temperature phase diagram for magnetic field $\boldsymbol{B} \parallel [100]$ of $PrIr_2Zn_{20}$. Red and blue symbols denote anomalies and characteristic temperatures derived from the specific heat and electrical resistivity, respectively. The contour plot indicates the field derivative of the magnetization $\mathrm{d}M/\mathrm{d}B$. (b) 4f specific heat over temperature C_{4f}/T as a function of magnetic field $\boldsymbol{B} \parallel [100]$ at 0.07 K. (c) Field evolution of the electrical resistivity's A parameter, given by $\rho = \rho_0 + AT^2$, on the left. On the right, field dependence of the Seebeck coefficient over temperature S/T [45] at a temperature of 0.08 K. [28] Reprinted figure with permission from Ref. [28]. ©2016 by the American Physical Society.

Figure 4.6(b) displays the differential electrical resistivity normalized to its value at the characteristic temperature $\Delta\rho(T)/\Delta\rho(T_0^{(\rho)})$, whereby the determination of the characteristic temperature $T_0^{(\rho)}$ is illustrated in the inset [28]. In analogy to the specific heat, very good accordance exists between the experimentally determined data and the theoretical prediction by the two-channel Anderson lattice model [28]. By contrast, a simple $\sqrt{T}$ dependence, as proposed by the single-impurity quadrupole Kondo model [121], cannot account for the experimentally observed behavior [28]. This finding is not surprising, as the Pr^{3+} ions are arranged periodically on the crystal lattice and a non-negligible intersite interaction must be present. Overall, the good conformity between the experimental results of Onimaru et al. [28] and the theoretical prediction by Tsuruta et al. [40] strongly suggests the formation of the quadrupole Kondo lattice effect in $PrIr_2Zn_{20}$.

Another interesting aspect of the study by Onimaru et al. [28] is the occurrence of FL behavior in the electrical resistivity in a small magnetic field regime approximately at the critical magnetic field of AFQ order. The phase diagram shown in Fig. 4.7(a)

illustrates this peculiarity [28]. Here, the red and blue circles and squares correspond to signatures and characteristic temperatures, found by Onimaru et al. [28] in the specific heat and the electrical resistivity, respectively. The contour plot illustrates the magnetic field derivative of the material's magnetization, which displays a clear enhancement at intermediate magnetic field and low temperature [28]. This coincides with the FL behavior arising in the electrical resistivity [28]. In their publication, Onimaru et al. [28] suggest that composite order [99,100], which is also referred to as hastatic order [122], is a possible mechanism to explain this interesting finding. As reviewed in the theory part of this thesis, composite order is proposed to be a possible yet exotic ground state of a quadrupole Kondo lattice [99,100]. In the F-channel diagonal composite order scenario, the degeneracy of the two quadrupole Kondo electron screening channels is broken, as one of the two channels hybridizes with the localized quadrupole moments into Kondo singlets [99]. FL behavior is a key signature of this exotic state of matter [99]. As both F-channel diagonal composite order, which is also termed as FH order, and quadrupolar order quench the quadrupole Kondo effect at low temperatures, they are competing mechanisms [99–102]. Van Dyke et al. [102] performed simulations and found that in zero magnetic field AFQ order is prevalent, while at intermediate magnetic field the FH order takes over and at high field an uncorrelated singlet ground state forms. This prediction matches very well with the phase diagram constructed by Onimaru et al. [28]. Besides the FL behavior and the enhancement of $\mathrm{d}M/\mathrm{d}B$ at intermediate magnetic field and low temperature, also the field dependence of $C_{4\mathrm{f}}/T$ at 0.07 K exhibits a distinct maximum, as shown in Fig. 4.7(b) [28]. Very similar behavior is reported for the electrical resistivity's A coefficient and the Seebeck coefficient over temperature S/T [45], which are displayed in Fig. 4.7(c) [28]. As an alternative to the composite order, Onimaru et al. [28] discuss the scenario that the quadrupole Kondo NFL state crosses over to a FL state in presence of a magnetic field, a mechanism that was originally proposed by Yotsuhashi et al. [123]. To further characterize this not yet fully understood phase at intermediate magnetic field, was a major motivation for the measurements of thermal expansion and magnetostriction carried out in the scope of this thesis. The experimental results are presented and discussed in the succeeding section.

4.2 Experimental Results

This section details the thermal expansion and magnetostriction measurement results obtained on single crystalline $PrIr_2Zn_{20}$. First, brief information is provided regarding the examined single crystals that were grown and characterized by a collaboration partner from Hiroshima University in Japan. Subsequently, the low temperature thermal expansion and magnetostriction results for $\boldsymbol{B} \parallel [001]$ and $\boldsymbol{B} \parallel [110]$ are presented. Main purpose of the measurements for $\boldsymbol{B} \parallel [001]$ was to search for unconventional behavior in vicinity of the critical field of AFQ order at around 5 T, where a significant enhancement of the Seebeck coefficient [45,46] as well FL behavior in the electrical resistivity [28] were reported. In addition, the effect of magnetic field $\boldsymbol{B} \parallel [110]$ was examined.

4.2.1 $PrIr_2Zn_{20}$ Single Crystals

The thermal expansion and magnetostriction measurements were performed on two differently oriented single crystalline samples of $PrIr_2Zn_{20}$, which were provided by T. Onimaru from Hiroshima University in Japan. Both samples originate from the same batch (#19)

Sample Nr.	*RRR*	Batch	Crystal Directions	Length
1	54	#19	[001]	1.295 mm
			[110]	1.557 mm
			$[1\bar{1}0]$	1.854 mm
2	54	#19	[111]	1.206 mm

Table 4.1: Properties of the two investigated single crystalline samples of $PrIr_2Zn_{20}$. The single crystals in this table were grown by K. T. Matsumoto and crystallographically oriented by K. T. Matsumoto and Y. Yamane. Provided length values have an accuracy of ± 0.001 mm. The given RRR value was measured by the collaborators on another single crystal from the same batch.

and were synthesized by K. T. Matsumoto[2], who also crystallographically aligned sample Nr. 1. Y. Yamane[2] crystallographically aligned sample Nr. 2. General information on both samples, such as the estimated residual resistivity ratio (RRR), batch number, crystallographic orientations and dimensions are summarized in Table 4.1. The given length values have an accuracy of ± 0.001 mm and the referenced RRR was determined by the Japanese collaborators on a single crystal from the same batch. The shapes of both samples are shown in Fig. 4.8. Sample Nr. 1 has a rectangular shape, whereby the three different pairs of parallel faces correspond to the [001], [110] and $[1\bar{1}0]$ direction. This orientation allows not only for relative length change measurements parallel to magnetic field applied along the [001] or [110] direction but also for relative length change measurements perpendicular to a magnetic field applied along the [100] direction. In this case, the single crystal can be aligned based on its [110] and $[1\bar{1}0]$ oriented sides, so that magnetic field points along the [100] direction and the relative length change is measured along the physically oriented [001] direction, which is perpendicular to the applied magnetic field direction. Based on the fact that for cubic symmetry the [100], [010] and [001] direction are degenerate, subsequently, always the $\langle 100 \rangle$ direction along which the magnetic field points, is defined as the [001] direction. Purpose of the thermal expansion and magnetostriction measurements along and perpendicular to $\boldsymbol{B} \parallel [001]$ was to determine the respective volume changes. Sample Nr. 2, on the other hand, has only two parallel faces that correspond to the [111] direction.

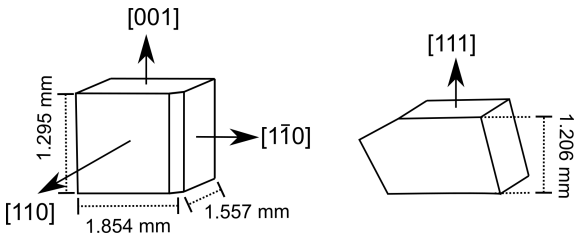

Figure 4.8: Sketches of the two differently oriented single crystalline samples of $PrIr_2Zn_{20}$ examined in this thesis. Indicated are shape, crystallographic orientations and dimensions.

[2]Laboratory for Magnetism in Novel Materials, Graduate School of Advanced Science and Engineering, Department of Quantum Matter, Hiroshima University, Higashi-Hiroshima, 739-8530, Japan.

4.2.2 Thermal Expansion

At first, the zero magnetic field linear thermal expansion coefficients of $PrIr_2Zn_{20}$ measured along the three crystallographic directions [001], [110] and [111] are presented and discussed. An important fact to keep in mind is that the quadrupolar Γ_3 ground state doublet of $PrIr_2Zn_{20}$ splits linearly in presence of a small strain $\varepsilon_{[001]}$ or $\varepsilon_{[110]}$. By contrast, in case of strain $\varepsilon_{[111]}$, no linear splitting of the ground state doublet is expected. As the capacitive dilatometer exerts via its flat springs a small uniaxial stress on the single crystal, measurements along different crystallographic directions are helpful to assess whether this effect has an impact on the obtained data. Subsequently, the linear thermal expansion coefficients obtained for $\boldsymbol{B} \parallel [001]$ and $\boldsymbol{B} \parallel [110]$ are detailed. In case of $\boldsymbol{B} \parallel [001]$, both the longitudinal and the transverse thermal expansion coefficient was measured. Based on the two coefficients, the volume thermal expansion coefficient could be inferred. A special focus of the research was to reveal possible volume changes at around 5 T, where previous Seebeck coefficient measurements indicated the formation of a strongly hybridized state and the electrical resistivity displays FL behavior [28, 45, 46]. Another central point was to compare the found anisotropy and volume effects with the respective behaviors in magnetic Kondo lattice materials. In the case of magnetic field $\boldsymbol{B} \parallel [110]$, only the longitudinal thermal expansion coefficient was measured. Due to the weaker splitting of the Γ_3 ground state doublet for $\boldsymbol{B} \parallel [110]$, a major motivation of the measurement was to set the obtained results in relation to the ones derived for $\boldsymbol{B} \parallel [001]$ and search for universal behavior.

Thermal Expansion in Zero Magnetic Field

The zero magnetic field thermal expansion coefficient of $PrIr_2Zn_{20}$ was determined along the crystallographic [001], [110] and [111] direction. The measurements along the [001] and the [110] direction were performed on sample Nr. 1 and the measurement along the [111] direction was carried out on sample Nr. 2. For detailed information on the two examined single crystalline samples, it is referred to Table 4.1. Figure 4.9 shows the three different linear thermal expansion coefficients $\alpha_{[001]}$, $\alpha_{[110]}$ and $\alpha_{[111]}$ as a function of temperature at zero magnetic field. The three data sets exhibit comparable behavior, they are positive at high temperature and display a clear phase transition signature at $T_Q \approx 0.11$ K, which indicates the formation of the AFQ ordered state. This finding is in good agreement with previous studies that covered elastic constant, specific heat and electrical resistivity measurements [27, 28, 37]. Unexpectedly, the magnitude of α varies slightly among the three examined crystallographic directions. This finding is at odds with the expected isotropic thermal expansion of a cubic crystal. A possible explanation for this behavior is a tiny extrinsic distortion, which is evoked by the small uniaxial stress exerted by the capacitive dilatometer's flat springs. It is recalled that a strain $\varepsilon_{[001]}$ couples linearly to the $\langle O_2^0 \rangle$ quadrupole moment and thus lifts the degeneracy of the Γ_3 ground state doublet. It is therefore conceivable that already a tiny uniaxial stress along the [001] direction, as applied by the miniaturized capacitive dilatometer, is sufficient to activate the $\langle O_2^0 \rangle$ quadrupole moment, which in turn evokes a tetragonal distortion that is superimposed on the intrinsic volume thermal expansion. A similar effect is present for α measured along the [110] direction, whereby a look on Eq. (2.39) and Eq. (2.42) implies that the coupling of $\langle O_2^0 \rangle$ to strain $\varepsilon_{[110]}$ is by a factor 1/2 reduced as compared to $\varepsilon_{[001]}$. Therefore, the experimentally observed smaller magnitude of $\alpha_{[110]}$ as compared to $\alpha_{[001]}$ is in line with the just described scenario and supports the assumption that a small extrinsic uniaxial stress induced contribution to the data is present. According to Eq. (2.43), no linear coupling

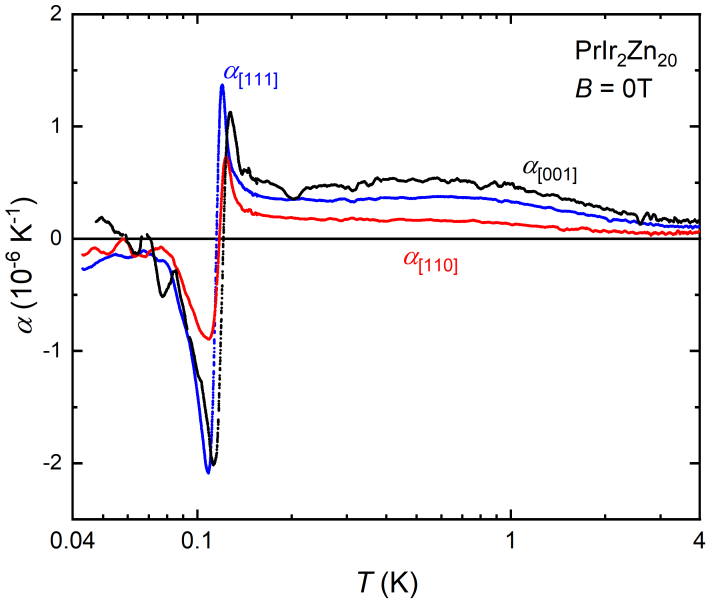

Figure 4.9: Temperature dependence of the thermal expansion coefficients $\alpha_{[001]}$, $\alpha_{[110]}$ and $\alpha_{[111]}$ of $PrIr_2Zn_{20}$ measured at zero magnetic field. $\alpha_{[001]}$ was already published in Ref. [124], whereby the here plotted $\alpha_{[001]}$ data is background corrected as compared to the published data.

between strain $\varepsilon_{[111]}$ and the quadrupolar ground state moments $\langle O_2^0 \rangle$ and $\langle O_2^2 \rangle$ exists and an uniaxial stress induced contribution to $\alpha_{[111]}$ is not expected. It is therefore a surprise that $\alpha_{[111]}$ is located in between $\alpha_{[001]}$ and $\alpha_{[110]}$. The unexpectedly large value of $\alpha_{[111]}$ may relate to a peculiar finding of the elastic constant measurement by Ishii et al. [37]. Here, in addition to the expected low temperature softening of the Γ_3-type elastic constant $(c_{11} - c_{12})/2$, a softening of the c_{44} elastic constant with Γ_5 symmetry was reported [37]. Even though a rattling effect of the Zn ions is under discussion to trigger this unexpected softening of the c_{44} elastic constant [37], further supportive experimental evidence for this scenario would be desirable. As $\varepsilon_{[111]}$ contains a contribution with Γ_5 symmetry, the small uniaxial stress exerted by the experimental setup along the [111] direction may evoke an additional contribution to $\alpha_{[111]}$, which arises from the softening of c_{44}. Another possible reason for the enlarged value of $\alpha_{[111]}$ is the fact that the measurement of $\alpha_{[111]}$ was carried out on sample Nr. 2, while the measurements of $\alpha_{[001]}$ and $\alpha_{[110]}$ were performed on sample Nr. 1. Even though both single crystals originate from the same batch, small differences in the sample quality may be present, which may affect the magnitude of α. Such a possible relation between disorder and the volume thermal expansion will be discussed more in detail in Section 5.2.2, which covers thermal expansion measurement results on the diluted sister compound $Y_{1-x}Pr_xIr_2Zn_{20}$.

Thermal Expansion in Magnetic Fields $B \parallel [001]$

This subsubsection is based on a publication in the scientific journal Physical Review B [124] from the 22nd of February 2019 of which I am the first author. I have carried out the thermal expansion and magnetostriction measurements, the respective data analysis as well as the CEF simulations presented therein. To simulate the temperature dependent expectation values of the quadrupolar operators at different magnetic fields, which are

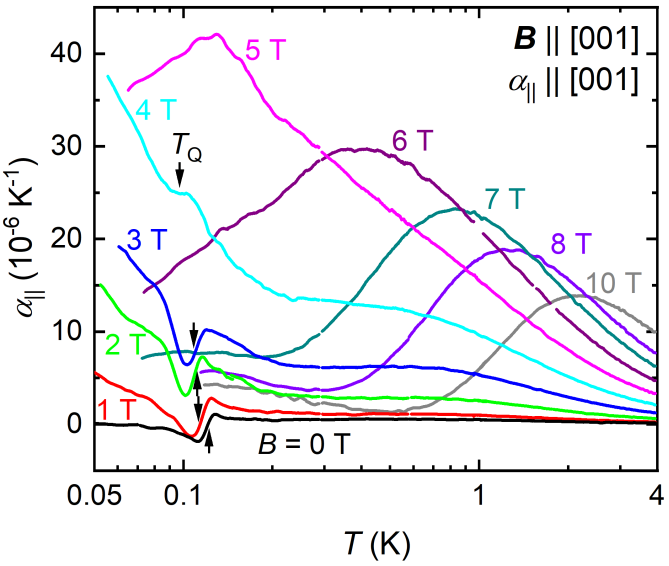

Figure 4.10: Longitudinal thermal expansion coefficient $\alpha_{\parallel}$ as a function of temperature measured at various magnetic fields $\boldsymbol{B} \parallel [001]$. The arrows labeled as T_Q indicate the phase transition temperature into the AFQ ordered state. Note that a dilatometer background contribution, which is insignificantly small as compared to the shown data, was not subtracted.
Adapted figure from Ref. [124]. ©2019 by the American Physical Society.

necessary to calculate the strain contributions arising from the CEF effect, a Mathematica based mean-field CEF program provided by T. Onimaru from Hiroshima University in Japan was used. The single crystalline sample employed for this study was, as already acknowledged in Section 4.2.1, grown and characterized by collaborators from Hiroshima University in Japan. All figures that are shown in this subsubsection and were adapted or reprinted from Ref. [124] were created by myself. First longitudinal thermal expansion measurements for $\boldsymbol{B} \parallel [001]$ on the system were performed in the framework of my master thesis [111]. These measurements were, however, carried out by use of an older type of dilatometer with a lower resolution. The longitudinal thermal expansion data presented in the following was remeasured in the scope of this thesis by use of the miniaturized capacitive dilatometer introduced in Section 3.2.1.

The longitudinal thermal expansion coefficient $\alpha_{\parallel}$ as a function of temperature measured at various magnetic fields $\boldsymbol{B} \parallel [001]$ is shown in Fig. 4.10. In zero magnetic field, $\alpha_{\parallel}$ is distinctly small but grows readily with the application of magnetic field. The significant enhancement of $\alpha_{\parallel}$ upon the application of magnetic field can be directly assigned to the quadratic splitting of the Γ_3 ground state doublet in magnetic field. This effect will be discussed more in detail at a later stage of this subsubsection, where the experimental results are set in relation to a CEF calculation. As outlined in the preceding subsubsection, at zero magnetic field, the thermal expansion coefficients measured along different crystallographic directions display a distinct phase transition signature at a temperature of $T_Q \approx 0.11\,\mathrm{K}$. As magnetic field is increased, T_Q shifts to lower temperature and is finally suppressed at a critical magnetic field value of $B_c \approx 5\,\mathrm{T}$. The evolution of T_Q with magnetic field is illustrated by black arrows in Fig. 4.10. As detailed before, previous studies specified the phase transition as the AF-type ordering of the Γ_3 ground state's quadrupole

moments [37, 120]. The evolution of the phase transition in magnetic field derived by the thermal expansion measurements is in very good agreement with earlier reports on the elastic constant, specific heat and electrical resistivity [27, 28, 37].

A quite peculiar finding of the thermal expansion measurements is the fact that $\alpha_{\parallel}$ does not vanish to zero for $T < T_{\mathrm{Q}}$ but diverges as soon as a small magnetic field is applied. While such a magnetic field induced low temperature divergence is commonly observed in the specific heat due to a nuclear Schottky contribution, this effect usually does not manifest itself in the thermal expansion. Also the fact that the low temperature divergence in $\alpha_{\parallel}$ vanishes at 5 T speaks against a nuclear contribution, for which a gradual increase with magnetic field would be expected. As the thermal expansion coefficient is thermodynamically connected to the negative pressure dependence of entropy, the divergent behavior at low magnetic field indicates remaining entropy inside the AFQ ordered phase. This is surprising, as the AFQ order at T_{Q} lifts the degeneracy of the ground state doublet and should consequently lead to a full release of the related ground state entropy of $S = R \ln 2$. Strikingly, also the specific heat measured by Onimaru et al. [28] provides indication of a small but finite residual entropy at low magnetic field, as shown in Fig. 4.3(b). In zero magnetic field, by contrast, the entropy derived by Onimaru et al. [28] vanishes as expected to zero as temperature declines to zero. Consequently, both the thermal expansion and the specific heat [28] indicate the presence of a small residual entropy in low magnetic field. The large and divergent linear thermal expansion coefficient suggests that the finite low temperature entropy is highly uniaxial stress dependent. Even though the quadrupolar Kondo effect, which comes along with a residual entropy, could principally be set in relation to the peculiar finding, hard evidence for such a connection cannot be provided at the moment.

While the low temperature longitudinal thermal expansion coefficient shows divergent behavior for magnetic fields $B \leq 4\,\mathrm{T}$, a clear maximum forms at 5 T. As magnetic field is further increased, the 5 T maximum gradually shifts to higher temperature and its peak value decreases in magnitude. Surprisingly, $\alpha_{\parallel}$ at high magnetic field increases again at very low temperatures. As the maximum in $\alpha_{\parallel}$ at high magnetic field is indicative of a Schottky-type anomaly, which measures the energy scale of the split Γ_3 ground state doublet, it is surprising that another contribution emerges at very low temperature. In addition, specific heat measurements suggested that the entropy is fully released at high magnetic field and low temperature, where the peculiar enhancement in $\alpha_{\parallel}$ was found [28]. As this unexpected behavior cannot be assigned to a particular physical effect at the moment, complementary measurements are desirable in order specify its physical origin. A notable feature found in $\alpha_{\parallel}$ is the prominent maximum at 5 T and low temperature. This finding reminds on the Seebeck coefficient, which features a maximum at comparable magnetic field and temperature values with a peak value that is by a factor of seventy enhanced as compared to its zero magnetic field value [45, 46]. As the Seebeck coefficient can be directly related to the density of states at the Fermi level, the huge value found in $PrIr_2Zn_{20}$ at 5 T was interpreted as an indication of a strongly hybridized state [46]. Also the specific heat exhibits a maximum at a similar position in the phase diagram and the electrical resistivity displays FL behavior that is accompanied by a distinct enhancement of its A coefficient [28]. The largely increased Seebeck coefficient and $\alpha_{\parallel}$ in combination with the respective findings in the electrical resistivity and specific heat are reminiscent of a strongly hybridized state. As hybridization effects usually come along with pronounced volume changes, volume thermal expansion and magnetostriction measurements are powerful to further characterize $PrIr_2Zn_{20}$'s yet unidentified intermediate magnetic field phase. To examine whether the notable enhancement in $\alpha_{\parallel}$ at intermediate field is connected to

a sizable volume change, the transverse thermal expansion coefficient $\alpha_\perp$ for $\boldsymbol{B} \parallel [001]$ was measured. Based on the $\alpha_\parallel$ and $\alpha_\perp$ data it is possible to derive the volume thermal expansion coefficient via the relation $\beta = \alpha_\parallel + 2\alpha_\perp$. To carry out the transverse thermal expansion measurements, the capacitive dilatometer was rotated by 90° with respect to the magnetic field direction. Before doing so, the $PrIr_2Zn_{20}$ single crystal had to be carefully aligned in the dilatometer. This process is briefly described in the following. As outlined in Section 4.2.1, the examined $PrIr_2Zn_{20}$ single crystal has a cuboid shape whose three different faces correspond to the crystallographic [001], [110] and [1$\bar{1}$0] direction. It is recalled that because of the material's cubic crystal symmetry, the [100], [010] and [001] direction are degenerate in zero field. The same holds for the [110] and the [1$\bar{1}$0] direction. In the following, the cubic ⟨100⟩ direction along which the magnetic field is applied is defined as the [001] direction. As magnetic field $\boldsymbol{B} \parallel [001]$ distorts the material tetragonally along the magnetic field direction, it is fair to make this assumption. The [100] and the [010] direction, which are perpendicular to the magnetic field direction, are assumed to remain degenerate. This assumption is confirmed by CEF calculations, which indicate that the expectation value $\langle O_2^2 \rangle$ vanishes to zero for $\boldsymbol{B} \parallel [001]$. As $\langle O_2^2 \rangle$ is directly proportional to the strain $\varepsilon_\mathrm{v} = \varepsilon_{xx} - \varepsilon_{yy}$, the in plane thermal expansion coefficients $\alpha_{[100]}$ and $\alpha_{[010]}$ have to be degenerate for $\boldsymbol{B} \parallel [001]$. Since the here examined single crystal has only a single physically aligned ⟨100⟩ direction, the thermal expansion was always measured along the same ⟨100⟩ direction, which is specified in Table 4.1 and Fig. 4.8 as the [001] direction with a length of 1.295 mm. While the alignment of the single crystal for a thermal expansion measurement parallel to magnetic field is straightforward, it is more tricky for the measurement perpendicular to magnetic field, as only a single aligned ⟨100⟩ direction exists. By taking advantage of the aligned ⟨110⟩ directions it is, however, possible to align the single crystal in the dilatometer in a way that the magnetic field points along the [100] direction that is located 45° off the aligned [110] and [1$\bar{1}$0] direction. By using aforementioned definition that the ⟨100⟩ direction along which the magnetic field points, corresponds to the [001] direction, the just specified [100] direction is labeled as the [001] direction and the perpendicular direction along which the transverse thermal expansion was measured denotes the [100] direction. The latter is thereby degenerate to the [010] direction.

Figure 4.11(a) shows the transverse thermal expansion coefficient $\alpha_\perp$ together with the already detailed data of $\alpha_\parallel$ at intermediate magnetic fields $\boldsymbol{B} \parallel [001]$. The volume thermal expansion coefficient calculated via the equation $\beta = \alpha_\parallel + 2\alpha_\perp$ as a function of temperature at the respective magnetic fields is shown in Fig. 4.11(b). The measurement results demonstrate that $\alpha_\parallel$ and $\alpha_\perp$ are highly anisotropic, whereby $\alpha_\perp$ approximately mirrors $\alpha_\parallel$. The size of $\alpha_\perp$, is, however, only half in magnitude as compared to $\alpha_\parallel$. Strikingly, the volume thermal expansion coefficient β is distinctly small when compared to the uniaxial coefficients. In addition, a sign change in β becomes evident at $B = 5\,\mathrm{T}$ and very low temperature. By further increasing magnetic field, the low temperature sign change in β becomes more pronounced and shifts to higher temperature. At elevated temperature, the curves of β determined at different magnetic fields fall on top of each other. This indicates an universal mechanism, pointing towards the quadrupole Kondo lattice effect, which was revealed in a preceding study to arise in a comparable temperature range via specific heat and electrical resistivity measurements [28]. As a clear theoretical prediction for the NFL behavior in the thermal expansion associated with the quadrupole Kondo lattice effect has not been discussed in literature so far, it is difficult to classify the found behavior. A detailed study on the relation between the linear and volume thermal expansion coefficients and the quadrupole Kondo effect is provided in Section 5.2.2, which

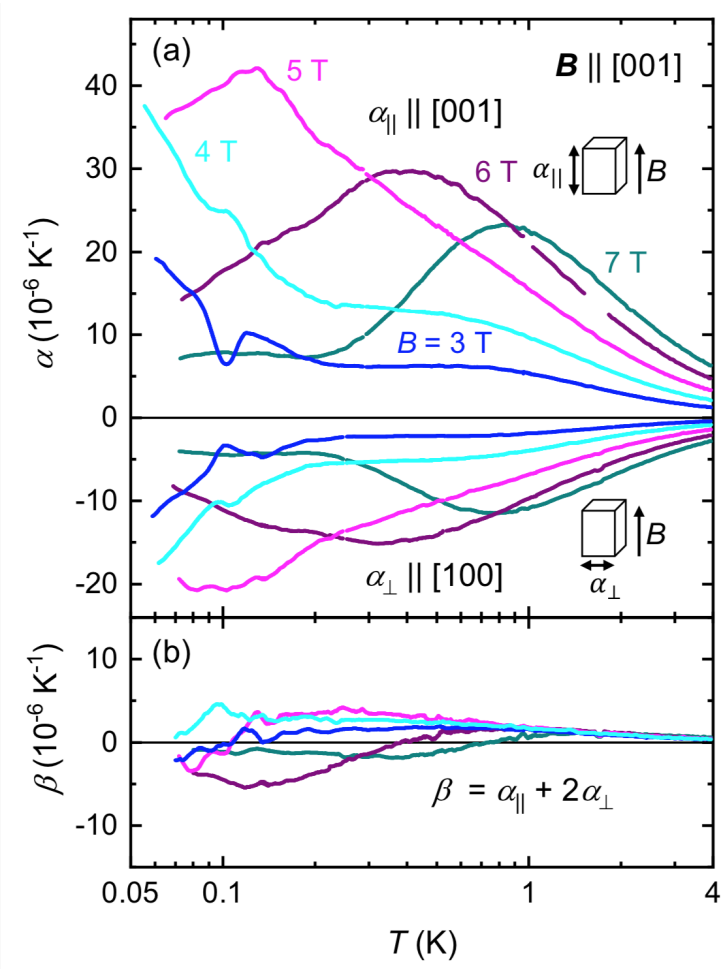

Figure 4.11: (a) Longitudinal and transverse thermal expansion coefficients $\alpha_{\parallel}$ and $\alpha_{\perp}$ as a function of temperature at selected magnetic fields $\boldsymbol{B} \parallel [001]$. (b) Volume thermal expansion coefficient calculated from the data of $\alpha_{\parallel}$ and $\alpha_{\perp}$ via the relation $\beta = \alpha_{\parallel} + 2\alpha_{\perp}$ at selected magnetic fields $\boldsymbol{B} \parallel [001]$. The here shown data is not corrected for the dilatometer background. The background contribution is, however, distinctly small as compared to the shown data. Reprinted figure from Ref. [124]. ©2019 by the American Physical Society.

covers thermal expansion measurement results on the diluted single-impurity quadrupole Kondo candidate $Y_{1-x}Pr_xIr_2Zn_{20}$.

In comparison to typical magnetic Kondo lattice systems, such as $CeRu_2Si_2$ [125] or $CeCu_6$ [126], which display a pronounced low temperature volume thermal expansion of order of magnitude $10^{-5}\,K^{-1}$, the size of the volume thermal expansion of $PrIr_2Zn_{20}$ appears to be distinctly small. In case of $CeRu_2Si_2$ [125], the significant volume expansion is attributed to magnetic correlations and in the case of $CeCu_6$ [126] to the highly pressure dependent Kondo coupling. The relatively small volume thermal expansion coefficient of $PrIr_2Zn_{20}$ implies that the pressure dependence of the relevant coupling constant has to be distinctly small as compared to the magnetic counterparts. As the volume thermal expansion curves presented in Fig. 4.11(b) exhibit universal behavior at elevated temperature and different magnetic fields, it is conceivable that the quadrupole Kondo lattice effect evokes the small but finite volume expansion. In this case, the respective coupling constant, whose pressure dependence determines the magnitude of β, would correspond

to the quadrupole Kondo coupling. Despite the distinct differences in the volume thermal expansion coefficient, the magnitude of the Seebeck coefficient of $PrIr_2Zn_{20}$ is surprisingly large and comparable in magnitude to the one of $CeRu_2Si_2$ and slightly smaller than the huge value of $CeCu_6$ [46, 127]. A graphical overview of the Seebeck coefficient values for a range of well known HF metals [127] together with the ones of selected quadrupolar Pr-based 1-2-20 systems is provided in Ref. [46]. In summary, the quite small volume thermal expansion coefficient in $PrIr_2Zn_{20}$ implies that the largely enhanced Seebeck coefficient of $PrIr_2Zn_{20}$ at 5 T is probably not directly related to a significant hybridization effect, as it is known from magnetic HF metals, and must therefore be triggered by another yet unidentified phenomenon.

In order to better understand the experimentally obtained data and to track down unconventional behavior, it is helpful to compare the experimental findings with a CEF calculation. As explicitly discussed in Section 2.3.2, for $\boldsymbol{B} \parallel [001]$, the strains along the cubic [100], [010] and [001] direction can be expressed in terms of the cubic symmetrized strains provided in Table 2.2 and read as

$$\left.\frac{\Delta L}{L}\right|_{[001]} = \varepsilon_{[001]} = \frac{1}{3}\varepsilon_{\mathrm{B}} + \frac{1}{\sqrt{3}}\varepsilon_{\mathrm{u}}, \tag{4.8}$$

$$\left.\frac{\Delta L}{L}\right|_{[100]} = \varepsilon_{[100]} = \frac{1}{3}\varepsilon_{\mathrm{B}} - \frac{1}{2\sqrt{3}}\varepsilon_{\mathrm{u}} + \frac{1}{2}\varepsilon_{\mathrm{v}}, \tag{4.9}$$

$$\left.\frac{\Delta L}{L}\right|_{[010]} = \varepsilon_{[010]} = \frac{1}{3}\varepsilon_{\mathrm{B}} - \frac{1}{2\sqrt{3}}\varepsilon_{\mathrm{u}} - \frac{1}{2}\varepsilon_{\mathrm{v}}, \tag{4.10}$$

where $\varepsilon_{\mathrm{B}} = \varepsilon_{xx} + \varepsilon_{yy} + \varepsilon_{zz}$ is the isotropic bulk strain with Γ_1 symmetry and $\varepsilon_{\mathrm{u}} = (2\varepsilon_{zz} - \varepsilon_{xx} - \varepsilon_{yy})/\sqrt{3}$ and $\varepsilon_{\mathrm{v}} = \varepsilon_{xx} - \varepsilon_{yy}$ are the anisotropic strains with Γ_3 symmetry. While ε_{B} corresponds to the small thermal expansion found in zero magnetic field, the anisotropic strains ε_{u} and ε_{v} become only active in presence of a suitable symmetry breaking perturbation. In this thesis, such a perturbation is realized via the application of magnetic field $\boldsymbol{B} \parallel [001]$, which distorts the crystal symmetry of $PrIr_2Zn_{20}$ from cubic to tetragonal. As already stressed before, the CEF calculation indicates that $\langle O_2^2 \rangle \approx 0$ for $\boldsymbol{B} \parallel [001]$ and consequently $\varepsilon_{\mathrm{v}} \approx 0$. According to Eq. (4.9) and Eq. (4.10), this implies that the two transverse strains $\varepsilon_{[010]}$ and $\varepsilon_{[100]}$ have to remain degenerate. Figure 4.11 reveals that the volume strain contribution is distinctly small as compared to the field induced anisotropic strain and can therefore be safely neglected in the theoretical calculation. Consequently, the experimentally observed behavior in magnetic field must mainly arise from the temperature dependent $\langle O_2^0 \rangle$ quadrupole moment that couples linearly to the Γ_3-type symmetrized strain ε_{u}, which is specified by the equation

$$\varepsilon_{\mathrm{u}} = \frac{n_{\mathrm{Pr}} g_{\Gamma_3}}{(c_{11}^0 - c_{12}^0)/2} \left\langle O_2^0 \right\rangle, \tag{4.11}$$

where the number of Pr^{3+} ions per volume is given by $n_{\mathrm{Pr}} = 2.751 \times 10^{27}\,\mathrm{m}^{-3}$ [37] and the Γ_3-type background elastic constant by $(c_{11}^0 - c_{12}^0)/2 = 50.74\,\mathrm{GPa}$ [37]. In order to derive the Γ_3-type strain ε_{u} and the longitudinal and transverse thermal expansion coefficients, it is necessary to simulate the temperature dependent expectation value $\langle O_2^0 \rangle$ at different magnetic fields $\boldsymbol{B} \parallel [001]$. In this thesis, the expectation values of the relevant multipole operators were calculated by means of a Mathematica based mean-field CEF program, which was provided by T. Onimaru from Hiroshima University in Japan. The program

can simulate both the temperature and the field dependence of magnetic dipole, electric quadrupole and magnetic octupole moments by evaluating a Hamiltonian of the form

$$\mathcal{H} = \mathcal{H}_{\mathrm{CEF}} - g_J \mu_{\mathrm{B}} \boldsymbol{J}\boldsymbol{H} - g_{\Gamma_3}[O_2^0 \varepsilon_{\mathrm{u}} + O_2^2 \varepsilon_{\mathrm{v}}] \\ - K_{\Gamma_3}[O_2^0 \langle O_2^0 \rangle + O_2^2 \langle O_2^2 \rangle] - K\boldsymbol{J}\langle \boldsymbol{J} \rangle. \quad (4.12)$$

As Eq. (4.12) contains various terms, its different contributions are briefly detailed in the following. The first term denotes the CEF Hamiltonian $\mathcal{H}_{\mathrm{CEF}}$ for cubic T_d point group symmetry that reads as [64]

$$\mathcal{H}_{\mathrm{CEF}} = W \left[\frac{x}{60}(O_4^0 + 5O_4^4) + \frac{1-|x|}{1260}(O_6^0 - 21O_6^4) \right]. \quad (4.13)$$

In the case of $PrIr_2Zn_{20}$, the CEF parameters W and x were determined by means of inelastic neutron scattering by Iwasa et al. [65] at $W = -1.22\,\mathrm{K}$ and $x = 0.537$. The second term is the Zeeman Hamiltonian with the gyromagnetic ratio g_J, the Bohr magneton μ_{B}, the angular momentum operator $\boldsymbol{J}$ and the magnetic field $\boldsymbol{H}$. The third term denotes the quadrupole-strain interaction term. The quadrupole-strain coupling constant g_{Γ_3} quantifies the interaction strength between the Γ_3-type symmetrized strains ε_{u} and ε_{v} and the Stevens operators of the same symmetry O_2^0 and O_2^2 with the respective expectation values $\langle O_2^0 \rangle$ and $\langle O_2^2 \rangle$. The fourth term specifies the interaction between quadrupole moments, where K_{Γ_3} is the quadrupole-quadrupole coupling constant. The fifth term denotes the interaction between excited dipole moments with the magnetic dipolar interaction constant K and the expectation value of the total angular momentum operator $\langle \boldsymbol{J} \rangle$. In order to simulate the multipolar expectation values, a quadrupole-quadrupole interaction coefficient $K_{\Gamma_3} = -0.0067\,\mathrm{K}$, a quadrupole-strain coupling constant $g_{\Gamma_3} = -38.0\,\mathrm{K}$ and a magnetic interaction $K = -0.19\,\mathrm{K}$ were employed. The quadrupole-quadrupole interaction constant was derived by T. Onimaru, who could reproduce the experimentally found AFQ order temperature of $T_{\mathrm{Q}} = 0.11\,\mathrm{K}$ by means of a mean-field calculation when using this value. The parameters $g_{\Gamma_3} = -38.0\,\mathrm{K}$ and $K = -0.19\,\mathrm{K}$ were used as fitting parameters and their values derived by fitting the theoretically calculated curves to the experimentally obtained thermal expansion data at 10 T. With reference to previous measurements by Onimaru et al. [28], it is fair to assume that the system resides in the fully localized state at this magnetic field value and comparison of the experimentally obtained data with the mean-field simulation is therefore justified. The so determined values of g_{Γ_3} and K agree well with the quadrupole-strain coupling constant $|g_{\Gamma_3}| = 30.9\,\mathrm{K}$ deduced by Ishii et al. [37] via an elastic constant measurement and the magnetic interaction constant $K = -0.35\,\mathrm{K}$ estimated by T. Onimaru based on previous magnetization measurements [25]. By using the just specified parameters, the temperature dependencies of various multipolar operators were simulated at different magnetic fields. The relevant expectation value $\langle O_2^0 \rangle$ was then transformed into the respective symmetrized strain ε_{u} via Eq. (4.11). By plugging the symmetrized thermal expansion coefficient $\alpha_{\mathrm{u}} = \partial_T \varepsilon_{\mathrm{u}}$ into Eq. (4.8) and Eq. (4.9), the longitudinal and transverse thermal expansion coefficient $\alpha_{\parallel} = \alpha_{[001]}$ and $\alpha_{\perp} = \alpha_{[100]}$ could be derived for $\boldsymbol{B} \parallel [001]$.

Figure 4.12 shows the simulated thermal expansion coefficients $\alpha_{\parallel}$ and $\alpha_{\perp}$ as a function of temperature at various magnetic fields $\boldsymbol{B} \parallel [001]$, whereby the inset provides a head-to-head comparison of the experimentally obtained data and the simulated one at selected magnetic fields. The calculation qualitatively reproduces the highly anisotropic behavior found in $\alpha_{\parallel}$ and $\alpha_{\perp}$ very well. At high magnetic field $B \geq 8\,\mathrm{T}$ and elevated temperature, the calculation and the experimentally determined data match nicely, which

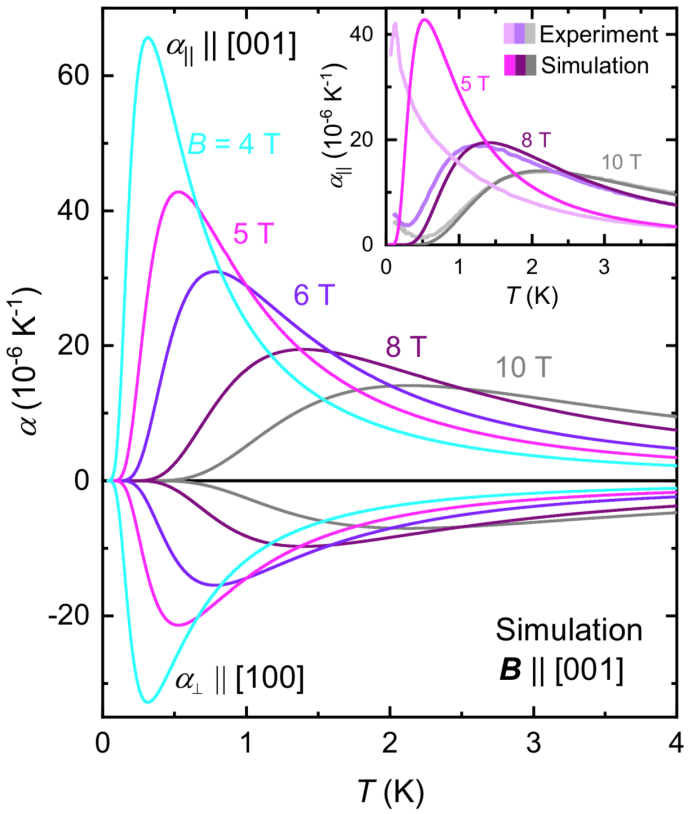

Figure 4.12: Simulated CEF longitudinal and transverse thermal expansion coefficients $\alpha_{||}$ and $\alpha_{\perp}$ as a function of temperature at different magnetic fields $\boldsymbol{B}$ || [001]. The inset displays both simulated and experimentally obtained data for $\alpha_{||}$ at elevated magnetic fields $\boldsymbol{B}$ || [001].
Reprinted figure from Ref. [124]. ©2019 by the American Physical Society.

indicates the fully localized nature of the quadrupolar Γ_3 ground state doublet. Only at very low temperature, the experimentally obtained high field data exhibits a peculiar low temperature increase that cannot be accounted for by the CEF simulation. By contrast, at an intermediate magnetic field of $B = 5\,\mathrm{T}$, distinct deviations between CEF simulation and the measurement results are present. These deviations become particularity evident on approaching the critical magnetic field of AFQ order, where FL behavior in the electrical resistivity, a low temperature maximum in the specific heat and a largely enhanced Seebeck coefficient were reported [28, 45, 46]. At a magnetic field of 5 T, the peak position in $\alpha_{||}$ is located at $T \approx 0.13\,\mathrm{K}$, which closely resembles the position of the maximum found in the Seebeck coefficient [45, 46] and the specific heat [28]. While it is difficult to assign this anomaly to a specific physical effect, the electrical resistivity, which shows FL behavior in a comparable magnetic field range, indicated that the unconventional behavior at 5 T may be caused by the emergence of diagonal composite order [28]. Note that the FH order scenario discussed by Zhang et al. [101] and Van Dyke et al. [102] can be considered as complementary to the diagonal composite order theory introduced by Hoshino et al. [99, 100]. In particular the work by Van Dyke et al. [102] on the FH order in cubic Pr-based 1-2-20 systems is of relevance for the here obtained experimental results, as the authors studied possible strain signatures of FH order. Van Dyke et al. [102] showed theoretically that FH order only manifests itself in form of a phase transition in

zero magnetic field and transforms into a rather broad crossover as soon as magnetic field is applied [102]. According to their calculations, at low magnetic field, the AFQ order is dominant, whose onset is indicated by a sharp discontinuity in the longitudinal thermal expansion coefficient $\alpha_{\parallel}$ [102]. By increasing magnetic field, the sharp phase transition signature in $\alpha_{\parallel}$ is replaced by a broad crossover anomaly that is indicative of the emerging FH order [102]. The theoretical prediction by Van Dyke et al. [102] matches well with the experimentally measured data of $\alpha_{\parallel}$, which displays a sharp discontinuity at low magnetic field that is indicative of AFQ order and a largely enhanced maximum at 5 T, which may assign to the possible crossover into the FH ordered state. Overall, the experimentally determined thermal expansion data is therefore in good accordance with the FH order scenario. Clear proof for the emergence of this novel phase can, however, not be provided solely on the basis of the thermal expansion data. Van Dyke et al. [102] also proposed that a broad crossover related to the FH ordered phase arises in the magnetostriction coefficient. This prediction is compared to the experimentally determined magnetostriction data in the following Section 4.2.3. Before, the longitudinal thermal expansion coefficient for $\boldsymbol{B} \parallel [110]$ is detailed.

Thermal Expansion in Magnetic Fields $\boldsymbol{B} \parallel [110]$

The focus of the following lines is on the thermal expansion coefficient $\alpha_{[110]}$ measured parallel to magnetic field $\boldsymbol{B} \parallel [110]$. Fig. 4.13 shows $\alpha_{[110]}$ as a function of temperature at various magnetic fields $\boldsymbol{B} \parallel [110]$. Similar to $\alpha_{[001]}$, $\alpha_{[110]}$ is distinctly small in zero magnetic field but grows steadily in magnitude as magnetic field increases. A clear phase transition signature is visible up to a critical magnetic field of $B_{\mathrm{c}} \approx 8\,\mathrm{T}$, which likely assigns to the transition into the AFQ ordered state. In the magnetic field range $0 \leq B \leq 6\,\mathrm{T}$, T_{Q} shifts to higher temperature as magnetic field is increased, while it is suppressed to lower temperature at 8 T and finally vanishes at 10 T. This finding is in good agreement with previous elastic constant measurement results by Ishii et al. [37]. At low magnetic fields $B \leq 6\,\mathrm{T}$, the phase transition signature as well as the divergent increase in $\alpha_{[110]}$ are reminiscent of the behavior found for $\boldsymbol{B} \parallel [001]$. Note that the low temperature anomaly in $\alpha_{[110]}$ at 8 T, which likely indicates a phase transition, has a much different appearance than the signature present for $B \leq 6\,\mathrm{T}$. Specifically, it shows a sudden drop to zero, instead of a sign change. Since the shape of the phase transition anomaly at 8 T is much different to the one found at smaller magnetic field, it is difficult to judge as to whether the signature also assigns to the AF-type ordering of the quadrupolar ground state moments or to another effect. At 10 T, a phase transition signature could not be found, which implies the suppression of the AFQ ordered state. Here, a clear maximum forms at around 0.25 K with a peak value of $\alpha_{[110]} \approx 9 \times 10^{-6}\,\mathrm{K}^{-1}$. This reminds on the behavior found for the longitudinal thermal expansion coefficient at 5 T for $\boldsymbol{B} \parallel [001]$, whose peak value is, however, approximately five times larger. It is likely that the physical mechanism behind these two anomalies has the same origin. As magnetic field is further increased, the maximum value decreases and its peak position moves to higher temperature. This behavior clearly reminds on a Schottky-type anomaly. To better understand and to correctly classify the experimentally observed behaviors, they are now compared to a CEF calculation, which simulates the effect expected for a fully localized Γ_3 ground state doublet. As magnetic field applied along the [110] direction does not only induced the $\langle O_2^0 \rangle$ but also the $\langle O_{xy} \rangle$ quadrupole moment, the theoretical analysis becomes more complicated as compared to the just discussed case, where $\boldsymbol{B} \parallel [001]$. In order to simulate the temperature dependence of the quadrupolar expectation values, again the CEF mean-field program by T. Onimaru was employed. The Hamiltonian evaluated by the

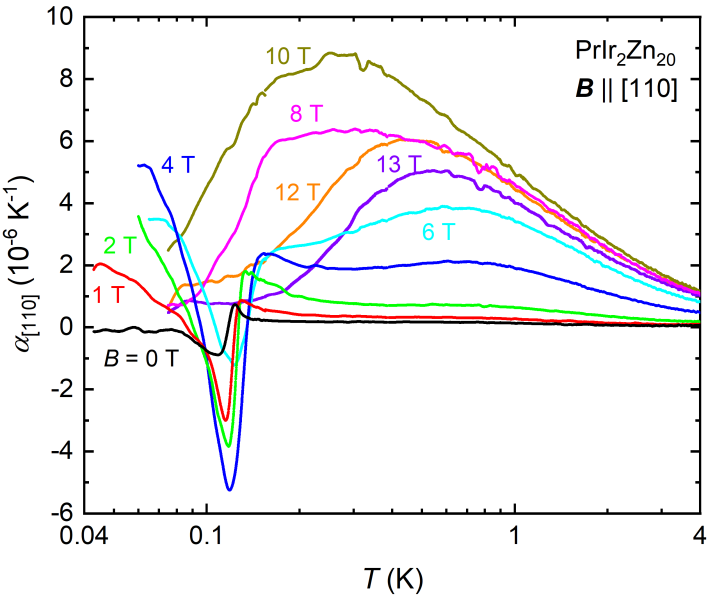

Figure 4.13: Temperature dependence of the longitudinal thermal expansion coefficient $\alpha_{[110]}$ of $PrIr_2Zn_{20}$ for different magnetic fields $\boldsymbol{B} \parallel [110]$.

program has a very similar form as the one for $\boldsymbol{B} \parallel [001]$, which is specified by Eq. (4.12). The only difference is that also a quadrupole-strain coupling term with Γ_5 symmetry has to be taken into account. A possible interaction between the Γ_5 quadrupole moments is disregarded in the following analysis, as no information on the magnitude of the respective interaction constant exists and an additional free parameter would further complicate the analysis. The Hamiltonian evaluated by the CEF program reads as

$$\mathcal{H} = \mathcal{H}_{\mathrm{CEF}} - g_J \mu_{\mathrm{B}} \boldsymbol{J}\boldsymbol{H} - g_{\Gamma_3}[O_2^0 \varepsilon_{\mathrm{u}} + O_2^2 \varepsilon_{\mathrm{v}}] - g_{\Gamma_5}[O_{xy}\varepsilon_{xy} + O_{xz}\varepsilon_{xz} + O_{yz}\varepsilon_{yz}] \\ - K_{\Gamma_3}[O_2^0 \langle O_2^0 \rangle + O_2^2 \langle O_2^2 \rangle] - K \boldsymbol{J} \langle \boldsymbol{J} \rangle , \quad (4.14)$$

whereby the first term denotes the cubic CEF Hamiltonian specified by Eq. (4.13) in the preceding subsubsection with the CEF parameters $W = -1.22\,\mathrm{K}$ and $x = 0.537$ [65] and the second term specifies the Zeeman Hamiltonian. The third and the fifth term cover the quadrupole-strain and quadrupole-quadrupole interaction contributions with Γ_3 symmetry. Here, the same parameters as derived in the preceding subsubsection were employed for the simulation, which are $g_{\Gamma_3} = -38.0\,\mathrm{K}$ and $K_{\Gamma_3} = -0.0067\,\mathrm{K}$. The fourth term takes account of the coupling between strains with Γ_5 symmetry ε_{xy}, ε_{xz} and ε_{yz} and the corresponding Stevens operators O_{xy}, O_{xz} and O_{yz}. The coupling strength between quadrupole and strain is thereby quantified by the quadrupole-strain coupling constant g_{Γ_5}. Its value has to be determined by fitting the theoretically calculated curves to the experimentally obtained high magnetic field data. The last term of Eq. (4.14) denotes the interaction between field induced dipole moments, whereby the interaction constant $K = -0.19\,\mathrm{K}$, which was also derived in the preceding subsubsection, was employed.

In order to ascertain which of the quadrupolar expectation values are of relevance for the calculation of the thermal expansion coefficient $\alpha_{[110]} = \partial_T \varepsilon_{[110]}$, the decomposition of $\varepsilon_{[110]}$ into the cubic symmetrized strains, as explicitly detailed in Section 2.3.2, is

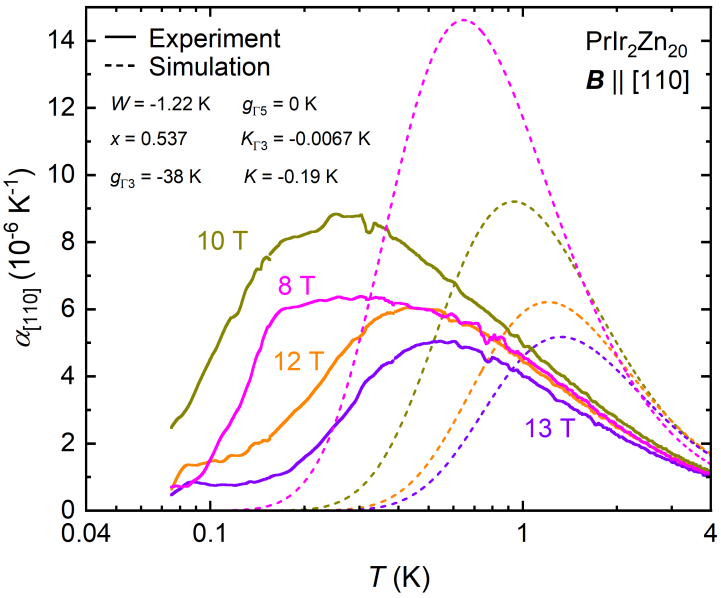

Figure 4.14: Comparison between the experimentally determined and the simulated thermal expansion coefficients $\alpha_{[110]}$ at high magnetic fields $\boldsymbol{B} \parallel [110]$. The simulation uses the CEF parameters $W = -1.22\,\mathrm{K}$ and $x = 0.537$ [65], a Γ_3-type quadrupole-strain coupling constant $g_{\Gamma_3} = -38.0\,\mathrm{K}$, a Γ_3-type quadrupole-quadrupole interaction constant $K_{\Gamma_3} = -0.0067\,\mathrm{K}$ and an interaction constant between excited dipole moments $K = -0.19\,\mathrm{K}$. Note that the Γ_5-type quadrupole-strain coupling was set to zero $g_{\Gamma_5} = 0$ in this calculation.

considered. The strain along the [110] direction reads as

$$\left.\frac{\Delta L}{L}\right|_{[110]} = \varepsilon_{[110]} = \frac{1}{3}\varepsilon_{\mathrm{B}} - \frac{1}{2\sqrt{3}}\varepsilon_{\mathrm{u}} + \varepsilon_{xy}, \tag{4.15}$$

which implies that the bulk strain ε_{B}, the Γ_3-type symmetrized strain ε_{u} and the shear strain ε_{xy} with Γ_5 symmetry are of relevance. As already mentioned in the preceding subsubsection, the contribution of ε_{B} has to be disregarded in the calculation, as it cannot be simulated. Based on the fact that the zero magnetic field thermal expansion is distinctly small as compared to the thermal expansion coefficient in magnetic field, the error that comes along with the negligence of ε_{B} can be considered as insignificantly small and is therefore not of any relevance for the simulated data at high magnetic field. The contribution from ε_{u} stems again from the temperature dependence of the quadrupolar expectation value $\langle O_2^0 \rangle$, as specified by the equation

$$\varepsilon_{\mathrm{u}} = \frac{n_{\mathrm{Pr}} g_{\Gamma_3}}{(c_{11}^0 - c_{12}^0)/2} \langle O_2^0 \rangle , \tag{4.16}$$

with the Pr^{3+} ion density $n_{\mathrm{Pr}} = 2.751 \times 10^{27}\,\mathrm{m}^{-3}$ [37] and the background elastic constant with Γ_3 symmetry $(c_{11}^0 - c_{12}^0)/2 = 50.74\,\mathrm{GPa}$ [37]. The strain ε_{xy}, on the other hand, arises from the linear coupling to the quadrupolar expectation value $\langle O_{xy} \rangle$ and derives as

$$\varepsilon_{xy} = \frac{n_{\mathrm{Pr}} g_{\Gamma_5}}{4 c_{44}^0} \langle O_{xy} \rangle, \tag{4.17}$$

whereby the background elastic constant was previously determined by Ishii et al. [37] at $c_{44}^0 = 51.45\,\mathrm{GPa}$. To start the theoretical analysis, only the contribution to $\varepsilon_{[110]}$ that

arises from ε_u is taken into account, while the contribution ε_{xy} is disregarded for the moment. The so simulated curves are shown in combination with the experimental results at high magnetic field $B \geq 8\,T$ in Fig. 4.14. At the highest measured magnetic field of 13 T, it turns out that the maximum suggested by the CEF calculation appears at a much higher temperature than the respective maximum in the experimentally obtained data. This suggests that a magnetic field of 13 T is not sufficient to drive the system into the fully localized state. Due to the weaker splitting of the Γ_3 doublet for $\boldsymbol{B} \parallel [001]$ than for $\boldsymbol{B} \parallel [110]$, the value of B_c moves to a higher magnetic field for the latter field orientation. In consequence, also the magnetic field value at which the ground state becomes fully localized is enhanced. It is therefore conceivable that correlation effects are still present at 13 T, which explains the distinct differences between the experimentally obtained and the simulated data. Taking account of the strain contribution ε_{xy} rather modifies the magnitude of the simulated thermal expansion coefficient than the maximum position. Consequently, it is not possible to determine g_{Γ_5} based on the thermal expansion measurement, as the applied magnetic field is too small to drive the system into the fully localized state. Likely much higher magnetic fields of up to 20 T would be required in order to deduce the value of g_{Γ_5} from the thermal expansion. With the employed dilution refrigerator, the generation of such a high magnetic field was, however, not possible, as the superconducting magnet is limited to a magnetic field of 13 T. A better approach is to determine g_{Γ_5} based on the magnetostriction data, which is detailed in the following subsection.

4.2.3 Magnetostriction

To further characterize the quadrupolar ground state of $PrIr_2Zn_{20}$, longitudinal and transverse magnetostriction measurements were carried out for $\boldsymbol{B} \parallel [001]$, which also allowed to infer the volume magnetostriction coefficient. Main motivation for the experiments was to search for possible signatures in the linear and volume magnetostriction coefficients that provide further details on the novel phase emerging at $B \approx 5\,T$. Furthermore, magnetostriction measurements parallel to magnetic field $\boldsymbol{B} \parallel [110]$ were carried out.

Magnetostriction in Magnetic Fields $\boldsymbol{B} \parallel [001]$

The magnetostriction results detailed in this subsubsection were already published in the scientific journal Physical Review B [124] on the 22nd of February 2019 together with the respective longitudinal, transverse and volume thermal expansion results for $\boldsymbol{B} \parallel [001]$ that were discussed in Section 4.2.2. I carried out initial measurements of the longitudinal magnetostriction of $PrIr_2Zn_{20}$ for $\boldsymbol{B} \parallel [001]$ in the framework of my master thesis by use of an older type of dilatometer [111]. The here presented longitudinal magnetostriction data was remeasured in the scope of this thesis by use of the miniaturized capacitive dilatometer introduced in Section 3.2.1.

Figure 4.15 displays the longitudinal, transverse and volume magnetostriction coefficients $\lambda_\parallel$, $\lambda_\perp$ and $\lambda_V = \lambda_\parallel + 2\lambda_\perp$ for $\boldsymbol{B} \parallel [001]$ measured at various temperatures. In analogy to the longitudinal and transverse thermal expansion coefficients, $\lambda_\parallel$ and $\lambda_\perp$ display highly anisotropic behavior, which becomes more distinct as temperature declines. $\lambda_\parallel$ is negative in the whole investigated magnetic field range, while $\lambda_\perp$ shows a positive value. The finding of $\lambda_\perp$ being the approximate mirror image of $\lambda_\parallel$ with roughly half of its magnitude, is reminiscent of the just discussed data of $\alpha_\parallel$ and $\alpha_\perp$ for $\boldsymbol{B} \parallel [001]$. This finding implies that the application of magnetic field $\boldsymbol{B} \parallel [001]$ triggers a nearly volume conserving tetragonal distortion, which clearly demonstrates that the symmetrized quadrupolar

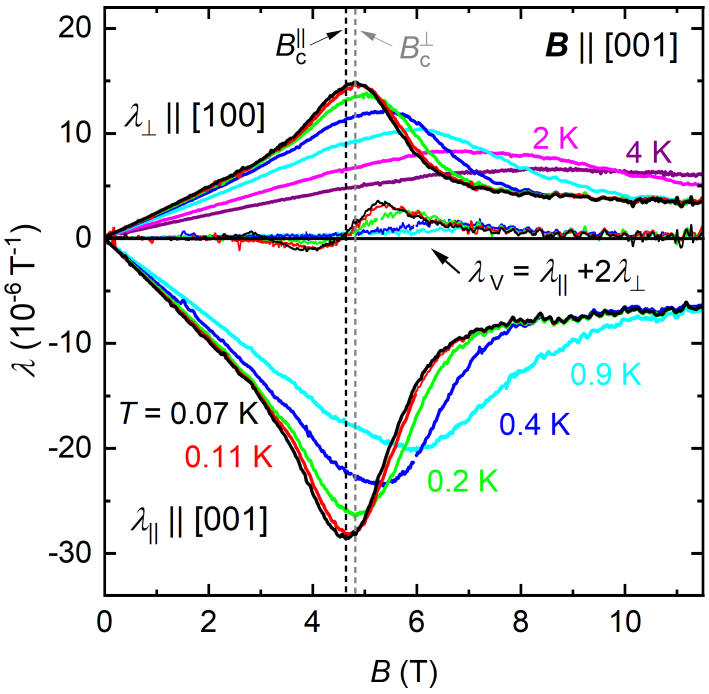

Figure 4.15: Magnetic field variation of the longitudinal and transverse magnetostriction coefficients $\lambda_{\parallel}$ and $\lambda_{\perp}$ for $\boldsymbol{B} \parallel [001]$ at different temperatures. The volume magnetostriction indicated by the arrow derives from the $\lambda_{\parallel}$ and $\lambda_{\perp}$ data via the relation $\lambda_V = \lambda_{\parallel} + 2\lambda_{\perp}$. Dashed black and grey lines specify the value of the critical magnetic field B_c at 0.07 K for $\lambda_{\parallel}$ and $\lambda_{\perp}$, respectively. The difference in B_c indicates a small misalignment of the single crystal for the magnetostriction measurement perpendicular to magnetic field. The magnetostriction data is not corrected for the dilatometer background. The latter can be considered as very small in comparison to the shown data.
Adapted figure from Ref. [124, SM]. ©2019 by the American Physical Society.

strain with Γ_3 symmetry $\varepsilon_u \sim \langle O_2^0 \rangle$ dominates the uniaxial magnetostriction. Both $\lambda_{\parallel}$ and $\lambda_{\perp}$ show a clear extremum at around 4.7 T at the lowest measured temperatures of 0.07 K and 0.11 K. The maximum forms in close vicinity of the critical field of AFQ order, which was specified by the just discussed thermal expansion measurements to be located in between 4 T and 5 T. When temperature is increased, the relatively sharp anomaly in $\lambda_{\parallel}$ and $\lambda_{\perp}$ broadens notably and moves to higher magnetic field. When comparing the magnetic field value at which $\lambda_{\parallel}$ and $\lambda_{\perp}$ peak at 0.07 K, it shows that the critical value assigned to the peak position of the transverse magnetostriction $B_c^{\perp}$ appears at a slightly higher magnetic field value than the one derived from the longitudinal magnetostriction $B_c^{\parallel}$. This is surprising as the field dependencies of both $\lambda_{\parallel}$ and $\lambda_{\perp}$ relate to $\partial_B \langle O_2^0 \rangle$ and the peak value is therefore expected to be identical for both measurements. Before discussing this issue more in detail, the volume magnetostriction coefficient is considered. With the help of $\lambda_{\parallel}$ and $\lambda_{\perp}$ one can derive the volume magnetostriction via the relation $\lambda_V = \lambda_{\parallel} + 2\lambda_{\perp}$, which is additionally plotted in Fig. 4.15. Its magnitude is distinctly small as compared to the uniaxial magnetostriction coefficients $\lambda_{\parallel}$ and $\lambda_{\perp}$, which is in line with the just detailed thermal expansion data. Interestingly, λ_V exhibits a small but clearly noticeable

sign change close to B_c. Having the just mentioned tiny difference in the critical magnetic field value of $B_c^{\parallel}$ and $B_c^{\perp}$ in mind, it is conceivable that the sign change in λ_V is an artificially generated effect that arises from the small difference in the $B_c^{\parallel}$ and $B_c^{\perp}$ values. In this regard, it is recalled that for the transverse magnetostriction measurement, the alignment of the sample with respect to the applied magnetic field is trickier as compared to the longitudinal magnetostriction measurement. Even though it was taken special care to align the single crystal as precisely as possible, a small misalignment of the single crystal inside the dilatometer with respect to the magnetic field direction cannot be excluded. As previously reported by Ishii et al. [37], the critical field of AFQ order depends sensitively on the applied magnetic field direction, whereby $B_c^{[001]} < B_c^{[110]} < B_c^{[111]}$. This implies a shift of B_c to a higher magnetic field value when the single crystal's [001] direction is slightly misaligned with respect to the magnetic field. Such a misalignment may have two possible origins. The first one is the already mentioned case that the single crystal was slightly misaligned when placed inside dilatometer. As the alignment process for the transverse magnetostriction measurement is tricky, it is conceivable that the related error is larger than for the longitudinal magnetostriction measurement. The second possibility is that the cutting process used by the Japanese collaborators to bring the single crystal to a cuboid shape with three crystallographically aligned faces comes along with a small error. To verify whether the first scenario causes the difference in the B_c values, a complementary magnetostriction measurement was carried out, whereby the single crystal was aligned as carefully as possible inside the dilatometer. As the second measurement approximately reproduced the $\lambda_\perp$ data obtained in the first run, it is concluded that the cutting process must be hold accountable for the small misalignment. The collaborators from Hirsohima University confirmed that a small misalignment of a few degree is an inevitable side effect of the cutting process and cannot be excluded. On the other hand, it is also conceivable that the sign change in λ_V is an intrinsic feature, which in turn would explain the small difference found in the B_c values of $\lambda_\parallel$ and $\lambda_\perp$. After carefully considering both scenarios, it is concluded that the sign change in the volume magnetostriction must be artificially induced due to a small misalignment and is not an intrinsic effect. To correct this small error arising from the misalignment, the magnetic field value of the transverse magnetostriction data was multiplied by a constant factor in order to rescale it onto the value found in the longitudinal magnetostriction measurement. At the lowest measured temperature of 0.07 K, this is fulfilled for $B_c^{\parallel} = 0.968 \times B_c^{\perp}$.

The so corrected data of $\lambda_\perp$ is shown together with the data of $\lambda_\parallel$ in Fig. 4.16(a). The volume magnetostriction calculated from the corrected linear magnetostriction coefficients is also plotted in Fig. 4.16(a), whereby the initially found sign change in vicinity of B_c is not present anymore. The volume thermal expansion measurements presented in the preceding subsection already suggested that the novel state forming at intermediate magnetic field is not accompanied by a notable change in volume, as it would be expected for a strongly hybridized state. The volume magnetostriction coefficient confirms this finding, as it is vanishingly small when compared to the longitudinal and transverse magnetostriction coefficients. Only in vicinity of B_c and at the lowest measured temperature, a minor enhancement in λ_V exists, which is in very good conformity with the volume thermal expansion results. In order to set the behavior present in $PrIr_2Zn_{20}$ in relation to the one of a magnetic Kramers system, the longitudinal, transverse and volume magnetostriction coefficients of its magnetic counterpart $YbIr_2Zn_{20}$, which were calculated from $\Delta L/L$ data taken from Ref. [128], are shown additionally in Fig. 4.16(a). The significant difference between the volume magnetostriction coefficients of $PrIr_2Zn_{20}$ and $YbIr_2Zn_{20}$ becomes immediately evident. $YbIr_2Zn_{20}$ exhibits a strongly hybridized FL ground state [128] and

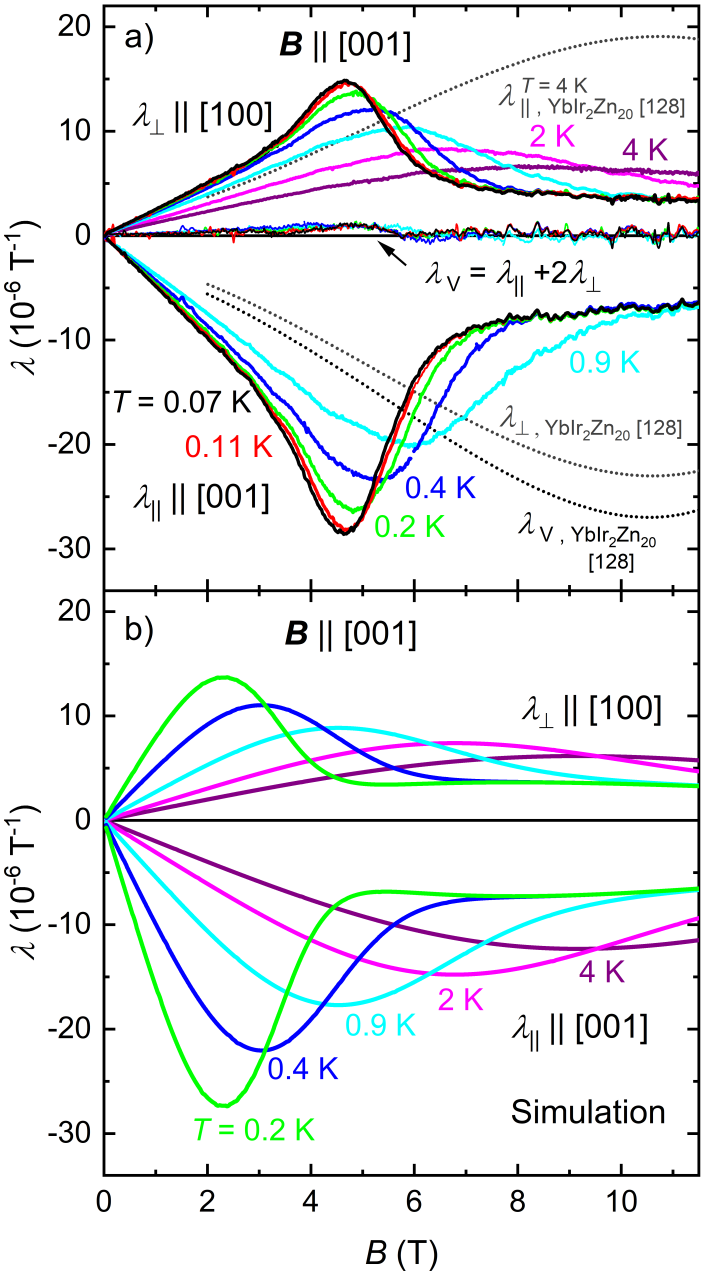

Figure 4.16: (a) Longitudinal and transverse magnetostriction coefficients $\lambda_{\parallel}$ and $\lambda_{\perp}$, together with the volume magnetostriction coefficient $\lambda_V = \lambda_{\parallel} + 2\lambda_{\perp}$ as a function of magnetic field $\boldsymbol{B} \parallel [001]$ at different temperatures. Note that the magnetostriction data is not corrected for the dilatometer background. The latter contribution can, however, be considered as very small in comparison to the shown data. In addition, $\lambda_{\parallel}$, $\lambda_{\perp}$ and λ_V of $YbIr_2Zn_{20}$ at $T = 4\,\mathrm{K}$, which were calculated from $\Delta L/L$ data taken from Ref. [128], are displayed. (b) CEF calculations of $\lambda_{\parallel}$ and $\lambda_{\perp}$ that employ the CEF parameters $W = -1.22\,\mathrm{K}$ and $x = 0.537$ [65], a Γ_3-type quadrupole-strain coupling constant $g_{\Gamma_3} = -38.0\,\mathrm{K}$, a Γ_3-type quadrupole-quadrupole interaction constant $K_{\Gamma_3} = -0.0067\,\mathrm{K}$ and an interaction constant between magnetic field induced dipole moments $K = -0.19\,\mathrm{K}$.
Adapted figure from Ref. [124].

its volume magnetostriction coefficient is at least one order of magnitude larger than the one of $PrIr_2Zn_{20}$. Takeuchi et al. [128] argue that the largely negative volume magnetostriction present in $YbIr_2Zn_{20}$ indicates that the valence of the material is altered from a non-magnetic Yb^{2+} towards a magnetic Yb^{3+} valence state upon the application of magnetic field. According to Eq. (2.9), which sets the volume magnetostriction in relation to the pressure dependence of magnetization, a negative volume magnetostriction indicates an increase of magnetization under hydrostatic pressure. As outlined in Section 2.1.3, the characteristically negative volume magnetostriction in Yb-based intermetallics originates from the fact that the valence state of a non-magnetic Yb^{2+} ion changes to the smaller and magnetic Yb^{3+} configuration under hydrostatic pressure. The fact that the volume magnetostriction coefficient of $PrIr_2Zn_{20}$ is insignificantly small as compared to the one of $YbIr_2Zn_{20}$ [128], reveals that the Pr^{3+} ion's valence state changes only marginally with magnetic field. At the same time, the finding indicates that the hydrostatic pressure dependence of the material's magnetization must be negligible small. This result is surprising as the Seebeck coefficient exhibits a prominent enhancement at around 5 T and the electrical resistivity displays FL behavior with an enhanced A coefficient, which implies the onset of hybridization effects for which a distinct volume change would be expected [28, 45, 46].

To better understand the experimental results, a CEF simulation was carried out by following the approach that was explicitly discussed in Section 4.2.2. In order to simulate the magnetic field dependence of the quadrupolar expectation values, the mean-field CEF program provided by T. Onimaru was employed. To recall the Hamiltonian that is evaluated by the mean-field program, it is referred to Eq. (4.12). Figure 4.16(b) shows the simulated $\lambda_{\parallel}$ and $\lambda_{\perp}$ data, whereby the same parameters that were used for the thermal expansion analysis were employed. These are the CEF parameters $W = -1.22\,\mathrm{K}$ and $x = 0.537$ [65], a quadrupole-strain coupling constant of $g_{\Gamma_3} = -38.0\,\mathrm{K}$, an interaction constant between the quadrupole moments with Γ_3 symmetry $K_{\Gamma_3} = -0.0067\,\mathrm{K}$ and an interaction constant between field induced dipole moments $K = -0.19\,\mathrm{K}$. At the highest measured temperature of 4 K, calculation and experiment agree well with each other, while pronounced discrepancies arise at low temperatures. At 0.2 K, for instance, the calculation predicts an extremum at around 2.3 T, while the experimentally determined extremum appears at a significantly higher magnetic field value of approximately 5 T. These stark differences between the simulated and experimentally obtained data clearly demonstrate that the low temperature behavior in the magnetostriction coefficient cannot be accounted for by a simple CEF effect. This conjecture is supported by the fact that B_c depends only weakly on temperature at 0.07 K and 0.11 K. As the value of B_c agrees well with the magnetic field values at which FL behavior in the electrical resistivity and a distinct maximum in the Seebeck coefficient and the specific heat were found [28, 45, 46], the extrema in the linear magnetostriction can be likely set in relation to the previous findings. Note that the relatively broad appearance of the low temperature extremum in the longitudinal and transverse magnetostriction coefficients would also be in line with the FH scenario proposed by Van Dyke et al. [102]. However, analogously to the thermal expansion, the magnetostriction results can only provide further indication of the possible emergence of FH order but no direct proof. Further measurements are therefore indispensable in order clarify the cause of the novel phase emerging at intermediate magnetic field.

Magnetostriction in Magnetic Fields $\boldsymbol{B} \parallel [110]$

After discussion of the magnetostriction results for $\boldsymbol{B} \parallel [001]$, the focus is now on the magnetostriction coefficient $\lambda_{[110]}$ measured parallel to magnetic field $\boldsymbol{B} \parallel [110]$. The re-

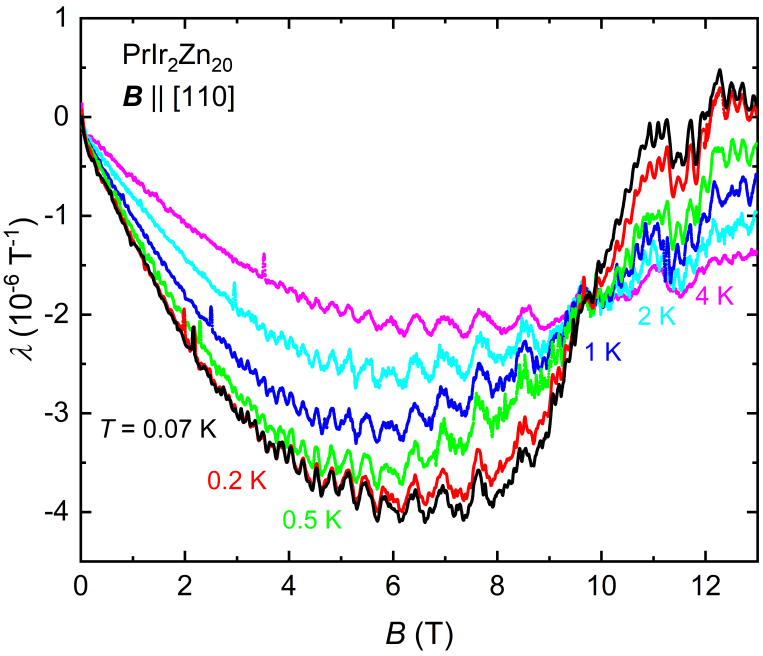

Figure 4.17: Longitudinal magnetostriction coefficient $\lambda_{[110]}$ as a function of magnetic field $\boldsymbol{B} \parallel [110]$ at different temperatures.

spective data at various temperatures is shown in Fig. 4.17. Analogously to $\lambda_{[001]}$, also $\lambda_{[110]}$ shows a negative value almost in the whole examined magnetic field range. Only the two data sets obtained at the lowest temperatures of 0.07 K and 0.11 K reveal a sign change from negative to positive at elevated magnetic field. Notably, the magnitude of $\lambda_{[110]}$ is by one order of magnitude reduced as compared to $\lambda_{[001]}$. At the lowest measured temperature of 0.07 K, a relatively broad minimum that peaks at around 7 T is present. The minimum position approximately coincides with the critical magnetic field value of the AFQ order, which was estimated based on the measurement of $\alpha_{[110]}$ to be in the range 6 T − 8 T. Increasing temperature has only very little impact on the minimum position but reduces the magnitude of $\lambda_{[110]}$ distinctly. Even though the low temperature minimum in $\lambda_{[110]}$ is much broader than the respective anomaly in $\lambda_{[001]}$, the temperature insensitivity of the minimum position at very low temperature is a common feature. By gradually increasing temperature, the shape of the minimum in $\lambda_{[110]}$ is slightly modified. The minimum position, however, shifts only marginally to lower temperature. At the highest measured temperatures of 2 K and 4 K, the minimum takes a rather broad shape. It is not surprising that the behaviors found in $\lambda_{[001]}$ and $\lambda_{[110]}$ are reminiscent of each other, as magnetic field applied along either of the two directions splits the ground state doublet. Furthermore, $\lambda_{[001]}$ and $\lambda_{[110]}$ directly measure the splitting of the ground state doublet, as both measurements depend linearly on the magnetic field derivative of the Γ_3-type symmetrized strain $\partial_B \varepsilon_\mathrm{u}$, which in turn shows proportionality to the respective quadrupolar expectation value $\partial_B \langle O_2^0 \rangle$. Since the splitting of the Γ_3 doublet is more pronounced for $\boldsymbol{B} \parallel [001]$ than for $\boldsymbol{B} \parallel [110]$, it is reasonable that the minimum position appears at a higher magnetic field value for the latter magnetic field orientation. Interestingly, all data sets contain distinct oscillations. These cannot be explained by conventional noise but assign to quantum oscillations, whereby an analysis of the related frequencies can be found in the appendix of this thesis.

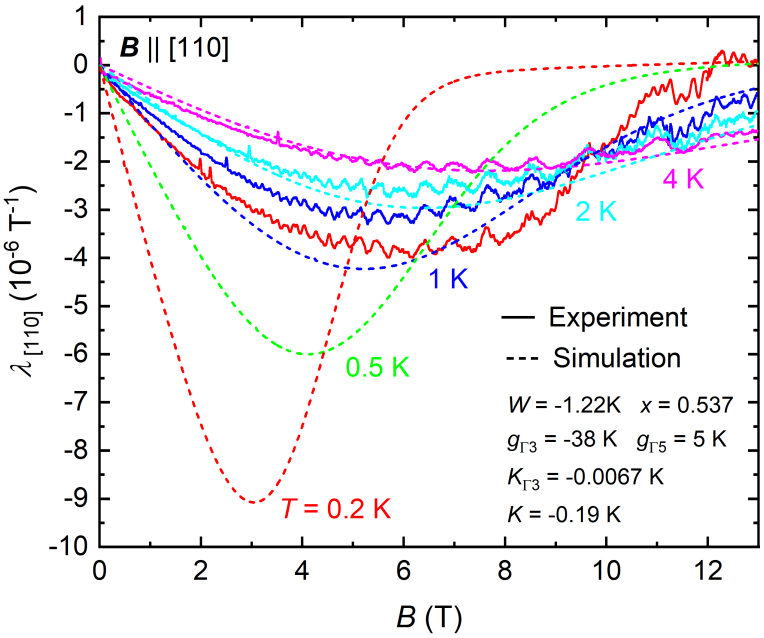

Figure 4.18: Magnetic field dependence of the simulated longitudinal magnetostriction $\lambda_{[110]}$ for $\boldsymbol{B} \parallel [110]$ as dashed lines together with the experimentally obtained data as solid lines at selected temperatures. For the simulation, the CEF parameters $W = -1.22\,\mathrm{K}$ and $x = 0.537$ [65], a Γ_3-type quadrupole-strain coupling constant $g_{\Gamma_3} = -38.0\,\mathrm{K}$, a Γ_5-type quadrupole-strain coupling constant $g_{\Gamma_5} = 5.0\,\mathrm{K}$, a quadrupole-quadrupole interaction constant $K_{\Gamma_3} = -0.0067\,\mathrm{K}$ and an interaction constant between excited dipoles $K = -0.19\,\mathrm{K}$ were used.

As Eq. (4.15) demonstrates, the magnetostriction coefficient $\lambda_{[110]} = \partial_B \varepsilon_{[110]}$ contains not only the Γ_3-type contribution $\varepsilon_\mathrm{u} \sim \langle O_2^0 \rangle$ but also a contribution that arises from $\varepsilon_{xy} \sim \langle O_{xy} \rangle$. While the quadrupole-strain coupling constant g_{Γ_3}, which quantifies the coupling between strain ε_u and the quadrupole moment $\langle O_2^0 \rangle$, was already specified in the preceding subsection, the CEF calculations discussed in the following furthermore revealed the quadrupole-strain coupling constant g_{Γ_5}, which quantifies the coupling between strain ε_{xy} and the quadrupole moment $\langle O_{xy} \rangle$. The respective Hamiltonian, which was evaluated by the mean-field CEF program provided by T. Onimaru, was already introduced by Eq. (4.14) in the preceding subsection. In this context, it was also elucidated that based on the $\alpha_{[110]}$ data, the deduction of the Γ_5-type quadrupole-strain coupling constant was not possible, as the applied magnetic field was not sufficient to drive the system into the fully localized state. By contrast, at a temperature of 4 K, the quadrupolar ground state appears to be in the fully localized state and fitting the CEF calculation to the measured data allowed for a precise determination of the Γ_5-type quadrupole-strain coupling constant. In order to derive the CEF magnetostriction, at first the contribution $\varepsilon_\mathrm{u} \sim \langle O_2^0 \rangle$ was calculated by using the parameters with Γ_3 symmetry provided in Section 4.2.2. The so simulated magnetostriction curve was then compared to the experimentally obtained data and the differences were attributed to the contribution ε_{xy} with Γ_5 symmetry. By adding the contribution of $\varepsilon_{xy} \sim \langle O_{xy} \rangle$ to the simulated data and varying the respective quadrupole-strain coupling constant g_{Γ_5}, it showed that a rather small value of $g_{\Gamma_5} = 5.0\,\mathrm{K}$ provided the best match between the experimentally determined and the simulated data. A possible volume contribution was again disregarded in the theoretical analysis. The fact

that the contribution ε_{xy} has the opposite sign as the contribution $-1/(2\sqrt{3})\varepsilon_{\mathrm{u}}$, explains the experimentally found sign change in $\lambda_{[110]}$ at low temperatures and at the highest measured magnetic field. This can be explained by the fact that the contribution ε_{xy} overcomes the contribution of ε_{u} at high magnetic field, which results in a sign change of $\lambda_{[110]}$. The CEF simulation results for $\lambda_{[110]}$ at different temperatures are shown in Fig. 4.18, whereby selected experimentally obtained data sets of $\lambda_{[110]}$ are shown for comparison. While at the highest measured temperatures of 2 K and 4 K, the simulated and the experimentally determined curves agree well with each other, the differences become stark as temperature is lowered. At 0.2 K, for instance, the simulation suggests a minimum at around 3 T, while the minimum in the respective measurement appears at a much higher magnetic field of 6.5 T. This is reminiscent of the behavior found in $\lambda_{[001]}$ and likely assigns to the unconventional phase that emerges close to the critical magnetic field of the AFQ ordered state. In vicinity of this yet unidentified state, both $\alpha_{[110]}$ and $\lambda_{[110]}$ display crossover like anomalies, which are somewhat broader in their appearance than the respective anomalies found in $\alpha_{[001]}$ and $\lambda_{[001]}$ at around 5 T. Nevertheless, the behavior present for both magnetic field directions is comparable and in both cases reminiscent of a crossover that may be related to the possible FH ordered phase [102]. As neither the thermal expansion nor the magnetostriction data could provide definite proof for the FH order scenario, further research is indispensable to correctly classify the unconventional behavior emerging at intermediate magnetic field. Future measurements of the electrical resistivity that examine the presence of FL behavior at around 6 T − 8 T for $\boldsymbol{B} \parallel [110]$ would be particularly insightful.

4.2.4 Phase Diagrams

On the basis of the just detailed thermal expansion and magnetostriction measurements, phase diagrams for $\boldsymbol{B} \parallel [001]$ and $\boldsymbol{B} \parallel [110]$ were constructed. Fig. 4.19 summarizes the results for $\boldsymbol{B} \parallel [001]$. The black circles denote the AFQ phase transition temperature T_{Q} deduced from the linear thermal expansion measurements. The green circles indicate the temperature of a plateau like feature T_{plat} found in the thermal expansion at small magnetic fields. With increasing magnetic field, this feature takes the shape of a clear maximum, whose peak value temperature T_{max} is indicated by red circles. At high magnetic fields $B \geq 8$ T, the latter can be well reproduced by a CEF calculation, which reveals its Schottky-type nature. At lower magnetic field, the maximum's shape is still reminiscent of a Schottky-type anomaly but slight deviations to the simulation point towards the onset of correlation effects. Quite significant deviations between the experimentally obtained and the simulated data sets are present for $B \leq 5$ T. A preceding study implied the emergence of a possible diagonal composite (hastatic) order at around 5 T [28]. Also the broad anomalies found in the linear thermal expansion and magnetostriction coefficient at around 5 T are in line with the theoretically proposed FH order scenario [102]. The intermediate field range is therefore denoted as FH ordered with a question mark put over, as further experiments are needed to clarify its nature. The blue squares correspond to anomalies found in the uniaxial magnetostriction coefficients. Here, the CEF calculations match well with the measured data obtained at temperatures in the Kelvin range, but cannot capture the behavior at low temperatures. Interestingly, at low temperatures the blue squares terminate into the possible FH ordered phase at around 5 T.

The measurement results obtained for $\boldsymbol{B} \parallel [110]$ are summarized in Fig. 4.20. Again, the black circles denote the phase transition temperature into the AFQ ordered state, as derived from the linear thermal expansion measurement. The grey circle corresponds to a kink like phase transition anomaly found in the linear thermal expansion coefficient,

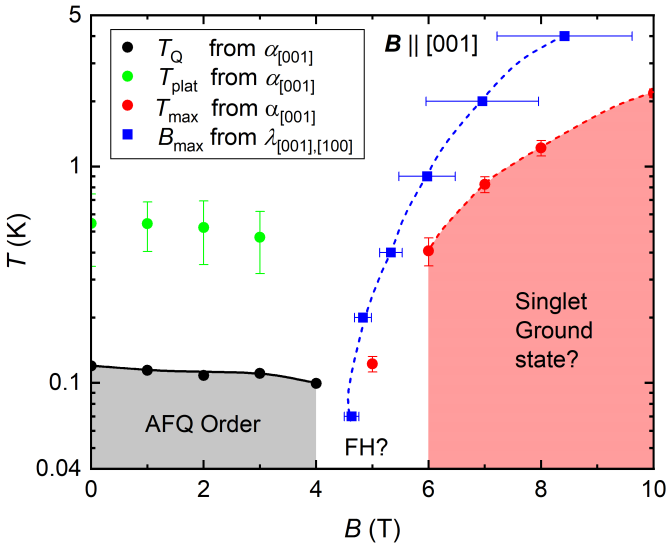

Figure 4.19: Phase diagram of $PrIr_2Zn_{20}$ for magnetic field $\boldsymbol{B} \parallel [001]$. Black circles denote the transition into the AFQ ordered state, as detected by the linear thermal expansion. Green circles correspond to a plateau like feature present in the linear thermal expansion coefficient at low magnetic field. Red circles denote a maximum found in the linear thermal expansion coefficient. Blue squares indicate the peak position of the extrema in the linear magnetostriction coefficients. Error bars quantify the uncertainty in the determination of the plotted temperature and magnetic field values.

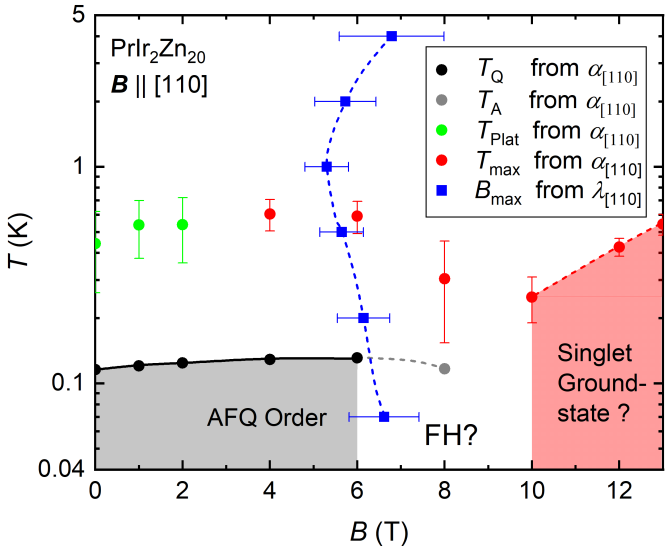

Figure 4.20: Phase diagram of $PrIr_2Zn_{20}$ for magnetic field $\boldsymbol{B} \parallel [110]$. Black circles indicate the phase transition into the AFQ ordered state, as suggested by the linear thermal expansion measurements. Green circles denote a plateau like feature and red circles a maximum found in the thermal expansion coefficient. Blue squares mark the minimum position in the linear magnetostriction coefficient. Error bars quantify the uncertainty, which comes along with the determination of the respective temperature and magnetic field values.

whose appearance is distinct from the phase transition anomalies found for $B \leq 6\,\mathrm{T}$. The green circles indicate the temperature of a plateau like feature T_{plat} in the linear thermal expansion coefficient at low magnetic field, which changes into a maximum with increasing magnetic field. The peak temperature of the maximum T_{max} is indicated by red circles. At the highest measured magnetic fields, the maximum reminds on a Schottky-type anomaly. The fact that the maximum peaks at a lower temperature than the corresponding CEF calculation, implies that remaining correlations are still present. The blue squares denote the minimum found in the linear magnetostriction coefficient. Similar to the behavior observed for $\boldsymbol{B} \parallel [001]$, the blue squares terminate close to the critical field of AFQ order.

Generally, both phase diagrams show very similar behavior. The main difference is that the phase boundary of the AFQ order is increased for $\boldsymbol{B} \parallel [110]$ as compared to $\boldsymbol{B} \parallel [001]$, which is reasoned in the weaker splitting of the Γ_3 ground state doublet for $\boldsymbol{B} \parallel [110]$ than for $\boldsymbol{B} \parallel [001]$. As the splitting of the ground state doublet is the main perturbation that counteracts the low temperature AFQ order, the obtained results are in good agreement with the theoretical expectation.

4.2.5 Summary

This section covered thermal expansion and magnetostriction measurement results obtained on single crystalline $PrIr_2Zn_{20}$ for magnetic fields $\boldsymbol{B} \parallel [001]$ and $\boldsymbol{B} \parallel [110]$. In the following, the key findings are briefly recalled.

- The zero field thermal expansion coefficient of $PrIr_2Zn_{20}$ measured along three different crystallographic directions $\alpha_{[001]}$, $\alpha_{[110]}$ and $\alpha_{[111]}$ is anisotropic, which is at odds with the theoretically expected isotropic thermal expansion of a cubic material. This indicates that the small uniaxial stress exerted by the dilatometer's flat springs is sufficient to break the material's cubic symmetry, which induces the $\langle O_2^0 \rangle$ quadrupole moment and therefore an additional contribution to $\alpha_{[001]}$ and $\alpha_{[110]}$. A peculiarity is that $\alpha_{[111]}$ is smaller in magnitude than $\alpha_{[001]}$ but larger than $\alpha_{[110]}$. As no linear coupling between strain $\varepsilon_{[111]}$ and the quadrupolar ground state moments with Γ_3 symmetry exists, a stress induced contribution for the measurement of $\alpha_{[111]}$ is not expected. As a possible cause for the enhancement of $\alpha_{[111]}$, the softening found in the c_{44} elastic constant by Ishii et al. [37] has to be mentioned. Another possible reason is that the measurement of $\alpha_{[111]}$ was carried out on a different piece of single crystal than the piece on which $\alpha_{[001]}$ and $\alpha_{[110]}$ were measured. Both pieces originated, however, from the same batch.

- To probe the response of the quadrupolar ground state to magnetic field, longitudinal and transverse thermal expansion as well as magnetostriction measurements were carried out for $\boldsymbol{B} \parallel [001]$. The experimental findings revealed that both thermodynamic probes display a significant uniaxial anisotropy. CEF calculations demonstrated that this behavior is caused by the field induced $\langle O_2^0 \rangle$ quadrupole moment, which manifests itself in a tetragonal distortion of the material. For $B \geq 8\,\mathrm{T}$, very good conformity between the experimentally obtained data and the CEF simulation proofed the fully localized nature of the Γ_3-type quadrupole moments at high magnetic fields. At a relatively high temperature of 4 K, also the experimentally determined magnetostriction coefficient agrees well with the simulated data. By contrast, close to the critical magnetic field of AFQ order at around 5 T and at low temperature, both the linear thermal expansion and the magnetostriction coefficients exhibit prominent extrema that cannot be taken account of by the simulation.

This anomalous behavior agrees well with the previously reported maxima in the specific heat [28] and the Seebeck coefficient [45, 46], which coincide with FL behavior in the electrical resistivity [28]. In particular the latter finding was interpreted as a signature of a possible FH order [101, 102], also referred to as F-channel diagonal composite order [99, 100]. Theoretical calculations by Van Dyke et al. [102] implied that in magnetic field $\boldsymbol{B} \parallel [001]$, the onset of FH order manifests itself in a crossover like anomaly in the longitudinal thermal expansion and magnetostriction coefficients, while a clear phase transition signature would only be expected in zero magnetic field. Indeed, the anomalies found in the thermal expansion and the magnetostriction coefficients are indicative of a crossover, which matches well with the prediction by Van Dyke et al. [102]. While this experimental finding provides further indication of the FH scenario, it cannot proof its actual existence. At low magnetic fields $B \leq 4\,\mathrm{T}$, the uniaxial thermal expansion coefficient displays a discontinuity that is in good conformity with the previously reported phase transition into the AFQ ordered state at $T_\mathrm{Q} = 0.11\,\mathrm{K}$ [27]. Surprisingly, in presence of a moderate magnetic field $B \leq 4\,\mathrm{T}$, the uniaxial thermal expansion coefficient diverges below T_Q. Thermodynamically, this peculiarity may relate to a small amount of largely pressure dependent entropy that is not released by the AFQ order. Indeed, specific heat measurements by Onimaru et al. [28] indicated an enhancement of the low temperature entropy in a comparable magnetic field range. At this moment, the origin for the unexpected divergence in the linear thermal expansion coefficient cannot be specified and complementary experiments are needed to clarify its nature. To further scrutinize the unconventional state at 5 T, the volume thermal expansion and magnetostriction coefficients were considered. In the whole examined magnetic field and temperature range, the volume changes are significantly smaller than the linear changes. Only very little enhancement of the volume thermal expansion and magnetostriction coefficient is present at around 5 T, which is at odds with a strongly hybridized state as implied by Seebeck coefficient measurements [45, 46]. In addition, comparison with the volume magnetostriction of the sister compound compound $YbIr_2Zn_{20}$, measured by Takeuchi et al. [128], demonstrated that the field induced volume changes are distinctly small in $PrIr_2Zn_{20}$. This suggests that the valence state of the non-Kramers Pr^{3+} ion is only marginally altered by the variation of magnetic field, which is distinct to the mixed-valent Kramers $Yb^{2+/3+}$ ion of the sister compound. The tiny volume magnetostriction also implies that the magnetization of $PrIr_2Zn_{20}$ varies only weakly upon the application of hydrostatic pressure.

- Measurements of the longitudinal thermal expansion and magnetostriction coefficients for $\boldsymbol{B} \parallel [110]$ revealed qualitatively comparable behavior to the results obtained for $\boldsymbol{B} \parallel [001]$. As the splitting of the Γ_3 ground state doublet for magnetic field $\boldsymbol{B} \parallel [110]$ is weaker than for $\boldsymbol{B} \parallel [001]$, AFQ order persists up to higher magnetic fields in the range $6\,\mathrm{T} - 8\,\mathrm{T}$. The longitudinal thermal expansion and magnetostriction coefficients for $\boldsymbol{B} \parallel [110]$ are approximately one order of magnitude smaller than the respective longitudinal coefficients obtained for $\boldsymbol{B} \parallel [001]$. At low magnetic field $\boldsymbol{B} \parallel [110]$, the longitudinal thermal expansion coefficient shows a divergence inside the AFQ ordered state and therefore reassembles the behavior found for $\boldsymbol{B} \parallel [001]$. Close to the critical magnetic field of the AFQ ordered state, the thermal expansion coefficient exhibits a characteristic low temperature maximum. Further increase of magnetic field continuously shifts the maximum to higher temperature, which is reminiscent of a Schottky-type anomaly. Differences between the measured data

and the simulated curves persist up to the highest applied magnetic field of 13 T, which suggests that correlation effects are still present. At the lowest measured temperature of 0.07 K, $\lambda_{[110]}$ shows a relatively broad minimum, which coincides with the critical field of AFQ order determined by the thermal expansion measurement. Similar to the thermal expansion coefficient, the low temperature magnetostriction could not be reproduced by the CEF simulation. Very good agreement between the experimentally determined and simulated magnetostriction curves is only present at a temperature of 4 K. In analogy to the measurement for $\boldsymbol{B} \parallel [001]$, also for $\boldsymbol{B} \parallel [110]$ unconventional behavior was found at magnetic field values just above the phase boundary line of the AFQ ordered state. To obtain further information on a possible relation to FH order, measurements of the specific heat and the electrical resistivity would be essential in order further clarify the nature of this unconventional phase emerging at intermediate magnetic field.

Chapter 5

$Y_{1-x}Pr_xIr_2Zn_{20}$

The observation of NFL behavior in $PrIr_2Zn_{20}$ by Onimaru et al. [28] and its successful description by a two-channel Anderson lattice model [40] called for more detailed studies on the system. It is thereby of particular interest to drive the quadrupolar Kondo lattice $PrIr_2Zn_{20}$ towards a possible single-impurity quadrupolar Kondo ground state by systematically substituting the Pr^{3+} ions with a total angular momentum of $J = 4$ by Y^{3+} ions with $J = 0$ [42, 43]. This unconventional state of matter is distinguished by NFL behaviors[1] emerging in the specific heat $C/T \sim \ln 1/T$ [16–18], electrical resistivity $\rho \sim 1 + c\sqrt{T}$ [41] and quadrupole-strain susceptibility $\chi_Q \sim \ln 1/T$ [16–18]. Another fascinating aspect is the theoretically expected residual entropy of $S = 1/2R \ln 2$ [17].

Recently, Yamane et al. [42, 43] found experimental indication for the single-impurity quadrupole Kondo effect in the specific heat and electrical resistivity of highly diluted single crystalline $Y_{1-x}Pr_xIr_2Zn_{20}$ with $x \leq 0.044$. Corroborative evidence for the formation of this exotic state was provided by Yanagisawa et al. [44], who reported a logarithmic temperature dependence of the quadrupole-strain susceptibility measured on a single crystal with a Pr concentration of $x = 0.034$. With reference to these experimental findings, highly diluted $Y_{1-x}Pr_xIr_2Zn_{20}$ can be considered as a prototype material to explore single-impurity quadrupole Kondo physics.

Historically, mainly diluted U-based materials, which include, for instance, the systems $U_xTh_{1-x}Ru_2Si_2$ [23, 24] and $U_xTh_{1-x}Be_{13}$ [19, 20], have been subject to extensive study due to emergent NFL behaviors, which were attributed to the quadrupole Kondo effect. Yet, clear proof for this scenario has not been found. A key issue with the U-based materials is the ambiguity in the specification of the CEF excitations, as the 5f electrons are rather delocalized and hybridize substantially with conduction electrons.

5.1 Physical Properties Review

Based on the currently available literature, this section provides an overview of the physical properties of single crystalline $Y_{1-x}Pr_xIr_2Zn_{20}$ ($x \leq 0.44$). Initially, the crystal structure, the ground state and the influence of local lattice distortions are reviewed [42, 43]. Subsequently, the NFL behaviors emerging in the specific heat [42, 43, 94] and the electrical resistivity [42, 43] as well as the renormalization of the $(c_{11} - c_{12})/2$ elastic constant [44], indicative of the single-impurity quadrupole Kondo effect, are detailed.

[1] These scaling equations are a special case of the overcompensated multichannel Kondo model, with $S = 1/2$ and $n = 2$, which was originally proposed by Nozières and Blandin [15].

5.1.1 Crystal Structure and Ground State

At room temperature, $Y_{1-x}Pr_xIr_2Zn_{20}$ ($x \leq 0.44$) exhibits a $CeCr_2Al_{20}$ crystal structure ($Fd\bar{3}m$ space group) [43], with a cubic T_d point group symmetry at the Pr sites[2]. Neither the specific heat nor the electrical resistivity give an indication of a structural phase transition down to temperatures of 3 K, below which characteristic NFL behavior emerges [43]. This suggests that the point group at the Pr sites is not altered from cubic T_d, which is a key prerequisite for the formation of the non-Kramers Γ_3 ground state doublet [43]. By contrast, a La substitution proved to be unsuitable to study single-impurity quadrupole Kondo behavior, as $LaIr_2Zn_{20}$ exhibits a structural phase transition at $T = 200$ K [97].

To confirm the Γ_3 ground state doublet of $Y_{1-x}Pr_xIr_2Zn_{20}$ ($x \leq 0.44$), Yamane et al. [42, 43] took account of the Schottky anomaly in the specific heat at approximately 10 K, which relates to the energy scale between the ground and the first excited state. A doublet-triplet model, which simulates the specific heat arising from an energy gap of $\Delta = 30$K between the Γ_3 ground state doublet and the first excited Γ_4 triplet state, indeed explains the experimentally found low temperature Schottky maximum very well [42, 43]. This result provides strong indication that the ground state of $Y_{1-x}Pr_xIr_2Zn_{20}$ ($x \leq 0.44$) is in fact a non-Kramers Γ_3 doublet and thus identical to the one of pure $PrIr_2Zn_{20}$ [42,43]. A characteristic Curie-type $1/T$ softening of the $(c_{11} - c_{12})/2$ elastic constant for $T < 2$ K, reported for a highly diluted sample with $x = 0.034$, strongly supports this conclusion [44]. By now, elastic constant measurements on single crystals with higher Pr doping have not been reported in literature.

Despite the absence of a structural phase transition and the clear indication of the Γ_3 ground state, local lattice distortions [42, 43], which arise due to the different ionic radii of the Y^{3+} and Pr^{3+} ion, are inevitable. This effect has to be considered carefully, as the degeneracy of the non-Kramers Γ_3 ground state is easily lifted by local strain fields that are induced by the substitution. Theoretically, the magnitude of these local lattice distortions has to correlate with the Pr impurity concentration as outlined in the following. In the dilute limit, the $8a$ sites adjacent to a Pr impurity site are primarily occupied by Y^{3+} ions and approximate preservation of the cubic T_d point group symmetry at a Pr impurity site is expected. On the other hand, substantial local lattice distortions, which possibly alter the local point group at a Pr site, are anticipated when half of the Y^{3+} ions are substituted by Pr^{3+} ions. In this case, the disorder around a Pr impurity site is the largest possible. Experimentally, the disorder effect becomes particularly evident when considering the RRR as a function of the Pr impurity concentration. While the host metal YIr_2Zn_{20} exhibits a very high RRR of 500 [43], the RRR of the Pr substituted samples is reduced rapidly with increasing Pr concentration due to enhanced electron-impurity scattering [43]. A single crystal with a Pr concentration of $x = 0.036$, for instance, only shows a RRR of 160 [129]. This value is further reduced to a RRR of 50 in case of a single crystal with $x = 0.085$ [43] and to a RRR of 8 for a single crystal with $x = 0.44$ [43].

5.1.2 Single-Impurity Quadrupole Kondo Effect

First indication for the appearance of the single-impurity quadrupole Kondo effect in $Y_{1-x}Pr_xIr_2Zn_{20}$ was reported by Yamane et al. [42,43], who studied the zero field specific heat and electrical resistivity of the material. Their findings suggest that the single-impurity quadrupole Kondo effect forms exclusively in highly diluted single crystals with

[2] This conclusion is based on conventional room temperature powder x-ray measurements [42,43]. High-resolution low temperature synchrotron measurements, by which tiny substitution induced local lattice distortions and a possible symmetry lowering are detectable, have not been reported yet.

$x \leq 0.044$, for which the specific heat and the electrical resistivity show unconventional temperature dependencies in accordance with the theoretically predicted NFL behavior for a single-impurity quadrupole Kondo hybridization [42,43]. Shortly afterwards, Yanagisawa et al. [44] presented their results on the elastic constant $(c_{11} - c_{12})/2$, which is a crucial thermodynamic probe to ascertain the quadrupole Kondo effect, as it is a direct measure of the Γ_3-type quadrupole susceptibility. Their finding of a logarithmic temperature dependence of the zero magnetic field $(c_{11} - c_{12})/2$ elastic constant agrees well with the theoretical prediction and provides further evidence for the single-impurity quadrupole Kondo scenario [44]. Both, the specific heat [94] and the elastic constant [44] of the highly diluted samples with $x \leq 0.044$ were also investigated in magnetic field, which splits not only the ground state doublet[3] but also the conduction bands and acts therefore as a major perturbation for the quadrupolar Kondo effect. The studies revealed that the NFL behaviors present in both thermodynamic quantities react indeed sensitively upon the application of magnetic field, which is in excellent agreement with the theoretical expectation [44,94]. In the following, the results from literature are briefly reviewed.

Behavior in Zero Magnetic Field

To start with, the focus is on the zero field specific heat and electrical resistivity results reported by Yamane et al. [42,43]. The zero field 4f specific heat over temperature C_m/T normalized to Pr mol as a function of temperature for differently doped $Y_{1-x}Pr_xIr_2Zn_{20}$ single crystals with $x \leq 0.44$ is shown in Fig. 5.1(a) [42]. For samples with a very low Pr doping $x \leq 0.044$, C_m/T diverges logarithmically as temperature declines, which is in consistence with a single-impurity quadrupole Kondo effect [42]. By contrast, single crystals with a higher Pr concentration $x \geq 0.085$ do not show divergent behavior but saturation in C_m/T at low temperatures, indicating the breakdown of the single-impurity quadrupole Kondo effect, which is likely caused by either disorder induced static strain fields or short range quadrupolar correlations [42].

As the single-impurity quadrupole Kondo effect relates to an anomalous residual entropy [17], analysis of the latter quantity is of high relevance. Figure 5.1(b) illustrates the 4f contribution to the entropy S_m normalized to Pr mol as a function of temperature for various doping x [42]. The three different horizontal black dashed lines represent entropy values that play a crucial role in the quadrupole Kondo model. The value of $S = R\ln 2$ corresponds to the entropy of the two-fold degenerated Γ_3 ground state. Theory suggests that this ground state entropy is only partially released by the quadrupole Kondo effect, resulting in a finite residual entropy value of $S = 1/2R\ln 2$ [17]. The black dashed line, located at the entropy value of $S = 3/4R\ln 2$ [18, 121], marks the characteristic single-impurity quadrupole Kondo temperature T_0 [42]. T_0 is specified by an arrow for each Pr concentration x and its evolution with x is illustrated in the inset of Fig. 5.1(b) [42]. The entropy data by Yamane et al. [42] clearly demonstrates that none of the investigated single crystals exhibits the theoretically expected residual entropy plateau at $S = 1/2R\ln 2$. It is notable, however, that the highly diluted single crystals with $x \leq 0.044$ display a substantial entropy at the lowest temperature of $T = 0.08\,\mathrm{K}$, which is gradually suppressed as the Pr concentration x is increased [42]. In case of the single crystals with $x \geq 0.085$, the absence of the residual entropy is not surprising, as also C_m/T displays deviations from the expected quadrupole Kondo behavior [42]. A plausible explanation for the breakdown

[3] An isolated quadrupolar non-Kramers doublet would not split in magnetic field. However, in $Y_{1-x}Pr_xIr_2Zn_{20}$, one of the Γ_3 ground state wave functions mixes with one of the first excited Γ_4 triplet state's wave functions, resulting in a quadratic splitting of the non-Kramers doublet in a magnetic field $\boldsymbol{B} \parallel [001]$. For details, see Section 4.1.2.

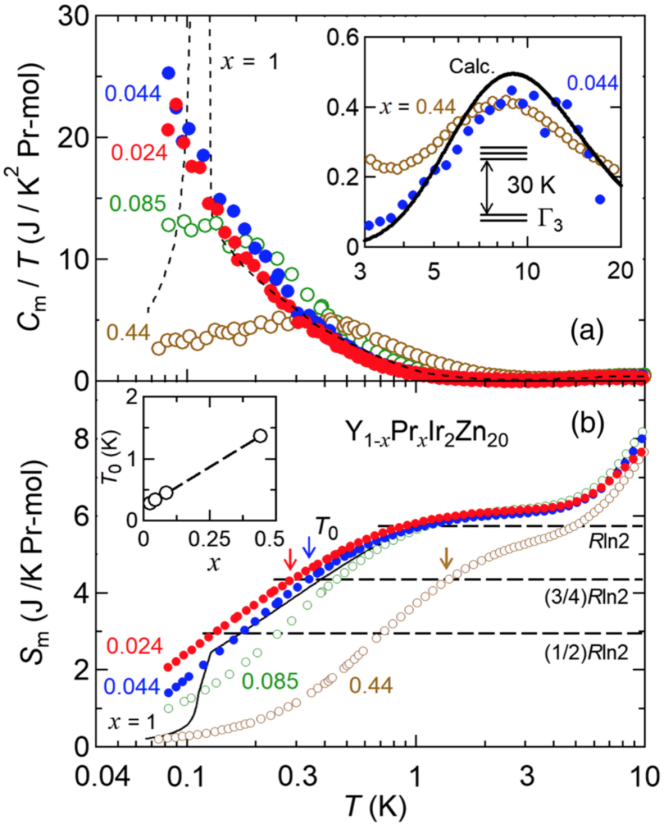

Figure 5.1: (a) Zero field 4f specific heat over temperature C_m/T normalized to Pr mol as function of temperature of various $Y_{1-x}Pr_xIr_2Zn_{20}$ ($x \leq 0.44$) single crystals and $PrIr_2Zn_{20}$ [27] as a dashed black line. The inset provides a comparison between the experimentally observed Schottky maximum at elevated temperature and a doublet-triplet model simulation. (b) Zero field 4f contribution to the entropy S_m normalized to Pr mol as a function of temperature of $Y_{1-x}Pr_xIr_2Zn_{20}$ ($x \leq 0.44$) and $PrIr_2Zn_{20}$ [28] as a black solid line. The characteristic temperature T_0, given by $S_m = 3/4R\ln 2$, is marked by an arrow for each Pr concentration x. Its evolution with x is shown in the inset. [42] Reprinted figure with permission from Ref. [42]. ©2018 by the American Physical Society.

of the NFL behavior are disorder induced local static strain fields that split the Γ_3 ground state doublet and therefore quench the residual quadrupole Kondo entropy [42]. In addition, the moderate Pr concentration might already induce short range quadrupolar correlations that counteract the quadrupole Kondo physics at low temperature [42]. By contrast, the absence of a residual entropy of $S = 1/2R\ln 2$ in the single crystals with $x \leq 0.044$ is unexpected, as a clear logarithmic temperature dependence was found in C_m/T [42]. However, also for small doping, a tiny substitution induced distortion of the crystal lattice, which results in a quenching of the ground state entropy, cannot be excluded [42]. Yamane et al. [42] argue that also the hyperfine interaction arising between the quadrupolar ground state and the atomic nucleus of the ^{141}Pr may account for the deviations from the theoretically predicted residual entropy. Moreover, a recent theoretical study by Tsuruta et al. [130] suggested that a significantly higher Pr dilution of order of magnitude 10^{-6} would be required to reach a single-impurity quadrupole Kondo ground state. It is

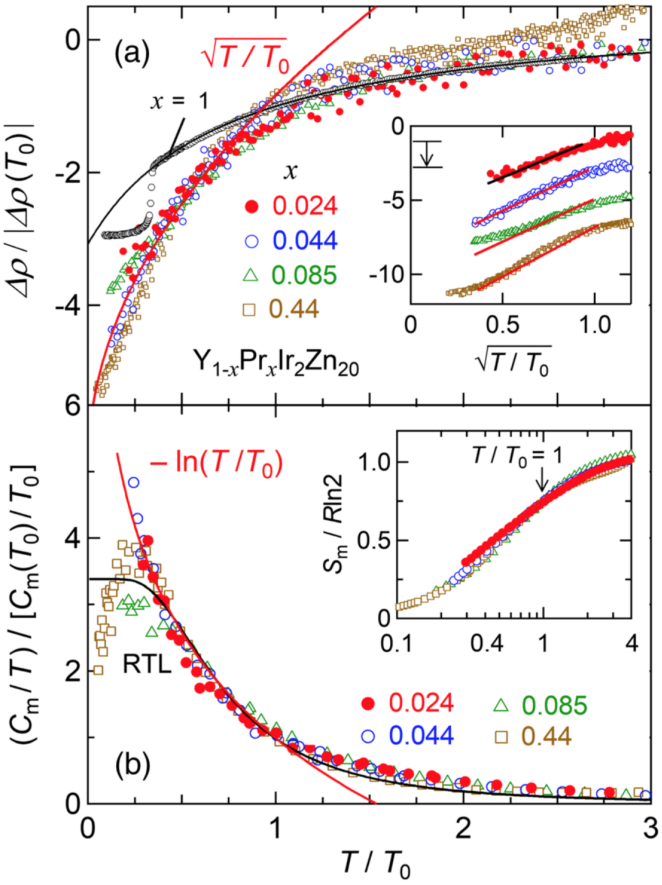

Figure 5.2: (a) Differential electrical resistivity normalized to its value at the characteristic temperature $\Delta\rho/|\Delta\rho(T_0)|$ versus T/T_0 for variously doped $Y_{1-x}Pr_xIr_2Zn_{20}$ single crystals with $x \leq 0.44$. The additionally shown red and black solid line are fits by the single-impurity quadrupole Kondo [121] and quadrupole Kondo lattice model [40, 131], respectively. The inset displays $\Delta\rho/|\Delta\rho(T_0)|$ versus $\sqrt{T/T_0}$. (b) 4f specific heat over temperature normalized to its value at the characteristic temperature $(C_m/T)/[C_m(T_0)/T_0]$ versus T/T_0 for differently doped $Y_{1-x}Pr_xIr_2Zn_{20}$ single crystals with $x \leq 0.44$. The red and black solid line are fits by the single-impurity quadrupole Kondo [121] and random two level model (RTL) [132, 133], respectively. The inset displays a scaling plot of the 4f entropy normalized to $R\ln 2$ versus T/T_0. [42]
Reprinted figure with permission from Ref. [42]. ©2018 by the American Physical Society.

thus conceivable that despite the very small Pr doping of $x = 0.024$ achieved by Yamane et al. [42], a tiny interaction between the quadrupole moments is still present that may account for the release of entropy in the highly diluted single crystals. Given that single-impurity quadrupole Kondo correlations exist, an universal scaling of the just discussed thermodynamic quantities with respect to the characteristic single-impurity quadrupole Kondo temperature T_0 is expected. Figure 5.2(b) by Yamane et. al. [42] illustrates such a scaling plot. Here, for $Y_{1-x}Pr_xIr_2Zn_{20}$ with $x \leq 0.44$, C_m/T normalized to its value at the characteristic temperature is plotted versus T/T_0 [42]. Indeed, for $T/T_0 > 0.5$, a scaling of the measured data is possible, which indicates universal behavior at elevated

temperatures, while at lower temperature clear deviations arise [42]. Yamane et al. [42] additionally show the theoretically expected single-impurity quadrupole Kondo behavior [121] as a red solid line, which is only in accordance with the data for $x \leq 0.044$. To verify a possible link between the low temperature deviations that arise in the moderately doped single crystals with $x \geq 0.085$ and disorder, Yamane et al. [42] simulated the effect of a distortion induced splitting of the Γ_3 doublet on C_m/T by employing a random two level (RTL) model [132,133]. The calculated specific heat resulting from a small splitting of $\Delta_{\Gamma_3} = 1.2\,K$, shown as a black solid line in Fig. 5.2(b), is in good accordance with the experimentally obtained specific heat of the single crystal with $x = 0.085$ [42]. By contrast, for the single crystal with $x = 0.44$, the RTL simulation, as shown in Ref. [43], describes the experimental data only to some extent. While the RTL model suggests saturation in C_m/T at low temperature, the experimental data displays a maximum, which implies the onset of short range quadrupolar correlations [42,43]. This finding by Yamane et al. [42,43] is conceivable as a Pr concentration of $x = 0.44$ is relatively high and the interaction between the quadrupole moments likely not negligible. The inset of Fig. 5.2(b) shows a scaling plot of the entropy normalized to $R\ln 2$ as a function of T/T_0, which confirms that also the entropy is governed by universal behavior [42].

Another crucial probe to detect single-impurity quadrupole Kondo behavior is the electrical resistivity, for which theory predicts an anomalous square root temperature dependence [41]. Yamane et al. [42] also performed electrical resistivity measurements, which provide further evidence for the single-impurity quadrupole Kondo scenario. Figure 5.2(a) illustrates the differential electrical resistivity of $Y_{1-x}Pr_xIr_2Zn_{20}$ ($x \leq 0.44$) normalized to its value at the characteristic temperature versus T/T_0 [42]. Just like the specific heat, also the electrical resistivity of the differently substituted single crystals of $Y_{1-x}Pr_xIr_2Zn_{20}$ can be nicely scaled by T_0, whereby deviations for higher doping with $x \geq 0.085$ at low temperature are less pronounced as compared to C_m/T [42]. The inset of Fig. 5.2(a), which shows the normalized differential electrical resistivity as a function of $\sqrt{T/T_0}$, highlights the low temperature deviations found in the moderately diluted samples with $x \geq 0.085$ [42]. This plot emphasizes that the anomalous $\sqrt{T}$ dependence found in the highly diluted single crystals with $x \leq 0.044$ is present in the whole examined temperature range, while for the higher doped single crystals with $x \geq 0.085$, discrepancies to the theoretically expected behavior become apparent at low temperature [42]. An interesting finding of the study by Yamane et al. [42] is the fact that the sign of the electrical resistivity is reversed as compared to the theoretically expected sign for the limit of weak coupling. Yamane et al. [42] point out that the found positive sign is predicted for the strong coupling limit and refer to a work by Affleck [93]. In summary, the specific heat and electrical resistivity results by Yamane et al. [42,43] suggest that the single-impurity quadrupole Kondo effect is present in highly diluted $Y_{1-x}Pr_xIr_2Zn_{20}$ with $x \leq 0.044$. By increasing the Pr concentration, the behavior is readily suppressed due to either a random splitting of the Γ_3 ground state doublet or short range quadrupolar correlations [42,43].

Besides the specific heat and the electrical resistivity, the quadrupole-strain susceptibility is the third key probe to identify a single-impurity quadrupole Kondo state. As explicitly discussed in the theory section of this thesis, the Γ_3-type quadrupole-strain susceptibility χ_Q can be experimentally determined via the measurement of the related $(c_{11} - c_{12})/2$ elastic constant. This was done by Yanagisawa et al. [44] who investigated a highly diluted $Y_{1-x}Pr_xIr_2Zn_{20}$ single crystal with $x = 0.034$ by means of the ultrasound technique and revealed a logarithmic variation of the $(c_{11} - c_{12})/2$ elastic constant with temperature for $T \leq 0.3\,K$, as shown in Fig. 5.5 of the following subsubsection [44]. This result is in perfect accordance with the measurements by Yamane et al. [42,43],

which provides quite strong evidence for the formation of the single-impurity quadrupole Kondo effect in highly diluted $Y_{1-x}Pr_xIr_2Zn_{20}$. Elastic constant results on higher doped single crystals have not yet been reported in literature and a comparison with the just discussed specific heat and electrical resistivity data [42, 43], which suggest breakdown of the single-impurity quadrupole Kondo effect for $x \geq 0.085$, is therefore not possible.

While the application of an uniaxial stress with Γ_3 symmetry, i.e. an uniaxial stress along the [001] direction, would be due to the linear coupling between the induced strain and the Γ_3 ground state doublet the most natural choice to perturb a quadrupolar Kondo metal and tune it away from the single-impurity quadrupole Kondo fixed point, such experiments are quite tricky to realize. As magnetic field applied along the [001] direction splits the ground state quadratically, it is expected to have a similar effect and is therefore another possible means to study the expected breakdown of the NFL behavior in detail. Specific heat [94] and elastic constant [44] literature results that deal with the magnetic field induced destruction of the single-impurity quadrupole Kondo ground state in $Y_{1-x}Pr_xIr_2Zn_{20}$ with $x \leq 0.044$ are reviewed in the following subsubsection.

Behavior in Magnetic Field

The impact of magnetic field applied along the [100] direction on the NFL behavior arising in highly diluted $Y_{1-x}Pr_xIr_2Zn_{20}$ was studied by Yamane et al. [94] via specific heat measurements on a single crystal with $x = 0.044$ and by Yanagisawa et al. [44] via elastic constant measurements on a single crystal with $x = 0.034$.

Figure 5.3 shows the 4f specific heat over temperature C_{4f}/T normalized to Pr mol as a function of temperature for different magnetic fields $B \leq 12\,\mathrm{T}$ [94]. For small magnetic fields $B \leq 2\,\mathrm{T}$, C_{4f}/T diverges logarithmically, which is indicative of the single-impurity quadrupole Kondo effect [94]. With increasing magnetic field, the divergence in C_{4f}/T is suddenly suppressed and a maximum forms instead [94]. The inset of Fig. 5.3 shows the 4f specific heat C_{4f} as a function of temperature for various magnetic fields $B \leq 12\,\mathrm{T}$ [94]. At low magnetic fields $B \leq 2\,\mathrm{T}$, the C_{4f} data by Yamane et al. [94] shows a

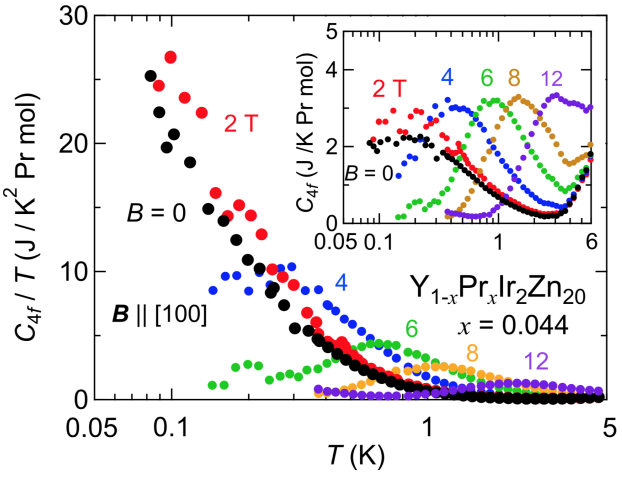

Figure 5.3: Temperature dependence of the 4f specific heat over temperature C_{4f}/T of $Y_{1-x}Pr_xIr_2Zn_{20}$ with $x = 0.044$ at various magnetic fields $\boldsymbol{B} \parallel [100]$. C_{4f} as a function of temperature at different magnetic fields in the inset. [94]
Reprinted figure from Ref. [94], which is licensed under a Creative Commons Attribution (CC BY) license. ©2018 Author(s).

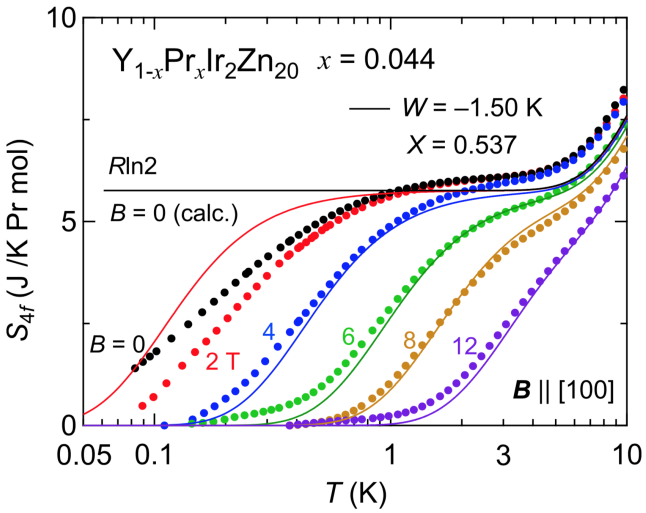

Figure 5.4: Temperature dependence of the 4f entropy S_{4f} of $Y_{1-x}Pr_xIr_2Zn_{20}$ with $x = 0.044$ at different magnetic fields $\boldsymbol{B} \parallel [100]$. CEF simulations of S_{4f} as a function of temperature at different magnetic fields are additionally shown as solid lines. [94]
Reprinted figure from Ref. [94], which is licensed under a Creative Commons Attribution (CC BY) license. ©2018 Author(s).

maximum at approximately 0.2 K, which continuously relocates to a higher temperature value with magnetic field. The maxima present at elevated magnetic field correspond to Schottky anomalies, which arise from the quadratic splitting of the ground state doublet in magnetic field, as Yamane et al. [94] confirmed by a careful analysis of the entropy in magnetic field. Figure 5.4 shows the temperature variation of the 4f entropy normalized to Pr mol at different magnetic fields $B \leq 12$ T and a CEF simulation for comparison [94]. For the simulation Yamane et al. [94] employed a slightly altered CEF parameter of $W = -1.50$ K as compared to $W = -1.22$ K [65], determined for $PrIr_2Zn_{20}$ by inelastic neutron scattering. This discrepancy possibly originates from a tiny distortion resulting from the partial substitution of the Pr^{3+} ions by the Y^{3+} ions [94]. At weak magnetic fields $B \leq 2$ T, where C_{4f}/T diverges logarithmically as temperature approaches zero, the simulated entropy and the experimentally determined one deviate substantially from each other, while they agree well with each other at high magnetic field [94]. This indicates local moment behavior at high magnetic field and suppression of the quadrupole Kondo hybridization due to the large splitting of the Γ_3 ground state doublet [94].

Measurements of the $(c_{11} - c_{12})/2$ elastic constant by Yanagisawa et al. [44] provided additional information on the evolution of the NFL state in magnetic field $\boldsymbol{H} \parallel [001]$. The upper part of Fig. 5.5 shows the background corrected relative change of the $(c_{11} - c_{12})/2$ elastic constant as a function of temperature for various magnetic fields $\mu_0 H \leq 14$ T applied along the [001] direction [44]. Note that Yanagisawa et al. [44] subtracted a field independent background contribution, which they specified via the measurement at a high magnetic field of 14 T. Their data of $(c_{11} - c_{12})/2$ reveals that a weak magnetic field in the range $0 \leq \mu_0 H \leq 1$ T has only negligible influence on the divergent behavior of $(c_{11} - c_{12})/2$, whereby the divergence seems to become even slightly more pronounced in small magnetic field [44]. At 1.5 T, the low temperature divergence is suppressed, which becomes more evident as magnetic field is further increased [44]. At 14 T, the initially observed softening

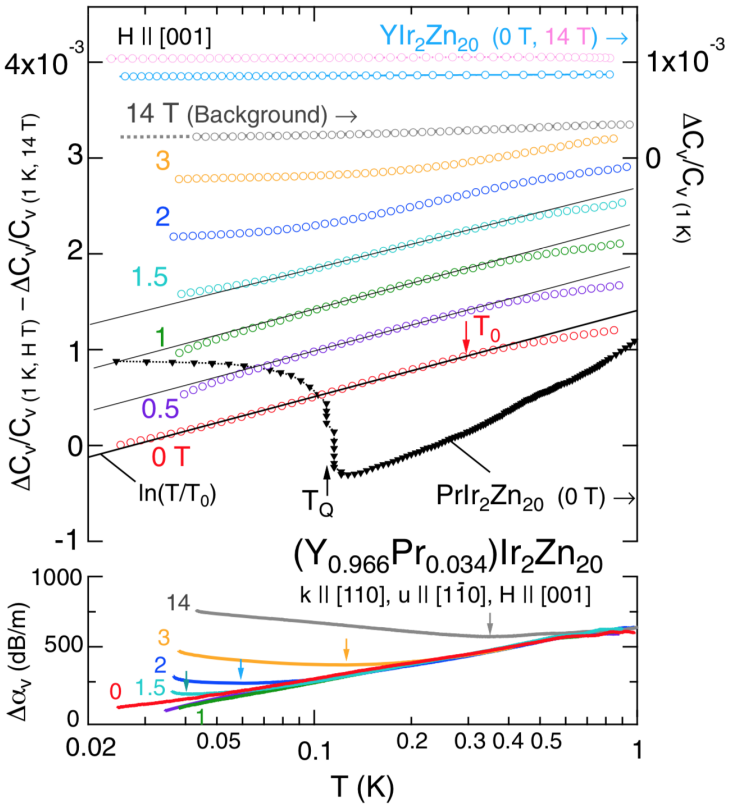

Figure 5.5: The upper part shows the background corrected relative change of the $c_\mathrm{v} = (c_{11} - c_{12})/2$ elastic constant as a function of temperature of $Y_{1-x}Pr_xIr_2Zn_{20}$ with $x = 0.034$ at various magnetic fields $\boldsymbol{H} \parallel [001]$ and $PrIr_2Zn_{20}$ [37] at zero field. The lower part shows the ultrasonic attenuation coefficient $\Delta\alpha_\mathrm{v}$ as a function of temperature at different magnetic fields. [44] Reprinted figure with permission from Ref. [44]. ©2019 by the American Physical Society.

vanishes and the data is reminiscent of the $(c_{11} - c_{12})/2$ elastic constant of the reference compound YIr_2Zn_{20}, which is additionally plotted in Fig. 5.5 [44]. Overall, the findings by Yanagisawa et al. [44] confirm that the NFL behavior is suppressed by a relatively small magnetic field and are therefore in good agreement with the specific heat results obtained by Yamane et al. [94]. The lower part of Fig. 5.5 shows the attenuation coefficient as a function of temperature for different magnetic fields, which displays an interesting increase at low temperatures and small magnetic field [44]. Even though a clear explanation for this unconventional behavior is not given by Yanagisawa et al. [44], they mention the field induced mixing of the Γ_3 ground state with the higher exited Γ_4 triplet as a possible cause. Yanagisawa et al. [44] also determined the quadrupole-strain coupling constant at $|g_{\Gamma_3}| = 19.0\,\mathrm{K}$. For more details on the elastic constant measurement it is referred to the publication by Yanagisawa et al. [44].

5.2 Experimental Results

In this section the thermal expansion and magnetostriction measurement results on single crystalline $Y_{1-x}Pr_xIr_2Zn_{20}$ are presented and discussed. Firstly, information on the ex-

amined single crystals, which were synthesized and characterized by a cooperation partner from Hiroshima University in Japan, is provided. Subsequently, the focus is on the thermal expansion and magnetostriction results. Main objective of the experiments was to search for unconventional behavior in highly diluted $Y_{1-x}Pr_xIr_2Zn_{20}$ to further characterize the material's possible single-impurity quadrupole Kondo ground state. In addition, two moderately doped single crystals were examined, for which specific heat and electrical resistivity measurements by Yamane et al. [42, 43] suggested the suppression of the single-impurity quadrupole Kondo state.

5.2.1 $Y_{1-x}Pr_xIr_2Zn_{20}$ Single Crystals

Thermal expansion and magnetostriction measurements were carried out on four differently doped single crystalline samples of $Y_{1-x}Pr_xIr_2Zn_{20}$ with $x = 0.033$, $x = 0.036$, $x = 0.09$ and $x = 0.49$, which were provided by T. Onimaru from Hiroshima University in Japan. The single crystals were synthesized and crystallographically oriented by Y. Yamane, who used a Zn self flux growth method and gives a very detailed description of the single crystal growth process in his doctoral thesis [129]. The Pr concentration of each of the four single crystalline samples mentioned above was carefully determined by either electron probe microanalysis (EPMA) or a magnetization measurement by the cooperation partner from Hiroshima University. This additional characterization is necessary as the Pr concentration of a single crystal typically undergoes small changes during the growth process. Furthermore, the Pr^{3+} ions are not uniformly distributed within the relatively large single crystals from which the provided small single crystalline samples used for the dilatometry were cut out. Therefore, scrutiny of each single crystal is crucial. The single crystal with a Pr concentration of $x = 0.49$ was characterized by EPMA at Hiroshima University. The given concentration value denotes the average of the concentration measured at ten different spots of the single crystal, whereby the standard deviation of the so estimated concentration is according to the collaborators $\Delta x = \pm 0.06$. Since the resolution of EPMA was not high enough to precisely determine the Pr concentration of the higher diluted single crystals with $x = 0.033$, $x = 0.036$ and $x = 0.09$, Y. Yamane specified their Pr concentration by measuring the magnetization at $T = 1.8\,\mathrm{K}$ and $B = 1\,\mathrm{T}$. A comparison of the experimentally measured value and the theoretical value derived by a CEF calculation then allowed for the estimation of each single crystal's Pr concentration. By contrast to the EPMA measurement, it is more difficult to determine the error bar of the concentration values derived by a magnetization measurement. The error can only be roughly estimated and is likely $5 - 10\%$ of the determined concentration value. It may, however, be larger for the single crystal with a Pr concentration of $x = 0.09$, for which a small inter-site interaction between the Pr^{3+} ions cannot be excluded. This may cause a small error, as the CEF calculation to which Y. Yamane compared the experimentally determined magnetization value does not take account of a possible inter-site interaction.

The basic properties of each single crystal, such as its Pr concentration, estimated RRR value, batch number, crystallographic orientations and dimensions are summarized in Table 5.1. The given RRR values, as reported in Refs. [43, 129], were determined by the collaborators on other single crystalline samples that originated from the same batches, as the here examined ones. The length value of each crystallographically oriented side was measured with an accuracy of $\pm 0.001\,\mathrm{mm}$. The sample shapes, crystallographic orientations and the respective length values are presented in Fig. 5.6. All four single crystals have an approximately rectangular shape with three different parallel surfaces. In case of sample Nr. 2 with $x = 0.036$, the three surfaces correspond to the [100], [010] and [001] direction, which are degenerate for a cubic crystal symmetry. Sample Nr. 1 originates

Sample Nr.	Pr concentration	RRR	Batch	Crystal directions	Length
1	$x = 0.033$	160 [129]	# 2	$[1\bar{1}0]$	1.082 mm
				[111]	1.533 mm
				$[11\bar{2}]$	0.701 mm
2	$x = 0.036$	160 [129]	# 2	[100]	0.920 mm
				[010]	1.143 mm
				[001]	2.376 mm
3	$x = 0.09$	25 [129]	# 1	[001]	1.487 mm
				[110]	1.045 mm
				$[1\bar{1}0]$	1.162 mm
4	$x = 0.49$	8 [43, 129]	# 1	[001]	1.714 mm
				[110]	1.010 mm
				$[1\bar{1}0]$	0.803 mm

Table 5.1: Properties of the single crystalline samples of $Y_{1-x}Pr_xIr_2Zn_{20}$ with $x \leq 0.49$ used for the thermal expansion and magnetostriction measurements. The given Pr concentrations were either determined by EPMA ($x = 0.49$) or by a magnetization measurement at 1.8 K and 1 T ($x \leq 0.09$). The RRR values were measured by the cooperation partner on other single crystalline samples from the same batches [43, 129]. All single crystalline samples have a roughly cuboid shape. The crystallographic orientations and the respective length values are given for each of the single crystals, whereby the length values have an accuracy of ±0.001 mm. The single crystals detailed in this table were synthesized and characterized by Y. Yamane.

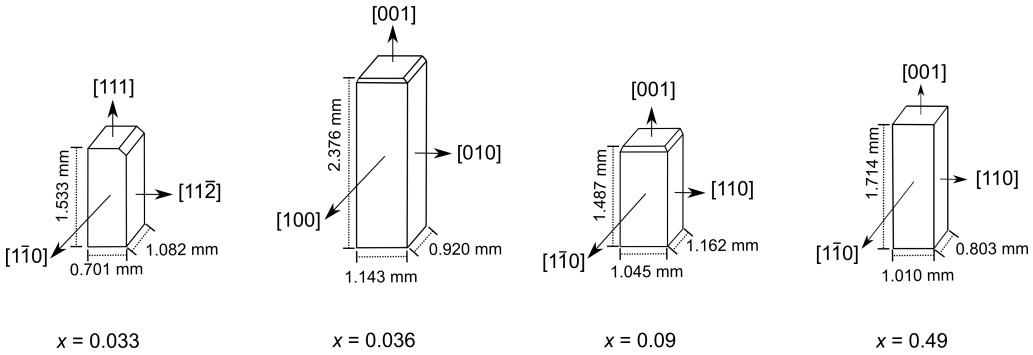

Figure 5.6: Sketches of the four differently doped $Y_{1-x}Pr_xIr_2Zn_{20}$ single crystalline samples investigated in this thesis. Indicated are shape, crystallographic orientations and dimensions.
This figure is also included in Ref. [134, SM].

from the same batch and has therefore a similar Pr doping level of $x = 0.033$. Its surfaces are, however, differently oriented and correspond to the $[1\bar{1}0]$, [111] and $[11\bar{2}]$ direction. The two higher doped single crystals with $x = 0.09$ and $x = 0.49$ are oriented in a way that their perpendicular surfaces denote the [001], [110] and $[1\bar{1}0]$ direction.

5.2.2 Thermal Expansion

As previous studies indicated that the quadrupole Kondo effect forms exclusively in highly diluted single crystals with $x \leq 0.044$ [42,43], the main focus of the thermal expansion measurements was on the two weakly doped single crystals with $x = 0.033$ and $x = 0.036$. The $\langle 100 \rangle$ oriented single crystal with $x = 0.036$ was utilized to study the zero magnetic field thermal expansion as well as anisotropy and volume effects for $\boldsymbol{H} \parallel [001]$[4]. To evaluate the anisotropy effects, longitudinal and transverse thermal expansion measurements were carried out. These measurements allowed for the determination of the symmetrized Γ_3-type thermal expansion coefficient α_{u}, which is proportional to the quadrupolar expectation value $\partial_T \langle O_2^0 \rangle$ and provides crucial information on the possible single-impurity quadrupole Kondo nature of the material's ground state. The determination of volume changes, on the other hand, is of relevance as hybridization effects typically couple to the volume due to the pressure dependence of the respective coupling constants, i.e. quadrupole Kondo coupling. Also a possible valence change of the rare earth ion would be accompanied by a distinct volume change. A downside of the thermal expansion measurement along a $\langle 100 \rangle$ direction arises from the linear coupling between the Γ_3-type quadrupole moments and strain along this crystallographic direction. As the here employed miniaturized capacitive dilatometer exerts via its flat springs a tiny uniaxial stress on the single crystal in measurement direction, an additional uniaxial stress induced contribution to the thermal expansion cannot be excluded. In order to quantify its impact, an additional thermal expansion measurement was carried out along the [111] direction of the single crystal with $x = 0.033$. A general feature of unstrained cubic materials is their isotropic thermal expansion, meaning that the linear thermal expansion coefficients measured, for instance, along the [001] and the [111] direction show the same behavior. As strain $\varepsilon_{[111]}$ does not couple linearly to the Γ_3 doublet, a thermal expansion measurement along this direction is powerful to reveal a possible uniaxial stress induced contribution to the thermal expansion coefficient measured along the [001] direction. To better classify the emerging behavior in the highly diluted single crystals, the longitudinal thermal expansion coefficients of two moderately diluted single crystals with $x = 0.09$ and $x = 0.49$ were measured for $\boldsymbol{H} \parallel [001]$. These measurements aimed to verify the findings of previous specific heat and electrical resistivity measurements, which excluded the formation of the single-impurity quadrupole Kondo effect in single crystals with a similar Pr doping [42, 43]. The measurements on the single crystals with $x = 0.036, x = 0.09$ and $x = 0.49$ were carried out along their [001] oriented side, which have length values of 2.376 mm, 1.487 mm and 1.714 mm, respectively. The measurements on the single crystal with $x = 0.033$ were performed along its [111] oriented side, which has a length value of 1.533 mm.

The longitudinal thermal expansion of the single crystal with $x = 0.036$ for $\boldsymbol{H} \parallel [001]$, as presented in Fig. 5.7(a), was measured together with Y. Yamane during his four week research visit at the University of Augsburg. All other experimental findings shown in this subsection, namely the transverse thermal expansion of the $x = 0.036$ single crystal for $\boldsymbol{H} \parallel [001]$, the thermal expansion of the $x = 0.033, x = 0.09$ and $x = 0.49$ single crystals as well as the thermal expansion of the $x = 0.033$ and $x = 0.036$ single crystals under higher uniaxial stress were obtained by me alone. Preliminary results before dilatometer background subtraction of the longitudinal, transverse and volume thermal expansion of

[4] As already outlined before, depending on the consulted literature, either the denotation B or H is used to denote the magnetic field. In case of an external magnetic field, both quantities relate as $B = \mu_0 H$ to each other. Note, when considering an internal magnetic field, this relation does not hold anymore as also the magnetization of the material has to be taken into account. In this subsection and the following subsection on the magnetostriction, the denotation $\mu_0 H$ is used to specify the external magnetic field.

the $x = 0.036$ single crystal presented in Fig. 5.7 of this thesis, were already shown in the doctoral thesis of Y. Yamane [129].

Highly Diluted Single Crystals ($x = 0.033$ and $x = 0.036$)

On the basis of the thermal expansion measurement results on $Y_{1-x}Pr_xIr_2Zn_{20}$, presented and discussed in this subsubsection, and the respective magnetostriction measurement results on the $x = 0.036$ single crystal, presented at a later stage of this section, a manuscript was prepared that was recently submitted to a scientific journal [134]. The specific heat data shown in this subsubsection was measured by Y. Yamane and S. Bachus. M. Garst[5] performed calculations on the divergent volume thermal expansion, which are reviewed at the end of this subsubsection. The just mentioned contributions of the collaborators are acknowledged at the respective places. Figures shown in the following that are also included in the submitted manuscript are indicated by the citation [134] in the figure caption. (*Note added before publication of this thesis: Above mentioned manuscript was published on the 6th of June 2022 in the scientific journal Physical Review Research* [134].)

Figure 5.7(a) and (b) show the longitudinal thermal expansion coefficient $\alpha_{\parallel}$ and the transverse thermal expansion coefficient $\alpha_{\perp}$ of $Y_{1-x}Pr_xIr_2Zn_{20}$ with $x = 0.036$ as a function of temperature at various magnetic fields $\boldsymbol{H} \parallel [001]$. Before continuing with the discussion of the data, the measurement process of $\alpha_{\parallel}$ and $\alpha_{\perp}$ is briefly described. Just to recall, the $x = 0.036$ single crystal has a cuboid shape, whose three different parallel faces all correspond to cubic $\langle 100 \rangle$ directions and are thus degenerate in zero magnetic field. As soon as a magnetic field is applied along one of these three indistinguishable directions, their degeneracy is lifted, as the crystal undergoes a tetragonal distortion. In consequence, the direction parallel to magnetic field is now distinguished from the two perpendicular ones. In the experiment, the thermal expansion was always measured along the same $\langle 100 \rangle$ direction, whereby the longest side of the single crystal with $L = 2.376\,\mathrm{mm}$ was chosen. In order to determine the longitudinal thermal expansion coefficient, the magnetic field was applied parallel to the measurement direction and to measure the transverse thermal expansion, the dilatometer was rotated by 90°, so that the magnetic field pointed along one of the two $\langle 100 \rangle$ directions perpendicular to the relative length change measurement direction. It is important to note that in the following the [001] direction is defined as the $\langle 100 \rangle$ direction of the single crystal along which the magnetic field points. This is justified as it is the magnetic field, which breaks the cubic crystal symmetry and therefore defines the distinguished direction[6]. In order to better understand the experimentally obtained data, CEF simulations of $\alpha_{\parallel}$ and $\alpha_{\perp}$ were carried out at selected magnetic fields $\boldsymbol{H} \parallel [001]$. The CEF calculations are additionally shown in Fig. 5.7(a) and (b) as dashed lines and were calculated by following the approach, which was explicitly discussed in Section 4.2.2. In order to simulate the expectation values of the quadrupole operators, again the Mathematica based CEF program provided by T. Onimaru was used to evaluate the Hamiltonian specified by Eq. (4.12). Due to the tiny Pr concentration of the single crystal, it was, however, assumed that the interaction between the quadrupole moments vanishes, i.e. $K_{\Gamma_3} = 0$. In addition, the interaction constant between excited dipole mo-

[5] Institute of Theoretical Solid State Physics, Karlsruhe Institute of Technology, 76131 Karlsruhe, Germany.

[6] As it will be shown at a later part of this subsubsection, not only magnetic field breaks the cubic symmetry of the material but also the very small uniaxial stress exerted by the flat springs of the employed miniaturized capacitive dilatometer on the single crystal in measurement direction. As the magnetic field induced anisotropic behavior dominates over the small uniaxial stress induced one, the latter effect is disregarded for the moment.

ments K was set to zero $K = 0$. Consequently, the Hamiltonian contains only the CEF term for cubic T_d point group symmetry, the Zeeman term and the quadrupole-strain coupling term. To simulate the thermal expansion coefficients, at first, the CEF parameters $W = -1.22\,\mathrm{K}$ and $x = 0.537$, as previously determined by Iwasa et al. [65] on pure $PrIr_2Zn_{20}$ by means of inelastic neutron scattering, were used. At a high magnetic field of 10 T, where it is justified to assume that the quadrupole moments are fully localized, the so calculated curves were, however, not in good accordance with the experiment. As the inter-site interaction between the Pr^{3+} ions can be considered as negligible for such a highly diluted system, it are primarily the CEF parameters W and x that determine the temperature dependence of $\alpha_\parallel$ and $\alpha_\perp$. The found discrepancies between simulated and experimentally obtained data therefore indicate a small difference between the CEF parameters of diluted $Y_{1-x}Pr_xIr_2Zn_{20}$ and pure $PrIr_2Zn_{20}$, which likely originates from the partial substitution of the Pr^{3+} ions by Y^{3+} ions. In consequence of the smaller ionic radius of a Y^{3+} ion as compared to a Pr^{3+} ion, the substitution with Y^{3+} ions strengthens the CEF effect, which in turn leads to an enhancement of the W parameter. Note that W serves as a scaling parameter in the cubic CEF Hamiltonian specified by Eq. (2.16) [64]. The specific heat study in magnetic field by Yamane et al. [94] on a single crystal with a similar Pr doping level of $x = 0.044$, which was reviewed in Section 5.1.2, also employed a modified CEF parameter value of $W = -1.50\,\mathrm{K}$ in order to obtain good agreement with the experimental data. In fact, by using the same value of $W = -1.50\,\mathrm{K}$ as Yamane et al. [94], very good accordance between the simulated and the experimentally obtained thermal expansion data was found at 10 T. The parameter $x = 0.537$, on the other hand, was not modified and is thus identical to the one suggested for pure $PrIr_2Zn_{20}$ by means of inelastic neutron scattering [65]. In addition, the number of Pr^{3+} ions per volume n_{Pr} and the Γ_3-type background elastic constant $(c^0_{11} - c^0_{12})/2$ are required parameters to carry out the simulation. The former calculates as $n_{\mathrm{Pr}} = (x \times Z)/a^3 = 0.101 \times 10^{27}\,\mathrm{m}^{-3}$, where $x = 0.036$ is the Pr concentration, $Z = 8$ [25] the number of formula units per unit cell and $a = 14.197 \times 10^{-10}\,\mathrm{m}$ [129] the lattice parameter of another single crystal from the same batch that exhibits a similar Pr doping level of $x = 0.044$. The background elastic constant value was previously reported in Ref. [44, SM] as $(c^0_{11} - c^0_{12})/2 = 52.771\,\mathrm{GPa}$, which was measured on a sample with a similar Pr doping of $x = 0.034$. The quadrupole-strain coupling constant g_{Γ_3} determines mainly the magnitude of the thermal expansion coefficient and has negligible influence on its temperature dependence. Its value was determined at $g_{\Gamma_3} = -28.9\,\mathrm{K}$ by fitting the CEF calculation to the experimentally obtained $\alpha_\parallel$ and $\alpha_\perp$ data at 10 T. This value is somewhat larger than the one derived by the elastic constant measurement $|g_{\Gamma_3}| = 19.0\,\mathrm{K}$ [44]. As a similar discrepancy between the quadrupole-strain coupling constant determined via the elastic constant [37] and the thermal expansion measurement was also found for $PrIr_2Zn_{20}$, a systematic error between the two methods likely causes this small deviation. To deduce the thermal expansion coefficients from the simulated quadrupolar expectation values, it is recalled that the Pr^{3+} ions in $Y_{1-x}Pr_xIr_2Zn_{20}$ have T_d point group symmetry. In this case, a magnetic field $\boldsymbol{H} \parallel [001]$ induces only the tetragonal $\langle O^0_2 \rangle$ but not the in plane $\langle O^2_2 \rangle$ quadrupole moment, meaning that only the Γ_3-type thermal expansion $\alpha_{\mathrm{u}} = \partial_T \varepsilon_{\mathrm{u}}$ is finite and $\alpha_{\mathrm{v}} = \partial_T \varepsilon_{\mathrm{v}}$ vanishes to zero. Just like for $PrIr_2Zn_{20}$, a possible bulk contribution was disregarded in the simulation, as Fig. 5.7(c) clearly demonstrates that the volume thermal expansion at high magnetic field vanishes to zero. Consequently, the simulated $\alpha_\parallel$ and $\alpha_\perp$ curves only contain the contribution from the thermal expansion coefficient with Γ_3 symmetry α_{u}. As the linear relation between the Γ_3-type strains ε_{u} and ε_{v} and the respective quadrupole moments $\langle O^0_2 \rangle$ and $\langle O^2_2 \rangle$ as well as the formulas for the calculations of the longitudinal and transverse strains for $\boldsymbol{H} \parallel [001]$

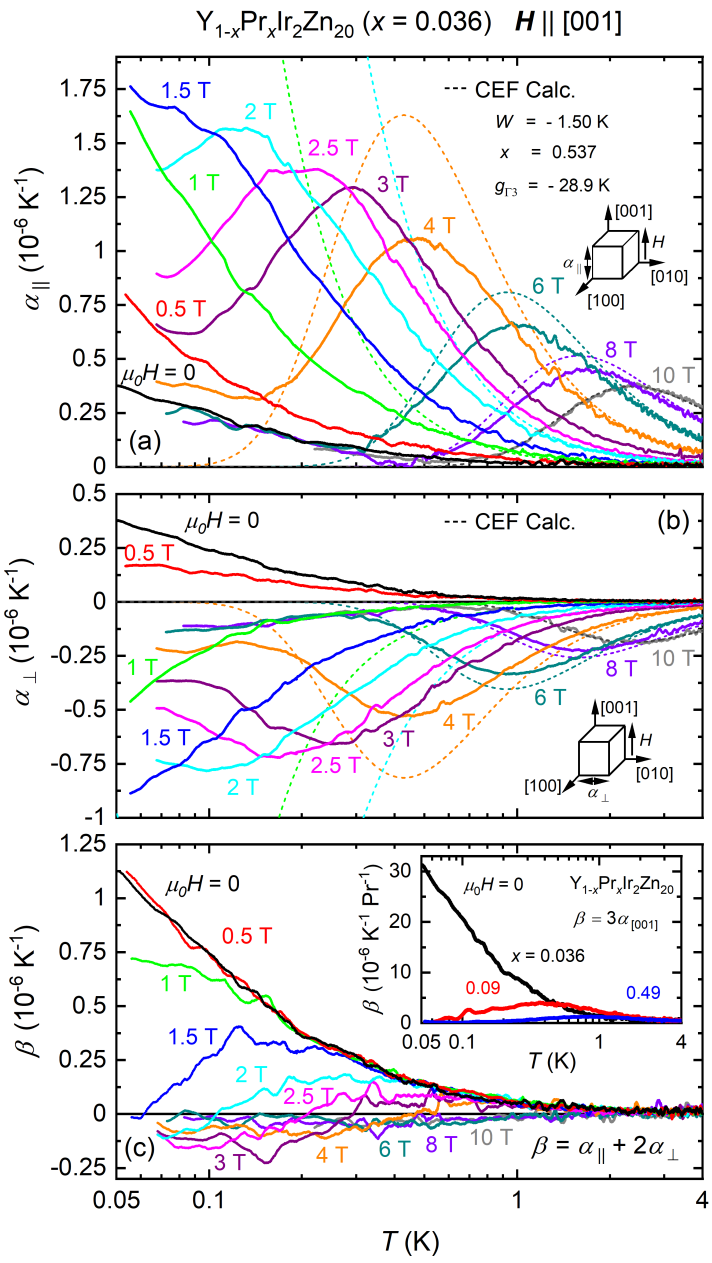

Figure 5.7: Temperature dependence of the longitudinal, transverse and volume thermal expansion coefficients $\alpha_{\parallel}$, $\alpha_{\perp}$ and β of $Y_{1-x}Pr_xIr_2Zn_{20}$ with $x = 0.036$ at different magnetic fields $\boldsymbol{H} \parallel [001]$. (a) $\alpha_{\parallel}$ and (b) $\alpha_{\perp}$ as a function of temperature at various magnetic fields. Additionally displayed dashed lines are CEF calculations that use the CEF parameters $W = -1.50\,\mathrm{K}$ and $x = 0.537$ and a quadrupole-strain coupling constant of $g_{\Gamma_3} = -28.9\,\mathrm{K}$. (c) Volume thermal expansion coefficient deduced from the longitudinal and transverse thermal expansion coefficients via the relation $\beta = \alpha_{\parallel} + 2\alpha_{\perp}$ as a function of temperature at various magnetic fields. The inset illustrates the zero magnetic field volume thermal expansion $\beta = 3\alpha_{[001]}$ for Pr concentrations of $x = 0.036$, $x = 0.09$ and $x = 0.49$, normalized to x.
This figure is also included in Ref. [134].

have already been explicitly discussed before, they are not recalled in this subsubsection. To call the relations back to memory it is referred to Section 2.3.2 and Section 4.2.2, where the calculation procedures of the CEF thermal expansion were detailed.

Before discussing the simulated longitudinal and transverse thermal expansion coefficients in detail, the focus is on the experimentally determined coefficients. Surprisingly, the positive zero magnetic field thermal expansion coefficient shown in Fig. 5.7(a) and (b) diverges on cooling down to the lowest measured temperature of 0.05 K. Upon the application of magnetic field $\boldsymbol{H} \parallel [001]$, $\alpha_{\parallel}$ grows in magnitude and its divergence becomes more pronounced until a threshold field of $\mu_0 H = 1\,\mathrm{T}$ is reached. By further increasing magnetic field, the divergence is gradually suppressed and at 2 T a clear maximum appears at around 0.12 K. With increasing magnetic field, the maximum gradually shifts to higher temperature and its peak value decreases. Unexpectedly, at high magnetic field, $\alpha_{\parallel}$ does not vanish as temperature declines to zero but starts to increase again. This observation is reminiscent of the behavior found in $PrIr_2Zn_{20}$, which was discussed in Section 4.2.2. The transverse thermal expansion coefficient $\alpha_{\perp}$, which is shown in Fig. 5.7(b), is negative at magnetic fields $\mu_0 H \geq 2\,\mathrm{T}$ and roughly mirrors the behavior of $\alpha_{\parallel}$, whereby its magnitude is approximately half as large as the one of $\alpha_{\parallel}$. By contrast, at low magnetic field, $\alpha_{\perp}$ shows a positive sign. The sign change occurring at low magnetic field can be explained by the gradual superposition of the positive zero field bulk expansion by the negative field induced Γ_3-type contribution.

In order to detect possible unconventional behavior arising from the single-impurity quadrupole Kondo effect, comparison between the experimental findings and the CEF calculations, i.e. the fully localized case, is crucial. Fig. 5.7(a) and (b) indicate that at high magnetic field $\mu_0 H \geq 6\,\mathrm{T}$, the CEF calculation reproduces the extrema in $\alpha_{\parallel}$ and $\alpha_{\perp}$ very well. As the applied magnetic field breaks the degeneracy of the ground state doublet, the observed high field extrema can be assigned to the energy scale that measures the splitting of the Γ_3 doublet in magnetic field. By contrast, the peculiar low temperature increase in $\alpha_{\parallel}$ and $\alpha_{\perp}$ at high magnetic field cannot be accounted for by the simulation. This points towards remaining correlations at very low temperature and high magnetic field. As already discussed in the context of $PrIr_2Zn_{20}$, a plausible explanation for this surprising behavior cannot be given at this point. In the intermediate magnetic field range, calculation and experiment agree moderately well with each other, whereby discrepancies become more significant as magnetic field decreases. At low magnetic fields $\mu_0 H \leq 2\,\mathrm{T}$, the differences between calculation and experiment are stark. Here, the experimentally obtained thermal expansion data is strongly suppressed as compared to the calculation, which points towards the onset of hybridization effects. For $\mu_0 H \leq 1\,\mathrm{T}$, which is in the single-impurity quadrupole Kondo regime [44], $\alpha_{\parallel}$ displays a clear divergence down to the lowest measured temperature. At a later stage of this subsubsection, where the symmetrized thermal expansion coefficient with Γ_3 symmetry α_{u} is detailed, it will be shown that this divergence is in accordance with the logarithmic temperature dependence of the quadrupole-strain susceptibility determined by the measurement of the elastic constant [44] and is therefore a clear signature of the single-impurity quadrupole Kondo effect.

With the help of $\alpha_{\parallel}$ and $\alpha_{\perp}$ one can calculate the volume thermal expansion coefficient $\beta = \alpha_{\parallel} + 2\alpha_{\perp}$, which is shown in Figure 5.7(c) for various magnetic fields $\boldsymbol{H} \parallel [001]$. At zero magnetic field, β was calculated as three times the average of the two zero magnetic field linear thermal expansion coefficients shown in Fig. 5.7(a) and (b). While the application of a small magnetic field of 0.5 T has no notable influence on the divergence of β and the application of 1 T only a very little one, further increase of magnetic field to a value of

1.5 T suppresses the divergence and a maximum appears instead. In the intermediate field range $2\,\mathrm{T} \leq \mu_0 H \leq 4\,\mathrm{T}$, the maximum in β is still clearly visible and a sign change in β appears at very low temperature. Further increase of magnetic field gradually suppresses the maximum at elevated temperature and increases the temperature at which the sign change occurs. In spite of the small signal, the sign change in β at very low temperature seems to be an intrinsic feature, which is unexpected as the quadrupole moments should be fully localized in this magnetic field range. As $\alpha_\parallel$ and $\alpha_\perp$ display an unconventional increase in a comparable temperature and magnetic field range as well, a connection between the two findings is likely. The observation of very similar behavior in $PrIr_2Zn_{20}$ points towards an universal feature, which should be examined more carefully in the future.

In the following, the unconventional behaviors in the linear and volume thermal expansion coefficients at low magnetic field are scrutinized and put in context with the single-impurity quadrupole Kondo scenario. In order to provide an explanation for the unconventional behavior at low magnetic field, it is briefly recalled that a magnetic field $\boldsymbol{H} \parallel [001]$ splits the ground state doublet quadratically and induces a thermal expansion contribution with Γ_3 symmetry α_u, which is proportional to the quadrupolar expectation value $\partial\langle O_2^0\rangle/\partial T$. As detailed at the beginning of this subsubsection, the field induced contribution α_u is cause for the highly anisotropic behavior found in $\alpha_\parallel$ and $\alpha_\perp$. By using the measurement results of $\alpha_\parallel$, $\alpha_\perp$ and β, as presented in Fig. 5.7, it is possible to deduce the symmetrized thermal expansion coefficient with Γ_3 symmetry α_u. According to Eq. (2.39), α_u can be calculated with the help of $\alpha_\parallel$ and β by using the equation

$$\alpha_\mathrm{u} = \sqrt{3}\left(\alpha_\parallel - \frac{1}{3}\beta\right) = \frac{n_{\mathrm{Pr}} g_{\Gamma_3}}{(c_{11}^0 - c_{12}^0)/2}\frac{\partial\langle O_2^0\rangle}{\partial T}. \tag{5.1}$$

α_u is shown together with the respective CEF simulation results in Fig. 5.8(a). As evidenced by Fig. 5.7(c), a sizable volume expansion only exists at small magnetic field, which explains that the temperature dependencies of $\alpha_\parallel$ and α_u are nearly identical at elevated magnetic field, where β is negligible small. In analogy to $\alpha_\parallel$ and $\alpha_\perp$, also the simulated and experimentally determined α_u data sets deviate substantially from each other at low magnetic field. To put these deviations into context, the quadrupole-field susceptibility $\chi_\mathrm{Q}^\mathrm{F}$ is considered, which quantifies the quadratic splitting of $\langle O_2^0\rangle$ as a function of a small magnetic field $\boldsymbol{H} \parallel [001]$ and is therefore defined as

$$\chi_\mathrm{Q}^\mathrm{F} = \frac{\partial\langle O_2^0\rangle}{\partial(\mu_0 H)^2}\Big|_{H\to 0}. \tag{5.2}$$

As pointed out in Section 4.1.2 on the example of $PrIr_2Zn_{20}$, the initial quadratic field dependence of $\langle O_2^0\rangle$ stems from the magnetic field induced mixing of the Γ_3 ground and the Γ_4 first excited state. Note that a free quadrupole moment also couples quadratically to magnetic field [73]. This effect can, however, be considered to be small as compared to the quadratic splitting of the ground state doublet that arises from the field induced mixing of the ground and the first excited state. Provided that the applied magnetic field $\boldsymbol{H} \parallel [001]$ is small, so that the quadratic coupling between quadrupole moment and magnetic field holds true in the considered temperature range, the field induced contribution α_u shows proportionality to $\partial_T \chi_\mathrm{Q}^\mathrm{F}$. It then holds

$$\alpha_\mathrm{u} = \frac{n_{\mathrm{Pr}} g_{\Gamma_3}}{(c_{11}^0 - c_{12}^0)/2}\frac{\partial\langle O_2^0\rangle}{\partial T} = \frac{n_{\mathrm{Pr}} g_{\Gamma_3}}{(c_{11}^0 - c_{12}^0)/2}(\mu_0 H)^2\frac{\partial\chi_\mathrm{Q}^\mathrm{F}}{\partial T}\Big|_{H\to 0}. \tag{5.3}$$

This relation suggests that the measurement of the symmetrized thermal expansion coefficient α_u is a direct and elegant means to deduce the quadrupole-field susceptibility that

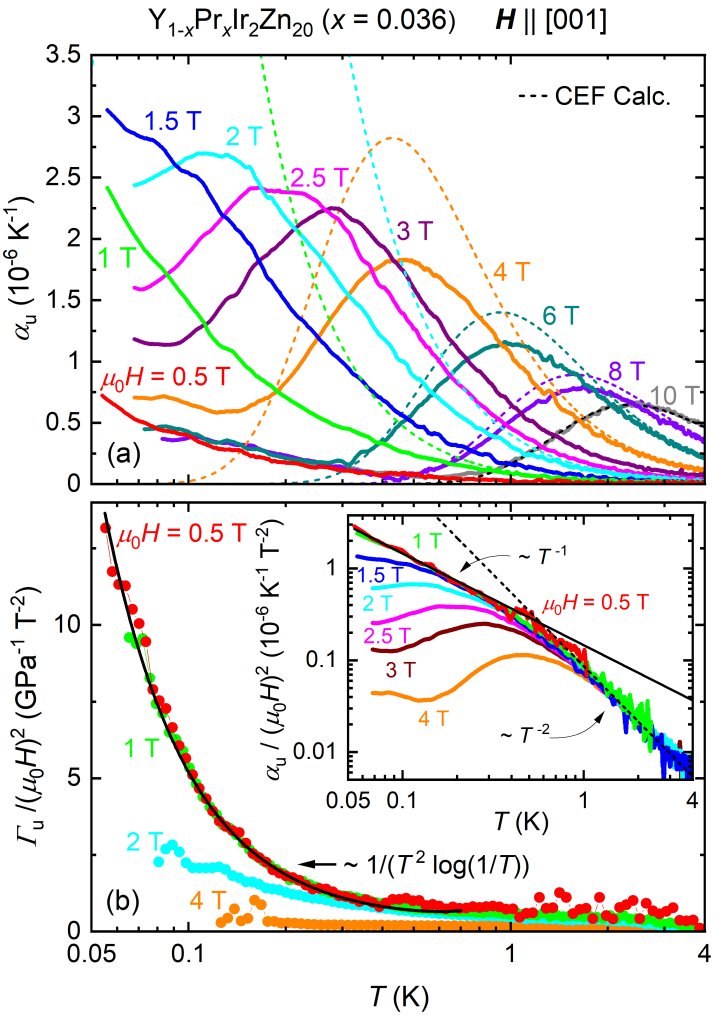

Figure 5.8: (a) Thermal expansion coefficient with Γ_3 symmetry α_u as a function of temperature at different magnetic fields $\boldsymbol{H} \parallel [001]$. In addition, CEF calculations are shown as dashed lines that use the CEF parameters $W = -1.50\,\mathrm{K}$ and $x = 0.537$ as well as a quadrupole-strain coupling constant $g_{\Gamma_3} = -28.9\,\mathrm{K}$. (b) Temperature dependence of the quadrupolar Grüneisen ratio $\Gamma_u/(\mu_0 H)^2$ at various magnetic fields $\boldsymbol{H} \parallel [001]$ and the anticipated temperature dependence of the single-impurity quadrupole Kondo effect as a black solid line. The inset illustrates $\alpha_u/(\mu_0 H)^2$ as a function of temperature at selected magnetic fields. Due to a low signal to noise ratio, the 0.5 T and 1 T data was truncated at high temperatures for reasons of clarity. The additionally shown black solid and dashed lines indicate the anticipated temperature dependencies of the single-impurity quadrupole Kondo effect $\sim T^{-1}$ and a fully localized Γ_3 ground state doublet $\sim T^{-2}$, respectively.
This figure is also included in Ref. [134].

quantifies the quadratic splitting of the quadrupolar ground state doublet in magnetic field. In order to verify the CEF temperature dependence of χ_Q^F, the CEF calculation detailed in Fig. 5.8(a) is recalled and analyzed more meticulously at low magnetic field. Figure 5.9 shows the already in Fig. 5.8(a) presented CEF thermal expansion coefficient

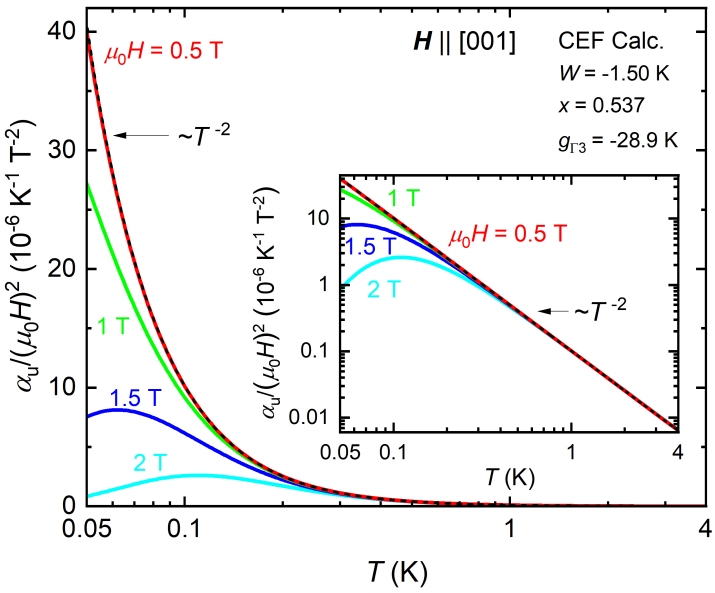

Figure 5.9: Simulated CEF thermal expansion coefficient with Γ_3 symmetry plotted as $\alpha_\mathrm{u}/(\mu_0 H)^2$ as a function of temperature at different magnetic fields $\boldsymbol{H} \parallel [001]$. The simulation is based on the CEF parameters $W = -1.50\,\mathrm{K}$ and $x = 0.537$ and on a quadrupole-strain coupling constant $g_{\Gamma_3} = -28.9\,\mathrm{K}$. The inset displays the same data shown on a double logarithmic scale.
This figure is also included in Ref. [134, SM].

with Γ_3 symmetry normalized to the second power of magnetic field $\alpha_\mathrm{u}/(\mu_0 H)^2$ as a function of temperature at various magnetic fields $\boldsymbol{H} \parallel [001]$. The inset shows the same data on a double logarithmic scale. As expected, the $\alpha_\mathrm{u}/(\mu_0 H^2)$ curves fall on top of each other at high temperature but deviate at low temperatures. Note, only when temperature is large as compared to the field induced splitting of the Γ_3 ground state, proportionality between α_u and $\partial_T \chi_\mathrm{Q}^\mathrm{F}$ can be expected. To deduce the temperature dependence of $\chi_\mathrm{Q}^\mathrm{F}$, the symmetrized thermal expansion coefficient α_u is analyzed at low magnetic field, where $\langle O_2^0 \rangle$ depends quadratically on magnetic field in the considered temperature range. The latter condition is fulfilled[7] at a low magnetic field of 0.5 T, where the CEF simulation shown in Fig. 5.9 suggests $\alpha_\mathrm{u}/(\mu_0 H)^2 \sim 1/T^2$. This, in turn, implies that $\chi_\mathrm{Q}^\mathrm{F} \sim 1/T$ in the temperature range $0.05\,\mathrm{K} < T < 4\,\mathrm{K}$. Strikingly, this temperature dependence is in line with the one of the quadrupole-strain susceptibility of a fully localized non-Kramers Γ_3 doublet $\chi_\mathrm{Q}^\mathrm{F} \sim \chi_\mathrm{Q} \sim 1/T$. For details on the quadrupole-strain susceptibility and its Curie-type temperature dependence, it is referred to Section 2.3.2. Since the quadrupole-strain susceptibility is renormalized from a Curie-type $1/T$ to a $\log 1/T$ temperature dependence when the single-impurity quadrupole Kondo effect is present, it is justified to assume that the quadrupole-field susceptibility undergoes the same renormalization to a logarithmic temperature dependence $\chi_\mathrm{Q}^\mathrm{F} \sim \chi_\mathrm{Q} \sim \log 1/T$. This implies for fully localized quadrupole moments and in presence of a small symmetry breaking magnetic field $\boldsymbol{H} \parallel [001]$ that $\varepsilon_\mathrm{u} \sim H^2/T$ and $\alpha_\mathrm{u} \sim H^2/T^2$. On the other hand, for quadrupole Kondo hybridized quadrupole moments one expects $\varepsilon_\mathrm{u} \sim H^2 \log 1/T$ and $\alpha_\mathrm{u} \sim H^2/T$. To verify whether the

[7] In the here considered temperature range from 0.05 K to 4 K, the quadratic coupling between $\langle O_2^0 \rangle$ and magnetic field is given up to a magnetic field of approximately 0.5 T. This becomes evident from the simulated longitudinal strain plotted as a function of $(\mu_0 H)^2$, which is shown in the appendix of this thesis.

experimental data is in line with this theoretical prediction, the experimentally determined symmetrized thermal expansion coefficient with Γ_3 symmetry normalized to magnetic field $\alpha_u/(\mu_0 H)^2$ for $\boldsymbol{H} \parallel [001]$ is plotted on a double logarithmic scale in the inset of Fig. 5.8(b). Note, as the data at 0.5 T and 1 T have a substantial noise level at high temperatures, the noisy high temperature data was cut off in this plot for reasons of clarity. The additionally plotted black solid and dashed lines indicate the temperature dependencies expected for the single-impurity quadrupole Kondo effect $\sim T^{-1}$ and for a fully localized Γ_3 ground state doublet $\sim T^{-2}$. Indeed, the experimentally obtained data can be very well scaled by $(\mu_0 H)^2$ and its temperature dependence for $\mu_0 H \leq 1\,\mathrm{T}$ and $T < 0.4\,\mathrm{K}$ is in very good conformity with the theoretically expected single-impurity quadrupole Kondo behavior. In addition, the plot nicely shows that the system crosses over at around 0.6 K from a single-impurity quadrupole Kondo hybridized state, where $\alpha_u/(\mu_0 H^2) \sim 1/T$, to a fully localized state, where $\alpha_u/(\mu_0 H^2) \sim 1/T^2$. The found behavior is in excellent agreement with the $(c_{11} - c_{12})/2$ elastic constant measured by Yanagaisawa et al. [44], which shows a logarithmic temperature variation below 0.3 K and a Curie-type $1/T$ dependence above 1 K. For $\mu_0 H > 1\,\mathrm{T}$, the characteristic low temperature divergence in $\alpha_u/(\mu_0 H^2)$ is steadily suppressed, as the quadratic splitting of the ground state doublet begins to dominate over the quadrupole Kondo physics. An additional perturbation arises from the magnetic field induced linear splitting of the two equivalent screening channels that over screen the quadrupole moment. The very good conformity between experiment and theory at low magnetic field provides direct evidence for the formation of the single-impurity quadrupole Kondo effect in highly diluted $Y_{1-x}Pr_xIr_2Zn_{20}$ and is fully in line with the previous specific heat, electrical resistivity and elastic constant results [42–44, 94].

To further characterize the possible single-impurity quadrupole Kondo ground state, the Grüneisen parameter Γ is employed. As explicitly discussed before, the bulk Grüneisen parameter Γ_B calculates as the ratio of the volume thermal expansion to the specific heat and diverges at a pressure sensitive QCP, where hydrostatic pressure serves as a direct control parameter of the criticality [54]. Such a divergence in Γ_B was found in a variety of HF metals that are located in vicinity of a hydrostatic pressure sensitive magnetic QCP [11]. By contrast, in the case of the single-impurity quadrupole Kondo critical point, a volume Grüneisen divergence is not expected. While hydrostatic pressure would certainly enhance the quadrupole Kondo hybridization, it does not break cubic symmetry and is therefore not effective to tune a system away from the single-impurity quadrupole Kondo critical point. Instead, the application of an uniaxial stress with Γ_3 symmetry, i.e. an uniaxial stress along a cubic $\langle 100 \rangle$ direction, couples linearly to the ground state doublet and is therefore a highly effective control parameter to drive a system away from its single-impurity quadrupole Kondo fixed point. A discussion with M. Garst revealed that this can be seen as an example of elastic QC discussed by Zacharias et al. [61]. In consequence, the respective Grüneisen parameter Γ_u is expected to diverge at the single-impurity quadrupole Kondo critical point. Γ_u calculates as the ratio of the just discussed thermal expansion coefficient with Γ_3 symmetry α_u to the molar specific heat C_m as

$$\Gamma_u = V_m \frac{\alpha_u}{C_m}. \tag{5.4}$$

Here, $V_m = 2.154 \times 10^{-4}\,\mathrm{m}^3/\mathrm{mol}$ is the molar volume, determined as $V_m = (N_A \times a^3)/Z$, where N_A is the Avogadro constant, $a = 14.197 \times 10^{-10}\,\mathrm{m}$ [129] the lattice parameter of a single crystal with a similar Pr doping of $x = 0.044$ and $Z = 8$ the number of formula units per unit cell [25]. As the quadrupolar Kondo effect leads to $\alpha_u \sim H^2/T$ and $C_m \sim T \log 1/T$, the respective Grüneisen parameter diverges as $\Gamma_u \sim H^2/(T^2 \log 1/T)$ at the single-impurity quadrupole Kondo critical point. The experimentally determined

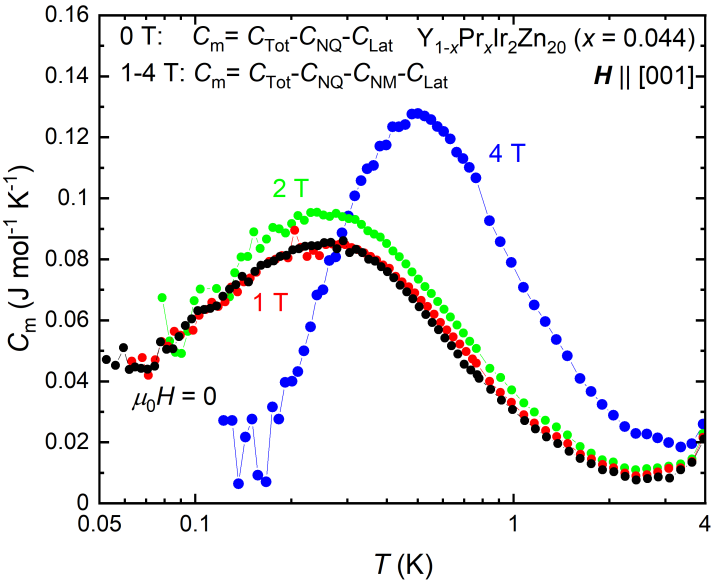

Figure 5.10: 4f contribution to the molar specific heat of $Y_{1-x}Pr_xIr_2Zn_{20}$ with $x = 0.044$ as a function of temperature at various magnetic fields $\boldsymbol{H} \parallel [001]$. C_m is corrected for a lattice, a nuclear quadrupole and a magnetic nuclear (only for the data measured at $\mu_0 H > 0\,\mathrm{T}$) contribution. The here shown specific heat data was measured and analyzed by Y. Yamane and S. Bachus. The high temperature part of C_m comes from Ref. [94].
This figure is also included in Ref. [134, SM].

Grüneisen parameter normalized to the second power of magnetic field $\Gamma_u/(\mu_0 H)^2$ as a function of temperature at various magnetic fields $\boldsymbol{H} \parallel [001]$ is shown in Fig. 5.8(b). At low magnetic field $\mu_0 H \leq 1\,\mathrm{T}$, the experimentally obtained data is in excellent agreement with the theoretical expectation, which is shown as a black solid line. This provides additional evidence for the quadrupolar Kondo nature of the ground state. The molar specific heat C_m used for the Grüneisen calculation was measured and analyzed by Y. Yamane and S. Bachus. The measurement was carried out on a single crystal that originates from the same batch as the single crystal used for the thermal expansion measurement and has a similar Pr doping level of $x = 0.044$. This is the same single crystal whose specific heat was already detailed before in Fig. 5.3 [94]. As the specific heat data in Fig. 5.3 has a quite high noise level at low temperatures, Y. Yamane and S. Bachus remeasured the specific heat of the single crystal at $T \leq 0.8\,\mathrm{K}$ by use of a better optimized experimental setup. For the Grüneisen analysis, this remeasured data was combined with the high temperature data at $T > 0.8\,\mathrm{K}$ from Ref. [94], which was already displayed in Fig. 5.3. The so derived specific heat data by Y. Yamane and S. Bachus is presented in Fig. 5.10. Note that C_m is corrected for a nuclear contribution and a lattice contribution. The nuclear contribution contains a quadrupolar component, which is already present in zero magnetic field, and a conventional magnetic field induced component. Y. Yamane determined the lattice contribution from a specific heat measurement on the reference compound YIr_2Zn_{20}. Despite the slightly higher Pr concentration of the single crystal with $x = 0.044$ used for the specific heat measurement as compared to the thermal expansion single crystal with $x = 0.036$, the sample employed for the specific heat measurement resides still in the single-impurity quadrupole Kondo regime, as Yamane et al. [42] clearly demonstrated. As both single

crystals have nearly the same Pr concentration, which is likely within the error bar of the determination method, α_u and C_m were not normalized to the Pr concentration before performing the Grüneisen analysis. It is noted that the Grüneisen parameter Γ_u at 0.5 T was calculated by using the C_m data measured at 0 T, as no data at 0.5 T exists. As Fig. 5.10 clearly shows, the specific heat curves at 0 T and 1 T are, within the error bar of the experiment, nearly identical. Consequently, the related error can be considered as negligible small. For the calculation of Γ_u at 1 T, 2 T and 4 T, α_u and C_m data sets were used, which were measured at an identical magnetic field.

After discussing the field induced quadrupolar response, which is in prefect agreement with the theoretical expected single-impurity quadrupole Kondo behavior, the focus is now on the unconventional divergence in the volume thermal expansion coefficient β found at zero and small magnetic field. To recall the data, which was already introduced at the beginning of this subsubsection, β at various magnetic fields $\boldsymbol{H} \parallel [001]$ is plotted again in Fig. 5.11(a). The inset displays the zero field volume thermal expansion coefficient $\beta = 3\alpha_{[001]}$ normalized to the Pr concentration x for various x. The fact that the divergence in β is already suppressed by a relatively small magnetic field of $\mu_0 H = 1.5$ T explicitly excludes a nuclear Schottky contribution as a possible cause for the unconventional volume collapse. In case of a nuclear Schottky contribution, a continuous increase of the divergence in β with magnetic field would be expected. Furthermore, a nuclear contribution usually does not manifest itself in the thermal expansion. The fact that the divergence appears in a similar magnetic field range as the single-impurity quadrupole Kondo behavior in α_u, C_m/T [94] and $(c_{11} - c_{12})/2$ [44], indicates a possible relation between the volume divergence and the single-impurity quadrupole Kondo ground state. Before providing possible scenarios that may account for this peculiar finding, extrinsic causes for the volume divergence should be excluded. In this regard, the small uniaxial stress exerted via the flat springs of the dilatometer on the single crystal has to be taken into consideration. As the thermal expansion coefficient of the $x = 0.036$ single crystal was measured along a cubic $\langle 100 \rangle$ direction, the small uniaxial stress exerted by the dilatometer results in a strain ε_u that couples linearly to the Γ_3 doublet. As shown by Yanagisawa et al. [44], the related $(c_{11} - c_{12})/2$ elastic constant of the material displays a logarithmic temperature variation at low temperature. According to Hook's law, this suggests that an unaixial stress applied along a cubic $\langle 100 \rangle$ direction induces an additional contribution to the thermal expansion coefficient $\alpha_{[001]} \sim \partial_T (c_{11} - c_{12})/2$. To elucidate whether the experimentally obtained thermal expansion contains such an uniaxial stress induced contribution, an additional thermal expansion measurement along the [111] direction of a similarly doped single crystal with $x = 0.033$ was carried out. This experiment is effective to cross-check the impact of uniaxial stress on the experimentally obtained $\alpha_{[001]}$ data, as an uniaxial stress induced strain $\varepsilon_{[111]}$ does not couple linearly to the Γ_3 ground state doublet. An extrinsic uniaxial stress induced contribution to the volume thermal expansion is therefore not expected for a measurement along the crystallographic [111] direction. Based on the fact that unstrained cubic materials feature an isotropic thermal expansion, meaning that $\alpha_{[001]} = \alpha_{[111]}$, possible deviations between these two measurements reveal unambiguously the presence of an uniaxial stress induced contribution to $\alpha_{[001]}$. Figure 5.11(b) shows a comparison between $\alpha_{[001]}$, measured on the single crystal with $x = 0.036$, and $\alpha_{[111]}$, measured on the single crystal with $x = 0.033$, at zero magnetic field. Both measurements were performed under small uniaxial stresses of $\sigma_{[001]} \approx -4$ MPa and $\sigma_{[111]} \approx -5$ MPa, respectively. This small uniaxial stress is an inevitable side effect of a relative length change measurement in the miniaturized capacitive dilatometer. The uniaxial stresses were estimated based on the force of $F \approx 4$ N [112], exerted by the flat

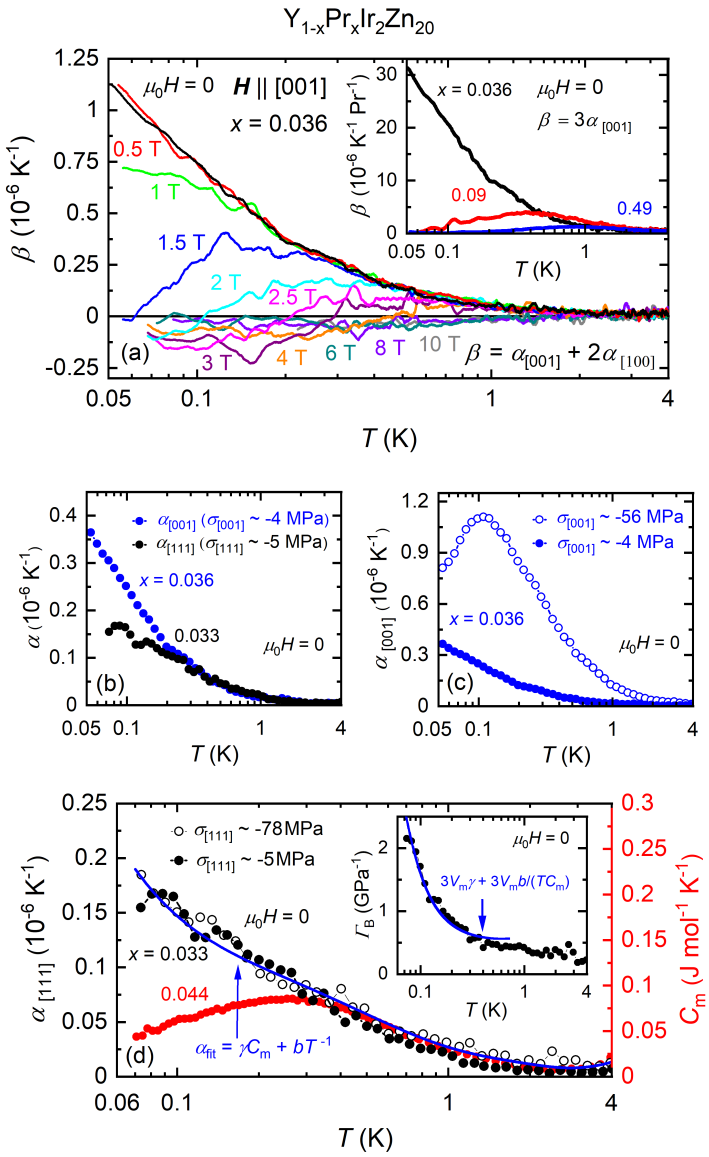

Figure 5.11: (a) Temperature variation of the volume thermal expansion coefficient $\beta = \alpha_{\parallel} + 2\alpha_{\perp}$ at different magnetic fields $\boldsymbol{H} \parallel [001]$. The inset displays the zero magnetic field volume thermal expansion coefficient $\beta = 3\alpha_{[001]}$ normalized to the Pr concentration x, for three different x values. (b) Zero magnetic field thermal expansion coefficients $\alpha_{[001]}$ and $\alpha_{[111]}$ as a function of temperature at low uniaxial stresses of $\sigma_{[001]} \approx -4\,\mathrm{MPa}$ and $\sigma_{[111]} \approx -5\,\mathrm{MPa}$, respectively. (c) Temperature dependence of $\alpha_{[001]}$ at low and high uniaxial stresses of $\sigma_{[001]} \approx -4\,\mathrm{MPa}$ and $\sigma_{[001]} \approx -56\,\mathrm{MPa}$, respectively. (d) Temperature dependence of $\alpha_{[111]}$ at low and high uniaxial stresses of $\sigma_{[111]} \approx -5\,\mathrm{MPa}$ and $\sigma_{[111]} \approx -78\,\mathrm{MPa}$, respectively. In addition, the zero field molar specific heat C_m, measured by Y. Yamane and S. Bachus, is shown in red. The high temperature part of C_m comes from Ref. [42]. A fit to $\alpha_{[111]}$ by use of the relation $\alpha_\mathrm{fit} = \gamma C_\mathrm{m} + bT^{-1}$ is plotted as a blue solid line. The inset shows the bulk Grüneisen parameter $\Gamma_\mathrm{B} = V_\mathrm{m}(3\alpha_{[111]}/C_\mathrm{m})$ as a function of temperature. The blue solid line is a fit to the data by the equation $\Gamma_\mathrm{fit} = 3V_\mathrm{m}\gamma + 3V_\mathrm{m}b/(TC_\mathrm{m})$. This figure is also included in Ref. [134].

springs of the miniaturized dilatometer[8] and the cross sectional areas of the examined single crystals. The cross sectional area was calculated from the length values of the two crystal sides perpendicular to the measurement direction, which are provided in Table 5.1. Note that this estimation is based on the assumption that the single crystals have a perfectly cuboid shape. The sketches of the investigated single crystals, which are shown in Fig. 5.6, indicate that this assumption is approximately justified. A comparison of the $\alpha_{[001]}$ and $\alpha_{[111]}$ data sets shown in 5.11(b) reveals small differences between the two measurements. In particular, the stronger divergence of $\alpha_{[001]}$ as compared to $\alpha_{[111]}$ suggests that the former expansivity contains a small but finite uniaxial stress induced contribution. Nevertheless, also $\alpha_{[111]}$ displays a clear divergence upon cooling, indicating that the divergence in $\alpha_{[001]}$ can only be partially triggered by the small uniaxial stress exerted by the flat springs of the dilatometer. An intrinsic divergent volume contribution must therefore also be present. To obtain further proof for this scenario, the uniaxial stress effect was examined more meticulously. To do so, $\alpha_{[001]}$ and $\alpha_{[111]}$ were measured in an uniaxial stress dilatometer [113]. The flat springs of this dilatometer are more rigid and the force acting on the single crystalline sample approximately fifteen times larger than the force exerted by the miniaturized capacitive dilatometer [112, 113]. Figure 5.11(c) shows a comparison between $\alpha_{[001]}$ measured at low and high uniaxial stresses of $\sigma_{[001]} \approx$ -4 MPa and $\sigma_{[001]} \approx$ -56 MPa, respectively. The force exerted by the uniaxial stress dilatometer on the sample in measurement direction was determined via the capacitance value at which the dilatometer was operated. This was done via the relation between the spring force and the capacitance value of the dilatometer derived by Küchler et al. [113], which is shown in Fig. 3.7. The $\alpha_{[001]}$ data obtained in the uniaxial stress dilatometer was measured at a capacitance value of $C \approx 19.5\,\mathrm{pF}$, which corresponds to a force $F \approx 58.7\,\mathrm{N}$. By taking the single crystal's cross sectional area into account, the uniaxial stress on the sample in measurement direction consequently calculates as $\sigma_{[001]} \approx -56\,\mathrm{MPa}$. As a substantial uniaxial stress acted on the single crystal in this experiment, it was examined with respect to a possible damage after the measurement was finished, whereby no evidence for a damage of the single crystal was found. The measurement in the uniaxial stress dilatometer clearly confirms the anticipated enormous impact of $\sigma_{[001]}$ on $\alpha_{[001]}$. Under a relatively high uniaxial stress of $\sigma_{[001]} \approx -56\,\mathrm{MPa}$, the divergent behavior in $\alpha_{[001]}$ vanishes. Instead a maximum arises at a temperature of approximately 0.11 K. This behavior is reminiscent of $\alpha_{\parallel}$ at a magnetic field of 2 T, as shown in Fig. 5.7(a), which is plausible, as both uniaxial stress and magnetic field applied along the [001] direction split the Γ_3 doublet. The suppression of the low temperature divergence in $\alpha_{[001]}$ demonstrates that the applied uniaxial stress of $\sigma_{[001]} \approx -56\,\mathrm{MPa}$ is sufficient to induce a splitting of the Γ_3 doublet that is strong enough to quench the quadrupole Kondo physics at low temperatures. By contrast, a notable impact of uniaxial stress $\sigma_{[111]}$ on $\alpha_{[111]}$ is not expected. In order to verify this assumption experimentally, $\alpha_{[111]}$ was also measured in the uniaxial stress capacitive dilatometer. A comparison between $\alpha_{[111]}$ at low and high uniaxial stresses of $\sigma_{[111]} \approx -5\,\mathrm{MPa}$ and $\sigma_{[111]} \approx -78\,\mathrm{MPa}$ is provided in Fig. 5.11(d). The measurement of $\alpha_{[111]}$ in the uniaxial stress dilatometer was carried out at a capacitance value of $C \approx 19.8\,\mathrm{pF}$, which corresponds to a force of $F \approx 59.1\,\mathrm{N}$. Taking the cross sectional area of the single crystal into account yields an uniaxial stress value of $\sigma_{[111]} \approx -78\,\mathrm{MPa}$. In analogy to the single crystal with $x = 0.036$, also the single crystal with $x = 0.033$ was examined with respect to a possible damage after the experiment. It is noted that the uniaxial stress induced tiny cracks in the single crystal. Despite the tiny cracks, the sample

[8] The given force value corresponds to a capacitance of 20 pF [112], which is close to the capacitance values at which the here shown measurement results were obtained.

was still one piece and did not break apart. It is therefore assumed that the small damage had no negative influence on the measurement result. Strikingly, the two $\alpha_{[111]}$ data sets obtained in the miniaturized and the uniaxial stress dilatometer do not differ from each other. This confirms unambiguously that the impact of $\sigma_{[111]}$ on $\alpha_{[111]}$ is negligible and the low temperature divergence in $\alpha_{[111]}$ indeed caused by a volume change. As the volume thermal expansion coefficient relates to the pressure dependence of entropy via the equation $\beta = -1/V(\partial_P S)$, the divergent β indicates the presence of a finite low temperature entropy that is distinguished by a significant hydrostatic pressure dependence. At a first glance, this result is surprising, as hydrostatic pressure does not break the material's cubic crystal symmetry and is therefore unsuitable to lift the degeneracy of the non-Kramers Γ_3 ground state doublet. A release of the low temperature entropy under hydrostatic pressure is consequently not expected. To emphasize the peculiarity of this finding, the molar specific heat C_m of a single crystal from the same batch with $x = 0.044$ is shown in Fig. 5.11(d) in red color. This is the same specific heat data set measured by Y. Yamane and S. Bachus, which was already presented in Fig. 5.10 in the context of the quadrupolar Grüneisen parameter analysis. It is recalled that the C_m data is corrected for a zero field nuclear quadrupole Schottky contribution and a lattice contribution. By contrast, the two data sets of $\alpha_{[111]}$ obtained at different uniaxial stresses are only corrected for the background contribution of the respective capacitive dilatometer. The suppression of the divergent volume thermal expansion at relatively small magnetic fields, as shown in Fig. 5.11(a), excludes a nuclear Schottky contribution to $\alpha_{[111]}$ and the vanishment of $\alpha_{[111]}$ at 4 K implicates that the lattice contribution to $\alpha_{[111]}$ is insignificantly small in the examined temperature range. The distinctly different behavior of $\alpha_{[111]}$ and C_m is a quite surprising finding, as the Grüneisen law suggests proportionality between the two thermodynamic quantities at mK temperatures, where the material should be governed by a single energy scale [54]. While C_m exhibits a distinct maximum at around 0.2 K, $\alpha_{[111]}$ diverges down to the lowest measured temperature of 0.07 K. To recall, Yamane et. al. [42,43] attributed the maximum in C_m to the single-impurity quadrupole Kondo effect as $C_\mathrm{m}/T \sim \log 1/T$. The clear difference between the specific heat and the volume thermal expansion coefficient implies the breakdown of Grüneisen scaling, which usually arises in HF metals at a QCP [11,58]. The bulk Grüneisen parameter, calculated as $\Gamma_\mathrm{B} = 3V_\mathrm{m}\alpha_{[111]}/C_\mathrm{m}$, is shown in the inset of Fig. 5.11(d). Γ_B displays an unconventional divergence at low temperature, which resembles the temperature dependence found in Γ_u. Note, for the calculation of Γ_B, neither $\alpha_{[111]}$ nor C_m were normalized to the Pr concentration based on the same reasoning discussed before in the context of Γ_u.

In order to identify the underlying mechanism that triggers the surprisingly different behavior in the specific heat and the bulk thermal expansion as well as the divergence in the bulk Grüneisen parameter, in the following, different scenarios are put under the microscope. As mentioned before, a divergence of the bulk Grüneisen parameter appears, for instance, in selected HF metals close to a magnetic QCP [58]. As the low temperature Kondo energy scale displays a significant pressure dependence, application of the latter is a highly effective means to tune a HF metal between its AFM ordered, QC and HF liquid ground states [11]. In the case of the single-impurity quadrupole Kondo critical point, a divergence of the bulk Grüneisen parameter is not expected, as hydrostatic pressure preserves the cubic crystal symmetry and does not tune the system away form its single-impurity quadrupole Kondo critical state. This implies a temperature independent Γ_B, whose magnitude directly reflects the pressure dependence of the quadrupole Kondo coupling constant. Consequently, a straightforward explanation in analogy to the magnetic HF metals cannot account for the experimentally observed divergence in the Grüneisen

parameter of highly diluted $Y_{1-x}Pr_xIr_2Zn_{20}$. To shed light on this peculiar experimental finding, M. Garst performed calculations, which take the elastic properties of the non-Kramers ground state doublet into account and revealed two possible scenarios that may account for the divergence in the volume thermal expansion emerging in highly diluted $Y_{1-x}Pr_xIr_2Zn_{20}$. The following lines review the key results of the calculations carried out by M. Garst, which comprise Eq. (5.5) and Eq. (5.6) and the associated explanations.

A hallmark of the single-impurity quadrupole Kondo effect is the related residual entropy. In a real system, however, as temperature approaches zero, this entropy will be ultimately released via the elastic coupling, i.e. the system undergoes a tetragonal distortion and the degeneracy of the ground state doublet is lifted. This lattice instability is triggered by the softening of the respective symmetrized elastic constant $(c_{11} - c_{12})/2$. As pointed out before, the strength of the coupling between this instability and the lattice is modulated by the quadrupole-strain coupling constant g_{Γ_3}. A first calculation carried out by M. Garst revealed that in case the quadrupole-strain coupling constant depends on hydrostatic pressure, the divergence in χ_Q, which causes the softening of $(c_{11} - c_{12})/2$, also manifests itself in the volume, as described by the following equation that suggests a correction to β due to dynamical strain fields

$$\delta\beta_{\mathrm{DSF}} = -\frac{1}{2}\left[\frac{\partial}{\partial p}\left(g_{\Gamma_3}^2 n_{\mathrm{Pr}}\langle\varepsilon_{\Gamma_3}^2\rangle_0 \frac{\partial\chi_Q}{\partial T}\right)\right] \overset{\mathrm{QKE}}{=} \frac{1}{2}\left[\frac{\partial}{\partial p}\left(g_{\Gamma_3}^2 n_{\mathrm{Pr}}\langle\varepsilon_{\Gamma_3}^2\rangle_0 A_Q^S\right)\right]\frac{1}{T}, \tag{5.5}$$

where $\chi_Q = A_Q^S \log 1/T$, under the assumption of quadrupolar Kondo correlations, which is justified based on the elastic constant results of Yanagisawa et al. [44] and the results on α_u discussed before. A_Q^S is a constant and $\langle\varepsilon_{\Gamma_3}^2\rangle_0$ are the zero point fluctuations of the Γ_3 doublet. A notable result is the proportionality between $\delta\beta_{\mathrm{DSF}}$ and the temperature derivative of the quadrupole-strain susceptibility $\partial_T\chi_Q$. Note that $\delta\beta_{\mathrm{DSF}}$ is only sizable when the term $g_{\Gamma_3}^2 n_{\mathrm{Pr}}\langle\varepsilon_{\Gamma_3}^2\rangle_0 A_Q^S$ displays a pronounced pressure dependence, whereby the contribution arising from the pressure dependence of the quadrupole-strain coupling constant $\partial_P g_{\Gamma_3}^2$ must be the dominant one.

In addition, M. Garst considered the impact of disorder induced static strain fields, which locally break the cubic symmetry at a Pr site, on the volume thermal expansion coefficient. In the materials examined in the scope of this work, such disorder may, for instance, be evoked by the partial substitution of the Pr^{3+} ions by Y^{3+} ions. As the Y^{3+} ions exhibit a smaller ionic radius than the Pr^{3+} ions, the substitution must alter the local point group symmetry at a Pr site. Even though the Pr doping of the here investigated single crystal is with 3.6 % very small and the sample quality very high, as evidenced by a RRR of 160 [129], tiny strain fields cannot be excluded. As the degeneracy of the Γ_3 doublet is easily lifted by such strain fields, even in the dilute limit, a tiny splitting of the Γ_3 ground state doublet is likely present. The large value of β indicates that these local strain fields must be highly susceptible to an externally applied hydrostatic pressure, which triggers another indirect coupling between the quadrupole Kondo physics and the volume. The essence of the second calculation carried out by M. Garst is that substitution induced static strain fields evoke another correction to the volume thermal expansion, which reads as

$$\delta\beta_{\mathrm{SSF}} \sim n_{\mathrm{Pr}}^3 \frac{\partial\chi_Q}{\partial T} \overset{\mathrm{QKE}}{\sim} \frac{1}{T}, \tag{5.6}$$

and therefore shows the same temperature dependence as $\delta\beta_{\mathrm{DSF}}$. The dependence of $\delta\beta_{\mathrm{SSF}}$ on the third power of n_{Pr} indicates that this correction is likely quite small for small doping but grows significantly by increasing Pr concentration. However, not only static strain fields caused by the Pr disorder, but also the ones related to dislocations

in the crystal structure can principally lift the degeneracy of the ground state doublet. According to M. Garst, the contribution to $\delta\beta_{\mathrm{SSF}}$ arising from conventional dislocations exhibits a linear dependence on the Pr density $\delta\beta_{\mathrm{SSF}} \sim n_{\mathrm{Pr}}\partial_T\chi_{\mathrm{Q}}$. In the case of the highly diluted single crystals, it is therefore conceivable that the static strain field contribution induced by dislocation dominates over the one induced by Pr disorder. In summary, M. Garst could show theoretically that in presence of the single-impurity quadrupole Kondo effect, both dynamical and static strain fields can principally induce the same divergent correction to the volume thermal expansion $\delta\beta \sim \partial_T\chi_{\mathrm{Q}} \overset{\mathrm{QKE}}{\sim} 1/T$.

When combining the two just specified contributions with the one arsing from the quadrupole Kondo coupling, which triggers the logarithmic divergence in C_{m}/T, the volume thermal expansion coefficient β of a single-impurity quadrupole Kondo hybridized metal reads as

$$\beta = \beta_{\mathrm{QKE}} + \delta\beta_{\mathrm{DSF,SSF}} = \gamma C_{\mathrm{m}} + \frac{b}{T}. \tag{5.7}$$

Note that the contribution to β arising from the quadrupole Kondo coupling β_{QKE} is estimated from the specific heat data C_{m} in zero field. As a low temperature divergence was not found in the C_{m} data, the contribution arising from static or dynamical strain fields, which is expected to show the same temperature dependence in the specific heat and in the volume thermal expansion coefficient, must be insignificant small. The scaling parameter γ in Eq. (5.7) denotes the Grüneisen parameter, which quantifies the hydrostatic pressure dependence of the quadrupole Kondo coupling constant. The parameter b in the second term is simply a constant. In order to verify the applicability of Eq. (5.7) to the experimentally obtained data, the blue solid line in Fig. 5.11(d) shows a fit to $\alpha_{[111]}$ by using Eq. (5.7). The excellent agreement with the experimentally obtained data confirms the theoretical prediction and reveals that the low temperature thermal expansion of $Y_{1-x}Pr_xIr_2Zn_{20}$ with $x = 0.036$ is indeed governed by two critical contributions. As both dynamical and static strain fields yield a contribution to β with the same $1/T$ temperature dependence, it is difficult to judge, which of the two contributions causes the divergent behavior in $\alpha_{[111]}$. To further clarify this issue, in the following, the specific heat and the bulk Grüneisen parameter are taken into account. A direct consequence of the different behavior in the low temperature specific heat $C_{\mathrm{m}}/T \sim \log 1/T$ and the thermal expansion $\alpha_{[111]} = \gamma C_{\mathrm{m}} + b/T$ is the divergence of the bulk Grüneisen parameter $\Gamma_{\mathrm{B}} = 3V_{\mathrm{m}}\gamma + 3V_{\mathrm{m}}b/(C_{\mathrm{m}}T)$, which is indicated by the blue solid line in the inset of Fig. 5.11(d). Interestingly, the temperature dependence of Γ_{B} resembles the behavior found in the quadrupolar Grüneisen parameter $\Gamma_{\mathrm{u}} \sim H^2/(T^2 \log 1/T)$.

The divergent and significantly enhanced Γ_{B} suggests that the related low temperature energy scale E^* shows a considerable pressure dependence, as [54]

$$\Gamma_{\mathrm{B}} \sim \frac{\partial E^*}{\partial p}. \tag{5.8}$$

To compare the magnitude of the obtained bulk Grüneisen parameter with the one of a magnetic HF metal at a QCP, the maximal value of $\Gamma_{\mathrm{B}} \approx 2.15\,\mathrm{GPa}^{-1}$ at the lowest measured temperature is multiplied by the background bulk modulus c_{B}^0 in order to obtain a dimensionless Grüneisen parameter. For this estimation, the background bulk modulus c_{B}^0 of $PrIr_2Zn_{20}$ was used, as no literature value for the diluted $Y_{1-x}Pr_xIr_2Zn_{20}$ system exists. The value $c_{\mathrm{B}}^0 = (c_{11}^0 + 2c_{12}^0)/3 = 94.05\,\mathrm{GPa}$ was estimated from the $c_{11}^0 = 161.7\,\mathrm{GPa}$ [37] and $(c_{11}^0 - c_{12}^0)/2 = 50.74\,\mathrm{GPa}$ [37] background elastic constants of $PrIr_2Zn_{20}$. This yields a dimensionless Grüneisen parameter of $\Gamma_{\mathrm{B}} \approx 202$ at 0.07 K, whose magnitude is comparable to magnetic HF metals at a QCP [58]. For the quadrupole-strain coupling

term, such a substantial pressure dependence is unexpected. Certainly, the application of hydrostatic pressure would lead to an increase of the quadrupole-strain interaction constant. However, a pressure dependence that has the same order of magnitude as the one of a HF metal at a QCP is quite surprising. From literature it is known that the free electron gas is described by an electronic Grüneisen parameter of $\Gamma_{\mathrm{elec}} = 2/3$ [52, p. 641], which would be the order of magnitude also expected for the quadrupole-strain coupling. Next, the likelihood of the disorder scenario, which deals with disorder induced local static strain fields is briefly discussed. Provided that the cubic symmetry of the system is slightly broken by static strain disorder, it is conceivable that also hydrostatic pressure may directly couple to the static strain fields and therefore serve as an indirect tuning parameter for the splitting of the Γ_3 ground state doublet. A large Grüneisen ratio is therefore generally more conceivable than for the dynamical strain field scenario. The fact that the static strain field contribution evoked by the Pr disorder to β must scale with the third power of n_{Pr}, casts, however, doubt on whether this effect can really account for the observed behavior. More likely would be a contribution that arises from conventional dislocations, which would scale linearly with n_{Pr}, as pointed out a a few lines before.

Consequently, even though both theoretical scenarios proposed by M. Garst imply a contribution to the volume thermal expansion whose theoretical temperature dependence is principally in line with the experimental finding, it is difficult to make a final statement on which of the two contributions may trigger the unconventional divergent behavior in the volume thermal expansion. Further experiments on the highly diluted single crystals may be helpful to clarify this issue. In order to quantify the pressure dependence of the quadrupole-strain coupling constant g_{Γ_3}, measurements of the $(c_{11}-c_{12})/2$ elastic constant under hydrostatic pressure would be a powerful means. In order to examine the impact of static strain fields more in detail, volume thermal expansion measurements on a series of differently doped $Y_{1-x}Pr_xIr_2Zn_{20}$ single crystals in the highly diluted range would allow to specify a possible scaling of the low temperature volume divergence with n_{Pr}. In addition, assessing the impact of local strain fields on the quadrupole Kondo physics by using other suitable local probes would be desirable.

Moderately Diluted Single Crystals ($x = 0.09$ and $x = 0.49$)

In this subsubsection, the thermal expansion results obtained on the two moderately diluted $Y_{1-x}Pr_xIr_2Zn_{20}$ single crystals with $x = 0.09$ and $x = 0.49$ are detailed. Purpose of the measurements was to gain better understanding of the quadrupole Kondo ground state by systematically studying the evolution of the unconventional behavior with increasing Pr doping. Furthermore, the results are compared to the previously published specific heat and electrical resistivity data by Yamane et al. [42, 43].

Figure 5.12 shows the temperature dependence of the longitudinal thermal expansion coefficient $\alpha_{\parallel}$ of single crystalline $Y_{1-x}Pr_xIr_2Zn_{20}$ with $x = 0.09$ at various magnetic fields $\boldsymbol{H} \parallel [001]$. Additionally shown dashed lines are CEF simulations. The quadrupolar expectation values used to calculate the CEF thermal expansion were simulated by use of the Mathematica based CEF program provided by T. Onimaru, which evaluates the Hamiltonian specified by Eq. (4.12). In order to carry out the simulation, the CEF parameters $W = -1.44\,\mathrm{K}$ and $x = 0.537$ were employed. Adjusting the W parameter to a value of $W = -1.44\,\mathrm{K}$ was necessary in order to obtain the best accordance with the experimentally measured data at 10 T. Note that this value is slightly smaller than the value of $W = -1.50\,\mathrm{K}$ used in the preceding subsubsection for the simulation of the thermal expansion of the single crystal with $x = 0.036$. A possible explanation for the reduction of W, which implies a weakening of the CEF effect, is the slightly higher Pr

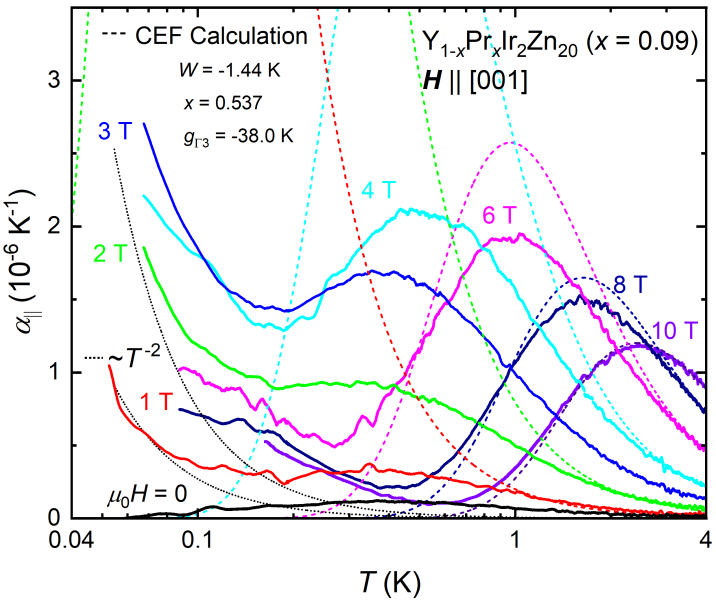

Figure 5.12: Longitudinal thermal expansion coefficient $\alpha_{\parallel}$ as a function of temperature of $Y_{1-x}Pr_xIr_2Zn_{20}$ with $x = 0.09$ at various magnetic fields $\boldsymbol{H} \parallel [001]$. The zero field thermal expansion coefficient is also included in Ref. [134]. Additionally shown dashed lines are CEF calculations that employ the CEF parameters $W = -1.44\,\mathrm{K}$ and $x = 0.537$ and a quadrupole-strain coupling constant $g_{\Gamma_3} = -38.0\,\mathrm{K}$.

concentration of the here examined single crystal as compared to the single crystal with $x = 0.036$. Another parameter necessary for the simulation is the number of Pr^{3+} ions per volume $n_{\mathrm{Pr}} = 0.251 \times 10^{27}\,\mathrm{m}^{-3}$, which was calculated by using the lattice constant of $a = 14.2017 \times 10^{-10}\,\mathrm{m}$ [129] of a single crystal with a similar Pr doping of $x = 0.085$. As $(c_{11}^0 - c_{12}^0)/2$ has not yet been reported in literature for a single crystal with a Pr concentration of $x = 0.09$, the literature value $(c_{11}^0 - c_{12}^0)/2 = 52.771\,\mathrm{GPa}$ [44, SM] of a single crystal with $x = 0.034$ was employed. The quadrupole-strain coupling constant was determined at $g_{\Gamma_3} = -38.0\,\mathrm{K}$ by the usual procedure, i.e. fitting the CEF calculation to the experimentally obtained data at the highest measured magnetic field of 10 T. Due to the relatively small Pr concentration of $x = 0.09$, it was assumed that the quadrupole-quadrupole interaction is negligible small and the quadrupole-quadrupole coupling constant was therefore set to zero in the calculation, i.e. $K_{\Gamma_3} = 0$. Also the interaction constant between the field induced dipole moments was neglected, i.e. $K = 0$. For the calculation of the longitudinal thermal expansion coefficient, the contribution of a possible bulk thermal expansion was disregarded, which follows the procedure applied before on pure $PrIr_2Zn_{20}$ and highly diluted $Y_{1-x}Pr_xIr_2Zn_{20}$ with $x = 0.036$. After this brief overview of the simulation parameters, the focus is now on the experimentally determined data.

The thermal expansion coefficient at zero magnetic field, which was already presented in the preceding subsubsection, shows a maximum at around 0.4 K and decreases continuously to zero as temperature declines. This behavior is in stark contrast to the divergence in zero magnetic field that emerges in the highly diluted single crystals with $x \leq 0.036$ and clearly excludes the formation of the quadrupolar Kondo effect. Based on the possible coupling between the volume and χ_{Q} by means of dynamical or static strain fields, as discussed a few pages before, a divergent volume thermal expansion coefficient would be

expected in presence of the single-impurity quadrupolar Kondo effect. As detailed in the preceding subsubsection, the small uniaxial stress applied by the miniaturized capacitive dilatometer causes an additional coupling to χ_Q, which would also induce a divergent contribution to the thermal expansion provided that the single-impurity quadrupole Kondo effect is present. The experimentally found suppression of the zero field thermal expansion coefficient with declining temperature consequently excludes a single-impurity quadrupole Kondo ground state. This finding is in very good conformity with the previously published specific heat data obtained on a single crystal with $x = 0.085$ by Yamane et al. [42,43], for which saturation in C_m/T at low temperature was reported. A possible explanation for the breakdown of the Kondo physics and the formation of the low temperature maximum is a splitting of the Γ_3 ground state doublet due to disorder [42, 43]. If the distortion induced splitting of the Γ_3 doublet dominates at low temperature over the quadrupole Kondo physics, a suppression of the logarithmic divergence in χ_Q is expected. The low temperature maximum in the volume thermal expansion supports this scenario. Also short range quadrupolar correlations might be a conceivable explanation [42].

Next, the longitudinal thermal expansion coefficient $\alpha_\parallel$ measured parallel to magnetic field $\boldsymbol{H} \parallel [001]$ is detailed. As soon as a magnetic field is applied, $\alpha_\parallel$ grows in magnitude, which is a direct consequence of the quadratic splitting of the Γ_3 doublet in magnetic field. Even though $\alpha_\parallel$ increases notably in magnitude with magnetic field, the position of the maximum at 0.4 K does not change up to threshold magnetic field of 3 T. Surprisingly, also for the $x = 0.09$ single crystal, a magnetic field induced divergence in $\alpha_\parallel$ develops at very low temperatures, which is most pronounced at approximately 3 T. By further increasing magnetic field, the divergence is still present but its magnitude declines. At low magnetic field, the field induced divergence is roughly proportional to $\sim 1/T^2$, as indicated by the black dotted line in Fig. 5.12. With reference to the preceding subsubsection, this can be interpreted as a signature of an unhybridized Γ_3 doublet for which $\alpha_u \sim \partial_T \chi_Q^F H^2 \sim H^2/T^2$ is expected for small $\boldsymbol{H} \parallel [001]$. Even though Yamane et al. [42, 43] suggested based on their specific heat measurement and RTL level calculation that the ground state of the material is likely already split, it is conceivable that a small fraction of the Pr^{3+} ions is not affected by this splitting and still shows a degenerate ground state. The degeneracy of the Γ_3 ground state doublet of this small fraction of Pr^{3+} ions may then be broken by the applied magnetic field. In consequence, the related α_u would show proportionality to $\partial_T \chi_Q^F$ for small $\boldsymbol{H} \parallel [001]$. In addition, the magnitude of the experimentally found divergence is distinctly small as compared to the CEF calculation, which is in line with only a small fraction of the Pr^{3+} ions being involved in this process. On the other hand, the thermal expansion result may also indicate that the field insensitive maximum at around 0.4 K does not relate to the disorder induced splitting of the Γ_3 ground state but to emergent short range quadrupolar correlations. Note that in pure $PrIr_2Zn_{20}$ also a field induced divergence in the low temperature thermal expansion was found inside the AFQ ordered phase. Consequently, both the thermal expansion coefficients obtained in zero and small magnetic fields exclude the formation of the single-impurity quadrupole Kondo ground state in the material. Specification of the possible ground state is, however, not possible based on the thermal expansion measurement results. Finally, the focus is on the $\alpha_\parallel$ data obtained at intermediate and high magnetic fields. Once the aforementioned threshold field of 3 T is breached, the maximum in $\alpha_\parallel$ at around 0.4 K begins to shift to higher temperatures with magnetic field. For $\mu_0 H \geq 4$ T, the continuous shift of the maximum to higher temperature and the reduction of its peak value strongly point towards a Schottky anomaly that arises from the splitting of the Γ_3 doublet in magnetic field.

In order to better classify the found behaviors, the experimentally obtained data is

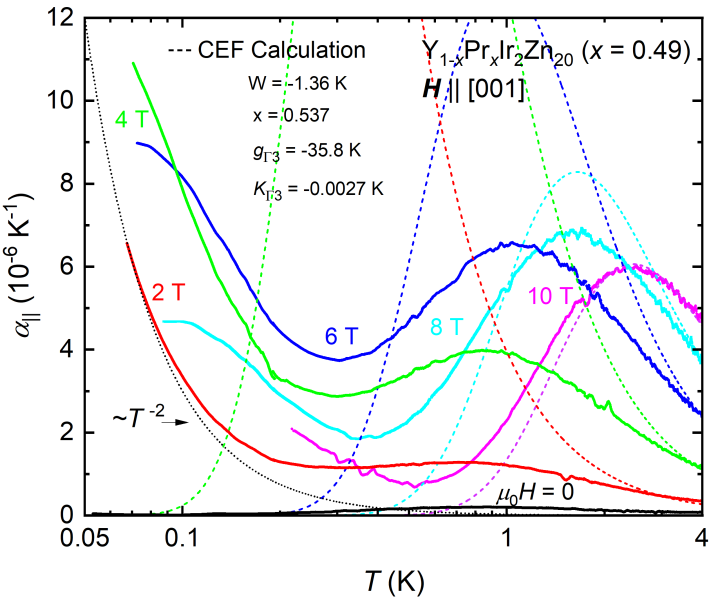

Figure 5.13: Longitudinal thermal expansion coefficient $\alpha_{\|}$ as a function of temperature of $Y_{1-x}Pr_xIr_2Zn_{20}$ with $x = 0.49$ at different magnetic fields $\boldsymbol{H} \parallel [001]$. The thermal expansion coefficient at zero magnetic field is also included in Ref. [134]. Additionally shown dashed lines are CEF calculations that employ the CEF parameters $W = -1.36\,\mathrm{K}$ and $x = 0.537$, a quadrupole-strain coupling constant $g_{\Gamma_3} = -35.8\,\mathrm{K}$ and a quadrupole-quadrupole interaction constant $K_{\Gamma_3} = -0.0027\,\mathrm{K}$.

compared with a CEF calculation in the following. In analogy to the before detailed results on pure $PrIr_2Zn_{20}$ and highly diluted $Y_{1-x}Pr_xIr_2Zn_{20}$ with $x = 0.036$, only the data at high magnetic field can be reproduced by the CEF simulation. The calculation therefore confirms the conjectured Schottky nature of the experimentally observed maximum at elevated temperatures and high magnetic fields $\mu_0 H \geq 6\,\mathrm{T}$. Analogously to $PrIr_2Zn_{20}$ and highly diluted $Y_{1-x}Pr_xIr_2Zn_{20}$ with $x = 0.036$, $\alpha_{\|}$ starts to increase again well below the Schottky maximum, which is unexpected, as the ground state should be a singlet. The peculiar low temperature enhancement manifesting itself at high magnetic fields must therefore be an universal feature that arises not only in the pure system but also in the diluted samples. As a convincing explanation for this highly unconventional behavior cannot be given at this point, future measurements have to address the high field phase emerging at low temperatures. After discussing the thermal expansion of the single crystal with $x = 0.09$, in the following, the effect of a further increasement of the Pr doping on the thermal expansion coefficient is examined on the example of a single crystal with a moderate Pr concentration of $x = 0.49$.

Figure 5.13 shows the temperature dependence of the longitudinal thermal expansion coefficient $\alpha_{\|}$ of $Y_{1-x}Pr_xIr_2Zn_{20}$ with $x = 0.49$ at various magnetic fields $\boldsymbol{H} \parallel [001]$, whereby the additionally shown dashed lines denote CEF simulations. The quadrupolar expectation values used to calculate the CEF thermal expansion coefficient were simulated by use of the Mathematica based CEF program provided by T. Onimaru, which evaluates the Hamiltonian given by Eq. (4.12). The simulation uses slightly modified CEF parameters of $W = -1.36\,\mathrm{K}$ and $x = 0.537$. Similar to the two higher diluted single crystals, the value of W had to be adjusted as compared to the one derived for pure $PrIr_2Zn_{20}$

by inelastic neutron scattering [65] in order to achieve a good accordance between the experimentally obtained data at 10 T and the simulated one. It is reasonable that the W parameter estimated for the single crystal with $x = 0.49$ is closest to the one of pure $PrIr_2Zn_{20}$ among the three diluted single crystals. Owing to the moderate Pr concentration of $x = 0.49$, a quadrupole-quadrupole interaction of $K_{\Gamma_3} = -0.0027\,\mathrm{K}$ was used for the simulation. The number of Pr^{3+} ions per volume $n_{Pr} = 1.363 \times 10^{27}\,\mathrm{m}^{-3}$ was calculated by use of the lattice parameter $a = 14.2215 \times 10^{-10}\,\mathrm{m}$ [43, 129], which is the one of a single crystal from the same batch having a similar Pr doping level of $x = 0.44$. The quadrupole-strain coupling constant was determined at $g_{\Gamma_3} = -35.8\,\mathrm{K}$ by scaling the simulated curve at 10 T to the experimentally determined data. Following the simulation procedures used for the other single crystals, a possible volume contribution to the thermal expansion was disregarded. It is justified to make this assumption for the moderately doped single crystal based on the vanishment of the volume thermal expansion at high magnetic field found both in the highly diluted and pure system. Before discussing the simulated thermal expansion data more in detail, the focus shall be on the experimentally obtained data.

Analogously to the single crystal with $x = 0.09$, the thermal expansion coefficient measured in zero magnetic field shows a maximum at a temperature of 0.85 K and vanishes to zero as temperature declines. By following the same line of reasoning applied to the single crystal with $x = 0.09$, the absence of a divergence in the zero field thermal expansion coefficient clearly excludes a single-impurity quadrupole Kondo ground state. Having the specific heat measurement results by Yamane et al. [42] in mind, the maximum in the thermal expansion can be likely assigned to short range quadrupolar correlations. Next, the behavior in magnetic field $\boldsymbol{H} \parallel [001]$ is scrutinized. As soon as magnetic field is applied to the material, a clear divergence arises in $\alpha_{\parallel}$ at the lowest measured temperatures. In close resemblance to the single crystal with $x = 0.09$, the divergence emerging at low magnetic field displays a temperature dependence $\sim T^{-2}$. As outlined before, this is the theoretically expected behavior for unhybridized Γ_3-type quadrupole moments in a small symmetry breaking magnetic field $\boldsymbol{H} \parallel [001]$. The distinctly small magnitude of the divergence as compared to the CEF calculation suggests that only a small fraction of the single crystal's Pr^{3+} ions can be accountable for the divergent behavior at low temperature. The maximum position in $\alpha_{\parallel}$ found in zero magnetic field depends only weakly on magnetic field up to 2 T. At magnetic fields of 4 T and 6 T a minor shift of the maximum to higher temperature can be observed. For $\mu_0 H \geq 8\,\mathrm{T}$, the maximum shifts noticeably to higher temperatures and its peak value decreases. This clearly indicates the Schottky nature of the high field maximum. Unexpectedly, and in analogy to the two lower doped $Y_{1-x}Pr_xIr_2Zn_{20}$ single crystals and to $PrIr_2Zn_{20}$, at high magnetic field, $\alpha_{\parallel}$ starts to increase again well below the Schottky maximum temperature. In concert with the other single crystals investigated in this thesis, the CEF calculation can only explain the physical effects emerging at high magnetic field. By contrast, at low magnetic field and low temperature, the experimentally found behavior deviates substantially from the theoretical expectation for a fully localized quadrupolar ground state doublet. In the moderately diluted single crystals with $x = 0.49$, the deviations can likely be related to emerging short range quadrupolar correlations [42].

In summary, the behaviors found in the thermal expansion coefficients of the single crystals with $x = 0.09$ and $x = 0.49$ are reminiscent of each other. In both samples, the absence of a divergence in the thermal expansion coefficient at zero magnetic field clearly excludes the quadrupole Kondo effect as the ground state of the system. Yamane et al. [42, 43] argued based on specific heat and electrical resistivity measurements that

the ground state is likely a short range quadrupole ordered or disordered state. While this conjecture is supported by the thermal expansion measurement, it is difficult to specify which of these two mechanisms is accountable for the suppression of the single-impurity quadrupole Kondo effect.

5.2.3 Magnetostriction

Besides the just detailed thermal expansion, also the magnetostriction of the three differently doped $Y_{1-x}Pr_xIr_2Zn_{20}$ single crystals with $x = 0.036$, $x = 0.09$ and $x = 0.49$ was measured as a function of $\boldsymbol{H} \parallel [001]$. In case of the highly diluted single crystal with $x = 0.036$, both longitudinal and transverse magnetostriction measurements were carried out in order to deduce the volume magnetostriction. For details on the measurement process of the longitudinal and transverse magnetostriction it is referred to Section 5.2.2, where the alignment process of the single crystalline sample in magnetic field was explicitly discussed. In addition, the longitudinal magnetostriction of two moderately doped single crystals with $x = 0.09$ and $x = 0.49$ was measured for reasons of comparison.

The longitudinal magnetostriction of the single crystal with $x = 0.036$, which is presented in Fig. 5.14(a), was measured together with Y. Yamane while he was staying at the University of Augsburg for a four week research visit. All other magnetostriction measurement results presented in this subsection, namely the transverse magnetostriction of the single crystal with $x = 0.036$ and the longitudinal magnetostriction of the single crystals with $x = 0.09$ and $x = 0.49$ were obtained by me alone. A preliminary analysis before dilatometer background subtraction of the longitudinal, transverse and volume magnetostriction of the single crystal with $x = 0.036$ presented in Fig. 5.14 of this subsection, was already shown in the doctoral thesis of Y. Yamane [129].

Highly Diluted Single Crystal ($x = 0.036$)

Together with part of the just detailed thermal expansion results, the magnetostriction results on the highly diluted $Y_{1-x}Pr_xIr_2Zn_{20}$ single crystal with $x = 0.036$, presented in this subsubsection, are also part of the submitted manuscript [134] mentioned in Section 5.2.2. Figures shown in the following that are also included therein are marked by the respective citation [134] in the figure caption. (*Note added before publication of this thesis: Above mentioned manuscript was published on the 6th of June 2022 in the scientific journal Physical Review Research* [134].)

Figure 5.14(a) displays both the longitudinal $(\Delta L/L)_{\parallel}$ and the transverse $(\Delta L/L)_{\perp}$ magnetostriction of $Y_{1-x}Pr_xIr_2Zn_{20}$ with $x = 0.036$ for $\boldsymbol{H} \parallel [001]$ at different temperatures, whereby the dashed lines denote CEF calculations. For details on the CEF simulation, it is referred to Section 4.2.2, which provides details on the simulation process. The quadrupolar expectation values, based on which the CEF magnetostriction curves were calculated, were simulated by using the Mathematica based CEF program provided by T. Onimaru, which evaluates the Hamiltonian specified by Eq. (4.12). In order to calculate the magnetostriction of the $x = 0.036$ single crystal, the same CEF parameters as employed for the simulation of the thermal expansion coefficient of the same sample, namely $W = -1.50\,\mathrm{K}$ and $x = 0.537$, were utilized. The same holds for the number of Pr^{3+} ions per volume $n_{\mathrm{Pr}} = 0.101 \times 10^{27}\mathrm{m}^{-3}$ and the Γ_3-type background elastic constant $(c^0_{11} - c^0_{12})/2 = 52.771\,\mathrm{GPa}$ [44, SM]. As the single crystal contains only a small fraction of Pr^{3+} ions, a possible inter-site interaction was disregarded in the calculation, i.e. $K_{\Gamma_3} = 0$. The same holds for the interaction between the field induced dipole moments, i.e. $K = 0$. The quadrupole-strain coupling constant was determined at $g_{\Gamma_3} = -35.0\,\mathrm{K}$

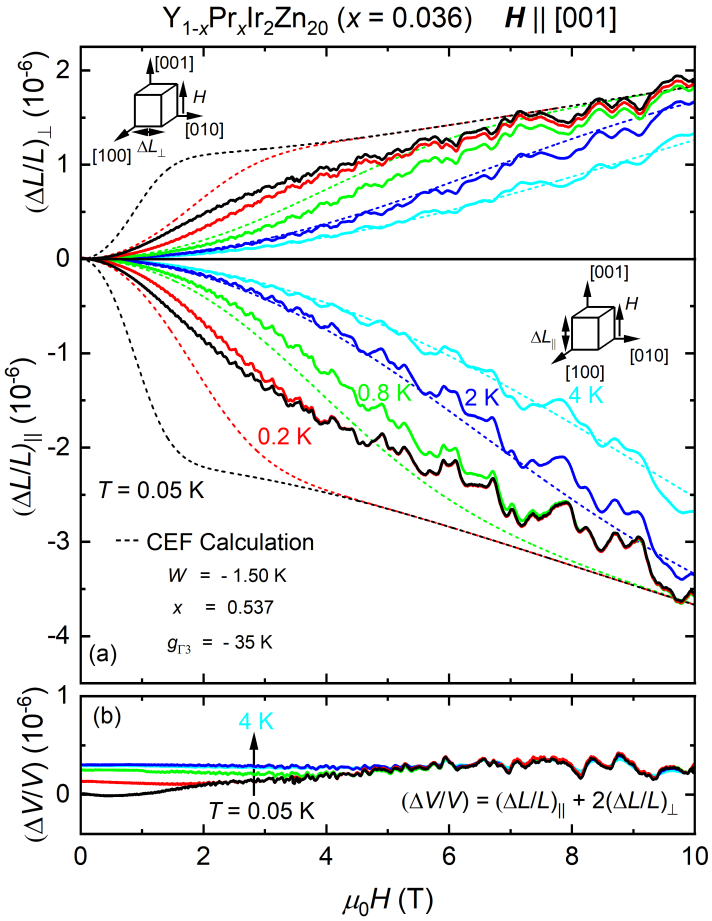

Figure 5.14: Magnetic field dependence of the longitudinal, transverse and volume magnetostriction $(\Delta L/L)_{\parallel}$, $(\Delta L/L)_{\perp}$ and $\Delta V/V$ for $\boldsymbol{H} \parallel [001]$ of $Y_{1-x}Pr_xIr_2Zn_{20}$ with $x = 0.036$ at various temperatures. (a) $(\Delta L/L)_{\parallel}$ and $(\Delta L/L)_{\perp}$ as a function of magnetic field at various temperatures. Additionally displayed dashed lines are CEF calculations, which were calculated by using the CEF parameters $W = -1.50\,\mathrm{K}$ and $x = 0.537$ and a quadrupole-strain coupling constant $g_{\Gamma_3} = -35.0\,\mathrm{K}$. (b) Volume magnetostriction $\Delta V/V = (\Delta L/L)_{\parallel} + 2(\Delta L/L)_{\perp}$ at various temperatures.
This figure is also included in Ref. [134, SM].

by comparing the CEF simulation to the experimentally obtained magnetostriction at a temperature of 4 K. This value is somewhat larger than the value deduced by the thermal expansion analysis, which suggested $g_{\Gamma_3} = -28.9\,\mathrm{K}$. As the 10 T Schottky maximum in the thermal expansion, to which the simulated data was fitted, appears at a slightly lower temperature of around 2.5 K, it is conceivable that the g_{Γ_3} value deduced from the thermal expansion analysis is a slight underestimate. In any case, the discrepancies are small and the derived value in good agreement with the elastic constant result of $|g_{\Gamma_3}| = 19.0\,\mathrm{K}$ [44]. A possible bulk contribution was neglected in the simulation, as the experimentally obtained data shown in Fig. 5.14 clearly demonstrates that the strain ε_{u} prevails over the bulk contribution ε_{B} at high magnetic field.

Before coming back to the simulated curves, the focus is on the experimentally determined magnetostriction data. $(\Delta L/L)_{\parallel}$ and $(\Delta L/L)_{\perp}$ for $\boldsymbol{H} \parallel [001]$, as presented in

Figure 5.14(a), display substantial anisotropy, which is a clear signature of the field induced $\langle O_2^0 \rangle$ quadrupole moment. While $(\Delta L/L)_\parallel$ exhibits a negative slope in the whole measured magnetic field range, $(\Delta L/L)_\perp$ shows a positive one. Both strains are approximately symmetric to each other with respect to the x-axis, whereby the magnitude of $(\Delta L/L)_\perp$ is only about half in size as compared to $(\Delta L/L)_\parallel$. This is reminiscent of the behavior found in $\alpha_\parallel$ and $\alpha_\perp$. As temperature declines, the anisotropy between $(\Delta L/L)_\parallel$ and $(\Delta L/L)_\perp$ becomes more pronounced. To better understand the just discussed behaviors, the experimentally obtained data is put in context with the CEF simulation. The comparison reveals that at elevated temperatures $T \geq 2\,\mathrm{K}$, the experimentally determined data and the simulated one match very well, while at low temperatures $T < 2\,\mathrm{K}$ clear deviations are present. The differences are most significant at very low temperature and low magnetic field, which reminds on the just discussed $\alpha_\parallel$ and $\alpha_\perp$ data obtained on the same single crystal. The magnetic field dependence of the volume magnetostriction $\Delta V/V = (\Delta L/L)_\parallel + 2(\Delta L/L)_\perp$, which is presented in Fig. 5.14(b), confirms this tendency. The small but finite volume changes found in the low magnetic field and temperature range are not compatible with the volume conserving Γ_3-type strains and point towards an additional contribution. Strikingly, the found behavior closely resembles the field dependence of the $(c_{11} - c_{12})/2$ elastic constant [44]. It is recalled that the volume thermal expansion β shows a divergence at low temperature that is readily suppressed by relatively small magnetic fields $\mu_0 H > 1\,\mathrm{T}$. It is therefore conceivable that the finite volume magnetostriction at low temperature, which sets in at approximately 1 T, relates to the suppression of the divergence in β with magnetic field. As stressed before, due to the fact that the length change measurements were carried out along a $\langle 100 \rangle$ direction, a small uniaxial stress induced contribution to the data cannot be excluded and might also partially contribute to the finite volume magnetostriction at low temperatures. As soon as a small uniaxial stress with Γ_3 symmetry is applied to the material, i.e. an uniaxial stress along a $\langle 100 \rangle$ direction, an additional strain contribution ε_u is induced, which shows proportionality to χ_Q. This may explain the resemblance to the field dependence of the $(c_{11} - c_{12})/2$ elastic constant [44]. However, as the thermal expansion measurements, which were carried out along different crystallographic directions and at various uniaxial stresses implicated, the additional contribution arising from the uniaxial stress acting on the single crystal via the dilatometer flat springs can only partially explain the divergent thermal expansion in zero magnetic field. It it thus conceivable that also the volume magnetostriction shows an intrinsic volume contribution that possibly arises from either dynamical or static strain fields, as discussed in the preceding subsection. As shown by M. Garst, the bulk strain assigned to both of the two contributions is proportional to χ_Q, which makes it difficult to extract the magnitude of the intrinsic volume and the extrinsic uniaxial stress induced contribution. In any case, the close relation between the field dependence of ε_B and $(c_{11} - c_{12})/2$ [44] indicates a direct connection between ε_B and χ_Q and is therefore in good agreement with the results on β.

While the observation of aforementioned deviations only indicates the presence of unconventional behavior, a more detailed analysis of the just presented magnetostriction data, which yields the magnetostriction coefficient with Γ_3 symmetry ε_u, is a powerful means to examine the possible quadrupolar Kondo nature of the ground state. As detailed before, ε_u is directly proportional to the expectation value $\langle O_2^0 \rangle$ and therefore a physical quantity of paramount importance. The fact that the volume magnetostriction $\Delta V/V$ is distinctly small as compared to the uniaxial magnetostriction $(\Delta L/L)_\parallel$ and $(\Delta L/L)_\perp$, as illustrated in Fig. 5.14, already implicates that the strain ε_u mainly generates the found magnetostriction. According to Eq. (2.39) and analogously to α_u, the Γ_3-type

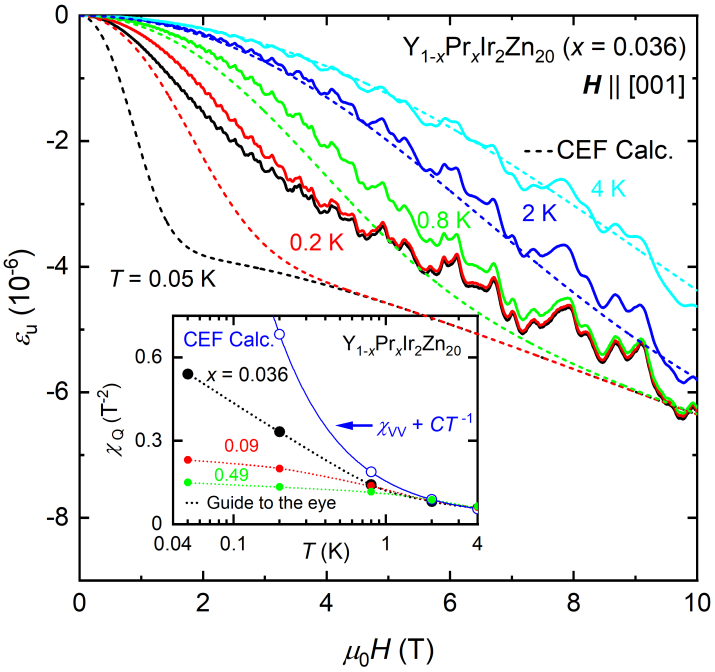

Figure 5.15: Magnetostriction coefficient with Γ_3 symmetry ε_u of $Y_{1-x}Pr_xIr_2Zn_{20}$ with $x = 0.036$ for $\boldsymbol{H} \parallel [001]$ at various temperatures. Additionally shown dashed lines are CEF calculations, which were simulated based on the CEF parameters $W = -1.50\,\mathrm{K}$ and $x = 0.537$ as well as a quadrupole-strain coupling constant $g_{\Gamma_3} = -35.0\,\mathrm{K}$. The inset shows the quadrupole-field susceptibility for different Pr concentrations x and the one derived from the CEF calculation. The theoretically calculated χ_Q can be well described by a divergent Curie-type contribution and a temperature independent Van Vleck contribution $\chi_\mathrm{Q} = CT^{-1} + \chi_\mathrm{VV}$. Dashed lines in the inset are guides to eye.
This figure is also included in Ref. [134].

magnetostriction coefficient ε_u can be calculated via the longitudinal $(\Delta L/L)_\parallel = \varepsilon_\parallel$ and the bulk magnetostriction $\Delta V/V = \varepsilon_\mathrm{B}$ as

$$\varepsilon_\mathrm{u} = \sqrt{3}\left(\varepsilon_\parallel - \frac{\varepsilon_\mathrm{B}}{3}\right). \tag{5.9}$$

A plot of the so determined ε_u in combination with CEF calculations, which were already discussed at the beginning of this subsubsection, is shown in Fig. 5.15. Note that the oscillations in the ε_u data, which are also present in the $(\Delta L/L)_\parallel$ and $(\Delta L/L)_\perp$ data shown in Fig. 5.14(a), are caused by quantum oscillations. An analysis of the related frequencies, which correspond well to the ones previously detected by elastic constant [44] and by magnetization measurements [129], can be found in the appendix of this thesis. As already outlined in the preceding subsection, the Γ_3-type symmetrized strain ε_u plays a crucial role when characterizing a quadrupolar ground state. It is recalled that the quadrupolar expectation value $\langle O_2^0 \rangle$ depends quadratically on a small magnetic field $\boldsymbol{H} \parallel [001]$

$$\langle O_2^0 \rangle = \chi_\mathrm{Q}^\mathrm{F} (\mu_0 H)^2 \Big|_{H \to 0}, \tag{5.10}$$

whereby the quadrupole-field susceptibility $\chi_\mathrm{Q}^\mathrm{F}$ serves as a proportionality constant. As explicitly detailed in Section 4.1.2, this quadratic coupling mainly arises from the mixing

of the Γ_3 ground state with the Γ_4 first excited state in magnetic field. With reference to the CEF simulation results discussed in the context of the thermal expansion coefficient α_u of the single crystal with $x = 0.036$, one expects $\chi_Q^F \sim \chi_Q \sim 1/T$ in case of a fully localized Γ_3 ground state doublet and $\chi_Q^F \sim \chi_Q \sim \log 1/T$ in case of a single-impurity quadrupole Kondo hybridized Γ_3 ground state doublet. Based on the proportionality between χ_Q^F and χ_Q, which was demonstrated in the previous subsection, in the following, simply the denotation χ_Q is employed to denote the quadrupole-field susceptibility. The strain ε_u on the other hand is directly proportional to the expectation value of the respective quadrupole moment

$$\varepsilon_u = \frac{n_{Pr} g_{\Gamma_3}}{(c_{11}^0 - c_{12}^0)/2} \langle O_2^0 \rangle. \tag{5.11}$$

By substituting Eq. (5.10) into Eq. (5.11) one obtains a quadratic relation between strain ε_u and magnetic field H, which reads as

$$\varepsilon_u = \frac{n_{Pr} g_{\Gamma_3}}{(c_{11}^0 - c_{12}^0)/2} \chi_Q (\mu_0 H)^2 \Big|_{H \to 0}. \tag{5.12}$$

Note that it is χ_Q, which determines the magnitude of the initial quadratic response of ε_u measured at different temperatures, as n_{Pr}, g_{Γ_3} and $(c_{11}^0 - c_{12}^0)/2$ can be assumed as temperature independent. Therefore, evaluation of the initial quadratic dependence of ε_u for small magnetic fields $\boldsymbol{H} \parallel [001]$ at different temperatures allows to directly deduce χ_Q. With this connection in mind, it becomes immediately evident that the weaker initial quadratic response of the experimentally determined ε_u as compared to the simulated one at low temperatures must stem from the suppression of χ_Q. As not only the quadrupole Kondo effect may evoke a suppression of χ_Q but also correlations between the quadrupole moments or a disorder induced splitting of the ground state doublet, a careful analysis of the temperature dependence of χ_Q is essential to clearly categorize the found behavior. Consequently, to deduce χ_Q as a function of temperature, the initial quadratic field dependence of the strain ε_u of $Y_{1-x}Pr_xIr_2Zn_{20}$ with $x = 0.036$ is analyzed at different temperatures. By plotting ε_u versus $(\mu_0 H)^2$, it is possible to determine the initial slope m via a linear regression at low magnetic field, based on which the value of χ_Q at a particular temperature can be deduced via the relation

$$\chi_Q = \frac{(c_{11}^0 - c_{12}^0)/2}{n_{Pr} g_{\Gamma_3}} m. \tag{5.13}$$

The determination process of the slope m is illustrated in Fig. 5.16(a) − (e), which shows ε_u as a function of $(\mu_0 H)^2$ at various temperatures and low magnetic field. The linear regression is indicated by the red solid line. While at very low temperatures, the magnetic field range in which ε_u depends quadratically on magnetic field is distinctly small and the splitting significant, this magnetic field regime enlarges as temperature is increased and the splitting becomes less strong. Note that the strain value at which deviations from the initial quadratic magnetic field dependence arise is comparable at all measured temperatures and corresponds to a value of $\varepsilon_u \approx -0.5 \times 10^{-6}$. As the onset of quantum oscillations complicates the analysis in particular at elevated temperatures, the upper bound of the quadratic field dependence could only be roughly estimated. By following the just discussed approach, the value of χ_Q was determined at five different temperatures, which are shown as black filled circles in the inset of Fig. 5.15. A similar analysis was carried out for the theoretically calculated CEF strain contribution. The respective χ_Q is shown in the inset of Fig. 5.15 by the blue open circles[9]. Its temperature

[9]The analysis of the initial quadratic field dependence of the simulated curves can be found in the appendix of this thesis.

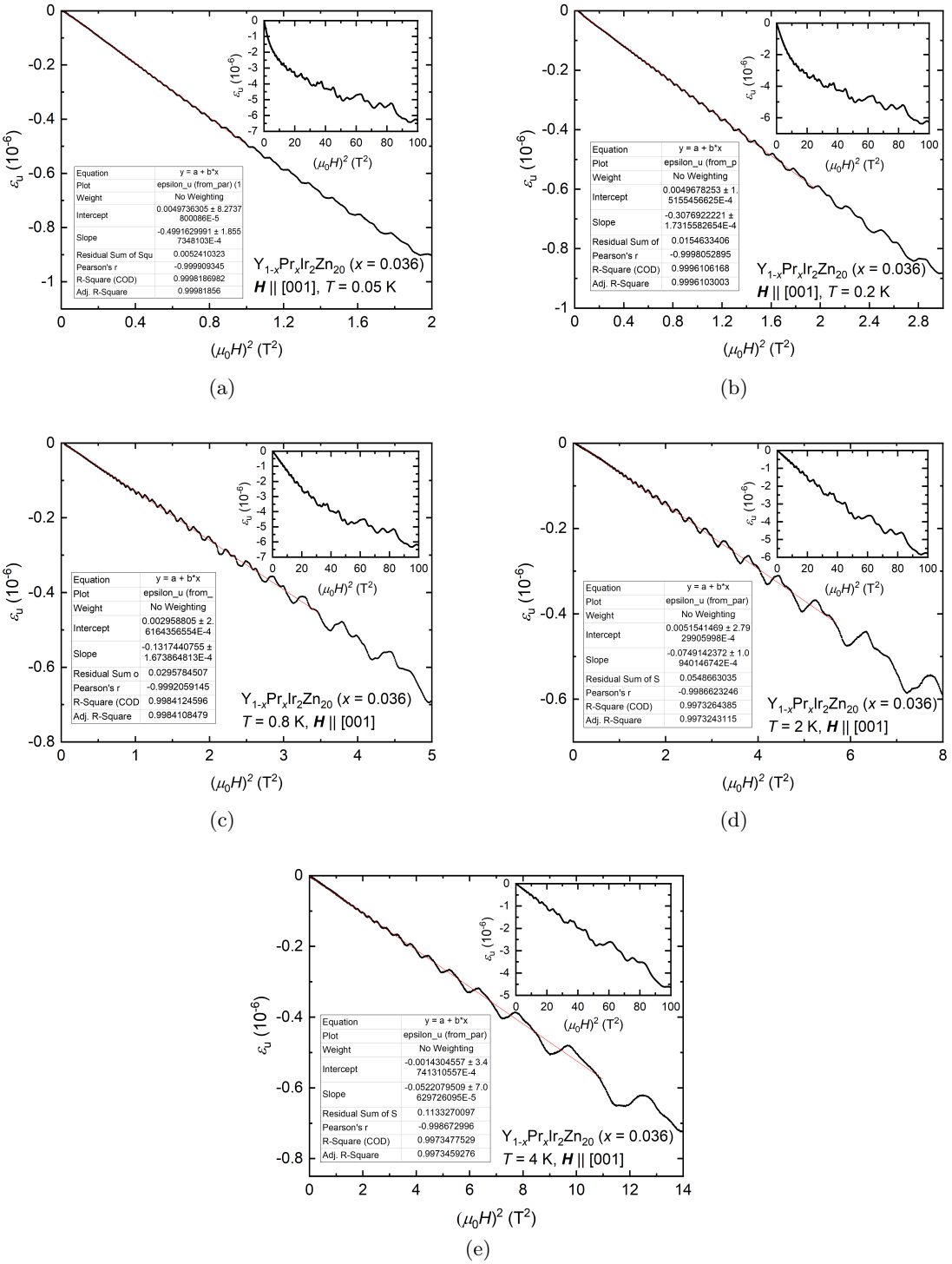

Figure 5.16: ε_u of $Y_{1-x}Pr_xIr_2Zn_{20}$ with $x = 0.036$ as a function of $(\mu_0 H)^2$ for small $\boldsymbol{H} \parallel [001]$ at different temperatures of (a) 0.05 K, (b) 0.2 K, (c) 0.8 K, (d) 2 K and (e) 4 K. Red solid lines are linear fits to the magnetostriction data. The insets show ε_u as a function of $(\mu_0 H)^2$ in the whole measured magnetic field range.

dependence can be well described by the equation $\chi_Q = \chi_{VV} + CT^{-1}$, as shown by the blue solid line. The constant offset χ_{VV} corresponds to a Van Vleck contribution, which arises from off-diagonal matrix elements of the quadrupole operator between the ground and exited state. Finite off-diagonal matrix elements for O_2^0 appear, for instance, in case of a mixing of the Γ_3 ground and the Γ_1 excited state. The term CT^{-1} on the other hand corresponds to a Curie-type susceptibility, which exhibits the same temperature dependence as the quadrupole-strain susceptibility of a fully localized Γ_3 doublet in cubic symmetry. For $T \leq 0.8\,\mathrm{K}$, χ_Q of the highly diluted single crystal with $x = 0.036$ shows a temperature dependence $\chi_Q \sim \log 1/T$, which is a clear signature of the quadrupole Kondo effect and therefore fully consistent with the results on α_u at small magnetic fields and the previously reported elastic constant study [44]. Additionally shown is χ_Q of the two moderately doped single crystals with $x = 0.09$ and $x = 0.49$, whereby details on their magnetostriction and the determination process of χ_Q are provided in the following subsubsection. By contrast to the single crystal with $x = 0.036$, χ_Q of the two moderately doped single crystals saturates as temperature declines, which excludes the formation of the single-impurity quadrupole Kondo effect. This finding is in very good agreement with the thermal expansion results detailed in the preceding subsection as well as the specific heat and electrical resistivity results by Yamane et al. [42, 43]. As mentioned before, the clear suppression of χ_Q with declining temperature in the two moderately doped single crystals points towards emerging short range quadrupolar correlations or a disorder induced splitting of the ground state doublet [42, 43].

Moderately Diluted Single Crystals ($x = 0.09$ and $x = 0.49$)

To study the breakdown of the single-impurity quadrupole Kondo effect in $Y_{1-x}Pr_xIr_2Zn_{20}$ with increasing Pr doping, as it was suggested by the previously detailed thermal expansion results as well as the specific heat and resisitivity results by Yamane et al. [42,43], more in detail, the longitudinal magnetostriction $(\Delta L/L)_\parallel$ of two moderately doped single crystals with Pr concentrations of $x = 0.09$ and $x = 0.49$ was measured for $\boldsymbol{H} \parallel [001]$. The results are detailed in the following.

Figure 5.17 displays the magnetic field dependence of $(\Delta L/L)_\parallel$ of $Y_{1-x}Pr_xIr_2Zn_{20}$ with $x = 0.09$ for $\boldsymbol{H} \parallel [001]$ at various temperatures. Moreover, CEF field calculations were performed by following the approach explicitly discussed in Section 4.2.2. The calculated curves are additionally shown as dashed lines in Fig. 5.17. The quadrupolar expectation values were simulated by using the Mathematica based CEF program provided by T. Onimaru, which evaluates the Hamiltonian given by Eq. (4.12). For the simulation, the same CEF parameters $W = -1.44\,\mathrm{K}$ and $x = 0.537$, determined from the simulation process of $\alpha_\parallel$ were employed. The same applies for the number of Pr^{3+} ions per volume $n_{Pr} = 0.251 \times 10^{27}\mathrm{m}^{-3}$ and the background elastic constant $(c_{11}^0 - c_{12}^0)/2 = 52.771\,\mathrm{GPa}$ [44, SM]. Fitting the simulation result to the experimentally determined $(\Delta L/L)_\parallel$ data at the highest measured temperature of 4 K yields a quadrupole-strain coupling constant of $g_{\Gamma_3} = -47.2\,\mathrm{K}$. This value is slightly larger than the value deduced from the thermal expansion analysis at 10 T, which gave back a value of $g_{\Gamma_3} = -38.0\,\mathrm{K}$. This is reminiscent of the difference in the quadrupole-strain coupling constants determined by the thermal expansion and magnetostriction measurements on the highly diluted single crystal with $x = 0.036$.

The experimentally obtained longitudinal magnetostriction of the single crystal with $x = 0.09$ shows a negative slope in the whole measured magnetic field range, whereby the relative length changes become more pronounced as temperature is reduced. This is comparable to the behavior found in the highly diluted single crystal as well as the

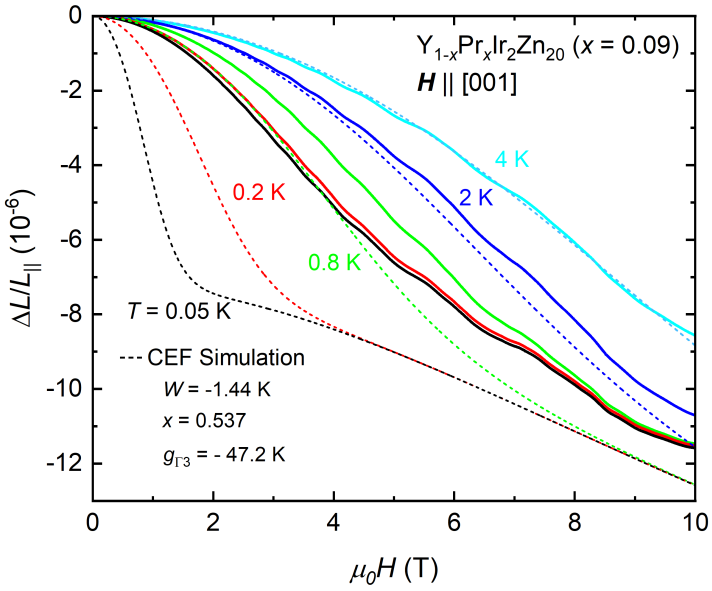

Figure 5.17: Longitudinal magnetostriction $(\Delta L/L)_{\parallel}$ as a function of magnetic field $\boldsymbol{H} \parallel [001]$ of $Y_{1-x}Pr_xIr_2Zn_{20}$ with $x = 0.09$ at various temperatures. Additionally shown dashed lines are CEF simulations for which the CEF parameter $W = -1.44\,\mathrm{K}$ and $x = 0.537$ and a quadrupole-strain coupling constant $g_{\Gamma_3} = -47.2\,\mathrm{K}$ were used.

pure system. To better understand the experimental findings, they are now set in relation to the just mentioned CEF simulation. Good agreement between experiment and simulation is only present at 4 K, while distinct differences arise as temperature is lowered. With decreasing temperature, the initial field dependence of the experimentally determined curves is clearly suppressed as compared to the simulation. It stands out that the observed differences between simulation and experiment are much more pronounced as in the case of the highly diluted single crystal with $x = 0.036$. This points towards a stronger suppression of χ_Q with declining temperature and is a first hint that the single-impurity quadrupole Kondo physics is quenched in this moderately doped single crystal. To quantify the temperature dependence of χ_Q, a similar approach as presented in the preceding subsubsection on the $x = 0.036$ single crystal was taken. As only $(\Delta L/L)_{\parallel}$ was measured for the $x = 0.09$ single crystal, the small field dependent volume contribution can, however, not be eliminated from the data. As the volume magnetostriction coefficients of both pure $PrIr_2Zn_{20}$ and highly diluted $Y_{1-x}Pr_xIr_2Zn_{20}$ with $x = 0.036$ are much smaller than the respective longitudinal magnetostriction coefficients, the error associated with the negligence of the volume magnetostriction can, however, be considered as vanishingly small. In consequence, under the assumption that the bulk magnetostriction is much smaller than the longitudinal magnetostriction $\varepsilon_B/3 \ll \varepsilon_{\parallel}$, the longitudinal magnetostriction can be related to the quadrupole field susceptibility via the equation

$$\varepsilon_{\parallel} \approx \frac{1}{\sqrt{3}} \frac{n_{Pr} g_{\Gamma_3}}{(c_{11}^0 - c_{12}^0)/2} \chi_Q (\mu_0 H)^2 \Big|_{H \to 0}. \tag{5.14}$$

As already discussed in the context of the single crystal with $x = 0.036$, by plotting $\varepsilon_{\parallel}$ versus $(\mu_0 H)^2$ and performing a linear regression at each temperature, the initial slope m can be determined. χ_Q at a certain temperature can then be directly derived via the relation

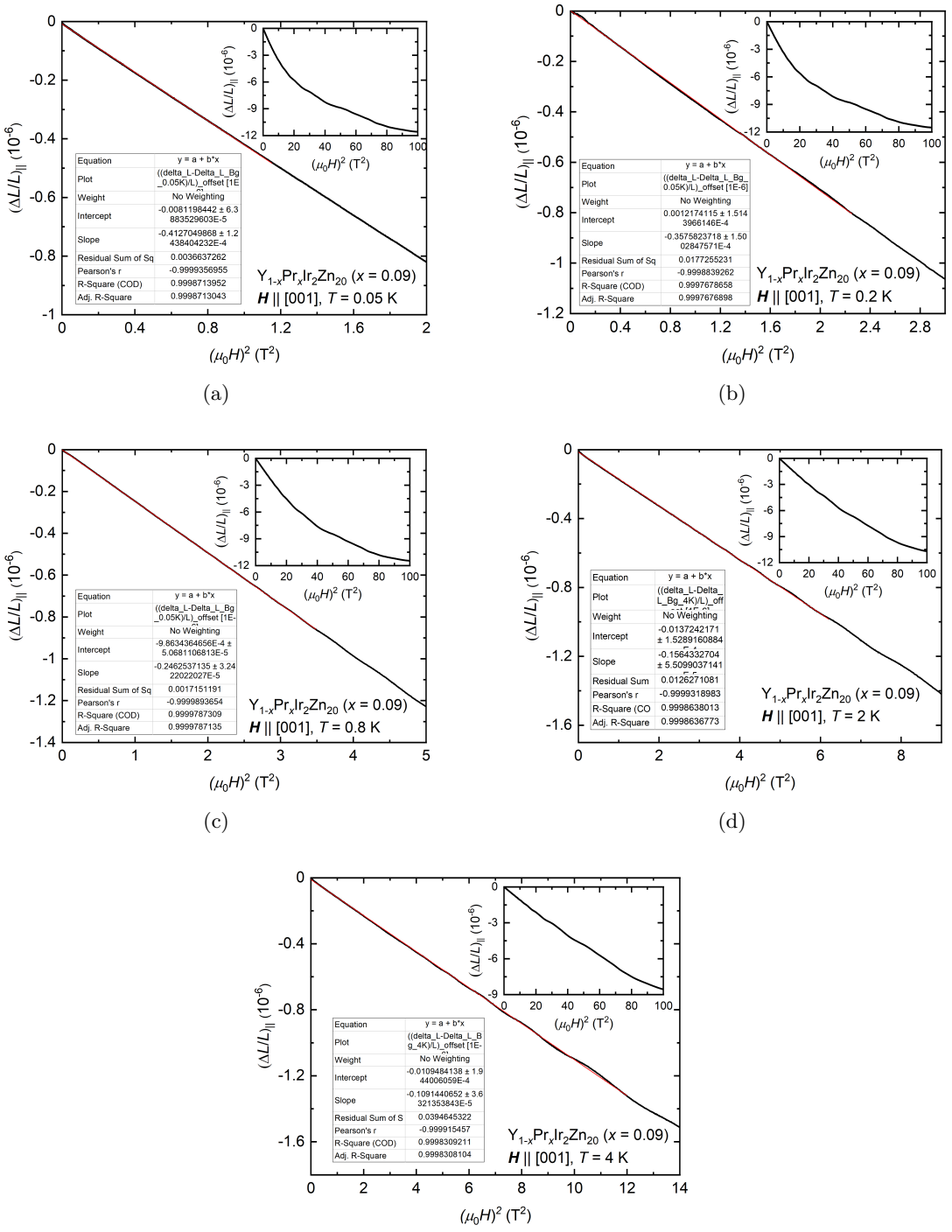

Figure 5.18: $(\Delta L/L)_{\parallel}$ of $Y_{1-x}Pr_xIr_2Zn_{20}$ with $x = 0.09$ as a function of $(\mu_0 H)^2$ for small $\boldsymbol{H} \parallel [001]$ at different temperatures of (a) 0.05 K, (b) 0.2 K, (c) 0.8 K, (d) 2 K and (e) 4 K. Red solid lines are linear fits to the magnetostriction data. The insets show $(\Delta L/L)_{\parallel}$ as a function of $(\mu_0 H)^2$ in the whole measured magnetic field range.

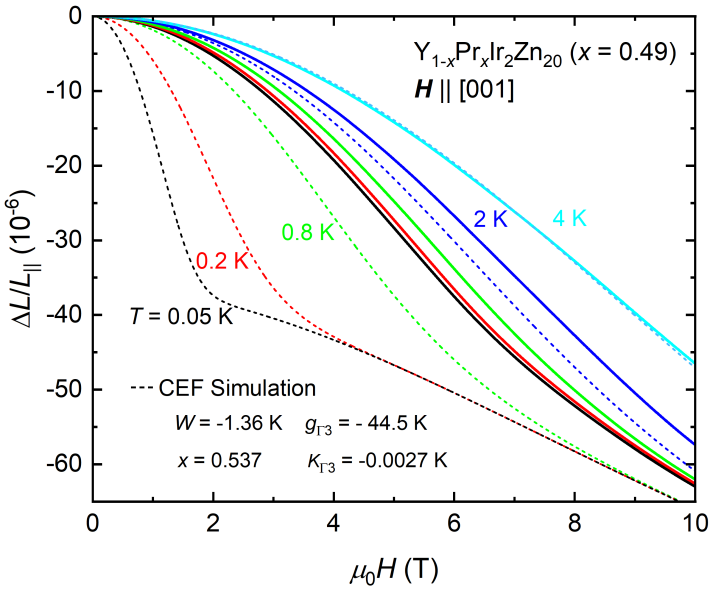

Figure 5.19: Longitudinal magnetostriction $(\Delta L/L)_{\parallel}$ as a function of magnetic field $\boldsymbol{H} \parallel [001]$ of $Y_{1-x}Pr_xIr_2Zn_{20}$ with $x = 0.49$ at various temperatures. Additionally shown dashed lines are CEF simulations based on the CEF parameter $W = -1.36\,\mathrm{K}$ and $x = 0.537$, a quadrupole-strain coupling constant $g_{\Gamma_3} = -44.5\,\mathrm{K}$ and a quadrupole-quadrupole interaction $K_{\Gamma_3} = -0.0027\,\mathrm{K}$.

$$\chi_{\mathrm{Q}} \approx \frac{(c_{11}^0 - c_{12}^0)/2}{n_{\mathrm{Pr}} g_{\Gamma_3}} \sqrt{3} m. \tag{5.15}$$

The longitudinal strain $(\Delta L/L)_{\parallel}$ as function of $(\mu_0 H)^2$ of the moderately diluted single crystal $Y_{1-x}Pr_xIr_2Zn_{20}$ with $x = 0.09$ at various temperatures is shown in Fig. 5.18(a)−(e). The red solid lines are linear regressions, which give back the slope m at each measured temperature. The insets show $(\Delta L/L)_{\parallel}$ as function of $(\mu_0 H)^2$ over the whole measured magnetic field range to emphasize that the quadratic field dependence is only given at small magnetic field. χ_{Q} is shown by red circles in the inset of Fig. 5.15 of the preceding subsubsection. χ_{Q} of the single crystal with $x = 0.09$ does not diverge and is thus substantially different to the logarithmically divergent χ_{Q} of the single crystal with $x = 0.036$. This excludes the formation of the single-impurity quadrupole Kondo effect, which is in very good agreement with the thermal expansion coefficient that does not show divergent behavior but exhibits a maximum at around 0.4 K. Also the specific heat and the electrical resistivity measured by Yamane et al. [42, 43] on a single crystal with $x = 0.085$ exclude the formation of the single-impurity quadrupole Kondo effect at low temperature, whereby either a short range quadrupole ordered or a disorder induced split ground state doublet likely accounts for the found behavior.

Finally, the focus is on the magnetostriction of the moderately doped single crystal with a Pr concentration of $x = 0.49$. Figure 5.19 displays the longitudinal magnetostriction $(\Delta L/L)_{\parallel}$ of $Y_{1-x}Pr_xIr_2Zn_{20}$ with $x = 0.49$ for $\boldsymbol{H} \parallel [001]$ at different temperatures in combination with CEF calculations that are plotted as dashed lines. The quadrupolar expectation values used for the simulation were calculated by using the Mathematica based CEF program provided by T. Onimaru, which evaluates the Hamiltonian given by Eq. (4.12). For the simulation, the same CEF parameters $W = -1.36\,\mathrm{K}$ and $x = 0.537$ and the same inter-site interaction of $K_{\Gamma_3} = -0.0027\,\mathrm{K}$ used in the previous subsection for the

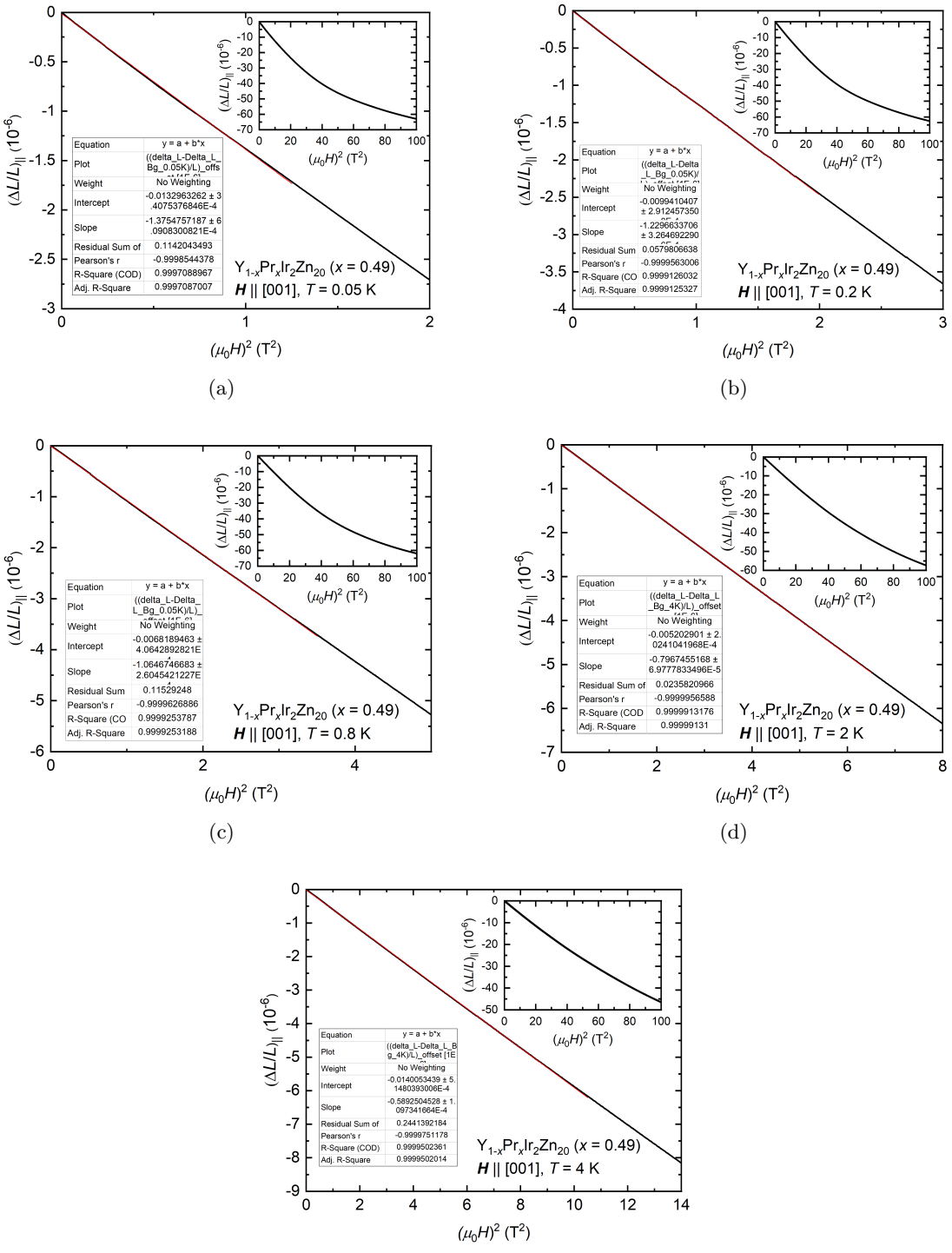

Figure 5.20: $(\Delta L/L)_{\parallel}$ of $Y_{1-x}Pr_xIr_2Zn_{20}$ with $x = 0.49$ as a function of $(\mu_0 H)^2$ for small $\boldsymbol{H} \parallel [001]$ at different temperatures of (a) 0.05 K, (b) 0.2 K, (c) 0.8 K, (d) 2 K and (e) 4 K. Red solid lines are linear fits to the magnetostriction data. The insets show $(\Delta L/L)_{\parallel}$ as a function of $(\mu_0 H)^2$ in the whole measured magnetic field range.

thermal expansion analysis, were employed. The same holds for the number of Pr^{3+} ions per volume $n_{Pr} = 1.363 \times 10^{27} m^{-3}$ and the background elastic constant $(c^0_{11} - c^0_{12})/2 = 52.771\,GPa$ [44, SM]. To estimate the quadrupole-strain coupling constant, the CEF calculation was fitted to the experimentally obtained magnetostriction data at 4 K, which gives back a value of $g_{\Gamma_3} = -44.5\,K$. As already observed in the weaker Pr doped single crystals, the value of g_{Γ_3} deduced from the magnetostriction measurement is slightly larger than the one determined from the thermal expansion analysis.

The experimentally determined longitudinal magnetostriction of the single crystal with $x = 0.49$ is negative in the whole examined magnetic field range and the response of the system to magnetic field becomes more pronounced as temperature is lowered, which is in good accordance with all the other examined single crystals. To further interpret the experimentally obtained data, it is compared to the CEF calculation. Good accordance between simulation and experiment is only present at the highest examined temperature of 4 K. As temperature decreases, clear differences between experiment and calculation become evident. These deviations are already quite substantial at a relatively high temperature of 2 K, which suggests a distinct suppression of χ_Q as compared to the CEF Curie-type temperature dependence. A possible cause for this finding is the relatively high Pr concentration of $x = 0.49$ and the concomitant inter-site interaction.

As for this single crystal only the longitudinal magnetostriction was measured, χ_Q was calculated by following the same approach applied before on the single crystal with $x = 0.09$. Under the assumption that $\varepsilon_B/3 \ll \varepsilon_{\parallel}$, the value of the quadrupole-field susceptibility was estimated by evaluating the initial quadratic dependence of the magnetostriction coefficient at five different temperatures, as shown in Fig. 5.20(a)−(e), and plugging the so determined slope m into Eq. (5.15). The so derived χ_Q is presented in the inset of Fig. 5.15 of the preceding subsubsection in green color. It shows that χ_Q of the single crystal with $x = 0.49$ is even stronger suppressed as compared to χ_Q of the single crystal with $x = 0.09$. This finding can likely be assigned to the larger inter-site interaction that is known to suppress the quadrupole susceptibility [44]. The magnetostriction results on the single crystal with $x = 0.49$ are in very good accordance with the thermal expansion coefficient at zero magnetic field, which is also strongly suppressed at low temperature, as shown in the inset of Fig. 5.11(a).

5.2.4 Summary

In this section, thermal expansion and magnetostriction measurement results obtained on differently doped single crystalline samples of $Y_{1-x}Pr_xIr_2Zn_{20}$ were presented and discussed. Main focus was thereby on a highly diluted single crystal with $x = 0.036$, as previous specific heat and electrical resistivity measurements revealed that possible single-impurity quadrupole Kondo behavior appears exclusively in single crystals with $x \leq 0.044$ [42,43]. The thermal expansion and magnetostriction measurement results fully support this scenario. The Γ_3-type symmetrized thermal expansion coefficient α_u and the respective Grüneisen parameter Γ_u turned out as powerful probes to study single-impurity quadrupole Kondo behavior and display divergences at low magnetic field that are in line with the theoretically expected single-impurity quadrupole Kondo behavior. In addition, an unexpected divergence in the volume thermal expansion was found that, even though hard to reconcile with the quadrupole Kondo effect at a first glance, provides further evidence for the single-impurity quadrupole Kondo scenario. Theoretical calculations by M. Garst suggested that this unconventional behavior arises from a possible coupling between volume strain and quadrupole-strain susceptibility, which is either realized via dynamical or static strain fields. Additional experiments on two higher doped single crystalline sam-

ples with $x = 0.09$ and $x = 0.49$ indicated that the quadrupole Kondo signatures appear exclusively in the single crystal with a tiny Pr concentration of $x = 0.036$ and are therefore in line with previous specific heat and electrical resistivity results by Yamane et al. [42,43]. The key findings of this section are briefly recalled in the following.

- The highly diluted $Y_{1-x}Pr_xIr_2Zn_{20}$ single crystal with $x = 0.036$ shows a peculiar divergent volume thermal expansion in zero magnetic field. Measurements of the transverse and longitudinal thermal expansion coefficients $\alpha_{\parallel}$ and $\alpha_{\perp}$ allowed to trace its evolution in magnetic field $\boldsymbol{H} \parallel [001]$. It showed that the unconventional divergence is highly field sensitive and already suppressed by a relatively small magnetic field $\mu_0 H > 1\,\mathrm{T}$, which is in excellent agreement with previous specific heat and elastic constant studies [44, 94]. Comparison of $\alpha_{\parallel}$ and $\alpha_{\perp}$ with a CEF calculation revealed substantial differences at low magnetic field that provide further indication for the presence of an unconventional correlation effect. At high magnetic fields $\mu_0 H \geq 6\,\mathrm{T}$, very good agreement between experiment and simulation suggested that the quadrupolar ground state moments are in the fully localized state.

- To analyze the uniaxial effects more in detail, the thermal expansion coefficient with Γ_3 symmetry α_{u}, derived from the measurement of $\alpha_{\parallel}$ and $\alpha_{\perp}$, was analyzed. In case the applied magnetic field $\boldsymbol{H} \parallel [001]$ is small, α_{u} is directly proportional to the temperature derivative of the quadrupole-field susceptibility and therefore a crucial physical probe for the characterization of the quadrupolar ground state. For $\mu_0 H \leq 1\,\mathrm{T}$ and low temperatures $T < 0.4\,\mathrm{K}$, α_{u} varies as $1/T$, which is fully in line with a single-impurity quadrupole Kondo hybridization. By contrast, at elevated temperatures $T > 1\,\mathrm{K}$, α_{u} shows a $1/T^2$ temperature dependence, which confirms the fully localized nature of the quadrupolar ground state. In addition, the Grüneisen parameter $\Gamma_{\mathrm{u}} = V_{\mathrm{m}}\alpha_{\mathrm{u}}/C_{\mathrm{m}}$ was employed to characterize the NFL behavior more in detail. Its divergence is expected at the quadrupolar Kondo critical point, whereby $\alpha_{\mathrm{u}} \sim H^2/T$ and $C_{\mathrm{m}} \sim T \log 1/T$ imply $\Gamma_{\mathrm{u}} \sim H^2/(T^2 \log 1/T)$. Indeed, at low magnetic field $\mu_0 H \leq 1\,\mathrm{T}$, Γ_{u} shows the theoretically expected temperature dependence. Finally, the evaluation of the initial quadratic field dependence of the symmetrized magnetostriction coefficient ε_{u} implicated a logarithmic temperature dependence of the quadrupole-field susceptibility at low temperature. All three experimental findings provided therefore strong corroborative evidence for the formation of the single-impurity quadrupole Kondo effect in highly diluted single crystalline $Y_{1-x}Pr_xIr_2Zn_{20}$. In consequence, the measurement of the Γ_3-type symmetrized thermal expansion and magnetostriction coefficient as well as the respective Grüneisen parameter turned out to be relevant probes to characterize quadrupolar Kondo metals and should be considered as complementary to the well established measurements of the specific heat, electrical resistivity and elastic constant.

- Another key point was to put the peculiar volume thermal expansion divergence in the highly diluted single crystal with $x = 0.036$ under the microscope. To exclude that the small uniaxial stress exerted by the flat springs of the dilatometer causes the divergence, measurements on a [111] oriented single crystal from the same batch with a similar Pr doping level of $x = 0.033$ were carried out. In addition, thermal expansion measurements on both the [001] and the [111] oriented single crystal were performed under higher uniaxial stress. The results clearly indicated the presence of a divergent uniaxial stress induced contribution that by itself can, however, not explain the observed divergence in the volume thermal expansion in zero magnetic field. Consequently, a small but finite intrinsic divergent volume thermal expansion

has to be present. As the divergent behavior in β is substantially different to the specific heat, the bulk Grüneisen parameter Γ_B diverges upon cooling. Its large value of $\Gamma_B \approx 2.15\,\mathrm{GPa}^{-1}$ at 0.07 K implies a significant pressure dependence of the respective energy scale that is comparable in magnitude to HF metals at a magnetic QCP [58]. The divergence in Γ_B is a surprising finding, as hydrostatic pressure per se does not break cubic symmetry and can therefore not be considered as a suitable control parameter for the single-impurity quadrupolar Kondo criticality. Theoretical calculations carried out by M. Garst suggested two possible scenarios that can principally explain the divergence found in the volume thermal expansion. The first scenario covers dynamical strain fields, which cause a contribution to the bulk strain that displays proportionality to χ_Q. Its magnitude scales with the pressure dependence of the quadrupole-strain coupling constant g_{Γ_3}. The second scenario deals with disorder induced static strain fields, which can principally arise from the Pr doping or from conventional dislocations in the crystal structure. Such static strain fields locally break the cubic symmetry at a Pr site and therefore the degeneracy of the non-Kramers Γ_3 ground state doublet. Similarly to the dynamic strain fields, the contribution to the bulk strain is proportional to χ_Q. Either of the two effects should, however, also trigger a similar divergence in the specific heat, which was not found in the experiment. An explanation for this inconsistency is that the respective low temperature energy scale must show a substantial hydrostatic pressure dependence. Such a significant pressure dependence is considered as unlikely for the case of dynamical strain fields but may be more realistic in the case of static strain fields. To further clarify this issue, future measurements of the elastic constant under hydrostatic pressure would be helpful to quantify the pressure dependence of the quadrupole-strain coupling constant. Detailed thermal expansion measurements on differently doped single crystals, on the other hand, would be insightful to examine a possible disorder effect more in detail.

- The thermal expansion and magnetostriction results obtained on two moderately doped single crystals with Pr doping levels of $x = 0.09$ and $x = 0.49$ are incompatible with a single-impurity quadrupole Kondo effect, which is in line with previous specific heat and electrical resistivity results by Yamane et al. [42, 43]. The distinct suppression of the zero field volume thermal expansion and the quadrupole-field susceptibility at low temperatures is distinct to the behavior revealed for the highly diluted single crystal with $x = 0.036$, whereby disorder induced static strain fields or short range quadrupolar correlations can be mentioned as possible causes [42, 43].

Chapter 6

Conclusion and Outlook

This thesis examined exotic quadrupole driven hybridization phenomena that arise in the cubic non-Kramers material $PrIr_2Zn_{20}$ and its diluted sister compound $Y_{1-x}Pr_xIr_2Zn_{20}$, using low temperature thermal expansion and magnetostriction measurements.

The key experimental finding on $PrIr_2Zn_{20}$ was a pronounced anisotropy in the longitudinal and transverse thermal expansion and magnetostriction coefficients for $\boldsymbol{B} \parallel [001]$ that assigns to a roughly volume conserving tetragonal distortion. With the help of CEF calculations it was shown that this behavior originates from the Γ_3-type symmetrized strain $\varepsilon_u \sim \langle O_2^0 \rangle$ that directly measures the splitting of the ground state doublet in magnetic field. In comparison to the uniaxial behavior, the temperature and field dependent volume effects are markedly small. This strong contrast suggests that hybridization effects in $PrIr_2Zn_{20}$ are rather weak and the valence state of the Pr^{3+} ion close to integer. These findings put the previous Seebeck coefficient measurement results [45, 46] and the thereof inferred emergence of a strongly hybridized state at intermediate field into perspective. The thermal expansion and magnetostriction measurement results imply that the novel phase at intermediate magnetic field, which comes along with FL behavior in the electrical resistivity [28], originates from a rather weak hybridization effect. The found behavior is also distinct from Ce- and Yb-based intermetallic compounds that typically exhibit pronounced volume effects that arise from the intermediate valence state of the rare earth ions. In order to verify as to whether the behavior found in $PrIr_2Zn_{20}$ is an universal feature of the class of Pr-based 1-2-20 materials, thermal expansion and magnetostriction measurements on other members of this family, such as the Al-based systems PrV_2Al_{20} and $PrTi_2Al_{20}$, would be insightful. In the case of $PrIr_2Zn_{20}$, it turned out as difficult to deduce corroborative evidence for the quadrupolar Kondo lattice effect on the basis of the thermal expansion and magnetostriction measurement results, as there is no clear theoretical prediction regarding its contribution to both thermodynamic quantities so far.

Specifying possible signatures of the single-impurity quadrupole Kondo effect in the thermal expansion and magnetostriction coefficients was the main objective of the experiments on the diluted system $Y_{1-x}Pr_xIr_2Zn_{20}$. The key findings were thereby obtained on two single crystals with a very low Pr doping of $x = 0.033$ and $x = 0.036$. Careful zero magnetic field thermal expansion measurements carried out along different crystallographic directions and at different uniaxial stresses revealed an unexpected divergence of the volume thermal expansion coefficient upon cooling. Even though M. Garst derived two theoretical scenarios that can principally set the found behavior in relation to the single-impurity quadrupolar Kondo effect, there remain open questions that should be addressed by future research. It is recalled that the absence of the theoretically proposed residual entropy of $S = 1/2R \ln 2$ reported by Yamane et al. [42] is another unsolved mystery. Further

research that examines a possible relation between these two peculiar findings is desirable. Direct evidence for the single-impurity quadrupolar Kondo effect was found in the linear thermal expansion and magnetostriction measured in low magnetic field $\boldsymbol{B} \parallel [001]$. With the help of the longitudinal and transverse thermal expansion coefficients, the symmetrized thermal expansion coefficient with Γ_3 symmetry was deduced that can be directly related to the quadrupole-field susceptibility for small $\boldsymbol{B} \parallel [001]$. The same holds for the symmetrized magnetostriction coefficient with Γ_3 symmetry. The quadrupole-field susceptibility quantifies the quadratic splitting of the ground state doublet in a magnetic field and turned out as an effective means to track down possible single-impurity quadrupolar Kondo behavior. The measurement of symmetrized strains in magnetic field as a method to deduce the quadrupole-field susceptibility was pioneered by Morin et al. [73], who used the approach to quantify quadrupole-strain coupling constants of a material at elevated temperature. In the scope of this thesis, a new aspect of this probe was revealed. CEF calculations demonstrated that the quadrupole-field susceptibility related to a fully localized cubic Γ_3 doublet exhibits the same Curie-type $1/T$ temperature dependence as the quadrupole-strain [16] and the non-linear magnetic susceptibility [135]. The experiments carried out on highly diluted $Y_{1-x}Pr_xIr_2Zn_{20}$ demonstrated that this Curie-type temperature dependence renormalizes in presence of a quadrupole Kondo hybridization to a characteristic logarithmic temperature dependence that is in line with the other two susceptibilities. While the measurement of the non-linear magnetic susceptibility [135] is another possible means to track down a quadrupolar Kondo state by perturbing the system via the application of magnetic field, identifying quadrupole Kondo correlations based on this quantity is generally complicated by a large Van Vleck-type background contribution that masks the interesting Curie-type contribution associated to the Γ_3 ground state doublet. Strikingly, in the case of the quadrupole-field susceptibility this effect is reversed, as the Curie-type contribution dominates over a small parasitic Van Vleck contribution. Thanks to the significant coupling between quadrupole moment and strain, even in a highly diluted single crystal with a Pr doping of just $x = 0.036$, the Γ_3-type contribution to the thermal expansion and magnetostriction is significant and the quadrupole-field susceptibility can be determined with very high precision. Measurements of the symmetrized thermal expansion and magnetostriction coefficients in a small magnetic field $\boldsymbol{B} \parallel [001]$ can therefore be considered as a genuine alternative to the well established elastic constant and non-linear magnetic susceptibility measurements, in order to characterize the non-Kramers ground state of a cubic quadrupolar Kondo metal. In the future, volume thermal expansion measurements on other prototypical single-impurity quadrupole Kondo systems would be helpful to clarify the nature of the peculiar volume divergence found in highly diluted $Y_{1-x}Pr_xIr_2Zn_{20}$.

Appendix

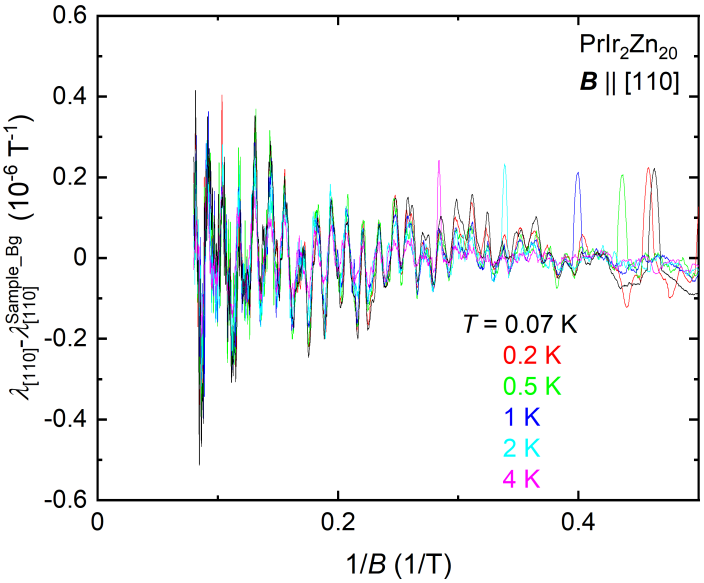

Figure A1: $\lambda_{[110]}$ corrected for the background magnetostriction of the sample as a function of the inverse of magnetic field $1/B$ of $PrIr_2Zn_{20}$ at different temperatures for $\boldsymbol{B} \parallel [110]$. The sample shows distinct quantum oscillations.

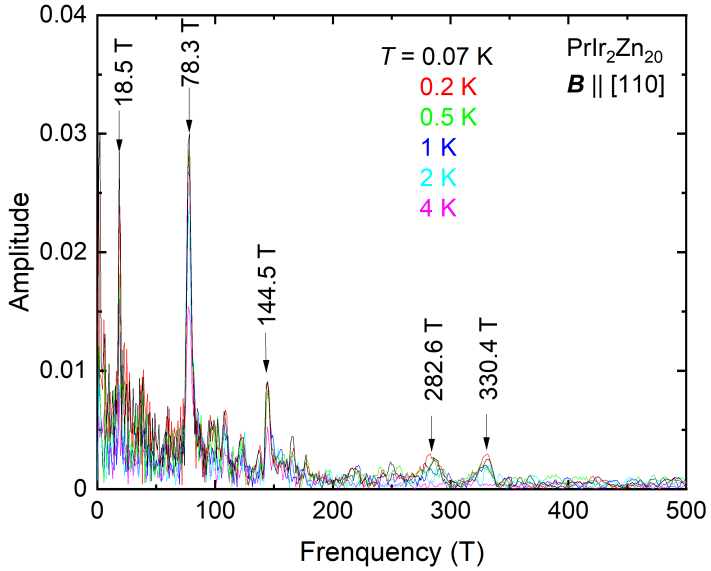

Figure A2: Fourier transformation of the $\lambda_{[110]}$ versus $1/B$ data shown in Fig. A1, whereby amplitude versus frequency is shown. The frequency of each of the found peaks is specified by an arrow.

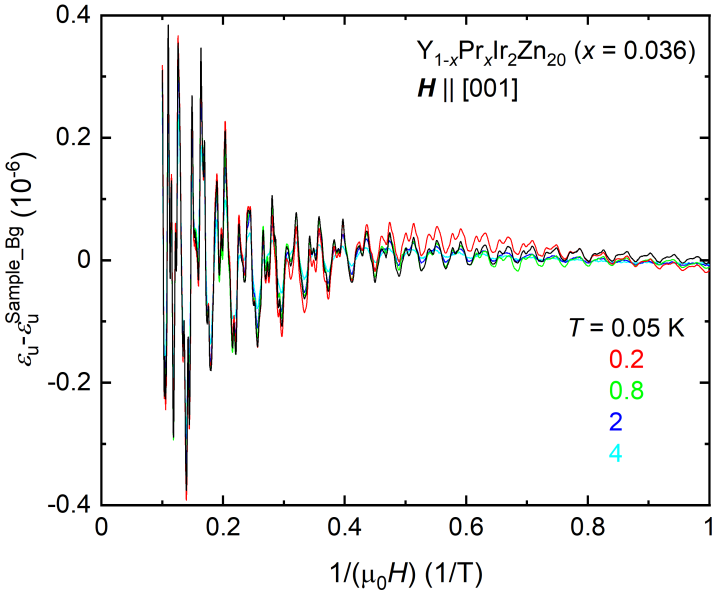

Figure A3: ε_{u} corrected for the background strain of the sample as a function of the inverse of magnetic field $1/(\mu_0 H)$ of $Y_{1-x}Pr_xIr_2Zn_{20}$ with $x = 0.036$ at different temperatures for $\boldsymbol{H} \parallel [001]$. The sample shows distinct quantum oscillations.

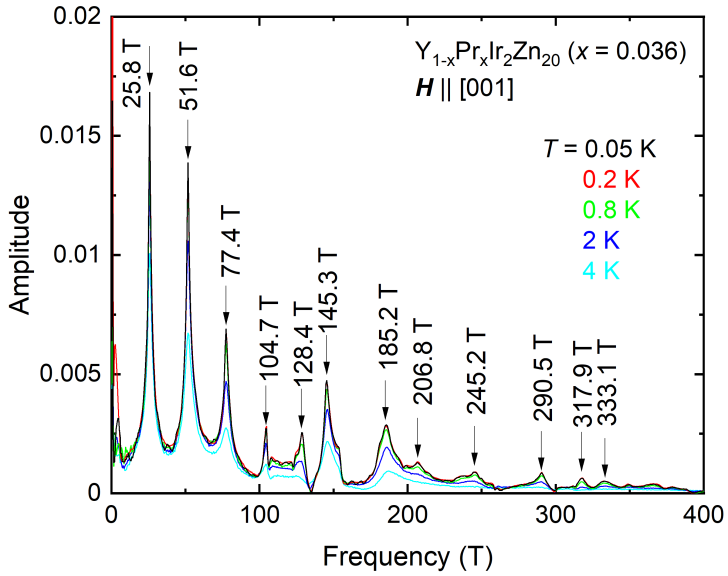

Figure A4: Fourier transformation of the ε_u vs. $1/(\mu_0 H)$ data shown in Fig. A3, whereby amplitude versus frequency is shown. The frequency of each of the found peaks is specified by an arrow.

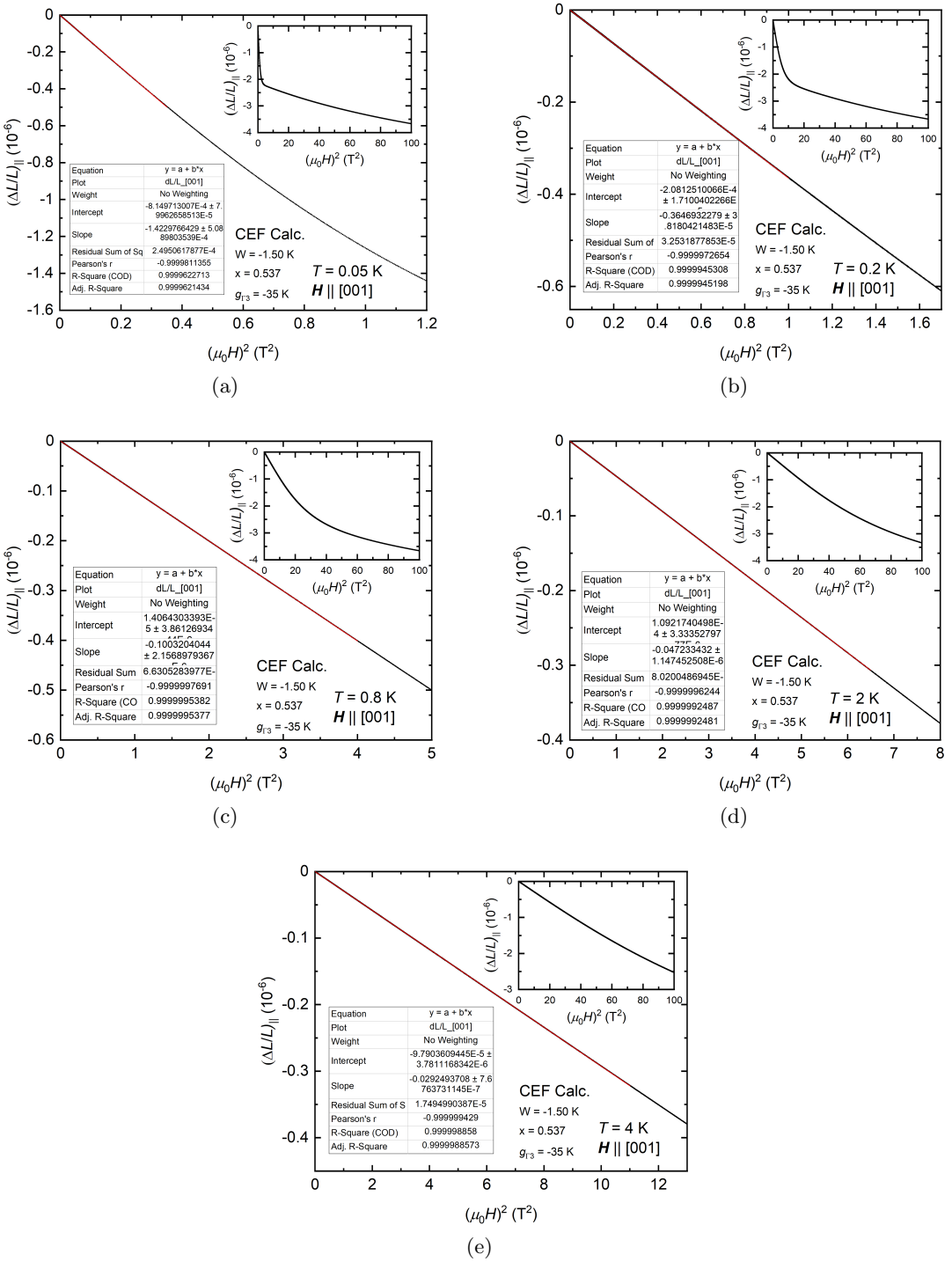

Figure A5: CEF simulation of $(\Delta L/L)_{\parallel}$ by using simulation parameters derived for $Y_{1-x}Pr_xIr_2Zn_{20}$ with $x = 0.036$ as a function of $(\mu_0 H)^2$ for small $\boldsymbol{H} \parallel [001]$ at different temperatures of (a) 0.05 K, (b) 0.2 K, (c) 0.8 K, (d) 2 K and (e) 4 K. Red solid lines are linear fits to the magnetostriction data. The insets show $(\Delta L/L)_{\parallel}$ as a function of $(\mu_0 H)^2$ in the whole simulated magnetic field range.

Bibliography

[1] N. F. Mott. The Basis of the Electron Theory of Metals, with Special Reference to the Transition Metals. *Proc. Phys. Soc. A*, 62(7):416–422, 1949. doi:10.1088/0370-1298/62/7/303.

[2] G. R. Stewart. Heavy-fermion systems. *Rev. Mod. Phys.*, 56(4):755–787, 1984. doi:10.1103/RevModPhys.56.755.

[3] N. Grewe and F. Steglich. Chapter 97 Heavy Fermions. In *Handbook on the Physics and Chemistry of Rare Earths*, volume 14, pages 343–474. Elsevier, 1991. ISBN 0444887431.

[4] Z. Fisk, J. L. Sarrao, J. L. Smith, and J. D. Thompson. The physics and chemistry of heavy fermions. *Proc. Natl. Acad. Sci. USA*, 92(15):6663–6667, 1995. doi:10.1073/pnas.92.15.6663.

[5] W. Meissner and B. Voigt. Messungen mit Hilfe von flüssigem Helium XI Widerstand der reinen Metalle in tiefen Temperaturen. *Ann. Phys.*, 399(8):892–936, 1930. doi:10.1002/andp.19303990803.

[6] W. J. de Haas, J. de Boer, and G. J. van dën Berg. The electrical resistance of gold, copper and lead at low temperatures. *Physica*, 1(7):1115–1124, 1934. doi:10.1016/S0031-8914(34)80310-2.

[7] J. Kondo. Resistance Minimum in Dilute Magnetic Alloys. *Prog. Theor. Phys.*, 32(1):37–49, 1964. doi:10.1143/PTP.32.37.

[8] C. Enss and S. Hunklinger. *Tieftemperaturphysik*. Springer-Verlag Berlin Heidelberg New York, 2000. ISBN 3-540-67674-0.

[9] K. G. Wilson. The renormalization group: Critical phenomena and the Kondo problem. *Rev. Mod. Phys.*, 47(4):773–840, 1975. doi:10.1103/RevModPhys.47.773.

[10] S. Doniach. The Kondo lattice and weak antiferromagnetism. *Physica B+C*, 91:231–234, 1977. doi:10.1016/0378-4363(77)90190-5.

[11] P. Gegenwart, Q. Si, and F. Steglich. Quantum criticality in heavy-fermion metals. *Nat. Phys.*, 4:186–197, 2008. doi:10.1038/nphys892.

[12] S. Blundell. *Magnetism in Condensed Matters*. Oxford University Press, 2001. ISBN 978-0-19-850591-4.

[13] D. L. Cox. Quadrupolar Kondo effect in uranium heavy-electron materials? *Phys. Rev. Lett.*, 59(11):1240–1243, 1987. doi:10.1103/PhysRevLett.59.1240.

[14] D. L. Cox. Quadrupolar Kondo effect in UBe_{13} (and other systems)? *Physica C*, 153-155:1642–1648, 1988. doi:10.1016/0921-4534(88)90437-6.

[15] P. Nozières and A. Blandin. Kondo effect in real metals. *J. Phys. France*, 41(3):193–211, 1980. doi:10.1051/jphys:01980004103019300.

[16] P. D. Sacramento and P. Schlottmann. The quadrupolar kondo effect: Lattice instability and large γ-values. *Phys. Lett. A*, 142(4):245–250, 1989. doi:10.1016/0375-9601(89)90323-X.

[17] A. M. Tsvelick. The thermodynamics of multichannel Kondo problem. *J. Phys. C: Solid State Phys.*, 18(1):159–170, 1985. doi:10.1088/0022-3719/18/1/020.

[18] P. D. Sacramento and P. Schlottmann. Low-temperature properties of a two-level system interacting with conduction electrons: An application of the overcompensated multichannel Kondo model. *Phys. Rev. B*, 43(16):13294–13304, 1991. doi:10.1103/PhysRevB.43.13294.

[19] F. G. Aliev, H. El Mfarrej, S. Vieira, and R. Villar. Anomalous ground state of $U_{0.9}Th_{0.1}Be_{13}$: Temperature dependence of the resistivity and magnetoresistance. *Solid State Commun.*, 91(10):775–778, 1994. doi:10.1016/0038-1098(94)90646-7.

[20] F. G. Aliev, S. Vieira, R. Villar, J. L. Martinez, C. L. Seaman, and M. B. Maple. Anomalous ground state in $U_{0.9}Th_{0.1}Be_{13}$. *Physica B*, 206-207:454–456, 1995. doi:10.1016/0921-4526(94)00488-H.

[21] C. L. Seaman, M. B. Maple, B. W. Lee, S. Ghamaty, M. S. Torikachvili, J.-S. Kang, L. Z. Liu, J. W. Allen, and D. L. Cox. Evidence for non-Fermi liquid behavior in the Kondo alloy $Y_{1-x}U_xPd_3$. *Phys. Rev. Lett.*, 67(20):2882–2885, 1991. doi:10.1103/PhysRevLett.67.2882.

[22] B. Andraka and A. M. Tsvelik. Observation of non-Fermi-liquid behavior in $U_{0.2}Y_{0.8}Pd_3$. *Phys. Rev. Lett.*, 67(20):2886–2889, 1991. doi:10.1103/PhysRevLett.67.2886.

[23] H. Amitsuka, T. Hidano, T. Honma, H. Mitamura, and T. Sakakibara. Evidence of unusual Kondo effects in dilute uranium compounds $U_xTh_{1-x}Ru_2Si_2$ ($x \leq 0.07$). *Physica B*, 186-188:337–340, 1993. doi:10.1016/0921-4526(93)90568-Q.

[24] H. Amitsuka and T. Sakakibara. Single Uranium-Site Properties of the Dilute Heavy Electron System $U_xTh_{1-x}Ru_2Si_2$ ($x \leq 0.07$). *J. Phys. Soc. Jpn.*, 63(2):736–747, 1994. doi:10.1143/JPSJ.63.736.

[25] T. Onimaru and H. Kusunose. Exotic Quadrupolar Phenomena in Non-Kramers Doublet Systems — The Cases of PrT_2Zn_{20} (T = Ir, Rh) and PrT_2Al_{20} (T = V, Ti) —. *J. Phys. Soc. Jpn.*, 85(8):082002, 2016. doi:10.7566/JPSJ.85.082002.

[26] A. Sakai and S. Nakatsuji. Kondo Effects and Multipolar Order in the Cubic $PrTr_2Al_{20}$ (Tr =Ti, V). *J. Phys. Soc. Jpn.*, 80(6):063701, 2011. doi:10.1143/JPSJ.80.063701.

[27] T. Onimaru, K. T. Matsumoto, Y. F. Inoue, K. Umeo, T. Sakakibara, Y. Karaki, M. Kubota, and T. Takabatake. Antiferroquadrupolar Ordering in a Pr-Based Superconductor $PrIr_2Zn_{20}$. *Phys. Rev. Lett.*, 106(17):177001, 2011. doi:10.1103/PhysRevLett.106.177001.

[28] T. Onimaru, K. Izawa, K. T. Matsumoto, T. Yoshida, Y. Machida, T. Ikeura, K. Wakiya, K. Umeo, S. Kittaka, K. Araki, T. Sakakibara, and T. Takabatake. Quadrupole-driven non-Fermi-liquid and magnetic-field-induced heavy fermion states in a non-Kramers doublet system. *Phys. Rev. B*, 94(7):075134, 2016. doi:10.1103/PhysRevB.94.075134.

[29] T. Onimaru, N. Nagasawa, K. T. Matsumoto, K. Wakiya, K. Umeo, S. Kittaka, T. Sakakibara, Y. Matsushita, and T. Takabatake. Simultaneous superconducting and antiferroquadrupolar transitions in $PrRh_2Zn_{20}$. *Phys. Rev. B*, 86(18):184426, 2012. doi:10.1103/PhysRevB.86.184426.

[30] T. Yoshida, Y. Machida, K. Izawa, Y. Shimada, N. Nagasawa, T. Onimaru, T. Takabatake, A. Gourgout, A. Pourret, G. Knebel, and J.-P. Brison. Anisotropic B–T Phase Diagram of Non-Kramers system $PrRh_2Zn_{20}$. *J. Phys. Soc. Jpn.*, 86(4):044711, 2017. doi:10.7566/JPSJ.86.044711.

[31] M. Tsujimoto, Y. Matsumoto, T. Tomita, A. Sakai, and S. Nakatsuji. Heavy-Fermion Superconductivity in the Quadrupole Ordered State of PrV_2Al_{20}. *Phys. Rev. Lett.*, 113(26):267001, 2014. doi:10.1103/PhysRevLett.113.267001.

[32] Y. Shimura, M. Tsujimoto, B. Zeng, L. Balicas, A. Sakai, and S. Nakatsuji. Field-induced quadrupolar quantum criticality in PrV_2Al_{20}. *Phys. Rev. B*, 91(24):241102, 2015. doi:10.1103/PhysRevB.91.241102.

[33] K. Matsubayashi, T. Tanaka, A. Sakai, S. Nakatsuji, Y. Kubo, and Y. Uwatoko. Pressure-Induced Heavy Fermion Superconductivity in the Nonmagnetic Quadrupolar System $PrTi_2Al_{20}$. *Phys. Rev. Lett.*, 109(18):187004, 2012. doi:10.1103/PhysRevLett.109.187004.

[34] T. J. Sato, S. Ibuka, Y. Nambu, T. Yamazaki, T. Hong, A. Sakai, and S. Nakatsuji. Ferroquadrupolar ordering in $PrTi_2Al_{20}$. *Phys. Rev. B*, 86(18):184419, 2012. doi:10.1103/PhysRevB.86.184419.

[35] M. Fu, A. Sakai, N. Sogabe, M. Tsujimoto, Y. Matsumoto, and S. Nakatsuji. Unveiling Quadrupolar Kondo Effect in the Heavy Fermion Superconductor PrV_2Al_{20}. *J. Phys. Soc. Jpn.*, 89(1):013704, 2020. doi:10.7566/JPSJ.89.013704.

[36] A. Sakai, K. Kuga, and S. Nakatsuji. Superconductivity in the Ferroquadrupolar State in the Quadrupolar Kondo Lattice $PrTi_2Al_{20}$. *J. Phys. Soc. Jpn.*, 81(8):083702, 2012. doi:10.1143/JPSJ.81.083702.

[37] I. Ishii, H. Muneshige, Y. Suetomi, T. K. Fujita, T. Onimaru, K. T. Matsumoto, T. Takabatake, K. Araki, M. Akatsu, Y. Nemoto, T. Goto, and T. Suzuki. Antiferro-Quadrupolar Ordering at the Lowest Temperature and Anisotropic Magnetic Field–Temperature Phase Diagram in the Cage Compound $PrIr_2Zn_{20}$. *J. Phys. Soc. Jpn.*, 80(9):093601, 2011. doi:10.1143/JPSJ.80.093601.

[38] I. Ishii, H. Muneshige, S. Kamikawa, T. K. Fujita, T. Onimaru, N. Nagasawa, T. Takabatake, T. Suzuki, G. Ano, M. Akatsu, Y. Nemoto, and T. Goto. Antiferroquadrupolar ordering and magnetic-field-induced phase transition in the cage compound $PrRh_2Zn_{20}$. *Phys. Rev. B*, 87(20):205106, 2013. doi:10.1103/PhysRevB.87.205106.

[39] K. Araki, Y. Shimura, N. Kase, T. Sakakibara, A. Sakai, and S. Nakatsuji. Magnetization and Specific Heat of the Cage Compound PrV_2Al_{20}. *JPS Conf. Proc.*, 3:011093, 2014. doi:10.7566/JPSCP.3.011093.

[40] A. Tsuruta and K. Miyake. Non-Fermi Liquid and Fermi Liquid in Two-Channel Anderson Lattice Model: Theory for PrA_2Al_{20} (A = V, Ti) and $PrIr_2Zn_{20}$. *J. Phys. Soc. Jpn.*, 84(11):114714, 2015. doi:10.7566/JPSJ.84.114714.

[41] I. Affleck and A. W. W. Ludwig. Exact conformal-field-theory results on the multichannel Kondo effect: Single-fermion Green's function, self-energy, and resistivity. *Phys. Rev. B*, 48(10):7297–7321, 1993. doi:10.1103/PhysRevB.48.7297.

[42] Y. Yamane, T. Onimaru, K. Wakiya, K. T. Matsumoto, K. Umeo, and T. Takabatake. Single-Site Non-Fermi-Liquid Behaviors in a Diluted $4f^2$ System $Y_{1-x}Pr_xIr_2Zn_{20}$. *Phys. Rev. Lett.*, 121(7):077206, 2018. doi:10.1103/PhysRevLett.121.077206.

[43] Y. Yamane, T. Onimaru, K. Uenishi, K. Wakiya, K. T. Matsumoto, K. Umeo, and T. Takabatake. Impurity quadrupole Kondo ground state in a dilute Pr system $Y_{1-x}Pr_xIr_2Zn_{20}$. *Physica B*, 536:40–42, 2018. doi:10.1016/j.physb.2017.07.062.

[44] T. Yanagisawa, H. Hidaka, H. Amitsuka, S. Zherlitsyn, J. Wosnitza, Y. Yamane, and T. Onimaru. Evidence for the Single-Site Quadrupolar Kondo Effect in the Dilute Non-Kramers System $Y_{1-x}Pr_xIr_2Zn_{20}$. *Phys. Rev. Lett.*, 123(6):067201, 2019. doi:10.1103/PhysRevLett.123.067201.

[45] T. Ikeura, T. Matsubara, Y. Machida, K. Izawa, N. Nagasawa, K. T. Matsumoto, T. Onimaru, and T. Takabatake. Anomalous Enhancement of Seebeck Coefficient in $PrIr_2Zn_{20}$. *JPS Conf. Proc.*, 3:011091, 2014. doi:10.7566/JPSCP.3.011091.

[46] Y. Machida, T. Yoshida, T. Ikeura, K. Izawa, A. Nakama, R. Higashinaka, Y. Aoki, H. Sato, A. Sakai, S. Nakatsuji, N. Nagasawa, K. Matsumoto, T. Onimaru, and T. Takabatake. Anomalous Enhancement of Seebeck Coefficient in Pr-Based 1-2-20 System with Non-Kramers Doublet Ground States. *J. Phys.: Conf. Ser.*, 592:012025, 2015. doi:10.1088/1742-6596/592/1/012025.

[47] P. Coleman. *Introduction to Many-Body Physics*. Cambridge University Press, 2015. ISBN 978-0-521-86488-6.

[48] N. W. Ashcroft and D. N. Mermin. *Solid State Physics*. Harcourt Brace College Publishers, 1976. ISBN 0-03-083993-9.

[49] K. Andres, J. E. Graebner, and H. R. Ott. $4f$-Virtual-Bound-State Formation in $CeAl_3$ at Low Temperatures. *Phys. Rev. Lett.*, 35(26):1779–1782, 1975. doi:10.1103/PhysRevLett.35.1779.

[50] C. Kittel. *Einführung in die Festkörperphysik*. Oldenbourg Wissenschaftsverlag GmbH, München, Wien, Oldenbourg, 2002. 13., korrigierte Auflage. ISBN 3-486-27219-5.

[51] L. D. Landau and E. M. Lifschitz. *Lehrbuch der Theoretischen Physik VII Elastizitätstheorie*. Akademie Verlag, Berlin, 1991. 7., überarbeitete Auflage. ISBN 3-05-500580-5.

[52] T. H. K. Barron, J. G. Collins, and G. K. White. Thermal expansion of solids at low temperatures. *Adv. Phys.*, 29(4):609–730, 1980. doi:10.1080/00018738000101426.

[53] E. Grüneisen. Theorie des festen Zustandes einatomiger Elemente. *Ann. Phys.*, 344(12):257–306, 1912. doi:10.1002/andp.19123441202.

[54] L. Zhu, M. Garst, A. Rosch, and Q. Si. Universally Diverging Grüneisen Parameter and the Magnetocaloric Effect Close to Quantum Critical Points. *Phys. Rev. Lett.*, 91(6):066404, 2003. doi:10.1103/PhysRevLett.91.066404.

[55] H. U. Häfner. Volume magnetostriction of intermediate valence systems. *J. Magn. Magn. Mater.*, 47-48:299–301, 1985. doi:10.1016/0304-8853(85)90422-6.

[56] M. Doerr, M. Rotter, and A. Lindbaum. Magnetostriction in rare-earth based antiferromagnets. *Adv. Phys.*, 54(1):1–66, 2005. doi:10.1080/00018730500037264.

[57] T. Miyake and H. Akai. Quantum theory of rare-earth magnets. *J. Phys. Soc. Jpn.*, 87(4):041009, 2018. doi:10.7566/JPSJ.87.041009.

[58] P. Gegenwart. Grüneisen parameter studies on heavy fermion quantum criticality. *Rep. Prog. Phys.*, 79(11):114502, 2016. doi:10.1088/0034-4885/79/11/114502.

[59] A. de Visser, J. J. M. Franse, and J. Flouquet. Magneto-volume effects in some selected heavy-fermion compounds. *Physica B: Condensed Matter*, 161(1):324–332, 1990. doi:10.1016/0921-4526(89)90156-7.

[60] M. Vojta. Quantum phase transitions. *Rep. Prog. Phys.*, 66(12):2069–2110, 2003. doi:10.1088/0034-4885/66/12/r01.

[61] M. Zacharias, I. Paul, and M. Garst. Quantum critical elasticity. *Phys. Rev. Lett.*, 115(2):025703, 2015. doi:10.1103/PhysRevLett.115.025703.

[62] J. M. D. Coey. *Magnetism and Magnetic Materials*. Cambridge University Press, 2018. ISBN 978-1-108-71751-9.

[63] K. W. H. Stevens. Matrix Elements and Operator Equivalents Connected with the Magnetic Properties of Rare Earth Ions. *Proc. Phys. Soc. A*, 65(3):209–215, 1952. doi:10.1088/0370-1298/65/3/308.

[64] K. R. Lea, M. J. M. Leask, and W. P. Wolf. The raising of angular momentum degeneracy of f-Electron terms by cubic crystal fields. *J. Phys. Chem. Solids*, 23(10):1381–1405, 1962. doi:10.1016/0022-3697(62)90192-0.

[65] K. Iwasa, H. Kobayashi, T. Onimaru, K. T. Matsumoto, N. Nagasawa, T. Takabatake, S. Ohira-Kawamura, T. Kikuchi, Y. Inamura, and K. Nakajima. Well-Defined Crystal Field Splitting Schemes and Non-Kramers Doublet Ground States of f Electrons in PrT_2Zn_{20} (T = Ir, Rh, and Ru). *J. Phys. Soc. Jpn.*, 82(4):043707, 2013. doi:10.7566/JPSJ.82.043707.

[66] Y. Kuramoto, H. Kusunose, and A. Kiss. Multipole Orders and Fluctuations in Strongly Correlated Electron Systems. *J. Phys. Soc. Jpn.*, 78(7):072001, 2009. doi:10.1143/JPSJ.78.072001.

[67] M.-T. Suzuki, H. Ikeda, and P. M. Oppeneer. First-principles Theory of Magnetic Multipoles in Condensed Matter Systems. *J. Phys. Soc. Jpn.*, 87(4):041008, 2018. doi:10.7566/JPSJ.87.041008.

[68] R. Shiina, H. Shiba, and P. Thalmeier. Magnetic-Field Effects on Quadrupolar Ordering in a Γ_8-Quartet System CeB_6. *J. Phys. Soc. Jpn.*, 66(6):1741–1755, 1997. doi:10.1143/JPSJ.66.1741.

[69] B. Lüthi. *Physical Acoustics in the Solid State*. Springer Verlag, Berlin, Heidelberg, New York, 2007. 2nd Printing of the First Edition. ISBN 978-3-540-72193-2.

[70] P. Morin, J. Rouchy, D. Schmitt, and E. du Tremolet de Lacheisserie. Quadrupole interactions in cubic rare earth intermetallics. *J. Phys. Colloques*, 40(C5):101–106, 1979. doi:10.1051/jphyscol:1979536.

[71] E. R. Callen and H. B. Callen. Static Magnetoelastic Coupling in Cubic Crystals. *Phys. Rev.*, 129(2):578–593, 1963. doi:10.1103/PhysRev.129.578.

[72] P. Morin and D. Schmitt. Quadrupole Interactions in Rare-Earth Intermetallic Compounds. *J. Phys. Colloques*, 49(C8):321–325, 1988. doi:10.1051/jphyscol:19888144.

[73] P. Morin, D. Schmitt, and E. du Tremolet de Lacheisserie. Parastriction: A new probe for quadrupolar interactions in rare-earth compounds. *Phys. Rev. B*, 21(5):1742–1751, 1980. doi:10.1103/PhysRevB.21.1742.

[74] P. Thalmeier and B. Lüthi. Chapter 96 The electron-phonon interaction in intermetallic compounds. In *Handbook on the Physics and Chemistry of Rare Earths*, volume 14, pages 225–341. Elsevier, 1991. ISBN 0444887431.

[75] V. A. Fateev and P. B. Wiegmann. The exact solution of the s-d exchange model with arbitrary impurity spin S (Kondo problem). *Phys. Lett. A*, 81(2):179–184, 1981. doi:10.1016/0375-9601(81)90056-6.

[76] T. Kasuya. A Theory of Metallic Ferro- and Antiferromagnetism on Zener's Model. *Prog. Theor. Phys.*, 16(1):45–57, 1956. doi:10.1143/PTP.16.45.

[77] C. Zener. Interaction Between the d Shells in the Transition Metals. *Phys. Rev.*, 81(3):440–444, 1951. doi:10.1103/PhysRev.81.440.

[78] K. Yosida. Magnetic Properties of Cu-Mn Alloys. *Phys. Rev.*, 106(5):893–898, 1957. doi:10.1103/PhysRev.106.893.

[79] K. Yosida. Anomalous Electrical Resistivity and Magnetoresistance Due to an $s-d$ Interaction in Cu-Mn Alloys. *Phys. Rev.*, 107(2):396–403, 1957. doi:10.1103/PhysRev.107.396.

[80] A. A. Abrikosov. Electron scattering on magnetic impurities in metals and anomalous resistivity effects. *Phys. Phys. Fiz.*, 2(1):5–20, 1965. doi:10.1103/PhysicsPhysiqueFizika.2.5.

[81] P. W. Anderson. Localized Magnetic States in Metals. *Phys. Rev.*, 124(1):41–53, 1961. doi:10.1103/PhysRev.124.41.

[82] P. W. Anderson. Local moments and localized states. *Rev. Mod. Phys.*, 50(2):191–201, 1978. doi:10.1103/RevModPhys.50.191.

[83] J. R. Schrieffer and P. A. Wolff. Relation between the Anderson and Kondo Hamiltonians. *Phys. Rev.*, 149(2):491–492, 1966. doi:10.1103/PhysRev.149.491.

[84] A. C. Hewson. *The Kondo Problem to Heavy Fermions*. Cambridge University Press, 1993. ISBN 0-521-36382-9.

[85] P. Nozières. A "fermi-liquid" description of the Kondo problem at low temperatures. *J. Low Temp. Phys.*, 17:31–42, 1974. doi:10.1007/BF00654541.

[86] P. Fazekas and E. Müller-Hartmann. Magnetic and non-magnetic ground states of the Kondo lattice. *Z. Physik B - Condensed Matter*, 85:285–300, 1991. doi:10.1007/BF01313231.

[87] C. Lacroix. Coherence effects in the Kondo lattice. *J. Magn. Magn. Mater.*, 60(2):145–152, 1986. doi:10.1016/0304-8853(86)90093-4.

[88] M. Lavagna, C. Lacroix, and M. Cyrot. Resistivity of the Kondo lattice. *J. Phys. F: Met. Phys.*, 12(4):745–757, 1982. doi:10.1088/0305-4608/12/4/015.

[89] M. A. Ruderman and C. Kittel. Indirect Exchange Coupling of Nuclear Magnetic Moments by Conduction Electrons. *Phys. Rev.*, 96(1):99–102, 1954. doi:10.1103/PhysRev.96.99.

[90] P. Schlottmann and P. D. Sacramento. Multichannel Kondo problem and some applications. *Adv. Phys.*, 42(6):641–682, 1993. doi:10.1080/00018739300101534.

[91] P. D. Sacramento and P. Schlottmann. Thermodynamics of the n-channel kondo model for general n and impurity spin S in a magnetic field. *J. Phys.: Condens. Matter*, 3(48):9687–9696, 1991. doi:10.1088/0953-8984/3/48/010.

[92] N. Andrei and C. Destri. Solution of the Multichannel Kondo Problem. *Phys. Rev. Lett.*, 52(5):364–367, 1984. doi:10.1103/PhysRevLett.52.364.

[93] I. Affleck. Conformal Field Theory Approach to the Kondo Effect. *Acta Phys. Polon. B*, 26:1869–1932, 1995.

[94] Y. Yamane, T. Onimaru, K. Wakiya, K. T. Matsumoto, K. Umeo, and T. Takabatake. Magnetic field effects on the specific heat of a diluted Pr system $Y_{1-x}Pr_xIr_2Zn_{20}$. *AIP Adv.*, 8(10):101338, 2018. doi:10.1063/1.5043132.

[95] D. L. Cox. Selection rules for two-channel Kondo models of U^{4+} and Ce^{3+} ions in metals. *Physica B*, 186-188:312–316, 1993. doi:10.1016/0921-4526(93)90563-L.

[96] D. L. Cox. The quadrupolar Kondo effect: A new mechanism for heavy electrons. *J. Magn. Magn. Mater.*, 76-77:53–58, 1988. doi:10.1016/0304-8853(88)90315-0.

[97] T. Onimaru, K. T. Matsumoto, Y. F. Inoue, K. Umeo, Y. Saiga, Y. Matsushita, R. Tamura, K. Nishimoto, I. Ishii, T. Suzuki, and T. Takabatake. Superconductivity and Structural Phase Transitions in Caged Compounds RT_2Zn_{20} (R = La, Pr, T = Ru, Ir). *J. Phys. Soc. Jpn.*, 79(3):033704, 2010. doi:10.1143/JPSJ.79.033704.

[98] M. Jarrell, H. Pang, D. L. Cox, and K. H. Luk. Two-Channel Kondo Lattice: An Incoherent Metal. *Phys. Rev. Lett.*, 77(8):1612–1615, 1996. doi:10.1103/PhysRevLett.77.1612.

[99] S. Hoshino, J. Otsuki, and Y. Kuramoto. Diagonal Composite Order in a Two-Channel Kondo Lattice. *Phys. Rev. Lett.*, 107(24):247202, 2011. doi:10.1103/PhysRevLett.107.247202.

[100] S. Hoshino, J. Otsuki, and Y. Kuramoto. Resolution of Entropy ln $\sqrt{2}$ by Ordering in Two-Channel Kondo Lattice. *J. Phys. Soc. Jpn.*, 82(4):044707, 2013. doi:10.7566/JPSJ.82.044707.

[101] G. Zhang, J. S. Van Dyke, and R. Flint. Cubic hastatic order in the two-channel Kondo-Heisenberg model. *Phys. Rev. B*, 98(23):235143, 2018. doi:10.1103/PhysRevB.98.235143.

[102] J. S. Van Dyke, G. Zhang, and R. Flint. Field-induced ferrohastatic phase in cubic non-Kramers doublet systems. *Phys. Rev. B*, 100(20):205122, 2019. doi:10.1103/PhysRevB.100.205122.

[103] F. Pobell. *Matter and Methods at Low Temperatures*. Springer-Verlag Berlin Heidelberg, 1996. 2nd Edition. ISBN 3-540-58572-9.

[104] J. Wilks and D. S. Betts. *An Introduction to Liquid Helium*. Oxford University Press, 1987. 2nd Edition. ISBN 0-19-851472-7.

[105] Z. Dokoupil, D. G. Kapadnis, K. Sreeramamurty, and K. W. Taconis. Specific heat of mixtures of ^{4}He and ^{3}He between 1°K and 4°K. *Physica*, 25(7):1369–1375, 1959. doi:10.1016/0031-8914(59)90058-8.

[106] R. De Bruyn Ouboter, K. W. Taconis, C. Le Pair, and J. J. M. Beenakker. Thermodynamic properties of liquid ^{3}He-^{4}He mixtures derived from specific heat measurements between 0.4°K and 2°K over the complete concentration range. *Physica*, 26(11):853–888, 1960. doi:10.1016/0031-8914(60)90037-9.

[107] J. P. Laheurte and J. R. G. Keyston. Behaviour of He^4 in dilute liquid mixtures of He^4 in He^3. *Cryogenics*, 11(6):485–486, 1971. doi:10.1016/0011-2275(71)90277-3.

[108] C. Ebner and D. O. Edwards. The low temperature thermodynamic properties of superfluid solutions of ^{3}He in ^{4}He. *Phys. Rep.*, 2(2):77–154, 1971. doi:10.1016/0370-1573(71)90003-2.

[109] T. A. Alvesalo, P. M. Berglund, S. T. Islander, G. R. Pickett, and W. Zimmermann. Specific Heat of Liquid He^3/He^4 Mixtures near the Junction of the λ and Phase-Separation Curves. I. *Phys. Rev. A*, 4(6):2354–2368, 1971. doi:10.1103/PhysRevA.4.2354.

[110] A. Ghozlan and E. J. A Varoquaux. *C. R. Acad. Sci. (Paris) Ser. B*, 280(189), 1975.

[111] A. Wörl. Novel types of Quantum Criticality in 4f-based Intermetallics. Master's thesis, University of Augsburg, Germany, 2016.

[112] R. Küchler, A. Wörl, P. Gegenwart, M. Berben, B. Bryant, and S. Wiedmann. The world's smallest capacitive dilatometer, for high-resolution thermal expansion and magnetostriction in high magnetic fields. *Rev. Sci. Instrum.*, 88(8):083903, 2017. doi:10.1063/1.4997073.

[113] R. Küchler, C. Stingl, and P. Gegenwart. A uniaxial stress capacitive dilatometer for high-resolution thermal expansion and magnetostriction under multiextreme conditions. *Rev. Sci. Instrum.*, 87(7):073903, 2016. doi:10.1063/1.4958957.

[114] R. Küchler, T. Bauer, M. Brando, and F. Steglich. A compact and miniaturized high resolution capacitance dilatometer for measuring thermal expansion and magnetostriction. *Rev. Sci. Instrum.*, 83(9):095102, 2012. doi:10.1063/1.4748864.

[115] R. Küchler, C. Stingl, Y. Tokiwa, M. S. Kim, T. Takabatake, and P. Gegenwart. Uniaxial stress tuning of geometrical frustration in a Kondo lattice. *Phys. Rev. B*, 96(24):241110(R), 2017. doi:10.1103/PhysRevB.96.241110.

[116] R. Pott and R. Schefzyk. Apparatus for measuring the thermal expansion of solids between 1.5 and 380K. *J. Phys. E: Sci. Instrum.*, 16(5):444–449, 1983. doi:10.1088/0022-3735/16/5/018.

[117] D. A. Ackerman and A. C. Anderson. Dilatometry at low temperatures. *Rev. Sci. Instrum.*, 53(11):1657–1660, 1982. doi:10.1063/1.1136879.

[118] K. Momma and F. Izumi. Vesta 3 for three-dimensional visualization of crystal, volumetric and morphology data. *J. Appl. Cryst.*, 44:1272–1276, 2011. doi:10.1107/S0021889811038970.

[119] T. Nasch, W. Jeitschko, and U. C. Rodewald. Ternary Rare Earth Transition Metal Zinc Compounds RT_2Zn_{20} with T = Fe, Ru, Co, Rh, and Ni. *Z. Naturforsch. B*, 52(9):1023–1030, 1997. doi:10.1515/znb-1997-0901.

[120] K. Iwasa, K. T. Matsumoto, T. Onimaru, T. Takabatake, J.-M. Mignot, and A. Gukasov. Evidence for antiferromagnetic-type ordering of f-electron multipoles in $PrIr_2Zn_{20}$. *Phys. Rev. B*, 95(15):155106, 2017. doi:10.1103/PhysRevB.95.155106.

[121] D. L. Cox and A. Zawadowski. Exotic Kondo effects in metals: Magnetic ions in a crystalline electric field and tunnelling centres. *Adv. Phys.*, 47(5):599–942, 1998. doi:10.1080/000187398243500.

[122] P. Chandra, P. Coleman, and R. Flint. Hastatic order in the heavy-fermion compound URu_2Si_2. *Nature*, 493:621–626, 2013. doi:10.1038/nature11820.

[123] S. Yotsuhashi and H. Maebashi. Crossover Temperature from Non-Fermi Liquid to Fermi Liquid Behavior in Two Types of Impurity Kondo Model. *J. Phys. Soc. Jpn.*, 71(7):1705–1711, 2002. doi:10.1143/JPSJ.71.1705.

[124] A. Wörl, T. Onimaru, Y. Tokiwa, Y. Yamane, K. T. Matsumoto, T. Takabatake, and P. Gegenwart. Highly anisotropic strain dependencies in $PrIr_2Zn_{20}$. *Phys. Rev. B*, 99(8):081117(R), 2019. doi:10.1103/PhysRevB.99.081117.

[125] A. de Visser, P. Haen, P. Lejay, and J. Flouquet. Thermal Expansion of Heavy-Fermion $CeRu_2Si_2$. *J. Phys. Colloques*, 49(C8):767–768, 1988. doi:10.1051/jphyscol:19888346.

[126] A. de Visser, A. Lacerda, P. Haen, J. Flouquet, F. E. Kayzel, and J. J. M. Franse. Thermal expansion of monocrystalline heavy-fermion $CeCu_6$. *Phys. Rev. B*, 39(16):11301–11306, 1989. doi:10.1103/PhysRevB.39.11301.

[127] K. Behnia, D. Jaccard, and J. Flouquet. On the thermoelectricity of correlated electrons in the zero-temperature limit. *J. Phys.: Condens. Matter*, 16(28):5187–5198, 2004. doi:10.1088/0953-8984/16/28/037.

[128] T. Takeuchi, S. Yasui, M. Toda, M. Matsushita, S. Yoshiuchi, M. Ohya, K. Katayama, Y. Hirose, N. Yoshitani, F. Honda, K. Sugiyama, M. Hagiwara, K. Kindo, E. Yamamoto, Y. Haga, T. Tanaka, Y. Kubo, R. Settai, and Y. Ōnuki. Metamagnetic Behavior in Heavy-Fermion Compound $YbIr_2Zn_{20}$. *J. Phys. Soc. Jpn.*, 79(6):064609, 2010. doi:10.1143/JPSJ.79.064609.

[129] Y. Yamane. *Non-Fermi Liquid Behaviors in Diluted Pr Systems (Y,Pr)T_2Zn_{20} (T = Ir, Co)*. Doctoral thesis, Hiroshima University, Japan, 2020.

[130] A. Tsuruta and K. Miyake. Unconventional Non-Fermi Liquid Properties of Two-Channel Anderson Impurities System, 2021. arXiv:1911.04683v4.

[131] A. Tsuruta, A. Kobayashi, Y. Ōno, T. Matsuura, and Y. Kuroda. Non-Fermi Liquid in Multichannel Degenerate Anderson Lattice. *J. Phys. Soc. Jpn*, 68(8):2491–2494, 1999. doi:10.1143/JPSJ.68.2491.

[132] W. A. Phillips. Tunneling states in amorphous solids. *J. Low Temp. Phys.*, 7(3):351–360, 1972. doi:10.1007/BF00660072.

[133] P. W. Anderson, B. I. Halperin, and C. M. Varma. Anomalous low-temperature thermal properties of glasses and spin glasses. *Philos. Mag.*, 25(1):1–9, 1972. doi:10.1080/14786437208229210.

[134] A. Wörl, M. Garst, Y. Yamane, S. Bachus, T. Onimaru, and P. Gegenwart. Divergent thermal expansion and Grüneisen ratio in a quadrupolar Kondo metal. *Phys. Rev. Research*, 4(2):L022053, 2022. doi:10.1103/PhysRevResearch.4.L022053.

[135] A. P. Ramirez, P. Chandra, P. Coleman, Z. Fisk, J. L. Smith, and H. R. Ott. Nonlinear Susceptibility: A Direct Test of the Quadrupolar Kondo Effect in UBe_{13}. *Phys. Rev. Lett.*, 73(22):3018–3021, 1994. doi:10.1103/PhysRevLett.73.3018.

List of Publications

Publications related to parts of the experimental results presented in this thesis:

- A. Wörl, M. Garst, Y. Yamane, S. Bachus, T. Onimaru, and P. Gegenwart. Divergent thermal expansion and Grüneisen ratio in a quadrupolar Kondo metal. *Phys. Rev. Research*, 4(2):L022053, 2022. doi : 10.1103/PhysRevResearch.4.L022053.

- A. Wörl, T. Onimaru, Y. Tokiwa, Y. Yamane, K. T. Matsumoto, T. Takabatake, and P. Gegenwart. Highly anisotropic strain dependencies in $PrIr_2Zn_{20}$. *Phys. Rev. B*, 99(8):081177(R), 2019. doi : 10.1103/PhysRevB.99.081117.

Publications related to the experimental method employed in this thesis:

- R. Küchler, A. Wörl, P. Gegenwart, M. Berben, B. Bryant, and S. Wiedmann. The world's smallest capacitive dilatometer, for high-resolution thermal expansion and magnetostriction in high magnetic fields. *Rev. Sci. Instr.* 88(8):083903, 2017. doi : 10.1063/1.4997073.

Other publications:

- Y. Shimura*, A. Wörl*, M. Sundermann*, S. Tsuda, D. T. Adroja, A. Bhattacharyya, A. M. Strydom, A. D. Hillier, F. L. Pratt, A. Gloskovskii, A. Severing, T. Onimaru, P. Gegenwart, and T. Takabatake. Antiferromagnetic Correlations in Strongly Valence Fluctuating CeIrSn. *Phys. Rev. Lett.*, 126(21):217202, 2021. doi : 10.1103/PhysRevLett.126.217202. (* Equal contribution).

- S. Bachus, I. A. Iakovlev, Y. Li, A. Wörl, Y. Tokiwa, L. Ling, Q. Zhang, V. V. Mazurenko, P. Gegenwart, and A. A. Tsirlin. Field evolution of the spin-liquid candidate $YbMgGaO_4$. *Phys. Rev. B*, 102(10):104433, 2020. doi : 10.1103/PhysRevB.102.104433.

Acknowledgments

Finally, I would like to thank all the people who supported me during this journey.

- My supervisor **Prof. Dr. Philipp Gegenwart** for the opportunity to work on a challenging yet exciting research topic. For always having an open ear for discussions and reminding me to focus on the important things when I lost track.
- **Priv.-Doz. Dr. Hans Albrecht Krug von Nidda** for agreeing on evaluating this thesis as a second reviewer.
- **Prof. Dr. Takahiro Onimaru** for the close collaboration during the last years. In particular for providing high quality and carefully characterized single crystalline samples of $PrIr_2Zn_{20}$ and $Y_{1-x}Pr_xIr_2Zn_{20}$. Furthermore, for the time and patience in teaching me the physics of quadrupolar Kondo metals. Thank you for establishing the fun soccer games after work and for all the other joint activities during research visits.
- **Prof. Dr. Markus Garst** for the successful collaboration and in particular for carrying out calculations that helped to shed light on the divergent volume thermal expansion in $Y_{1-x}Pr_xIr_2Zn_{20}$. For the many insightful discussions and always finding time to answer my never ending questions. Also for the ability to explain theoretical physics in a way that also an experimentalist can understand.
- **Dr. Yoshifumi Tokiwa** for sharing his broad experience and knowledge in low temperature physics. Also for the encouraging words and the good vibes that helped me to overcome one or the other difficult time in the low temperature lab.
- **Dr. Yu Yamane** for the growth and characterization of the $Y_{1-x}Pr_xIr_2Zn_{20}$ single crystals. Also for the interesting discussions on physics and other topics as well as the common cooking evenings and other leisure activities during research visits.
- **Sebastian Bachus**, **Sven Esser**, **Andreas Schneider** and **Maximilian Uhl** for the great atmosphere in the office and the memorable moments we shared together.
- **Birgitta Eisenschmidt** and **Christine Schäfer** for the pleasant conversations and the support with administrative matters.
- **All members of the Chair of Experimental Physics VI** for the positive working environment and the good atmosphere.
- Last but not least, **my family** and **my girlfriend Bora** for the continuous support and encouragement.